2010

Investigation and modeling of viscoelastic moduli for multilayered polymeric systems using high frequency ultrasonic waves

Todd Mathew Fernandez

Investigation and Modeling of Viscoelastic Moduli for Multilayered Polymeric Systems Using High Frequency Ultrasonic Waves

by

Todd Mathew Fernandez

A thesis submitted in partial fulfillment of the requirements for the degree of Master of Science in Mechanical Engineering from the Rochester Institute of Technology, Rochester NY.

THESIS RELEASE PERMISSION
ROCHESTER INSTITUTE OF TECHNOLOGY
DEPARTMENT OF MECHANICAL ENGINEERING

Title of Thesis:

Investigation and Modeling of Viscoelastic Moduli for Multilayered Polymeric Systems Using High Frequency Ultrasonic Waves

I, Todd M. Fernandez, herby grant permission to Wallace Memorial Library of R.I.T to reproduce my thesis in whole or in part. Any reproduction will not be for commercial use or profit.

Signature:_____

Date:_____

ROCHESTER INSTITUTE OF TECHNOLOGY
DEPARTMENT OF MECHANICAL ENGINEERING
ROCHESTER, NY.

CERTIFICATION OF APPROVAL

MASTERS OF SCIENCE DEGREE DEFENCE

The Master of Science Degree Dissertation for Todd M. Fernandez has been examined and approved by the thesis committee as satisfactory for the defence required for the Masters of Science Degree in Mechanical Engineering

Dr. B. Varela, Advisor	Date
Dr. M. Helguera	Date
Dr. B. Jadamba	Date
Dr. A. Khan	Date
Dr. E. C. Hensel	Date

Investigation and Modeling of Viscoelastic Moduli for Multilayered Polymeric Systems Using High Frequency Ultrasonic Waves

by

Todd Mathew Fernandez

A thesis submitted in partial fulfillment of the requirements for the degree of Master of Science in Mechanical Engineering from the Rochester Institute of Technology, Rochester NY.

Abstract:

Mechanical characterization of both the bulk and individual layer properties of layered polymer stacks provides important information for their use in novel applications. A single technique to measure both the bulk and layer properties is atempted. Ultrasonic testing provides an opportunity to determine the mechanical characteristics for layered samples in the form of the complex mechanical moduli. These moduli express the viscoelastic properties of the materials. Using ultrasound, this can be done for the bulk and the layers in a single test. With ultrasound, the ability to determine the complex moduli in single layers has been demonstrated. The moduli were determined within the expected range. The ultrasonic testing has also allowed the determination of the speed of sound of the individual layers in a 2 layer sample consisting of layers of Polycarbonate and Poly(methyl methacrylate). Internal interference limited the ability to measure attenuation. To attempt to allow for analysis of these complex waveforms, a secondary technique for waveform analysis has been proposed and developed. This method employs a finite element simulation to replicate the experiment. By deriving a simulation with the complex moduli as inputs, it is possible to use the simulation results to measure the moduli of multilayered samples. This is done comparatively through iteration of the simulation inputs. When a set of inputs creates a simulated result matching the experimental scans, a solution has been found. A preliminary version of the simulation is presented and demonstrated.

Acknowledgments

My work would not be complete without thanking the wonderful people who have helped me throughout this process. Without their support and guidance, I could never have completed this process. First, I thank my family and friends. Without them, I would not be where I am today. I am especially thankful to my parents for always being there for me through thick and thin, 7 years of college, and co-ops on both coast with an unending willingness to listen.

I must also recognize the researchers at CLiPS for supporting and funding our work and helping us define our direction. For their assistance with all of my ultrasonic testing and analysis, I thank Dr. Diane Dalecki at the University of Rochester for the use of her lab facilities, Nick Berry at the University of Rochester who provided many moments of clarity during testing, and Dr. Maria Helguera from the Center for Imaging Science for her guidance in experimental work and analysis. For their enormous help with the implementation of my analytical simulation, I whole heartedly thank Dr. Baasansuren Jadamba and Dr. Ahktar Khan of COS. I must also thank Dr. Varela for all of his assistance, guidance, advice, and willingness to take me on as a graduate student. I have known Dr. Varela since I was a stubborn freshman and he was my advisor. He has provided me with advice and support for which I am, and will always be, truly grateful.

Most importantly, I must thank my wife Maggie. She has been my biggest supporter and champion for almost 6 years. Often, she has believed in me more than I have believed in myself. She is my best friend and biggest supporter and this thesis is dedicated to her.

This material is based upon work supported by the National Science Foundation under Award No. DMR-0423914

Table of Contents

List of Symbols and Units

C_{long}	Longitudinal speed of sound (m/s)
C_s	Shear speed of sound (m/s)
ρ	Density (kg/m^3)
Z	Acoustical impedance (Ns/m^3)
f	Frequency (Hz,MHz)
E	Tensile Modulus (GPa)
E’	Storage Modulus (GPa)
E’’	Loss Modulus (GPa)
δ	Phase Lag (rad)
ω	Phase velocity (rad/sec)
λ	Wavelength (m,μm)
σ	Stress, also expressed as T (Pa,GPa)
η	Viscosity (Pa*s)
α	Attenuation coefficient (dB/mm)
ν	Poisson’s ratio
R	Reflective coefficient
T	Transmissive coefficient

CMM Coordinate Measuring Machine

CLiPS Center for Layered integrated Polymer Systems

DMA Dynamic Mechanical Analysis

FEM Finite Element method, as called FEA for finite element analysis

FFT Fast Fourier Transform

NDT Non-destructive Testing

NSF National Science Foundation

ODE Ordinary Differential Equation

PC Polycarbonate

PDE Partial Differential Equation

PMMA Poly(methyl methacrylate)

SEM Scanning Electron Microscope

STC Science and Technology Center

TOF Time of Flight (s,μs,ns)

List of Figures

List of Equations

List of Tables

Chapter 1

Introduction

Advances in materials science have led to significantly improved novel materials, often with useful and advanced engineering properties. One specific category of these materials is known as polymer-layered systems. These materials contain repeating layers of thin film polymers that form a single thicker polymer matrix. By tailoring the specific materials, individual layer thicknesses, and number of layers specifically tuning the properties for a select application is possible. This leads to new challenges in analyzing the different combinations, yet provides an almost limitless array of polymer combinations that are adjustable to application specific properties for a large number of purposes.

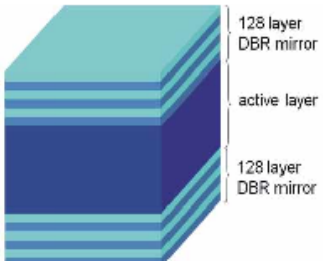

Figure 1-1 Dye-doped laser using layered polymer surface layers[1]

Research on many of these material stacks is ongoing. Most of the current work surrounds their use in optical applications, electrical applications, and numerous mechanical applications, including gas membranes. One use of polymer systems currently under investigation is their use as portions of dye-doped lasers[1], an example cross-section of which can be seen in Figure 1-1. Some work however, has gone into developing techniques to investigate the mechanical properties of these materials using multiple different methods

tailored to specific situations and to the properties under study. The layering of polymers provide unique opportunities due to the unique properties of the chemical mechanical bond commonly called the interphase[2], and the use of multiple unique materials combining to form a single structure. A thorough analytical model correlation of the polymer stacks must combine models of the individual polymer constituents with a model representing the unique characteristics of the interface bond. The analytical correlation must take into account the interlayer bond, as well as the separate viscoelastic behavior of each material. This correlation lies at the core goals of the work presented here. Developing an effective understanding and model of these materials is a necessary component of taking them beyond the research phase and into industrial implementation and use.

To represent complexity and flexibility of these materials, the term 'Layered Polymeric Systems' is used by Case Western Reserve University. Case is the lead partner for the National Science Foundation funded research center CLiPS. The CLiPS center has functioned as a research partner providing guidance and support, including the manufacturing of sample sets for experimental analysis.

1.1 CLiPS

The Center for Layered Polymeric Systems, or CLiPS, is a multifaceted research center pursuing both the development and implementation of what they refer to as "Polymer Plus"[3]. The center has developed under the National Science Foundation (NSF) Science and Technology Centers (STC) program[4] located at Case Western Reserve University. The center's mission is to develop a centralized base for both polymer research and polymer engineering to ease the transition of new technologies in multidisciplinary emergent technical disciplines[3]. RIT functions as an affiliate institution through Dr. Varela[1] and Dr. Lagner[2]. The

[1] Dr. Benjamin Varela (bxveme@rit.edu 09-2012)
[2] Dr. Andreas Lagner (axlsch@rit.edu 08-A256)

focus of the RIT component of research has been on mechanical properties and analysis. The overall research goals of CLiPS are more wide-ranging and multifaceted.

1.1.1 CLiPS goals and research objectives

CLiPS has broken the ongoing research into four research 'platforms'. These include the underlying enabling manufacturing technology, activities in the fields of mechanical; optical; and electronic realm, and investigations into novel applications and innovative usage of unique properties[2]. These goals are determined to support the overall progress of the center's research mission.

As defined by CLiPS[4] the overarching goal is to continue development of the layered polymeric systems and their manufacturing technology. They plan to work with the applications and utilization of the technology in parallel and use this development to train and educate polymer scientists and engineers in the industrial realm and to build affiliations between academia and industry.

The enabling technology in use at CLiPS is the forced assembly of coextruded micro and nanometer thickness polymer layers. CLiPS has developed technology they refer to as forced assembly coextrusion. The technology, while previously widely available, has been refined to produce nanometer thickness layers[5]. The layers are individually extruded and then forcibly combined, before being multiplied. This technology is the manufacturing basis for the development of novel applications[3]. With the flexibility of the enabling technology, CLiPS is currently developing multiple potential applications.

One of the first research areas that was pursued by CLiPS was the use of layered polymer as gas membranes and membranes for the development of precisely controllable nanoscale transport phenomena[3]. One example of their application is in the packaging of

[3] Discussed further in 1.1.2

perishable foods. The film coverings on perishable foods need to prevent oxygen access to the food and reduce water penetration through the coverings. The layered polymers are useful for combining the individual best properties of multiple materials into a single film that is tailored to perform multiple functions well. These single films can also incorporate reactive films, which not only block oxygen but absorb it as well[3]. Further, CLiPS has demonstrated[6] the ability to use the enabling technology and the inherent interphase to create enhanced oxygen permeation properties by creating confined crystallization in individual layers. Other potential applications include 'smart' pharmaceutical packaging, improved microelectronics packaging, and biologically inert materials[3].

The third research platform of the CLiPS center is the deployment of layered technologies as optical technologies. Current examples of the layered polymers are as nonlinear lensing and as all polymer lasers[1]. A schematic of these lasers is seen in Figure 1-1 and the technology demonstrates the integrated improvements offered by the layered polymer systems. CLiPS has used the flexibility of the enabling forced assembly technology to provide polymer structures of a high index (for concentrating emitted laser light) while also protecting the polymer dye from damage due to oxygenation (a common problem in polymer lasers). An example of the Laser Output can be seen in Figure 1-2

CLiPS is also working on several other technological developments. These include a wide, and ever widening, array of potential applications of forced assembly multilayered polymer structures. These applications include usage as dielectrics in high capacity capacitors, the

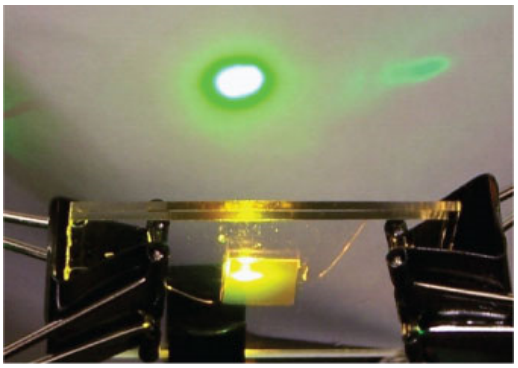

Figure 1-2 Image of Output from an all polymer laser constructed by CLiPS using multilayer forced assembly multilayered high index polymer refracting surfaces[1]

combination of forced assembly with self-assembling polymer technology, controlling polymer crystallization, and the use of photo patterning on multilayered polymers[3][4].

1.1.2 CLiPS manufacturing

The CLiPS center has been responsible for manufacturing all the polymer samples used for experimentation. The layers are manufacturing at their facility on the Case University campus using a custom designed dual extrusion setup [1]. The setup, as seen in Figure 1-3, is responsible for the creation of the layered polymer systems from the constituent materials. The system utilizes two off the shelf melt pump and extruder systems. The systems create a pair of films each consisting of one of the two constituent materials. These two melt pumps are tied to a coextrusion feed block that forces the layers into adhering contact and preparing the 2-layered stream for introduction into the layer multiplying elements[7]. The pumps themselves are independently adjustable to modulate the relative volume fractions and layer thicknesses between the two materials. The layer multiplying elements can be repeated as necessary and give the ability to increase the number of layers by potentially any factor of two. The layer multiplier illustrated in Figure 1-4 shows the multiplication process going from 2-4 layers;

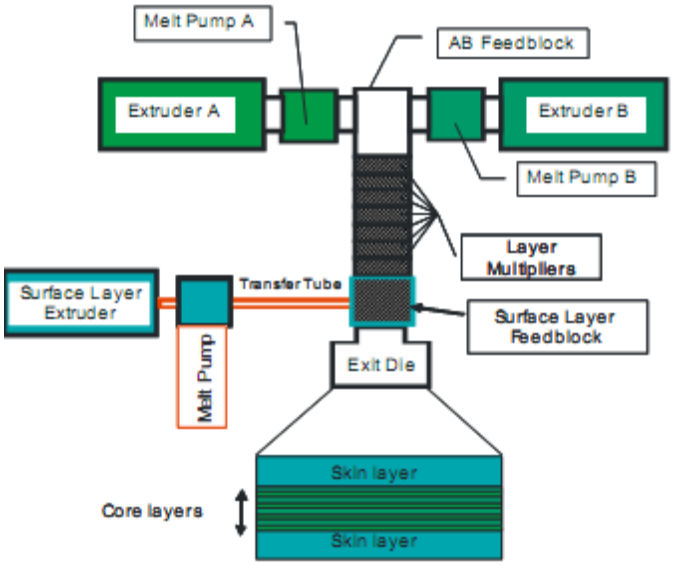

Figure 1-3 Diagram of Layered Polymer Manufacturing System[7]

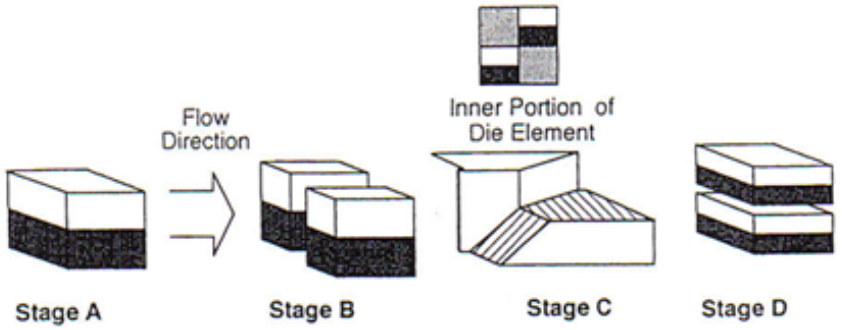

Figure 1-4 Schematic of layer multiplying die for increasing layer count from 2-4.[7]

however, it is effectively identical to multiplications that occur from 4 to 8 layers or more. The multiplication dies work by splitting the layers width wise with a vertical cut before forcing the separate streams onto paths, which creates an overlap and a four-layered structure as detailed in stages A through D[7]. The process occurring in the die is shown in Figure 1-4. This process is then repeated, as necessary, to create the necessary number of layers.

After the requisite number of multiplications have occurred, the layered stream is fed through a final feed block, which both sets a final thickness and creates a protective skin layer on both sides of the stream from a third, sacrificial material[1]. The process has multiple levels of adjustment to allow for precise manufacturing of very specific structures. The current manufacturing capability includes the ability to select both materials from any melt-extrudable polymer, the ability to independently adjust the volume fraction of each polymer (and with that the layer thickness), the ability to adjust the number of layers as well as the final set thickness of the stack. CLiPS also employs techniques such as biaxial stretching which CLiPS has shown allows further customization of properties such as oxygen permeation[8].

1.2 Goal and Objectives

The overall goal of this work is to investigate the viscoelastic properties of layered polymers using ultrasonic analysis. We believe ultrasonic techniques will allow the determination of properties of both the bulk material and individual layers in a non-destructive manner. Currently, CLiPS is testing these properties using other methods such as dynamic

mechanical analysis (DMA) and destructive tensile testing. These methods only allow determination of the bulk properties at this point in time. Ultrasounic techniques have not yet been employed for characterization of polymer layers. Hence, there is a significant potential for future technological development of this method in the CLiPS application.

To accomplish our goal, three specific objectives were laid out. The first was to investigate methods for mechanical characterization. This involved determining the methodology currently in use by CLiPS and others, and the exact ultrasonic techniques that could be feasibly implemented. The second was to attempt to determine the complex moduli for the layered polymers. The complex moduli would suffice for initial characterization of mechanical properties. The third research objective was to develop a model of ultrasonic propagation in thin layered polymers. This model would help in achieving the two prior goals, and would provide a thorough understanding of the mechanical behavior through extension of the experimental analysis capabilities.

1.2.1 Investigate methods for mechanical characterization of CLiPS stacks

The first goal was to make a determination on what experimental techniques would be useful for measurement and analysis of the material properties. The characterization effort involves methods for the determination of bulk properties of the entire stack, as well as the micro and macro properties of the individual layers. Prior research by CLiPS[9] demonstrates the relative complexity of the internal behavior. This is due to the size of the layers, more complexity in modeling of the layers macro properties, and the complicating factors that are created by the internal polymer interfaces.

Case was pursuing work on bulk characterization of mechanical properties. Their work focuses on characterizing the entire stack at once using dynamic mechanical analysis (DMA), and related techniques which measure the samples bulk mechanical response, do not possess

the resolution to measure the properties of individual layers. Therefore, the focus was adjusted to develop methods for characterization of the internal properties.

1.2.2 Determine complex mechanical moduli of layered polymers

The overarching intent of the goals discussed in 1.2.1 and 1.2.3, is to provide a method of determining the viscoelastic properties of the internal layers of a layered polymer stack. There are a number of ways to express the material properties, which represent the behavior of viscoelastic materials. The method employed here will be the use of the dynamic modulus. The dynamic modulus is the time dependant ratio of stress to strain, which is used in viscoelastics to express the phase lag and absorptive properties these materials display. The dynamic modulus is expressed as a complex pair containing a real and imaginary term. For example, the dynamic expression of Young's modulus would be E=E'+iE''. The real term (E') expresses the elastic stored energy and the imaginary term (E'') represents dissipated energy. They are known as the storage and loss modulus' respectively.

Measuring these two parameters allows for a basic but effective characterization of viscoelastic materials. The goal is to determine these properties using a combination of the experimental and simulation techniques proposed above. The intent is to determine E' and E'' for the individual constitutive layers, and if this is successful, compare the individual E' and E'' results to those of the bulk material.

1.2.3 Develop simulation model of ultrasonic propagation

To supplement the experimental measurements work on the development of a method of providing a simulation of the wave propagation was also performed. This was the final objective, an ability to fully access and utilize the gathered mechanical properties. The identification of properties from a returned ultrasonic signal can often prove difficult. When this is further complicated by complex behavior, such as is created by the interphase area in

multilayered samples, quantitative analysis of data is made very difficult. However, many implementations of ultrasonic testing rely on a qualitative comparison to a known “good” signal. If instead, a qualitative match could be made between the collected experimental signal and a simulation of known inputs, a match could be assumed and a quantitative analysis would be unnecessary. This becomes increasingly necessary as the number of the layers increases and their thickness decreases.

To achieve the goal of qualitative data analysis, we proposed to create a simulation of the experiment. This requires the development of a model for ultrasonic wave propagation in multiple layers of varying polymers. The goal is to develop as general a model as possible so that minimal changes will allow applicability to an expanding number of material property profiles and stack geometry. Given the constraints of the ultrasonic experimentation, the simulation is to be one-dimensional. The model is created using numerical techniques to reduce the number of assumptions and restrictions that are often inherent with the development of experimental correlation models and other direct solutions.

Chapter 2

Background Information

The use of ultrasound for material characterization has been effectively and widely deployed for quite some time. However, there are long standing limitations on the ability to interpret data from testing. Adding complicating factors such as multiple layers, extremely thin samples, interphase influence, and viscoelasticity makes drawing out results from ultrasonic testing more difficult. In simple cases, results can be drawn from direct analysis of waveform data. However, there are cases, one of which is presented here, where it is difficult to directly discern results from the data sets that are gathered. One of the goals of this work is to provide an expansion of the analysis abilities in complex cases. This expansion of capability provides potential new avenues for analysis of data that allow divining of results not otherwise discernable.

In this work, finite element analysis is utilized to perform a simulation of the ultrasonic experiment being performed. The simulation and experiment are setup with a certain set of inputs. While the experimental setup uses the test samples, the simulation utilizes a set of material properties that are of interest. Given these conditions, the simulation inputs are varied to allow the results to match those achieved through experimental data gathering. This allows indirect, iterative, characterization of a relatively complex layered viscoelastic material that would otherwise not be possible using current practice. This is a novel approach and allows the extension of a set of techniques to a new operating window of interest to ongoing research in the field.

2.1 Experimental Testing

The experimental portion of this work involves the gathering of data using high frequency ultrasonic testing. This testing allows the investigation of the properties of multiple individual layers of polymer simultaneously. This would not have been possible using a physical technique such as dynamic mechanical analysis.

The use of ultrasound for material testing and investigation has become more prevalent in recent decades. Most people are familiar with ultrasonic imaging as applied to sonography for obstetrics. However, applied to industrial fields, ultrasound has two separate uses. First, is the ability to determine and detect defects and potential flaws. Ultrasound as a technique for non-destructive testing and quality control has been widely deployed both in labs and in the field. The second use of ultrasound is for the determination of mechanical properties using nondestructive and noninvasive testing methods. These methods also have the added advantage of being able to more accurately determine properties during time dependent phenomena such as cure cycles[10] or in samples that are difficult to test using traditional means[11]. The interest here lies in the second usage, and the following sections provide a concentrated overview of the general knowledge base necessary for an in-depth technical discussion of the field specifics as provided in the literature review section.

2.1.1 Overview of ultrasound

Ultrasound is the term applied to high frequency sound waves. As such, there is a strong, and obvious, behavioral relationship to sound waves. The dividing threshold between sound and ultrasound is given as 20 kHz in frequency. This threshold is based on the assumed upper limits of human hearing, ultrasound being any sound beyond the human hearing frequency threshold. The propagation of waves occurs through the same mechanism as that of

normal sound waves, the transmission of cyclic sound pressure via the vibration of materials at the molecular level forming a sinusoidal time history of this pressure.

Ultrasonic propagation naturally occurs in three dimensions. However, for clarity, it is simpler to look at a one-dimensional path initially. This allows the discussion to be confined to longitudinal waves and shear waves in a single dimension rather than a two or three dimensional model. Longitudinal waves are those that propagate along the axis of the emitted sound and are of most direct use for this thesis. The analysis of these longitudinal waves forms much of the basis of ultrasonic analysis. Understanding this propagation involves several factors, including attenuation[4] and dispersion[5], and modeling must include the realization that the molecules oscillate in three-dimensional space as well as in time. As the propagation model is also a function of both the material and properties of the ultrasonic input pulse, it directly controls time effects.

For the simplified case, in an arbitrary single direction, we can create a basic model of a simplified standing ultrasonic wave as seen in Equation 2-1. In this expression of the solution, u_0 refers to the maximum amplitude of u, which is the displacement while k is the wave number and ω is the angular frequency. Both ω and k can be reformulated to utilize more basic inputs as seen in Equation 2-2. The wave number dictates the spatial frequency of the oscillating wave. This extremely simplified case is the beginning of the discussion. It is not feasible for true modeling and the FEM techniques later applied.

$$u(x,t) = u_o \cos(\omega t - kx)$$

Equation 2-1 General single dimension model of propagation in an arbitrary direction, x.

[4] **Attenuation** A gradual diminishing in the strength of something; A reduction in the level of some property with distance, especially the amplitude of a wave

[5] **Dispersion** The phenomenon in which the phase velocity of a wave depends on its frequency, or alternatively when the group velocity depends on the frequency. Media having such a property are termed *dispersive media*.

$$\omega = 2\pi f \quad (a)$$

$$k = \frac{\omega}{c} \quad (b)$$

Equation 2-2 (a) Calculation of angular frequency from the wave frequency, f, in Hz. (b) Equation for the wave number from the angular frequency and the speed of sound in the host material, denoted by the speed of sound in the material, c.

From this basic solution, one can recreate the one-dimensional wave equation by taking the second derivative with respect to position and the second derivate with respect to time. These components can be seen in Equation 2-3. By re-substituting in Equation 2-1, it is possible to simplify the derivatives significantly giving the final form seen in a and b. From there, it is possible to set Equation 2-3a and Equation 2-3b equal to one another, which will give the single dimensional version of the wave equation.

$$\frac{\partial^2 u}{\partial x^2} = -u_0(-k)^2 \cos(\omega t - kx) = -k^2 u(x,t) \quad (a)$$

$$\frac{\partial^2 u}{\partial t^2} = -u_0(\omega)^2 \cos(\omega t - kx) = -\omega^2 u(x,t) \quad (b)$$

Equation 2-3 (a) Second derivative of Equation 2-1 with respect to x. (b) Second derivative of Equation 2-1 with respect to t.

This gives us a final form as seen in Equation 2-4 which, as stated, is achieved by setting the equations equal to one another. This is very similar to the generalized wave equation, unsurprising given the expected behavior. The differential terms are, in fact, identical to the general form. The difference comes in the usage of c^2 instead of density and stiffness to dictate propagation rate. The modeling of Equation 2-4 will be discussed further in section 2.2, but from this form, we can learn a significant amount about the actual propagation of ultrasonic waves in solids.

$$\frac{\partial^2 u}{\partial x^2} = \frac{1}{c^2}\frac{\partial^2 u}{\partial t^2}$$

Equation 2-4 One-dimensional wave equation expressed using speed of sound, c.

If the formulation were applied to a small differential element onto which a stress is applied, the response would be best modeled under Newton's First Law. For this case, the stress (σ_x) is assumed to have come from the sound pressure of an ultrasonic wave. Assuming a uniform cross section, and constant mass, Equation 2-4 can be rewritten in simplified form as follows, using the density of the material, ρ.

$$\frac{\partial \sigma_x}{\partial x} = \rho \frac{\partial^2 u}{\partial t^2}$$

Equation 2-5 Simplified form of Equation 2-4 for constant mass and cross section using Newton's first law

From Equation 2-5, it is possible to rewrite the equation set in a manner that allows the determination of a base formulation for the speed of sound. The equation uses the stress in x, noted with σ_x. The first step is expanding σ_x and then taking the derivative with respect to x.

$$\sigma_x = E\frac{\partial u}{\partial x} \quad (a)$$

$$\frac{\partial \sigma_x}{\partial x} = E\frac{\partial^2 u}{\partial x^2} \quad (b)$$

Equation 2-6 (a) Formulation of elastic stress in the pure x direction. (b) Derivative of (a) with respect to x

Equation 2-6(b) and Equation 2-5 can be combined and simplified. What this shows is that the speed of propagation can be expressed using the density and elastic modulus when propagation is restricted to the longitudinal direction.

$$c_l = \sqrt{\frac{E}{\rho}}$$

Equation 2-7 Basic expression of longitudinal speed of sound in an elastic solid.

The same approach can be applied for consideration of propagation in shear, normal to the longitudinal propagation. As would be expected, propagation in shear is governed by the shear modulus, G, allowing the speed of sound in shear to be written as:

$$c_s = \sqrt{\frac{G}{\rho}}$$

Equation 2-8 Basic expression of speed of sound in shear in an elastic solid.

The speed of sound in a given material, generally notated 'c', is used throughout ultrasound to both model properties and as a material identifier during experimentation. An expansion of these derivations to a more complex case, including multiple dimensions, continues in a similar manner. Utilizing a standard expansion in a three dimensional body, Lamé constants can be introduced to allow simultaneous expression of longitudinal and shear stresses as seen in Equation 2-9.

$$\begin{pmatrix} \sigma_{xx} \\ \sigma_{yy} \\ \sigma_{zz} \\ \sigma_{yz} \\ \sigma_{xz} \\ \sigma_{xy} \end{pmatrix} = \begin{bmatrix} (2\mu+\lambda) & \lambda & \lambda & 0 & 0 & 0 \\ \lambda & (2\mu+\lambda) & \lambda & 0 & 0 & 0 \\ \lambda & \lambda & (2\mu+\lambda) & 0 & 0 & 0 \\ 0 & 0 & 0 & 2\mu & 0 & 0 \\ 0 & 0 & 0 & 0 & 2\mu & 0 \\ 0 & 0 & 0 & 0 & 0 & 2\mu \end{bmatrix} \begin{pmatrix} \varepsilon_{xx} \\ \varepsilon_{yy} \\ \varepsilon_{zz} \\ \varepsilon_{yz} \\ \varepsilon_{xz} \\ \varepsilon_{xy} \end{pmatrix}$$

Equation 2-9 Expanded form of 3-dimensional stress tensor. Sorted to simplify cross multiplication and isolate shear and longitudinal waves.

Using this formulation, it is possible to derive equations for wave propagation in two or three dimensions. For a further discussion of these derivations, the reader is directed to the works by Graff[12] and Auld[13] as complete resources. It is also possible to solve for base material properties directly from the speeds of sound determined through experimentation. This is the property of use when ultrasound is utilized for mechanical testing.

2.1.2 Use of ultrasound in mechanical testing

The determination of the mechanical properties using ultrasound can be achieved using a known, derivable, set of equations. If the longitudinal and shear speed of sound in a material are determined, it is possible to utilize them to determine the elastic modulus, the Poisson's ratio (v), and the tensile modulus (E) directly. Through a more detailed analysis, it is also possible to more completely characterize a material property up to and including complex moduli and viscoelastic time history properties. For simplicity, the discussion begins with the most basic material properties as seen in Equation 2-10.

$$E = \rho C_s^2 \left(\frac{3C_l^2 - 4C_s^2}{C_l^2 - C_s^2} \right) \quad (a)$$

$$\nu = \frac{1 - 2\left(\frac{C_s}{C_l}\right)^2}{1 - 2\left(\frac{C_s}{C_l}\right)^2} \quad (b)$$

Equation 2-10 (a) Equation for determination of Young's Modulus from shear and longitudinal velocity of sound. (b) Equation for determination of Poisson's ratio from shear and longitudinal velocity of sound.

From Equation 2-10, it is also possible to rearrange the components to calculate the bulk modulus and shear modulus, as well as other basic properties, such as Lamé constants. To get to this point though, one must have a basic understanding of the data analysis used to gather the shear and longitudinal speeds of sound. The determination of these is done through the determination of ultrasonic time of flight.

The time of flight is calculated from the A-scan. An example A-scan can be seen in Figure 2-2 on the next page. It is the generation of a plot, which displays the returned signal collected by the experimental equipment. The standard A-scan plot utilizes an X-axis in the time domain, and a Y-axis from representing the recorded amplitude, measured in volts. This is the standard expression of a single data gathering experiment in ultrasound.

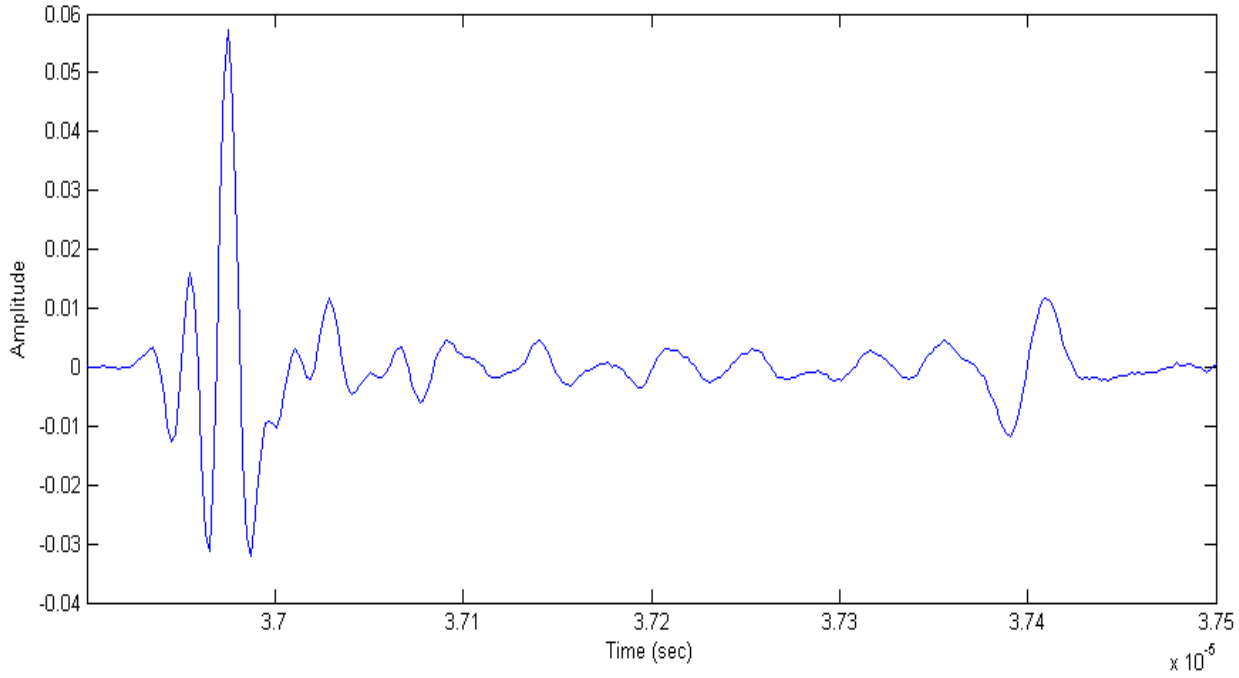

Figure 2-2 Example A-scan showing multiple peaks and strong front and back reflections and some internal reflections.

The determination of material properties can be made by determining the time between pulses. To gather the data, there are two potential arrangements of ultrasound equipment with which to gather data. While the methods are similar, the equations for calculating material properties do vary according to setup. A schematic of the methods can be seen in Figure 2-1.

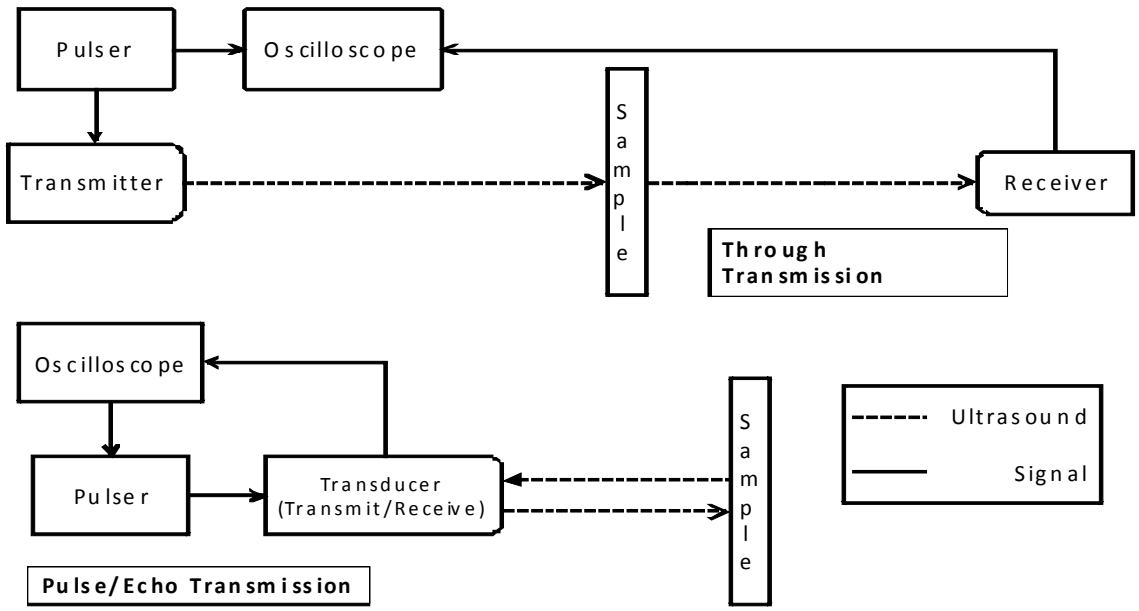

Figure 2-1 Diagram of through transmission and pulse echo transmission arrangements for ultrasonic testing.

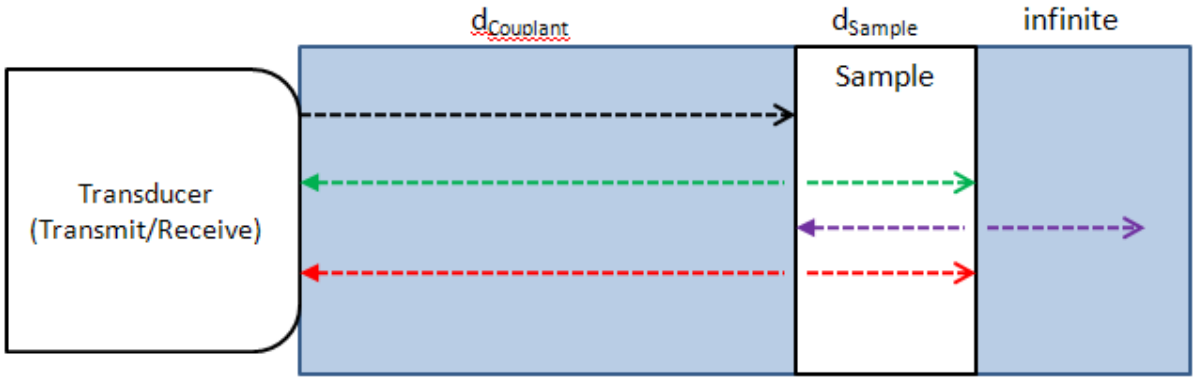

Figure 2-3 Visualization of wave propagation in for pulse echo determination of speed of sound in a sample material.

In the case presented herein, pulse echo transmission is used exclusively, and is the method that will be derived. Pulse echo utilizes a single transducer that both transmits the initial ultrasonic pulse, and then receives the reflected pulses from the sample. This is different from through transmission testing which utilizes separate transmitting and receiving elements. Where the methods truly differ is in how the equations are derived for data analysis and interpretation. To understand the derivation, it helps to visualize the wave propagation that occurs. Figure 2-3 diagrams the ultrasonic reflections and transmissions.

In the above figure, a signal (black line) is emitted from the transducer. It travels a distance through a couplant material before reaching the front surface of the material under investigation. The couplant material, most commonly water, is utilized to ensure optimize transmission between the transducer and the sample. This is important to prevent unintended and disruptive reflections and noise. At the front surface, the energy splits, with a portion of the wave energy being reflected back to the source and the remainder of the energy entering the test sample. The reflected energy (green line) returns to the transducer while the remainder continues to propagate through the sample. The returned signal creates a first return pulse. The energy that was transmitted through the front surface performs a similar reflection off the back surface. This creates a second return pulse, which is traveling towards the transducer in

the sample material (purple line). The return pulse splits again at the front surface of the sample (red line) before returning a second pulse to the transducer.

The pulse's amplitude will have split 3 times; however, the timing of the pulse is what is directly of interest to modeling the speed of sound. The model can be built from knowledge of the wave propagation properties as seen in Equation 2-11. For the first reflection, the pulse must traverse the couplant material twice. For the second pulse, the time of flight includes the time of flight of the first pulse, as well as the time of flight created by traversing the sample material twice, once after crossing the front surface, and once after reflecting off the back surface of the sample.

$$t_0 = TOF_{First\ reflection} = \frac{d_{couplant}}{c_{couplant}} + \frac{d_{couplant}}{c_{couplant}} \qquad (a)$$

$$t_1 = TOF_{Second\ reflection} = \frac{d_{couplant}}{c_{couplant}} + \frac{d_{couplant}}{c_{couplant}} + \frac{d_{sample}}{c_{l,sample}} + \frac{d_{sample}}{c_{l,sample}} \qquad (b)$$

$$t_1 = t_0 + \frac{2(d_{sample})}{c_{l,sample}} \qquad (c)$$

Equation 2-11 (a) time of flight of first reflected pulse (b) time of flight of second reflected pulse (c) combined time of flight equation in simplified form.

Given that the time of the returned pulses is recorded as part of the experimental setup, Equation 2-11c can be solved for the speed of sound of the sample material. The solution requires knowledge of the sample thickness, but is independent of the ultrasonic setup. Unlike through transmission, pulse echo determination is independent of sample location, instead relying on the delay between front and back surfaces. It is also independent of the speed of sound of the couplant. The final equation is shown below. Given viscoelastic material complications, which will be discussed later, it should be noted that Equation 2-12 is only valid for a given frequency if the speed of sound in viscoelastic materials has a frequency dependence.

$$c_{l,sample} = \frac{2(d_{sample})}{t_1 - t_0}$$

Equation 2-12 For the calculation of longitudinal speed of sound in a sample using pulse echo ultrasonic testing.

Modeling the acoustical impedance and speed of sound, from the change in amplitude, is also possible. This occurs through the calculation of the acoustical impedance and the reflective and transmissive characteristics of a material boundary. The amplitude in an ultrasonic pulse is directly related to the amount of energy emitted from the transducer at a given frequency. Higher amplitude at an identical frequency defines a higher energy. The amplitude-tracking model uses the ability to mathematically express that energy-splitting phenomenon that occurs at material boundaries. Any wave experiences a split when it encounters a sudden medium change. When an ultrasonic pulse encounters a material boundary, the portion of the energy (and amplitude) transmitted and reflected is related to the acoustic impedance as seen in Equation 2-13.

$$R_{(\text{reflective coefficient})} = R(Z_1, Z_2) = \left(\frac{Z_2 - Z_1}{Z_2 + Z_1}\right)^2 \qquad (a)$$

$$T_{(\text{transmissive coefficient})} = T(Z_1, Z_2) = 1 - \left(\frac{Z_2 - Z_1}{Z_2 + Z_1}\right)^2 \qquad (b)$$

Equation 2-13 Expression for the (a)reflective and (b)transmissive coefficients of a medium interface for acoustic wave propagation.

These equations are determined by the differences in the acoustical impedance between the medium that the wave is currently propagating in (labeled Z_1) and the medium that the wave is crossing the boundary into (labeled Z_2). The derivation utilizes the property of wave transmission that requires continuity across the boundary. The acoustical impedance can be found using very similar properties to that used to find material constants from the time based signal analysis discussed earlier.

$$Z = \rho c$$

Equation 2-14 Calculation of acoustical impedance in a medium using density of the medium (ρ) and speed of sound in the medium (c).

With amplitude tracking, the same goal exists; to calculate the speed of sound for the purposes of calculating material properties. However, it is more difficult to measure shear wave propagation effectively and accurately due to the realities of surface refraction and alignment. To utilize amplitude tracking, it is simplest to begin with a visualization of the wave propagation just as was done for a time-based analysis. The visualization can be seen in Figure 2-4 and is identical to that for a time-based analysis. However, for amplitude tracking, it is only necessary to track the first reflected peak. Tracking multiple peaks makes it possible to determine more properties, but the determination of speed of sound can be determined from the characteristics of the front surface reflection.

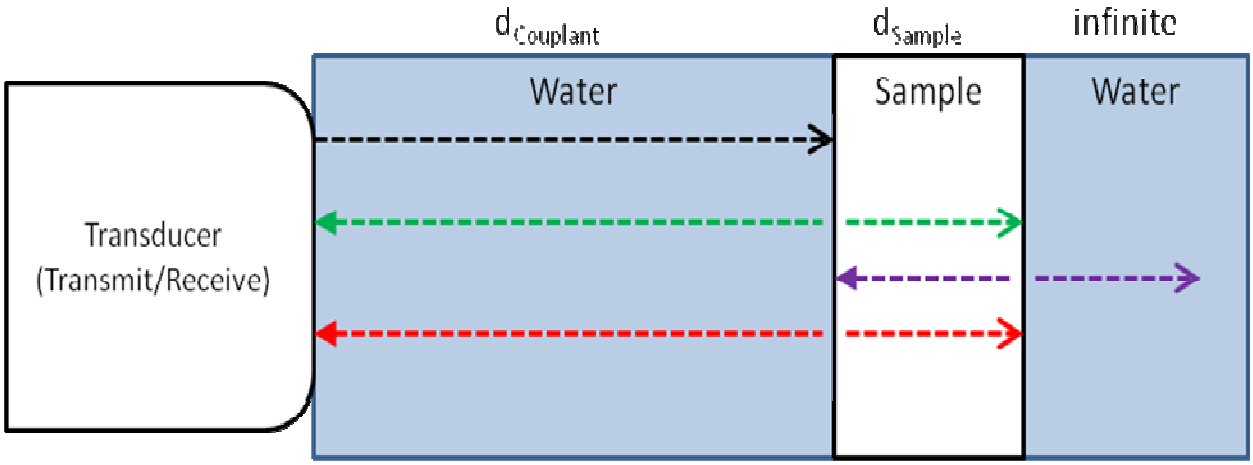

Figure 2-4 Visualization of wave path for amplitude tracking using pulse echo.

$$A_{\text{first peak}} = A_{\text{Transducer}} * R(Z_1, Z_2)$$

$$A_{\text{first peak}} = A_{\text{Transducer}} * \left(\frac{Z_{Sample} - Z_{Water}}{Z_{Sample} + Z_{Water}}\right)^2$$

Equation 2-15 Calculation of the amplitude of the first returned pulse from Figure 2-4 using Equation 2-13 expression of reflective coefficient

The first returned peak known to be the reflected portion of the initial emitted wave. Using equation Equation 2-13, generating an equation for the expected returned amplitude is possible. From there, the equation can be solved for the acoustic impedance of the sample material. This is seen in Equation 2-16.

$$Z_{Sample} = \frac{\sqrt{\frac{A_{\text{first peak}}}{A_{\text{Transducer}}}} + 1}{1 - \sqrt{\frac{A_{\text{first peak}}}{A_{\text{Transducer}}}}} Z_{Water}$$

Equation 2-16 Equation 2-15 solved for the acoustical impedance of the sample.

Using the same technique, generating an equation for the second reflected peak is possible. Similar to the model for the first peak, this expression takes into account all encountered boundaries. In this case, the peak pulse will have encountered the front boundary twice and the back boundary once leading to three terms expressing the reflection and transmission effects. This is seen in Equation 2-17. Despite the ability to express the second peaks mathematically, it is not possible to solve directly for the impedance of the sample. However, the ability to mathematically express the amplitude reflection of multiple peaks, is important if the sample has multiple layers or has a significant change in properties of its thickness. While utilizing amplitude analysis is a potential option for the determination of material properties, some significant drawbacks impede the effective use for direct and simple determination of the speed of sound. The most important of these is the necessity of modeling the impedance of the couplant. The couplant impedance is commonly a known; however, it is known only to a given precision.

$$A_{\text{second peak}} = A_{\text{Transducer}} * T\left(Z_{Water}, Z_{Sample}\right) * R\left(Z_{Sample}, Z_{Water}\right) * T\left(Z_{Sample}, Z_{Water}\right)$$

Equation 2-17 Basic solution for the determination of the amplitude of the second returned pulse from the diagram in Figure 2-4

Time based analysis is designed to mitigate or minimize the effect of the experimental environment phenomena on calculations. The problems occur more heavily when amplitude analysis is employed, given that amplitude modulation employs the propagation of energy and the measurement of that energy as opposed to simply when such propagation occurs. With amplitude modulation, the solution for the sample's material properties and speed of sound also require the utilization of the couplant material properties.

Combining amplitude tracking and time analysis allows calculation of viscoelasticity by separately calculating both speed of sound (from time analysis) and attenuation (from amplitude analysis). Together, these properties can be used to fully determine viscoelastic properties of a sample material. The usage of ultrasound for determination of viscoelasticity will be discussed further in section 3.2.

2.1.3 Normal ultrasound testing procedures

For the actual implementation of ultrasonic testing, a specific set of procedures must be implemented and followed, as with any experimental work, to see effective repeatable results. To execute testing, pre experimental work must consider equipment, techniques, calibration methods, and the specific application. A specific setup for the case utilized in this work is discussed later in section 4.1.1. This section gives an overview of the components involved to allow for a more detailed discussion in the experimental section.

Several components of equipment are involved in running the actual experiment. Together, they generate, emit, receive, record, process, and analyze the ultrasonic signal to allow the gathering of data. A basic experimental setup will include at minimum a pulser/receiver, a transducer, and an oscilloscope. Most setups also utilize a computer for data processing and data storage as well as a tank, which contains a liquid couplant to better link the samples and transducers. This general setup is shown in Figure 2-5 on the next page.

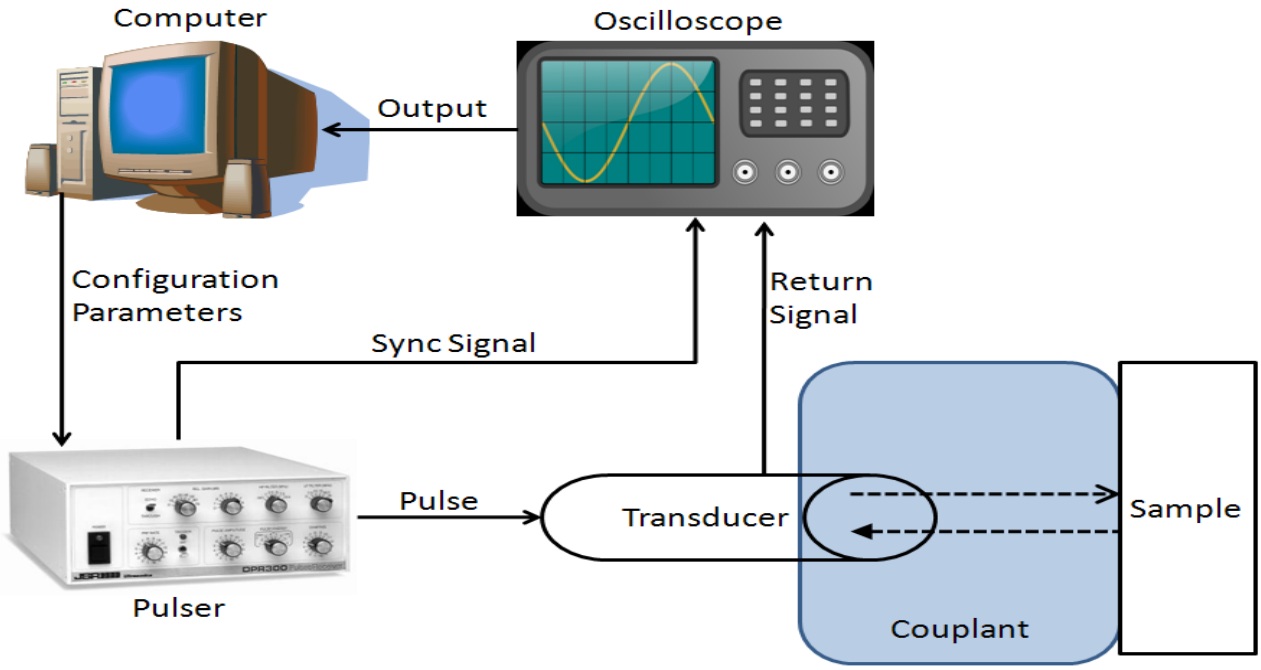

Figure 2-5 Basic configuration of standard ultrasonic experimental setup.

Of the main equipment, the pulser/receiver and the transducer are the two components specialized for use in ultrasonic testing. The pulser/receiver is responsible for generating the ultrasonic input signal that propagates through the experimental setup and records the received echo. It also transmits a syncing signal to the oscilloscope for timing alignment. The transducer is responsible for emitting the pulse utilizing a piezoelectric element to generate the sound pressure wave from the electrical signal that is provided by the pulser. Together, these two components are the heart of an ultrasonic testing setup.

The circuitry of the pulser/receiver is responsible for the overall configuration of the pulse that is sent into the transducer and through the material. This circuitry is responsible for generating the short, high intensity (large amplitude and energy) electrical pulse with utmost precision. Most pulsers/receivers also utilize adjustable parameters that allow the user to configure a number of parameters including the amplitude, pulse length, and repetition rate. The energy of the pulse is often transmitted at voltages as high 800V. Often, they are also able to slightly adjust the frequency of the emitted pulse as well, although this is mostly dictated by the specific transducer chosen. Higher end pulser may also provide some receiving and signal

processing capabilities. These can be used to perform some preprocessing tasks before the signal is passed on for further analysis.

The transducer is responsible for converting the electrical signal sent from the pulser to a sound pressure wave that is emitted into the sample under test. There are two main types of transducers, contact and immersion. As implied by its name, contact transducers work by being placed in direct intimate contact with the sample under test, utilizing a thin layer of couplant to fill gaps. Immersion transducers are common in lab testing, and provide some benefits where it is feasible to wholly submerge a test sample.

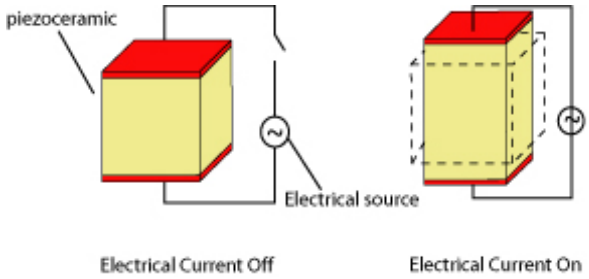

Figure 2-6 Diagram of active element of a piezoelectric ultrasonic transducer. The piezoelectric material can be seen in yellow and the electrodes in red.

The transducer works using the piezoelectric effect. The active portion of the transducer is made of a piezoelectric ceramic sandwiched between two electrodes. The basic layout is shown in Figure 2-6. The piezoelectric characteristics of the material cause it to change shape when an electrical current is applied across the active material. When this happens, the individual molecules in the material will align causing a change in shape of the material. This change is known as electro-constriction and is the phenomenon that changes the electrical signal into a pressure wave. This phenomenon is also used in reverse by the receiving transducer to generate an electrical signal from returning acoustic pressure being applied to the piezoelectric material causing a change in the electric field of a permanently polarized piezoelectric material.

The parameters of the transducer are a direct function of the shape and size of the transducer's piezoelectric element. The shape of the transducer's active element can be customized to create a specific focal distance, which is useful in immersion or other noncontact ultrasonic testing. The thickness of the active element region can be adjusted to create a specific center frequency required by the user. The formulation of this can be seen in Equation 2-18. This thickness is calculated from the wavelength that the user wishes to create. This applies to both immersion and contact transducers

$$t_{active} = \frac{c_{initial\ medium}}{2f_{transducer}}$$

Equation 2-18 Method for calculation of required active area thickness.

The other main piece of equipment necessary for most ultrasonic testing is the oscilloscope. The requirements of the oscilloscope are defined in terms of the required precision for the specific testing. However, with normal ultrasonic frequencies in the MHz range, the requirements for an oscilloscope for ultrasonic testing can be very stringent. Higher end oscilloscopes allow for a number of specific advantages. They can collect data at much higher rates allowing for the necessary precision. If a 1MHz pulse is utilized for testing, an oscilloscope must take data at a much higher rate, likely at least 100 MS/sec (mega-samples/sec) to effectively gather data. Often, higher precision oscilloscopes of 500MS/sec or above, are used to collect the required precision. These oscilloscopes also allow detailed control of triggering, and outputting of data over RS232 or USB to enable offline analysis.

A number of experimental techniques can be employed or combined, to gather different versions of the ultrasonic data. These configuration changes can employ multiple arrangements of equipment, and different techniques of using this equipment to gather data. The technique employed in this thesis is 'normal beam inspection'. In normal beam inspection, the equipment and sample are arranged so that the propagation of sound waves occurs normal to the sample.

This requires tight tolerance alignment of the transducer and sample because the active element of the transducer and the surface of the sample must be parallel for the signal to propagate accurately. Within normal beam inspection, there are two possible configurations of transducers, either pulse-echo or through transmission can be used.

The other possible configuration is known as angled beam inspection. Angle beam inspection relies on the angle of incidence in a material to generate signals. Angled beam inspection is a very useful technique because it introduces a shear wave into the sample. The differences in arrangement between the two configurations can be seen in Figure 2-7. It is useful for extended characterization, and it is especially useful in detecting flaws in areas such as welds. However, it is not used within this thesis work and so further discussion is unnecessary.

A more detailed discussion of the experimental procedures and equipment will be carried out later. This description is sufficient for introducing the work being carried out. There are significant technical challenges to the utilization of ultrasound in the manner it is applied

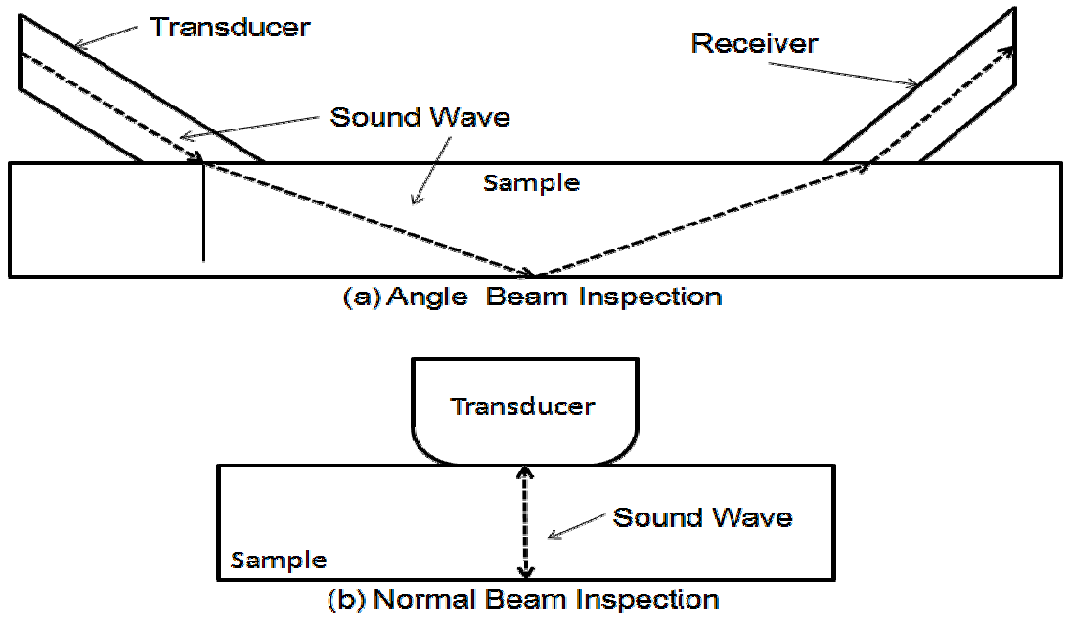

Figure 2-7 Diagram of (a) angle and (b) normal beam inspection techniques for ultrasonic testing of materials

here. These challenges include the realities of viscoelasticity, the challenges of a polymeric interphase (a concept which will be addressed later), and variability within the samples themselves. Discussion of these challenges, and the approach taken to find solutions will be discussed later, but build upon the techniques and theory discussed here.

2.2 Mechanical behavior of polymers

A number of techniques are used to model the mechanical behavior of polymers. The techniques use different methods to express the complex behavior that results when polymers are exposed to load. This accounts for the varied phenomena driving a mechanical response. These constituent phenomena include elastic mechanics, viscoelastic mechanics, the physical and chemical structure of the polymers, anisotropy as well as time and temperature dependence when under load[14]. While a very basic knowledge of mechanics and polymer science is presumed, the following discussion details a more complete understanding of the topics at hand.

Elastic mechanics as a mathematical tool are applicable to some simple and limited cases for explaining polymer behavior[14]. These include loads applied for short times and for loads of small deformation. Elastic theory is also useful as a starting point from which to develop more complete polymer mechanics models[14]. Using elastic theory for polymer mechanics is identical to elastic theory for other solids. Stress and strain are notated through the use of six independent quantities, three in the normal directions (principal directions) and three in shear to indicate the state of stress and strain in a material or structure[12]. The best example of this applied to polymers is rubber-like polymers. These polymers, commonly classified as rubbers, show very little viscoelasticity and will return to their original shape nearly instantaneously when released from loads. While not truly elastic, the elastic portion of their behavior is dominant and far outweighs contributions from viscous component [14]. This rubber like phase is one of several possible behavioral phases including crystalline and amorphous

(called glass like)[15]. While a discussion of these individually is beyond the scope of this work, the understanding of the underlying principles is helpful. Only in very rare cases does polymer behavior satisfy the characteristics of elastic theory. Mechanical polymer behavior is more commonly described through viscoelastics[14][15].

To properly derive and understand polymer mechanics, one must first consider five components of mechanical behavior that are demonstrated in polymers. These are generally accepted as: time dependent response to loading, non-linear response to inputs, very high allowable strain to failure, anisotropy, and low level yielding and non-recovery from strains[15]. These five phenomenological conditions combine elastic and viscous behavior of materials to form the basis of a theoretical viscoelastic mechanical response. The most common and practical manner of modeling this is through viscoelastic theory. Ward states "the behavior of materials of low molecular mass is usually discussed in terms of two particular types of ideal material: the elastic solid and the viscous liquid"[14]. This is because a polymer displays components of both.

$$\sigma_{elastic} = E\epsilon \qquad (a)$$

$$\sigma_{viscous} = n\frac{d\epsilon}{dt} \qquad (b)$$

Equation 2-19 (a) Stress in a purely elastic material. (b) Stress in a purely viscous material.

A polymer has the ability to absorb, hold, and release energy like an elastic solid while viscous liquids can absorb energy, but not return it, and have no definite shape. Mathematically speaking, the change is one where strain rates must be considered in addition to strain[15]. An elastic stress can be modeled as a function of stiffness and strain as seen in Equation 2-19a. A stress in a viscous fluid can be modeled as a function of the viscosity (η) of the fluid and the rate of shear on the material (Equation 2-19b). From these most basic forms, it is possible to

develop more complete and effective techniques for modeling the response behavior of polymers.

There are multiple practical models describing the mechanical behavior of polymers under load[16]. The applicable model varies based on a number of factors including temperature and loading frequency. Common models used to describe behavior include the Maxwell Model, the Kelvin-Voigt model, the standard linear solid model, the viscous model, and the generalized Maxwell model[14]. None of these models are capable of fully describing the full spectrum behavior of polymer loading, but rather they each are capable of modeling a smaller section of the whole behavioral envelope[16]. These different models can visually be expressed using different combinations of springs and dampers.

Expressing the behavior through nonlinear assumptions and modeling of the time based stress strain response is also possible. However, this discussion of viscoelastic theory is beyond the scope of this work. Readers are directed to other resources including Findley and Payne[17].

What all of these models have in common is a hysteresis loop under a loading and unloading cycle that causes the energy loss associated with viscoelastics. Properties of viscoelastic materials are commonly expressed in similar ways to elastic materials. The response of a repeating stress, such as a sine wave loading applied during dynamic mechanical analysis (DMA), is a useful comparative tool. An elastic material will have a response showing only an amplitude change relatable to its stiffness. A viscoelastic material will show a magnitude change, but will also show a phase change in response. This observation, leads to properties expressible as a complex modulus. This complex modulus for tensile loading is shown in Equation 2-20. The complex modulus can be drawn from the DMA or other types of testing using the equations seen in Equation 2-21. The two components are separately known as the storage (E') and loss (E'') modulus. The storage modulus represents the elastic energy

storage component of material behavior and the loss modulus representing the hysteretic energy dissipation from the viscous portion. The phenomenon that results is shown in Figure 2-8. The complex moduli components use δ to express the phase lag for viscoelastic materials.

$$E = E' + iE''$$

Equation 2-20 Dynamic modulus expression of complex viscoelastic material properties

$$E' = \frac{\sigma_o}{\varepsilon_o} cos\delta \quad (a) \qquad\qquad E'' = \frac{\sigma_o}{\varepsilon_o} sin\delta \quad (b)$$

Equation 2-21 Equations for calculating the components of complex viscoelastic moduli from DMA testing data. (a) equation for the storage modulus (b) equation for the loss modulus

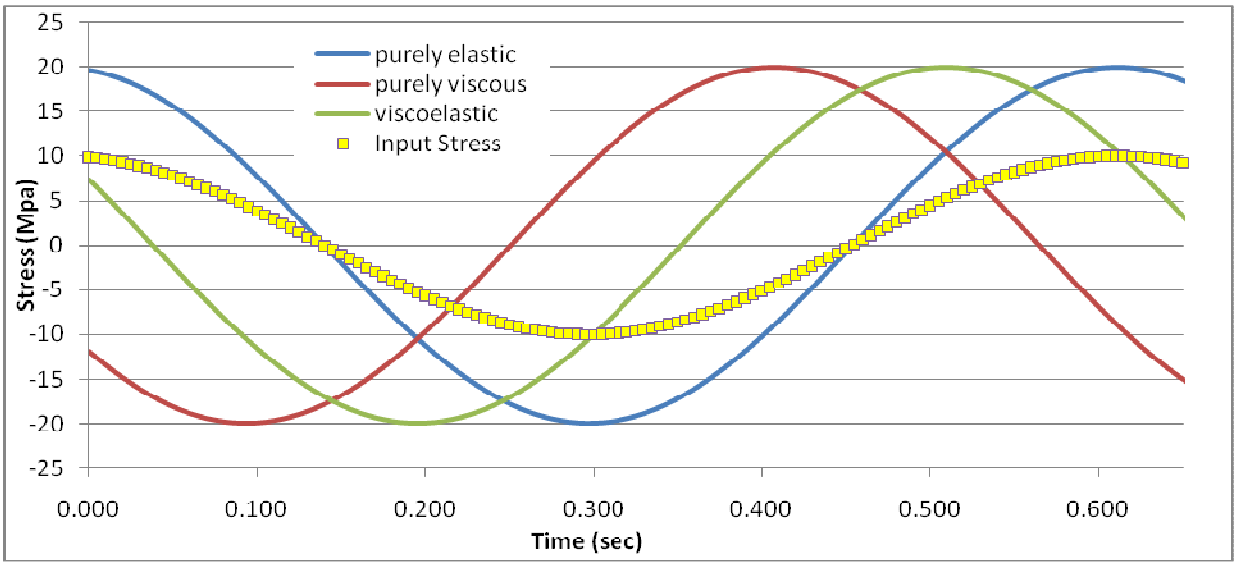

Figure 2-8 Plot of stress responses to a sinusoidal cyclical input for different material types.

The properties modeled on polymers stem from the structure and characteristics of the polymers themselves. In this work, the primary polymers are polycarbonate (PC) and Poly(methyl methacrylate) (PMMA). The primary driving factors of the properties of these materials are the physical and chemical properties of the molecular structure. Both PC and PMMA are thermoplastics and used commonly as alternatives to glass. The properties of these materials that dictate mechanical properties most reliably are the degree of polymerization and of crystallinity as well as the average molecular weight. Degree of polymerization refers to the number of units that form a linked network from individual molecules of the constituent

materials. These very long chains form from strong covalent molecular bonds, while the intermolecular bonds form from weaker van der Waals effects. The degree of polymerization is a measure of the number of repeating units in the polymer and is directly related to the average molecular weight of the polymer. Polymers with different degrees of polymerization can be chemically identical; however, polymers with a higher degree of polymerization (and higher molecular weight) often will have different resulting mechanical and thermal properties such as higher mechanical strength and a higher melting temperature.

In the polymer field, crystallinity is used to describe 3 dimensional ordering of the repeating chains. They differ from amorphous regions in that they show folding and stacking of chains. This differs from cross linking in that there is no direct chemical bond from chain to chain and only overlapping and layering that form secondary reinforcing actions. The regions that do not show these behaviors are referred to as amorphous. A polymer may show a structure anywhere from fully amorphous to (theoretically) fully crystalline. The measure of crystallinity is expressed in terms of the weight fraction of the crystalline to non-crystalline areas of the polymer. Crystalline polymers contribute certain structural properties that differ from amorphous regions in polymers. Higher crystallinity creates polymers that are more impact resistant and tougher than amorphous polymers. Crystallinity also contributes to higher levels of light scattering. Given the similar mechanisms to acoustical scattering, this is a property of interest to this thesis.

Anisotropy is not directly applied in the work here, the work is restricted to a single dimension. However, anisotropy is mentioned here both as an important contribution to the discussion on polymer properties, and as a comment on the limitations of the method employed here. The techniques employed, transverse ultrasound and the associated FEA modeling, do not provide the ability to measure and characterize the anisotropic properties of the layered polymers. With the small deflections and methods which are modeled here, the small strain

effects do not display the true anisotropic nature of the polymers[14]. The anisotropy displayed in polymers is due to the oriented methods used to manufacture them, which creates chains more inclined to align in a certain direction. This inevitably creates a single, stiffest direction and variable stiffness throughout due to the variations in chain length in directions. This is most commonly expressed through generalized Hooke's law and a variation, rather than equality, of the elastic constants in the three axial constants[14],[15]. These phenomena are likely to be more pronounced in production methodologies such as those used by CLiPS. This has been widely discussed and addressed in literature[18],[19].

2.3 Mathematics

The simulation aspect of this thesis relies on a mathematical model of an ultrasonic experiment. The mathematical operator of interest is the wave equation, Equation 2-22, where c is the speed of propagation.

$$\frac{\partial^2 u}{\partial t^2} = c^2 \nabla^2 \mathrm{u}$$

Equation 2-22 Wave equation in generalized operator form.

The wave equation can be solved directly using several techniques; however, complicating factors make a direct solution infeasible in the presented case. The first factor is the more complex nature of the material properties. While implementing a finite element scheme that includes damping and viscoelastic behavior is a well-studied field, implementing time history and the associated complexity into a direct solution, has not been as well studied. A direct solution would also face additional complications from the multiple layers and multiple reflective-transmissive interfaces that occur within the solution space. The multiple layers create areas of very nearly asymptotic change in material properties at material interfaces. For this reason, a technique employing a numerical solution would likely be able to better create a representative simulation. In this thesis, both finite difference and finite element are employed. Finite

difference is utilized in a preliminary manner to provide validation of physics and definition of the problem. Finite element is employed to create a more accurate and detailed model. The specific models used are discussed later.

The purpose of both techniques is to use numerical techniques to solve differential equations. Numerical techniques are most often implemented through the use of a computer to perform repeated simple calculations where determining the direct solution of a problem is either impractical or impossible. Most numerical models are a form of numerical analysis used to produce estimates of derivatives through simplified mathematical modeling. On a larger scale, they can be used to produce in depth simulations of complex systems accounting for governing equations, boundary conditions, and other phenomena that may be very difficult to implement in a direct model.

2.3.1 Finite Difference Modeling

Finite difference is a numerical analysis technique employed to provide approximate solutions to derivatives and differential equations. There are a number of different techniques within the finite difference discipline which can be used to produce derivative approximations. These techniques include explicit, implicit, and Crank-Nicolson methods.

At its most simple, the goal is to approximate derivatives of functions using numerical solutions. The most basic form of finite difference is seen here:

$$f'(a) \cong \frac{f(a+h) - f(a)}{h}$$

Equation 2-23 Finite difference approximation of the derivative of an a function f

The first derivative form makes a linear approximation of the slope of a curve through adjacent points. This formulation, called forward difference, approximates the derivative of the arbitrary function, f, as the change in the evaluated value of the function, f(a+h)-f(a), over the

change in location of the evaluation. Given the linear approximation, it is unsurprisingly similar to the calculation of the slope of a line. However, in a more complicated non linear function, this would serve only as an approximation. The exact value of the derivative is expressible as a limit of Equation 2-23.

$$f'(a) = \lim_{h \to 0} \frac{f(a+h) - f(a)}{h}$$

Equation 2-24 Definition of the numerical derivative for some arbitrary function f(a) determined using forward finite difference.

The same techniques can be used to express higher order derivatives. Knowing that the second derivative of a function can be expressed as the derivative of the first derivative, finite difference can simply be applied to the first derivative to form the 2nd.

$$f''(a) = \frac{f'(a+h) - f'(a)}{h} = \frac{f(a+h) - 2f(a) + f(a-h)}{h^2}$$

Equation 2-25 Second order finite difference.

This same pattern can be applied to higher order derivatives using the same technique. It can also be expanded using a more robust, multipoint models of the derivative which provide lower errors. Finite difference can also be used to form partial derivatives using different dimensional steps in different principle directions.

To apply the finite difference scheme, the derivatives in the wave equation are estimated with the finite difference approximations. The domain of the solution (time, space, or a combination) is then discretized into a mesh of 'nodes' or location at which a solution will be calculated. With the equation in differential, it can then be solved algebraically for the solution. This is done using one of three methods. The simplest method is explicit, where the solution is solved for the next point in the mesh. For the simulation we developed, this method is used. This technique is clearly demonstrated in the derivation of the solution to our problem in section

5.3. Readers requiring a further introduction are directed to Ames[20] for a more detailed discussion than is relevant for this introduction.

2.3.2 Finite Element Modeling

Similar to finite difference modeling, the finite element method is a way of discretizing an ODE or PDE over a known domain using numerical techniques where it is infeasible, or impossible, to determine an exact solution. The finite element method allows for approximations of the solution to these equations.

The finite element method is used to either wholly eliminate the differential equation when used for steady state problems which are formed solely in the physical domain, or to generate an ODE system for non steady state simulations. Finite element is often employed over more complicated domains and domains with highly variable step sizes. Finite element is so called because it involves the discretization of a whole domain into a number of discrete sub domains which are known as elements. Finite element is of significant importance to modern engineering study. Many engineering problems are expressable as PDE's, but the formation of generalized solutions over complex physical and time domains is difficult.

The first step in the finite element method process is the modification of the form of the PDE into a 'weak' variational form. For an arbitrary PDE of the form in Equation 2-26, a variational formulation is formed by multiplying through by an arbitrary smooth function v. The arbitrary function is used to solve for the boundary conditions on the x domain.

$$u''(x) = f(x) \quad x\epsilon[0,1]$$

Equation 2-26 Example PDE for finite element method

$$\int_0^1 f(x)v(x)\,dx = \int_0^1 u''(x)v(x)\,dx$$

Equation 2-27 Variational form of example PDE.

The variational formulation is then integrated by parts to form an equation that can be discretized using basis functions, and which includes the boundary conditions. The basis functions are used to replicate the behavior of the solution within the elemental sub domain. The integration by parts terms are used to generate the matrix equation. In a static domain, the matrix equation can be solved and create the approximate solution, for the non steady state case, the matrix equation forms the ODE which must be solved.

This is one of the flexibilities of finite element. The basis functions are chosen to meet the boundary conditions of the elements, they can be homogeneous, inhomogeneous, and make use of either Dirichlet or Neumann boundary conditions as appropriate. This is the major flexibility in the finite element method over finite difference. The ability to select appropriate basis functions, such as sinusoidal or polynomial, provides a benefit over the assumed linear approximation most commonly used in PDE's with behavior in the time domain as well.

For a steady state problem such as that in Equation 2-26, a solution can be found directly from the solving of the variational form. However, the finite difference method is also useful for solving non steady states as mentioned above. For the case in which it will be applied here, the variational method in the finite difference generates an ODE readily familiar to the mechanical engineering field. The general form becomes very similar to that of a spring mass system in a purely elastic problem, and a spring-mass-damper system for an attenuative or viscoelastic material. In effect, the finite element discretization allows for the reformulation of the discretized sub domains as individual ODE systems containing inertial, resistance, and attenuation components as appropriate. These components represent the behavior that is modeled through the variational formulation of each element and its properties. However, the overarching principle, is that the use of the variational formulation has reformulated the problem into an ODE of the generalized form seen.

$$[M]\{\ddot{U}\} + [D]\{\dot{U}\} + [K]\{U\} = \{R\}(f(x,t)$$

Equation 2-28 Matrix-vector form of ODE generated through FEM discretization

This reformulation uses a mass matrix (M), a damping matrix (D), and a stiffness matrix (K) to formulate the PDE as an ODE. The ODE form allows for a multitude of methods to be employed to solve the ODE. The most common approaches would be through the use of diagonalization, the creation of a system of first order ODE's, or finite difference discretization in the time domain. Notably, the special case of a tridiagonal matrix arises in problems with one spatial domain, such as the one employed here. This special case provides both opportunities and drawbacks that are addressed in the formulation of the model.

These techniques can be expanded and redefined to deal with specific problems in numerous ways. The use of the finite element method for analysis and simulation has continued to grow in recent years. With constantly expanding field of research, there are often specific resources that can be found to detail prior work done to address individual situations. The relevant prior work in simulation for our problem will be covered in chapter 3, and the full derivation of our solution and its results will be covered in chapter 5.

Chapter 3

Literature Review

The intent of the research in this thesis is to combine multiple approaches to develop a method for interrogating, understanding, and recreating the properties of the layered polymer structures developed by CLiPS. This method entails the inclusion of multiple extended complexity elements over the modeling of a simple structure such as a block of aluminum or steel. To understand the basis for this multifaceted approach, it is important to understand the current state of research and literature in the related technical fields that are the basis for this work.

The thesis goals, as noted in section 1.2, draw from viscoelastic mechanical properties of polymers, ultrasonic testing of viscoelastic materials, and numerical simulation of a complex time dependant experiment. As will be seen in chapters 4 and 5, these components combine to allow the obtaining of data and results that would be inconclusive if not effectively interrelated. While the individual components are well studied, the dependant usage and combination of these techniques is something we believe to be unique. The major and minor components as discussed below are the technical resources utilized to draw these conclusions.

However, as the polymer layers grow thinner, a new phenomenon emerges. Due to the nature of the polymers, the interfacial region is not sharply delineated but instead shows a level of molecular mixing that creates a so called “interphase” region[5]. This interphase region is currently a subject of ongoing research and study[21]. The interphase region requires separate approaches and modeling due to measurably different material properties. This has been reported by and is currently part of the research performed at CLiPS[2]. This concept differs

from copolymerization[14] in that there are no covalent bonds formed, they are wholly separate polymers[22]. While the polymers remain separate, they form a region of unique behavior at the boundary due to a measurable change in properties. This so-called 'interphase' region is an interesting portion of the study at hand, and a relatively new field with significant research resources currently deployed towards development of a further understanding of it.

3.1 Behavior of Interphase Region

The behavior in the interphase region is studied by several sources and is of great interest to research into the extensibility of the CLiPS manufacturing technology. The research on the interphase region has been multifaceted, partially because the interphase is yet to be fully understood. The actual formation of the interphase, as seen in Figure 3-1, as well as the change in properties and other basics of the field have been compiled by several sources. Sottos and McCullough[21] present an overview of the current state of research surrounding polymer interphases. They discuss the current state of research, approaches to mechanical modeling, and comments on the formation and mechanical characterization. Space also is

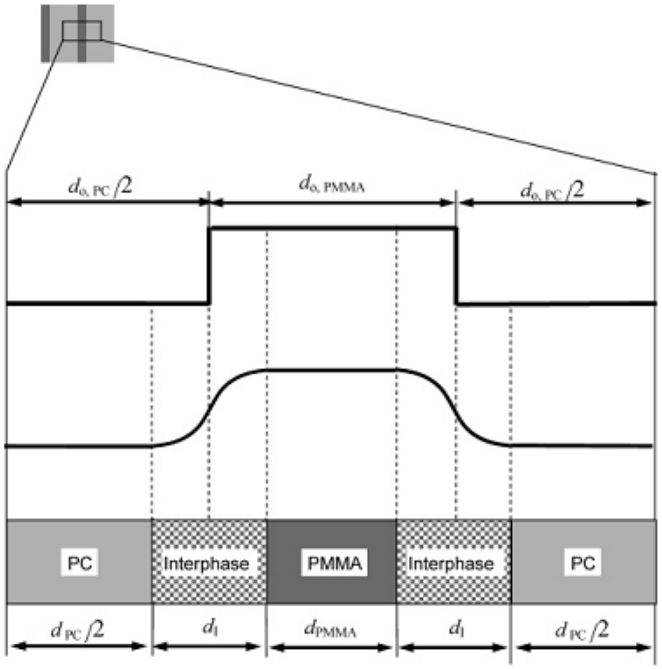

Figure 3-1 Expanded schematic of the interphase region of forcibly assembled polymers [5]

given to note current gaps in understanding and research in the field. The work is an effective summarization and provides a good starting point for this discussion. Lipatov[18] addresses differences that occur during formation and structural differences relating to preparation and thermodynamic variations between the interphase component materials in more detail providing a sufficient technical introduction to the material.

One of the research areas has focused on the effect of the interphase on testing of thin film materials, which commonly uses rigid substrates as a backing to allow for measurement of time based load response. Zhou and Komvopoulus[23] reported on using nanoscale dynamic mechanical analysis (nDMA) to study the behavior of polymer films deposited on a much stiffer substrate[23]. Given the deposition to a far more rigid substrate, they use the term interface as opposed to interphase to represent the lessened overlap of the individual layers. This paper concludes that a rearrangement of the molecular chain structures at and near the interface causes a change in the viscoelastic behavior. The testing performed shows a reduction in the complex viscoelastic moduli in the interphase region. The reduction occurred on both the storage and the loss modulus (E' and E''). This was demonstrated by the testing of multiple thickness samples. By testing multiple thickness depositions, the authors were able to back out the interphase effect from the varying ratio of layer thickness to interphase thickness (which is assumed fairly constant). They propose as a mechanism, wherein the constrained molecular chains near the interfacial boundary are confined and their mobility is reduced, "restricted small-scale mobility of the main chains"[23]. This is significantly relatable to the modeling work contained within this thesis and will likely provide a check on continued extensibility to thinner and thinner layers. Krupicka et al[24] further study this effect and are able to demonstrate varying levels of effect as micro indentation testing approaches the interface[24]. They report that the rigid substrate contribution creates a reduction in the viscous and an increase in the equilibrium (stiffness) component of the material properties. This correlation to Zhou is

expected, and the authors propose the ability to determine the Poisson's ratio of thin film polymers using the nanoindentation and tensile testing they used in the paper.

The CLiPS technology also enables a more detailed study of the interphase region. Liu et al. reported in 2005 on this use saying specifically, "The high fraction of interphase makes it possible to probe the interphase with conventional tools of polymer analysis"[5]. This is somewhat of a boon to the field, eliminating the need for specialized equipment capable of performing measurements on the nanoscale. As part of this paper, characterization of oxygen permeability of the constituent materials and the interphase was performed, however, this was of a secondary focus. The main focus was on manufacturing large amounts of interphase material. The paper reports on testing showing an ability to create an entirely interphase layer of PMMA, and propose a future expansion in the ability to create entirely interphase materials. The authors also investigate the stability limit of the layer thickness during coextrusion, the reported results found breakdown to occur when layer thickness were pushed below 5nm for PMMA[5]. Liu has also reported later on the ability of the manufacturing technique to generate entirely interphase materials[9] that further extend the manufacturing capabilities in use. Liu provides a schematic of the interphase area in a multilayered structure, which is shown in Figure 3-1. Figure 3-1 shows a labeling of the dimensions used to characterize the relative dimensions of interphase and local pure materials (In this case polycarbonate and Poly(methyl methacrylate). In this depiction, there is further labeling relating to Liu's study of variable oxygen permeability of the interphase, d_i, which was shown to be demonstrably different from the permeability shown by the pure polymers[5][9]. The conclusions really reflect the necessity for further study of interphase regions in polymers. Liu reports an ability to change the sizes of the interphase zones, and the ability to model and measure the properties. However, the research does not yet explain the exact formation mechanism and a method of clearly identifying the regions themselves. Liu reports some success with a proposed mechanism

related to an observed, and not fully explained, volume change that became more observable as the ratio of interphase was increased[9].

The examples above demonstrate one of the abilities for study provided by the CLiPS layer multiplication technology. The technology, as noted, creates a higher percentage of interphase for study that is of use to researchers. This is important as other work, specifically by the researcher, Possart, notes these issues when using traditional films. Possart specifically states “Quantitative information on mechanical interphase properties is obtainable only by considerable efforts since interphases belong to the class of buried layers, i.e. they are located between bulk polymer and substrate, which impedes a majority of experimental techniques”[25]. As CLiPS trends towards creating ever-thinner layers for specific applications, the layer thickness approaches the sizes of the polymer molecule size, the size and amount of interphase eases the ability for study to take place[9].

3.2 Determination of properties through ultrasound

The use of ultrasound for mechanical testing has been widely deployed in industry. Ultrasonic testing is used for a multitude of nondestructive structural interrogation, both as a flaw detection and evaluation technique and as a technique for the determination of material properties. The capabilities of ultrasonic testing allow for investigation of features not readily measurable through mechanical testing. For this thesis, two main categories of ultrasonic measurement are of interest. The first is measurement and analysis of viscoelastic materials and their properties. The second is of ultrasonic measurements of mechanical properties in multilayered structures. Combined, these two factors represent a model of the experiments carried out here.

3.2.1 Overall mechanical

Mechanical property determination using ultrasound relies on the analysis of reflected return signals. A-scans from single layer samples generate two echos as the ultrasonic pulse impacts both the top and bottom surface of the sample. A good example of these analysis techniques is shown by Jarlath[26] to determine mechanical properties of polymers. Jarlath[26] uses both direct evaluation techniques (directly analyzing the return signals) and analysis of fast Fourier transforms (FFT's) to make determinations of properties.

$$C = \frac{2d_{sample}}{t_{peak\,2} - t_{peak\,1}}$$

Equation 3-1 Equation for calculation of the speed of sound in a material calculated from the A-scan returns gathered through ultrasonic testing[26].

Specific properties are calculated by measuring the speed of sound in the material. This is done using the thickness of the sample, d_{sample}, (a known, measurable value) and the measured time of flight, which is determined from the ultrasonic returns, as seen in Equation 3-1. If the density is also known, it is possible to determine some material properties directly from the time of flight. These properties include the determination of the elastic modulus[11]. Secondary calculations and properties can be achieved using analysis of the attenuation and phase velocity that occurs in the test sample. Phase velocity is calculated using the standard FFT equation set[26]. The attenuation, α, can be calculated from A-scan as seen in Equation 3-2. The attenuation is determined by change in peak amplitude (A) and is measured separately from the peak amplitude change due do reflection and transmission.

$$\alpha = 20log\left(\frac{A_1}{A_2}\right)\frac{1}{\Delta d}$$

Equation 3-2 Attenuation (db/mm) calculation for ultrasonic test samples utilizing front and rear surface reflected amplitudes[26].

The peak amplitudes, can be combined with the determined speed of sound to further validate properties through a known ratio of reflection and transmission coefficients to model

wave travel within a test sample when the properties of the coupling fluid are known[27]. Combined, these can be used to achieve the complex moduli expressions as seen in Lippert[11] and in Jarlath[26] in Equation 3-3. The full model of a material can be made using several combined equations, which Lippert more fully discusses, and which are used throughout this thesis for modeling and data analysis. The most direct of these expressions is using the attenuation (α), phase velocity(v), and angular velocity (ω). As the attenuation approaches 0 the material approaches a purely elastic, material, E'' from Equation 3-3(b) would approach 0 as no energy loss occurs[18].

$$E' = \rho v^2 \frac{\left(1 - \left(\frac{\alpha v}{\omega}\right)^2\right)}{\left(1 + \left(\frac{\alpha v}{\omega}\right)^2\right)^2} \quad (a)$$

$$E'' = 2\rho v^2 \frac{\left(\frac{\alpha v}{\omega}\right)}{\left(1 + \left(\frac{\alpha v}{\omega}\right)^2\right)^2} \quad (b)$$

Equation 3-3 (a)Equation for the tensile storage modulus and (b) Equation for tensile loss modulus expressed using ultrasonic measurement properties[26].

3.2.2 Ultrasonic measurement of viscoelastic materials

When moving from the measurement of elastic to viscoelastic materials, the loss modulus component of Equation 3-3 becomes non-trivial. This means that return signals are subject to both the amplitude change from the interface reflection and transmission, as well as attenuation due the viscoelastic nature of the polymer materials[26]. Given the wide variety of applications, which are apparent in this field, there is significant available literature to draw from. This is partially because property testing and verification can take place at the same time as flaw detection[28]. The measurement of the viscoelastic parameter portion is done through a combined parameter analysis which includes the energy absorption (which is much larger in viscoelastics) as well compression wave speed, shear wave speed, and density as in elastic materials[29]. One of several methods of experimental determination of viscoelastic parameters

was detailed by Baghani[30]. Baghani utilizes a rheometry experimental setup combined with the ultrasonic probing to gather data. The rheometry device allows variable dynamic forces to be applied to samples during ultrasound elastography studies. From A-scan data gathered, two techniques were used to do the analysis. First, a peak to node method was utilized. This method estimates Young's modulus based on the pattern observed in the A-scan data. The method can also tolerate small levels of viscoelasticity. This is done by using analysis within the individual pulses, rather than a more generalized solution derived from spacing on timed reflected A-scans[30].

$$c^2(\omega) = \begin{cases} \frac{E}{\rho} & (a) \\ \frac{E}{\rho} + i\frac{B\omega}{\rho} & (b) \end{cases}$$

Equation 3-4 Parameter model of elastic(a) and viscoelastic(b) utilized for analysis of

The method however, cannot fully articulate the viscous nature of time-based relaxation present in polymers and viscoelastics. The second method utilized by Baghani is a model fitting method utilizing a least squares approach to fit a parametric viscoelastic model to the A-scan data. In this case, the model that was used can be seen in Equation 3-4 and was combined with the Voight model to develop a generalized solution which was fitted to the A-scan data[30]. Results from Baghani showed the ability to fit parameters and results to a solution with less than 10% error. Given that Baghani does not make note of active and tight controls on temperature, it is likely that some of this error can be attributed to variable conditions especially given the amount of change in similar testing reported by Jarlath[26].

Other works have taken different approaches. Safaeinili et al.[28] used a method of an angular ultrasonic scan to gather data and perform a viscoelastic parameter analysis. This allows for measurement of the shear wave velocity in addition to the longitudinal velocity. This technique allows a more direct calculation of viscoelastic parameters[11],[28],[29]. Lippert

provides a method using reflected waves and a static arrangement of ultrasonic transducers[11]. The authors were able to develop an experimental equation, which links the shear and compression wave speed using the experimental parameters. The authors were able to replicate the results of Kulmyrzaev[31]. The results utilized the incident angle of the mode-converted wave to calculate the complex components of the compression and shear waves. This is important due to the higher rate of attenuation that viscoelastics display in shear wave propagation[11]. Lippert was also able to demonstrate that the returned signal is directly based on G*, the magnitude of the complex modulus of the material under test.

A final method of interest was proposed by authors Hull and Langton[32]. Hull et al propose an identifying parameter that can be used as a unique material identifier. The Hull and Langton technique utilizes a wideband frequency scan to measure attenuation and speed of sound. From this information, they generate test signature, as seen in Equation 3-5, which is theoretically unique to the material under test. The authors demonstrated the ability to generate a unique identifier for several similar polymers similar to polymers used in this work[32]. This ability to combine the speed of sound, a general material parameter, with the attenuation, a pointer to viscoelastic properties, is potentially directly useful to the work here. However, their experimental technique and results are drawn from a method that may not be feasible or applicable to multilayered materials because of its reliance on through transmission.

$$S = \alpha c_{long} = \left(\frac{A}{d}\right) * \left(\frac{d}{t}\right) = A/t$$

Equation 3-5 Solution for the unique material signature, S, as developed by Hull et al[32]. Utilizes the attenuation (α) and the speed of sound (V).

Cumulatively, these techniques make use of wave reflections, wave transmission, and general wave characteristics to perform a determinative analysis of signal returns. These examples make use of certain assumptions based on the testing of singular materials. However, given the more complicated case of multiple layers of differing materials, a different

set of techniques must be applied[33]. Without repeated interfaces between the material under test, and the infinite material in use, the correlation of properties to amplitude changes and associated calculations for attenuation determination do not work. A separate class of investigations have undertaken property determination and ultrasonic testing in multilayered materials.

3.2.3 Ultrasonic measurement in multilayered materials

The measurement of properties in multiple layers of a material within a test sample requires the replication of these techniques over several peaks and reflections within a set experimental sample. Most investigation of multiple layered media has been in regards to defect detection and investigation of delamination of individual layers[34-36]. However, it is also possible to utilize ultrasound to perform mechanical analysis through either direct measurement or in combination with a more detailed analysis.

Two authors, Belleval and Potel[37],[38], have done significant work relating to ultrasound in multilayered materials. The two most relevant papers span both sides of the issue. The first[38] discusses methods for modeling the propagation in multilayered media. This work demonstrates their method for the reduction of numerical stabilities. As they discuss, these numerical instabilities need to be controlled to allow for effective simulation. The instabilities occur because of high power exponential terms and their inherent problems when media become too thick[38]. When these situations occur, the cross products necessary in solutions become either very large and approach infinity, or very small and create accuracy problems. The current solutions that have been proposed to this problem can be made numerically stable, but at the cost of significant increases in computer memory which lead to limitations on simulation size[39]. The author's technique utilizes so called 'super layers' to help subdivide and organize the problem into repeating units prior to utilizing simulation and modeling of Floquet waves[38]. They demonstrate their technique on the simulation of

multilayered carbon epoxy composite plates. They conclude that the technique successfully solves the presented problem while also allowing for the correct simulation of the imaginary and infinite terms arising from the boundary regions between layer which cause reflection and allow transmission[38].

The other Belleval and Potel paper discusses the numerical modeling of propagation in adhesive bonding testing[37]. This is a relatively similar case to that presented in this thesis. The purpose of the paper is the utilization of the prior discussed technique[38] for a specific application. That application is the investigation and analysis of composite structure bonding and the detection of voids or defects. This occurs through the propagation of an ultrasonic pulse through a composite structure and adhesive bond. The Belleval and Potel technique[38] is applied to help detect and analyze non-obvious defects and areas of poor quality that may not have been apparent through normal NDT visual analysis. This technique is demonstrated through a comparison of experimental results for areas of good and bad adhesion. While similar in profile and overall amplitude, significant differences can be shown when a wider band scan is utilized and this is demonstrated by the authors using their propagation simulation comparatively to the experimental work performed[37].

Another approach is detailed by Raišutis et al.[35] Their goal is to utilize signal processing to enhance imaging and quality control of multilayered electronic components. These components are similar in manufacture to our samples, but differ in that they display little or no viscoelastic properties, and use much thicker layers with less creation of an interphase and a much smaller component of interphase behavior[5]. The authors' goal was to utilize processing not on individual A-scan, but in bulk to generate images which more clearly detailed defects and also visually differentiated between different types of defects[35]. To do this, the authors calculated the reflections and transfer functions of the returned signal at all points of a C-scan. Delaminations and defects change these functions in different and identifiable ways.

The shifts in the functional behavior that occurs at these points can be used as identifiers for different behavior. Using these spatial processing techniques, the authors successfully demonstrated the ability to detect interlayer delaminations, and areas where certain layers were missing or damaged. The authors also demonstrated the ability to accurately detect the extent of the region on which the defect occurred[35]. While defect detection is not the goal of this thesis, the methodology for discretization and analysis of individual layers within a multilayered system are of use from a mathematical standpoint for the analysis of the experimental data gathered.

Huo and Reis[40], however, take a more analytical approach to the analysis of multilayered data. Their goal is not defect detection, it is measurement and determination of material properties of layer within a structural sandwich. The data analysis techniques are applied to testing of an adhesive layer within a windshield structure consisting of two glass plates bonded together. There exists a modeling technique for the properties of the interior adhesive layer, representing it as a set of spring constants. The authors' goal is to utilize ultrasonic testing to determine the constants and the behavior of this inner layer. The authors base their study on the ability to discretized Pummel levels, a measure of adhesion and adhesive strength, in the internal layer. The actual testing was performed using an angle beam inspection arrangement of transducers. Initial results showed an ability to clearly differentiate between the different levels of adhesion via the energy of the reflected peaks[40]. However, a more detailed analysis was necessary to allow the determination of the parametric model components.

The authors go on to demonstrate the ability to identify different stiffness of adhesive through changes in the propagation velocity. This is a phenomenon that is to be expected, and can be mathematically characterized as described earlier in Equation 2-7. It is also a characteristic of wave propagation that is relatively easy to determine, but the use the

confirmation of its validity in layered materials is useful. The authors' main goal however, is to study and measure the attenuation. The attenuation in this setting is a function of the level of adhesion, the thickness of the adhesive layer, and the mechanical characteristics of the adhesive. This is a similar situation to that in this thesis in terms of the goals and the variables involved.

Huo and Reis[40] achieved their goals through a combination of simulation and signal analysis. For the signal analysis, they made an assumption of the level of adhesion (Pummel scale) based on the measurements they took initially which allowed this determination. They then took a number of samples and were able to determine the relative effects of variances of mechanical properties and variances of thickness. They showed that velocity dependence (for both the S_0 and A_0 wave mode) varies significantly in response shape over frequency due to varying mechanical properties. They also showed shifts, but only small changes in the shape of response, for the varying thicknesses[40]. The authors also demonstrated an exponential increase in attenuation related to the increase in thickness, again, this is to be expected and is simply a validation tool to prove results and methodology. They continue with a robust study of all factors related to this testing and their effect on results. They present results on variation of all potential factors including the variation of the glass layers, which displayed a minimal affect on the results found.

The authors conclude that it is quite feasible to use this technique to analyze the complex system characteristics. They specifically note, that higher frequencies, starting above 1MHz, seemed to demonstrate more clearly the behavior of interest. They also note the ability to decouple the specific changes in the returned signals to allow accurate model alignment and determination of individual properties[40].

The techniques used by Huo and Reis[40] however are limited by the same physical problems as any ultrasonic technique. As the thickness of the samples, and the layers within the samples, decreases, the level of precision and the ability to separate information in the time spectrum decreases. One approach to this is to move to a light based measurement system[41]. The potential of utilizing a system of laser based testing removes some of the limitations of ultrasonics. Ultrasonics as a measurement technique begin to degrade as the thickness of samples, or layers within samples, approach the wavelength of the investigative wave pulse. Cheng et al.[41] were able to demonstrate the usage of laser based investigation to determine the properties of very thin films produced by CLiPS[3] by way of measurement of dispersion and Brillouin scattering[41]. The data gathered from these experiments, combined with numerical simulations of mathematical replicas, allowed them to determine the elastic (but not viscoelastic) properties through the analysis of phonon dispersion[41]. The study was quite successful, validating the techniques which the authors planned to expand in the future to further study the CLiPS layer technology in a similar way to the techniques employed in this thesis.

As noted in the discussion of the literature above, certain aspects of the investigation of material properties in layered media are believed to require the collection of additional data developed through simulation as a method of completely and accurately determining properties. The need is due simply to the number of independent parameters and variables involved in the characterization of a multilayered sample. It only increases when the complicating factor of viscoelasticity is added. This increased need for modeling is complicated by the realities of what is being modeled. Fortunately, there is significant research to support this.

3.3 Modeling

In addition to consulting the relevant literature on the experimental side of this field, one must investigate the relevant literature for simulating the same complicating factors that affect the experimental side. However, this discussion can be broken up slightly more effectively, individually discussing the simulation of ultrasound and ultrasonic propagation, and separately, discussing the simulation behavior at the layer interfaces. The behavior at the layer interface is the only major complicating factor. The polymer behavior is inherently resolved in the bulk propagation model. The boundary conditions that occur at layer interfaces are the factor responsible for the reflected signal, and are of significant interest.

3.3.1 Modeling of ultrasonic propagation

A very basic model of ultrasonic propagation is presented by the researchers Chertov and Maev[27]. They develop a one-dimensional model of ultrasonic propagation employing finite difference. The model used simulates ultrasonic propagation during a spot welding process. Similar to this thesis, the authors hope to use the simulation as a comparative tool to data gathered experimentally. The authors use the simulation to model the 'perfect' conditions of the manufacturing process. The actual process data can then be compared to model results for validation and quality control.

This simulation is of interest to this work for two reasons. First, the simplified single dimensional aspect, and the authors work on it, helps to nullify concerns about simulation error. Using a single dimensional simulation to model an inherently multidimensional process, such as sound wave propagation, introduces unavoidable error. The authors address this and demonstrate technique validity[27]. Second, the authors employ non-constant material properties. The material properties used by the authors are variable, both continuously and discontinuously. The process being modeled by the authors, welding, contains changes in the

speed of propagation due to differing materials of the electrode and the material being welded. At material boundaries, discontinuous material property changes occur. The modelling of these boundary conditions is directly relevant to this thesis.

There are also changes in propagation speed due to changes in material temperature and material phase during welding. These properties vary with time, and in a continuous manner. The techniques developed serve to improve the modeling of complex material property situations. This behavior is very similar to that observed within the interphase of a polymer interphase. The authors develop a finite difference model accounting for these conditions. This model was used as a rough basis for a more complex model developed for the computational methods employed by this thesis to model propagation in polymers.

However, the analysis and model from Chertov[27] is somewhat simplistic in its handling of the boundary conditions, doesn't employ any viscoelasticity, and carries inherent stability problems in its use of finite difference. The full model can be seen in Equation 3-6. It can be noted from the model, that as the zstep decreases, the model becomes increasingly unstable.

$$u_i^{n+1} = ru_{i-1}^n\left(f_i^n + \frac{f_{i-1}^n - f_{i+1}^n}{4}\right) + ru_{i+1}^n\left(f_i^n + \frac{f_{i+1}^n - f_{i-1}^n}{4}\right) + 2u_i^n(1 - rf_i^n) - u_i^{n-1}$$

$$r = \frac{\Delta t^2}{\rho_i^n \Delta z^2} \qquad f = \rho c_l$$

Equation 3-6 Chertov[31] model of propagation. n super scripts denote time step, i sub scripts denote z step.

Several other models provide a more robust solution using variations of the finite element method. Of note, are those developed by Stucky and Lord[42] and by You et al.[43]. Both develop useful models, highlighting different characteristic areas for improvement. You concentrates on a more direct method, involving the decoupling of 3D simulations using the z axis axisymmetry inherent to directed ultrasonic pulses. Stucky concentrates on utilizing the limited bandwidth of the ultrasonic transducers to reduce the amount of time history information

that must be stored to effectively simulate the attenuative and time shifting nature of fully viscoelastic materials. Both of these serve to reduce the memory footprint of simulations through a reduction of the information, such as previous time steps, that must be stored to create an accurate simulation.

The work by You[43] provides a helpful comparison to the goals of this work. The author utilizes decoupling, making use of the radial symmetry about the z axis. The author also utilizes a cylindrical coordinate system for the model development. This creates a set of 4th rank matrices when the derivative equations are expanded and written in matrix form. The formulation is made using standard variational calculus techniques. This technique was used to develop a model for the non-absorptive case. The authors successfully use the non-absorptive case as a demonstration of the fully modeled behavior, and a validation of their initial efforts to decouple the propagation directions.

$$T = CS \quad (a) \qquad T = CS + \eta \frac{\partial S}{\partial t} \quad (b)$$

Equation 3-7 (a)Non-absorptive stress tensor model (b)Absorptive stress tensor model for use in finite element model of wave propagation.

You[43] then proceeds to detail the same technique, complicated with the introduction of the energy absorption terms. This change was made, at the most basic through an adjustment in the governing equation by addition of a time dependant term in the stress tensor. Both tensor models can be seen in Equation 3-7. Effectively the same procedure is carried out using variational calculus to develop a solution. The addition of the absorptive term creates an added term to the energy functional which in the end, is modeled through the inclusion of a separate elemental damping matrix. The damping portion of the functional is determined through the viscosity term, η. To express the viscosity term, the author utilizes empirically determined curves, which model the degree of attenuation and anisotropy in the material. This technique creates a finite element model, where the time history behavior is rolled into the damping matrix

and does not require the storage of the time history. The issue that arises though, is that the damping curves, which can contain anywhere from 2 to 21 terms, must be obtained experimentally to create a model. If this technique were employed, it would require the number of independent variables in the simulation to be significantly increased. This would have made it far more difficult to find a material solution, which produces matching simulation results to the experimental results.

Stucky and Lord[42], apply a somewhat similar technique to actually create the simulation from the input parameters. The difference from You[43] is that Stucky[42] uses the standard linear model to develop a viscoelasticly compliant single matrix representing the full material properties. Stucky utilizes the material properties that are in use in our simulation, the complex moduli, to form the property matrices. The real and imaginary portion of the property expressions, are not separated. This reduces the number of matrices stored from 3 to 2, and cutting the memory requirement by a third. The tradeoff is that this method requires a full storage of the relaxation spectra to calculate the material properties, so that the material property can be correctly recalculated based on the local oscillatory spectrum at that element.

3.3.2 Modeling of ultrasonic propagation at a material interface

The property changes at a material interface create a reflective boundary that must be addressed in any solution. Both finite difference and finite element simulations model this behavior. However, a further review was undertaken to more deeply understand the properties of wave propagation at the interface. The boundary condition that occurs creates the reflected signal, which is the intended output of the simulation. Accurately modeling the reflections is at the root of producing an accurate simulation of the experimental work. Two works were considered providing different portions of information.

Belgroune[44] provides for a more theoretical study of propagation at the interface. The authors utilize a method wherein the ultrasonic field is decomposed, into the constituent plane waves. The model they develop uses a derivation of the Snell laws for refraction and a more robust formulation of the transmissive coefficient. The transmissive coefficient definition is interesting in its inclusion of the angle of incidence, through the use of unit vectors on the interface through a multi axis coordinate system. The model used for the transmissive coefficient of compression waves, can be seen in Equation 3-8. In this formulation, ρ_s represents the density material on the appropriate side of the interface, and the derivative term is the scalar potential energy of the propagating wave.

$$T_n(x_1', x_3'; t) = \rho_s \frac{\partial \varphi(x_1', x_3'; t)}{\partial t}$$

Equation 3-8 Definition of the transmissive coefficient of an ultrasonic wave propagating into a solid across a discrete material interface

The coordinate system used is based on the nominal direction of propagation through the decomposition process. In an expanded case, the proposed method would be quite useful to the work presented in this thesis. However, the method relies on the use of a 2 or more dimensional simulation. The experimental simulation we present encounters limitations both in time of simulation and in the memory requirements, while only using 1 dimension. The required expansion to 2-dimensions to implement Belgroune's technique is not currently feasible. However, this work was used to help define alignment tolerances for experimental testing.

Further, Belgroune's methodology relies on an asymptotic assumption of the change in material properties at the interface. While the model produced in this thesis does make that assumption, flexibility in that is important for future work. As the layer thickness decreases, the previously discussed interphase becomes important. Variable material properties near the

interface, as opposed to an asymptotic change, must be modeled. Currently, this is done by making no assumption of material behavior in the solution, and implementing material properties in the pre processor development of the elemental and global matrices. Inducing the asymptote assumption into the solver would prevent this change being made.

Fisher and Brinson[45] present a different technique, including the implementation of a finite element scheme. The paper does not analyze ultrasonic propagation, instead concentrating on mechanical response. Their study is directed at fibrous composites, but includes a discussion of the viscoelastic interphase generated from the polymeric matrix materials used. The authors provide a slightly different interpretation of the interphase concept as it applies to their work. The interphase of interest to the authors occurs at the boundary between two significantly different materials (100x change in properties) rather than very similar materials (10-20% change in properties). However, the result is the same, modelling a change in material properties over a small relative distance.

The authors develop their solution using a non-linear displacement general solution. This includes a component initiating the time history declination caused by the viscoelastic materials. The general solution can be expressed in a basic form as:

$$u_i(x,t) = \bar{u}_i(x,\omega)e^{iwt}$$

Equation 3-9 Separable general solution to displacement using frequency (ω), position (x), and transformed u denoted by overbar. From Fisher and Brinson

This form allows the implementation of the complex moduli, similar to the implementation we will use, which is seen here in Equation 3-10, and is expressed slightly differently than the normal form seen earlier in Equation 2-20. The problem arises when this form is implemented. Because of the imaginary portion of the modulus, using it to directly create a simulation produces imaginary results. The results must therefore be transformed over the expected frequency range.

$$\bar{K}^*(\omega) = i\omega\bar{K}(\omega) = i\omega \int_0^\infty K(t)\, e^{-iwt} dt$$

Equation 3-10 Integral expression of complex bulk modulus.

To avoid the problems of imaginary results, two micro-mechanical methods were employed by the authors. These were the Mori-Tanaka method and the Benveniste[46] method. The Benveniste solution is more applicable to the case we present and is shown by Fisher and Brinson to quite effectively match the results achievable through the imaginary FEA results. The Benveniste derivation however, specifically separates and includes a discrete interphase. Based on the available literature on interphase material behavior, this would present an opportunity for effective modelling of the interphase effects on propagation. This could be achieved through minimal modification of the solver developed in our work as future work. However, the current simulation of layers that are at least 2 orders of magnitude larger than the interface makes the inclusion of these minimal effects an unnecessary use of already stressed computational power for the presented cases.

Chapter 4

Experimental Work

4.1 Layout and Setup

The equipment used to gather data reflected relatively standard practice for ultrasonic testing. The experimental setup can be seen in Figure 4-1. The sample is held inside the sample holder which is utilized to suspend and align the sample under test, normal to the transducer which is mounted directly above. The vertical separation distance of the transducer and the sample is adjustable using the motorized linear slides. The linear slides allow for positioning, and scanning, in an incremental and precise fashion in all 3 axes. The rest of the equipment comprises the data acquisition system with a pulser and oscilloscope connected to the transducer.

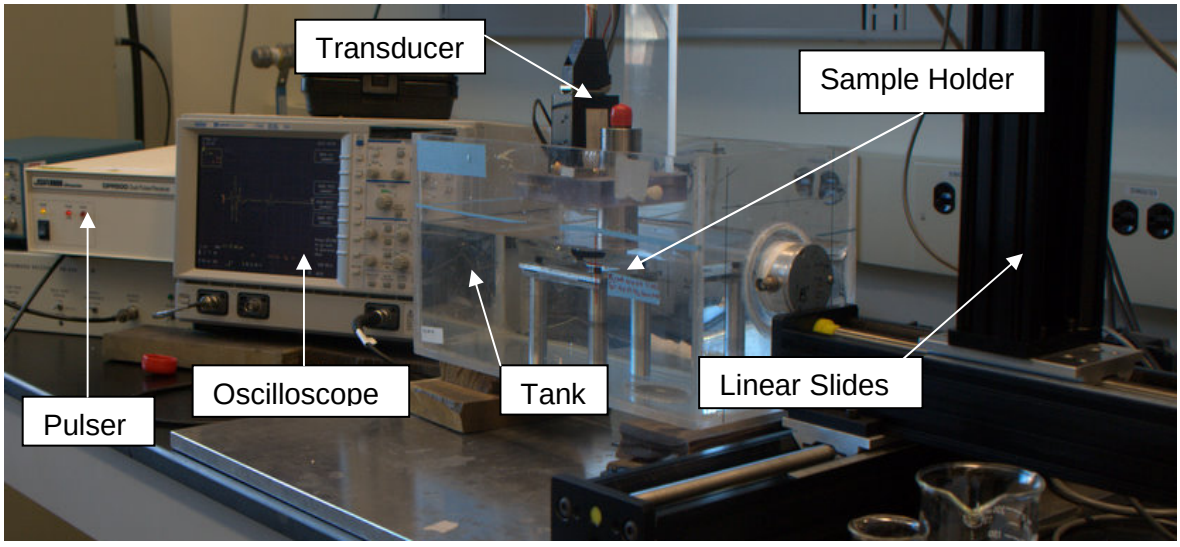

Figure 4-1 Overall Experimental Setup including Pulser, Oscilloscope, Tank, Sample Holder, Transducer, and Linear Positioning Slides

While modern developments have enabled the usage of ultrasonic testing with air as a couplant, immersion testing in a water bath was selected as the experimental method for a

number of reasons. Given the intent to study internal properties of the samples, the increase of the transmissive coefficient at the surface of the sample from a change in infinite materials is extremely helpful. As are shown in Equation 4-1 and Equation 4-2, changing to immersion testing changes the surface transmission coefficient from .0005 to .875. This means that the amount of ultrasonic energy transmitted into the sample increase by a factor 1,750.

$$Z = \rho c_l \left(\frac{gm}{cm^2 sec}\right) * 10^5 \;\; Z_{air} = 0.004 \quad Z_{water} = 1.48 \quad Z_{PMMA} = 3.1$$

Equation 4-1 Calculation of acoustical impedance for experimental comparison.

$$T = 1 - (\frac{Z_2 - Z_1}{Z_2 + Z_1})^2 \quad T_{water/PMMA} = 0.875 \quad T_{air/PMMA} = 0.0005$$

Equation 4-2 Calculation of transmission coefficient for water to PMMA and air to PMMA ultrasonic boundary propagation.

Without this change, the amount of transmitted energy would not be sufficient to create measurable reflections from the interior boundaries in the samples. Within ultrasonic testing, there is an inevitable and acceptable level of noise. To create opportunities for interrogation of material samples, the level of returned signal must exceed this noise by a factor sufficient to allow clear determinations of reflected signal behavior. When internal interfaces are of interest, such as when a multilayered material is under test, a higher energy propagating into the sample allows clearer reflected signals from the internal interfaces to be measured. A couplant with better-matched impedance creates a higher transmissive coefficient and allows better interrogation of the sample.

While this same effect may have been accomplished via a transducer directly coupled to the sample via a thin layer of couplant, it was decided to use a full immersion tank for a number of reasons. This includes the ability to move the transducer over the surface in a automated fashion that does not put a load on the surface using stepper motors. The softness of the samples under test creates a situation where the force necessary to bring a transducer and

sample into intimate contact with a thin layer of couplant would cause unacceptable levels of deflection away from a perfectly normal angle of incidence of the transducer emitted pulse. It can also potentially cause physical compression in the material samples at varying rates due to varying layer stiffness, which can skew measurements in a way that would create unacceptable levels of error.

4.1.1 Equipment Detail

The specific equipment utilized was chosen to allow for maximum flexibility and accuracy in the scanning performed. The heart of the system was the transducer selected. Due to the thin individual layers that were to be characterized, a relatively high frequency transducer was used. The transducer chosen was an Olympus[47] V3332 with a nominal center frequency of 50MHz and a focal distance of 13mm (0.5”). Further, a larger immiscible transducer package (designated SU/RM) was selected to allow for a larger delay line[6] and longer window in which the returning signal will not interfere with the internal case reflections. The transducer and remote pulser attachment are shown in Figure 4-2. The transducer is designed to produce a heavily damped broadband signal.

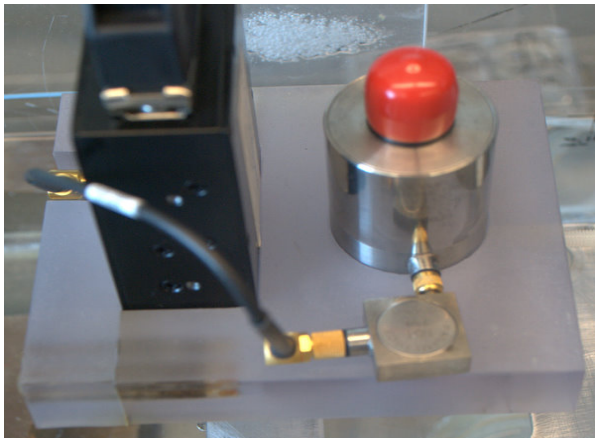

Figure 4-2 Olympus V3332 50MHz transducer and JSR Remote Pulser (black box)

[6] Delay Line: delay between input and output signal. In ultrasonics, refers to the window between internally reflected pulses inherent in the use of ultrasonic transducer cases and focusing lensing.

In Figure 4-2, remote pulser module is shown. The use of the remote pulser facilitates the utilization of a shorter analog connection between the pulser and transducer. The remote pulser works to provide a higher level of signal integrity and better quality results by reducing opportunities for Interference and noise pickup, and less signal attenuation. Both the remote pulser module and the main pulser module are products of JSR[48]. The main pulser module is controlled through an RS-232 serial interface from the same computer used for data logging. It is responsible for generating the transmitted pulse using high-speed switching electronics as well as routing the generated pulse signal, trigger signal, and the measured reflected signal to the remote pulser module. The remote pulser module uses this information to control the actual transducer over a single wire, using the trigger signal to switch between sending the generated pulse signal to the transducer and listening to reflected energy gathered by the transducer. The main pulser module then performs basic wave filtering, using user configurable high and low pass filters. The pulser module then passes the returned signal to a high speed oscilloscope.

The oscilloscope utilized for the experimental work carried out here needed to be of a high precision due to the tight timing involved in making determinations of the speed of sound in the materials. Using the initial estimations of experimental values, estimating the expected time of flight was possible. For the two major materials, PC and PMMA, the generally accepted values for the speed of sound are 2200m/s[49] and 2750m/s[49] respectively. The anticipated layer thickness is approximately 60microns. This allows for an estimated time of flight of 54ns (nanoseconds) in PC and 44ns in PMMA using Equation 4-3. To allow measurement at this precision, a LeCroy[50] LT342 oscilloscope with a sample rate of 500MS/s (10^6 samples per second) was used.

$$\Delta t_{TOF} = \frac{2d}{c_l}$$

Equation 4-3 Method for calculation of the time of flight of an ultrasonic signal in a solid material. Derived from Equation 2-12

At a sample rate of 500MS/s, the oscilloscope records an amplitude (voltage) reading from the pulser every 2ns. This leads to an estimation of 27 data points per time of flight when measuring a PC sample, and 22 points when measuring PMMA. The data did prove sufficient to differentiate pulses and draw conclusions from the sample, however for a further study, it is likely more information per measurement would prove useful.

The oscilloscope was the end device in the basic data collection chain, and was responsible for formatting of the data and sending it over an RS-232 serial connection to the computer used for data compilation and analysis. The oscilloscope was also responsible for framing the data points that were being transferred. Due to the rate of transfer of the serial bus protocol, the amount of data transferred was limited through the configuration of the data request command issued by the data acquisition computer to a specific number of data points. The data transmitted to the data acquisition computer includes every data point recorded by the oscilloscope starting at the first point after the trigger event. The trigger event is passed from the pulser to the oscilloscope to align the timing of the recording cycle beginning and concluding in the oscilloscope. This timing is changed in the oscilloscope using an adjustable delay, an improperly adjusted delay can be seen in Figure 4-3. The example in Figure 4-3 would

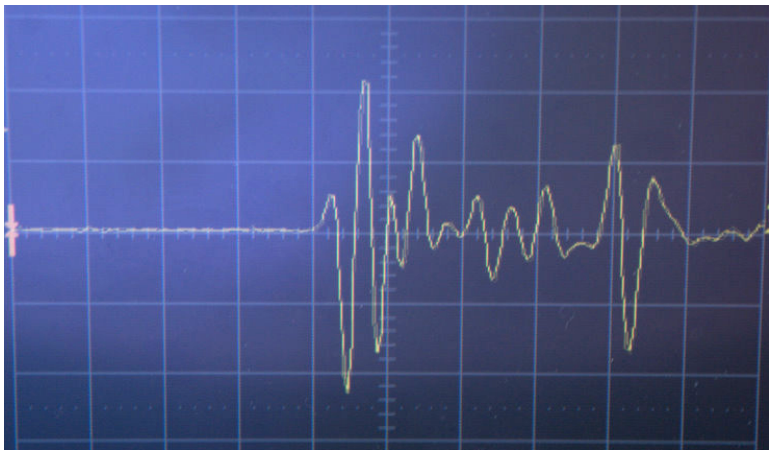

Figure 4-3 Improperly adjusted delay on reflected signal displayed on oscilloscope screen.

unnecessarily record a series of data points leading up to the signal. The delay allows a user to make a timing adjustment between the time when the trigger command is received the pulser and the time the recording cycle begins on the oscilloscope. This enables the user to configure the data recording cycle to begin just before the signal of interest begins. A more accurate technique would be to utilize the internal capabilities of the oscilloscope to create a level trigger, which detects and begins recording based on sensing the leading edge of the returned signal. When tested, this proved inaccurate, and tended to adjust at rates that caused the loss of data in the beginning of the signal.

The data acquisition continues until a specific number of points are recorded, a number determined from the data transfer command that the computer issues to the oscilloscope. In the same way as the delay command, changing the number of points recorded bounds the end of the signal recorded. While recording more data would have simplified the initial scan

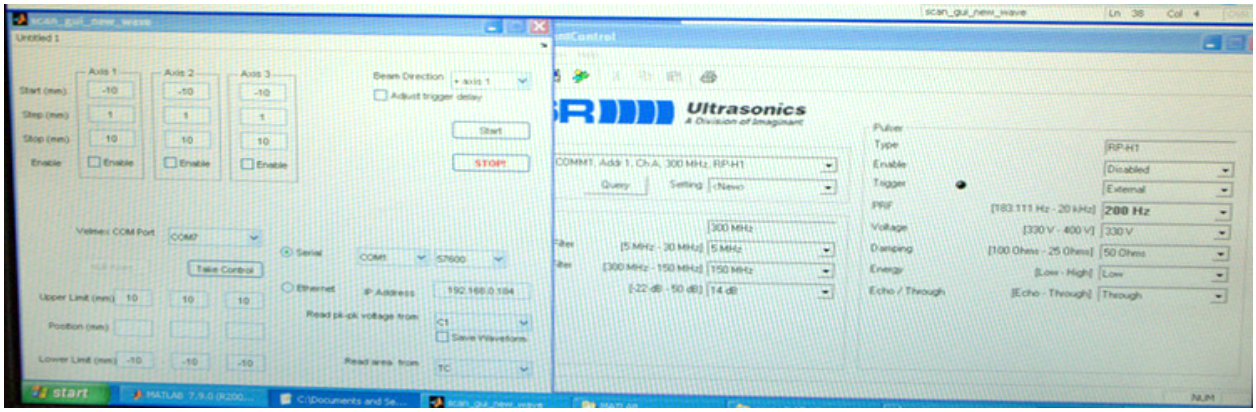

Figure 4-4 Image of JSR and Matlab GUI

configuration, it would also contribute to slowing the scanning process through an unnecessary recording of data. Further, that extraneous data would be of no analytical use. Notably, the output of data through the serial bus occurs at the rate data points are gathered and is independent of the time scale zooming performed on the oscilloscope display. The output of data occurs at the same rate it is gathered, in this case 500MS/s. The computer used, a

standard desktop PC, which provided a high level system control over the experimental apparatus.

Through the use of Matlab, and a proprietary piece of JSR software, the data acquisition computer controls the operation of all experimental equipment. The pulser is controlled through the JSR software, and is an input only system, which is static during the course of a scan. The Matlab software is controlled through a GUI interface. The Matlab GUI is responsible for the configuration of the scans, controlling the axis of scanning (X, Y, and Z), the step size, and the scan limits. The underlying code is responsible for all communication with the oscilloscope, which includes sending an RS-232 request for data, and receiving the RS-232 to data and recompiling into a Matlab variable. Matlab also performs initial processing of that data and writes a file containing all of the data recorded. For example, a point observation would generate a single A scan. In a one dimensional scan, called a B-scan, an image is generated from the plotting of individual A-lines recorded from the oscilloscope. The resulting image shows the recorded data in the visual realm, but is of limited use beyond visual high-level signal integrity checking. This is useful because of gaps that do occur due to drop outs in the RS-232 protocol, which can cause individual scans to not be recorded.

The last usage of the data acquisition computer is to provide a high-level control of the linear slides, which control the location of the transducer in all 3 axes. The control is performed using a third RS-232 serial port. The underlying code in Matlab performs a two-way

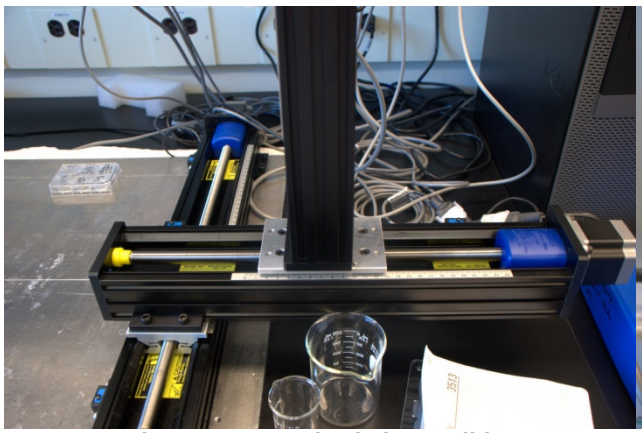

Figure 4-5 Motorized Linear Slides

Figure 4-6 Velmex stepper controllers

communications handshake with the motion controller, to ensure proper location is achieved prior to recording the A scan from the oscilloscope.

The motion controllers, seen in Figure 4-6, and linear slides, seen in Figure 4-, are manufactured by Velmex[51]. The controllers and slides collectively allow for automated and precise location within the scanning envelope. Two motion controllers are utilized in this case. The first controller manages all movement in the X and Y (in plane with the sample) and is used for most scans that were run. The second controller is solely responsible for controlling the Z (normal to sample) axis and is used to adjust the focus of the transducer with respect to the sample.

4.1.2 Experimental Methodology

The overall intent of the experimental equipment was to gather the individual A scans from which material property data can be derived. The data used to determine material properties is contained within the directly reflected signals. However, the ability to take multiple scans in multiple directions allows for the gathering of far more data in a short period. It also allows for the investigation of the variance of properties over the scan area. Therefore, a series of scans and procedures were developed to allow repeatable, and comparable, gathering of data across multiple samples of the same (and different) materials and layer counts. The overall goal was to provide repeatable, easily comparable data between multiple, drastically different, experimental samples.

4.1.3 Mounting

All samples are suspended in the water tank using a custom designed and machined sample holder specifically engineered for the samples in use. The sample holder requirements included the ability to suspend an area of the sample in the clear, while supporting it at a height

sufficient to minimize potential reflections off the bottom of the tank, effectively creating an infinite boundary condition on the backside.

The infinite condition is created by making the reflections off the back of the tank occur much later (about 6 times) than the signal of interest. This vertical standoff also allows sufficient space to bring the transducer within the focal distance of the sample surface. The stand that was developed, seen in Figure 4-8, utilizes 3 legs to ensure stability of the stand. It also contains two clamps, one at each end which are used to hold the sample taught, and as flat as possible, The goal is not to provide a preload on the sample, but to ensure the sample is as flat as possible for two reasons. The first, is to ensure that the reflected signals arrive at similar times. This enables better data collection because it narrows the number of data that must be collected by narrowing the timeframe in which the reflected signal will return to the transducer. The second reason, is that holding the sample as near to perfectly normal and flat as possible maximizes the magnitude of the returned signal by reducing reflections that do not return to the transducer due to the angle of incidence. Keeping this true, allows for the return to be consistent and comparable cross multiple samples and differentiable across different sample types.

The stand also contains a window machined into it, Figure 4-7, This is the area that is used for the actual scanning, creating an open area allows for the ultrasonic signal to pass

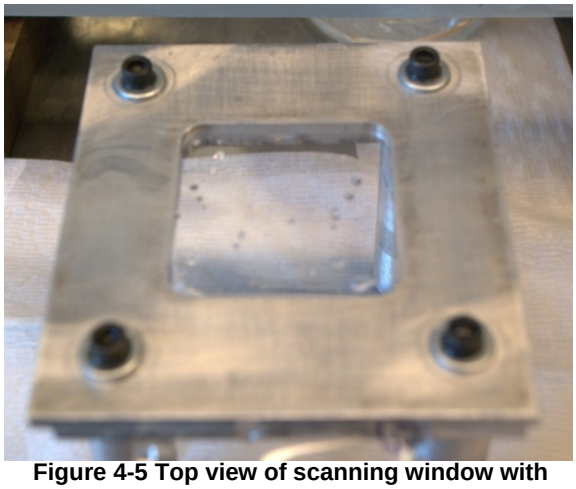

Figure 4-5 Top view of scanning window with polymer sample installed

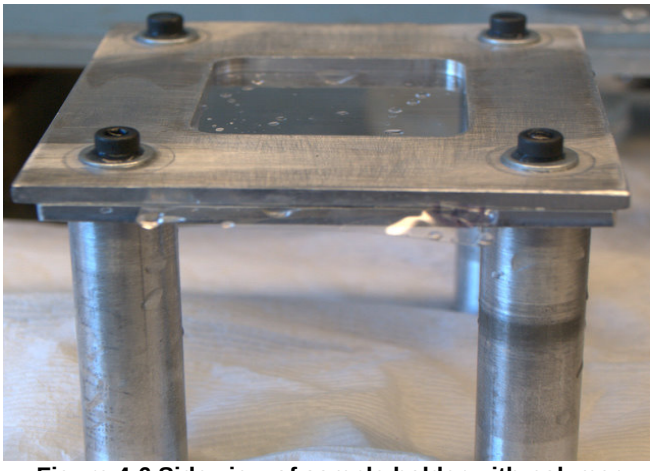

Figure 4-6 Side view of sample holder with polymer sample installed.

unimpeded from the transducer, through the sample, to the back of the tank. With a 0.5” focal length transducer, and a 3” tall stand with an open area on the top and bottom, it is possible to easily isolate the signal that occurs from the sample under test while still holding the sample flat enough to allow effective data collection.

4.1.4 Focusing

To undertake the actual scanning of samples, a sample is first mounted into the sample holder. The motion controllers are then used to bring the transducer within the X and Y range of the sample window, and then within the approximate focal distance of the surface of the sample. From this point, the actual signal from the sample is located. This signal must be differentiated from the internal reflections generated by the transducer case and focusing lens. Once the manual alignment is complete, a small scan is undertaken utilizing the Z axis only. By stepping through the Z axis, it is possible to locate the distance at which the reflected return signal is at a maximum. This is the point at which the the transducer is correctly focused and the point at which the scans are carried out in X and Y. The maximized signal is important in that it allows for the maximum amount of data, both in amplitude and data clarity.

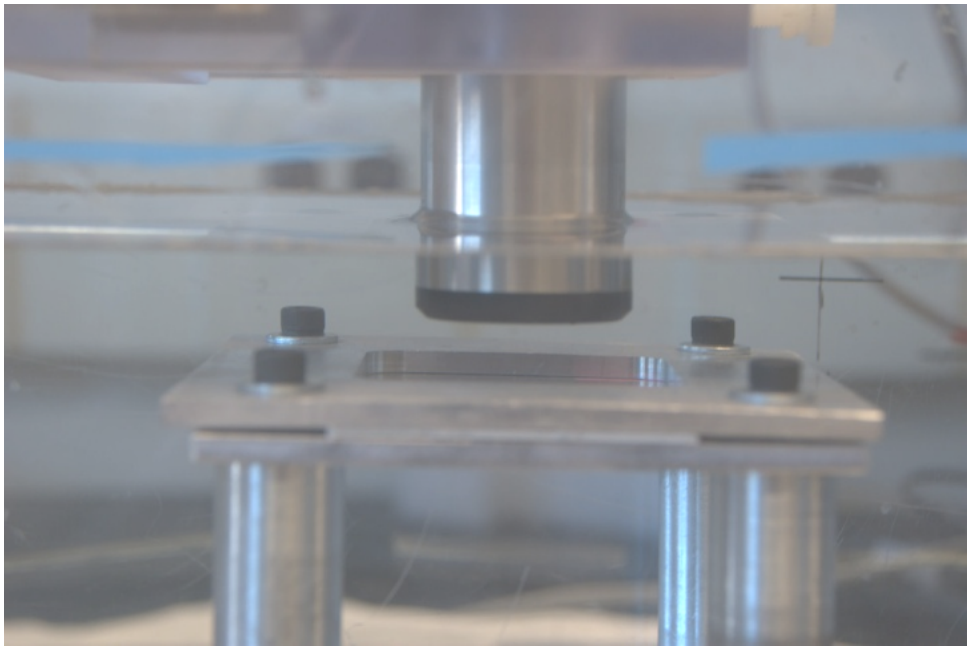

Figure 4-7 Transducer and sample holder at approximate focal distance separation

Focusing was performed as close as possible to the center of open are of the sample holder. The goal of this is to minimize any changes in the distance between the transducer and the sample, minimizing changes in the delay between reflected signals.

4.1.5 Alignment

Once the transducer is focused, a scan was utilized to measure and ensure reasonable flatness when mounting the sample. This test involved collecting A scans over the exsposed area of the sample. The collected A scans have the time of the first peak identified. From the differences in the time at which the first reflected peak is received, a map of the shape of the sample surface can be created. One scan can be seen in Figure 4-10. This figure shows that the maximum peak occurs between 3.835×10^{-5} sec and 3.859×10^{-5} sec after the signal was emitted. This shows a spread of 0.24 µsec, with the effect being amplified by the scale of the plot and for clarity. When plotted, the profile of the nonflat surface becomes clearly visible through the changes in the time to peak. Next, peak time is recalculated into distance.

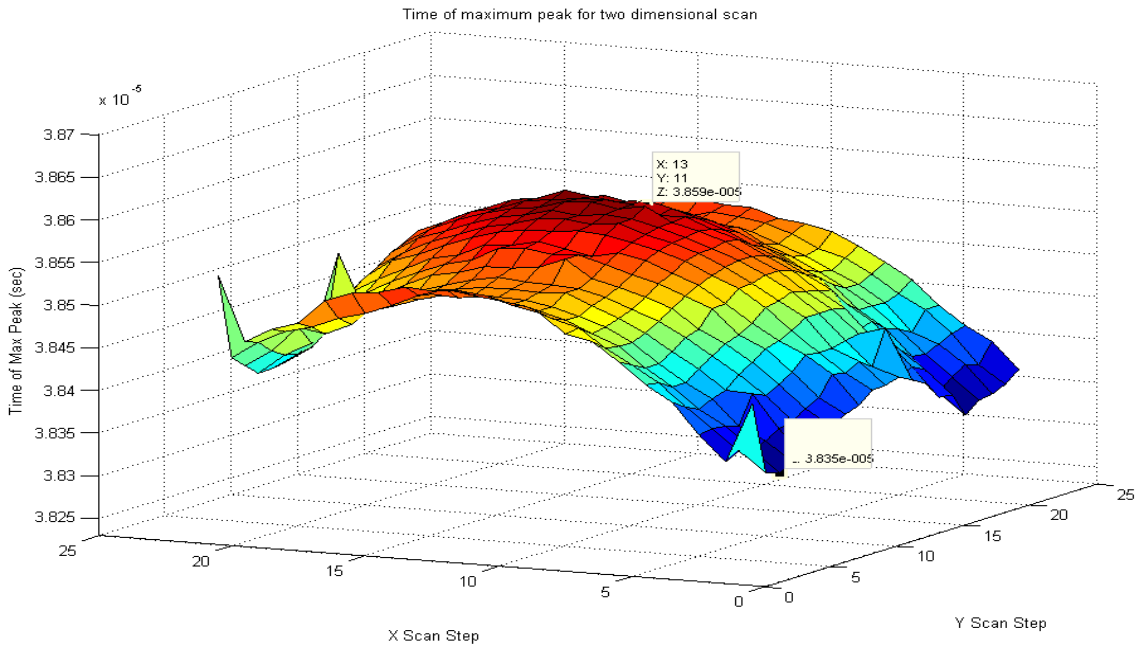

Figure 4-8 Surface plot of time to first peak over scan area of ±5cm in both axis

Knowing that the signal is propagating in water, the speed of sound is approximately 1480m/s, and calculating the distance spread between the highest and lowest point of the surface being scanned is possible. In this case, as seen Figure 4-11, the spread can be measured as 0.02894m to 0.02876m or 0.00018m (180μm). Further, it allows calculation of the two sides of a triangle, and from that, the angle of the sample out of normal. Knowing the low point occurs nearest the corner of the sample, and the high point occurs at the center, the angle is 0.15^{o} between the max and the minimum height. If the angle was found to be greater than 0.25^{o}, the samples were removed and remounted to ensure normality to the transducer.

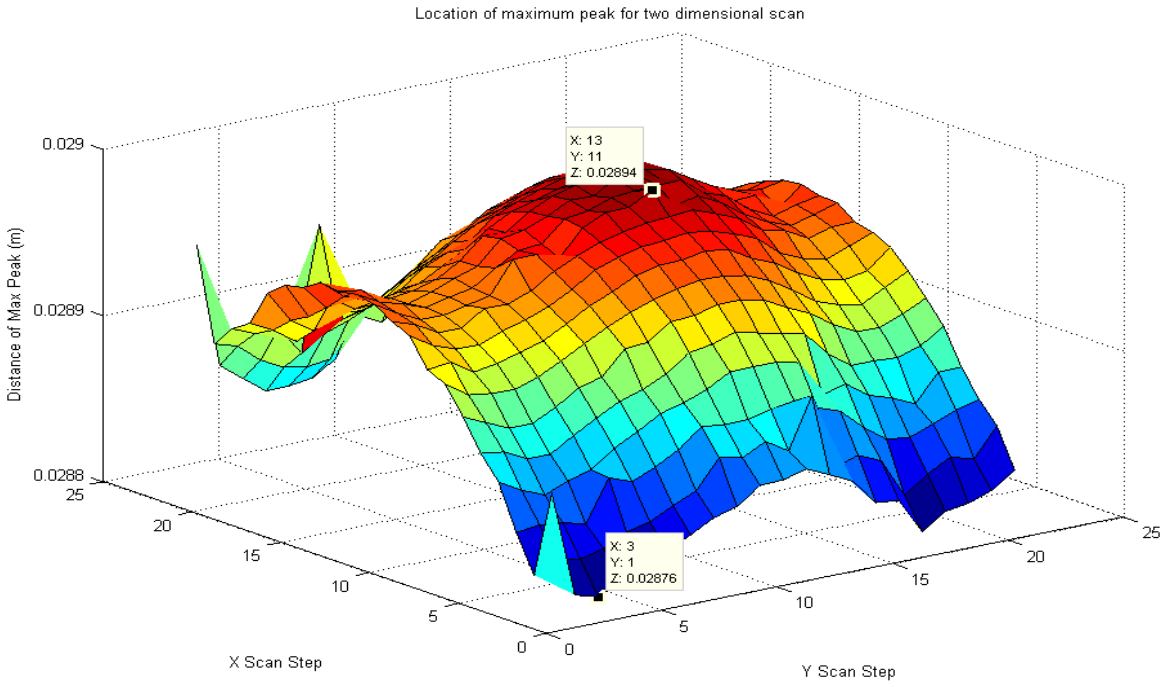

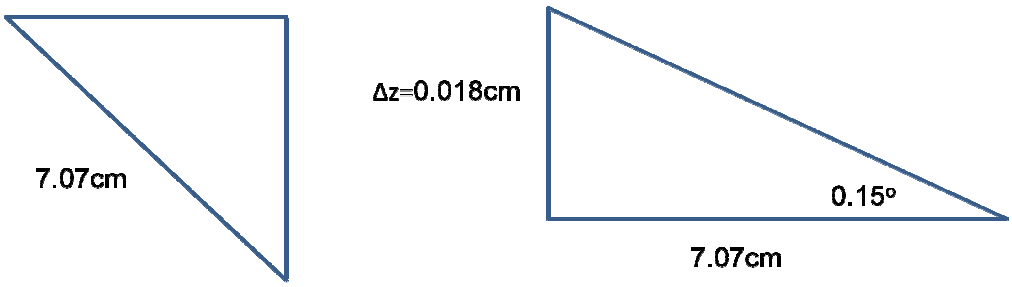

Figure 4-9 Calculation of maximum out of normal angle

4.1.6 Experimental Scans

Once a reasonable flatness, determined as a maximum angle less than 0.25^{o} was determined, a series of scans were run on each sample. The scans were run in multiple directions at multiple pulse amplitudes. This allows for ensurance of material properties, and to investigate the spread of material properties, over a wider area. Scanning at multiple amplitudes also allows for finding a balance where maximum detail can be obtained. Too low an amplitude does not show the underlying characteristics necessary for data analysis and makes discerning the reflected pulse from noise sources difficult. Too high an amplitude will overpower subtleties in the signal which cause other problems in data analysis.

The following scans where run on each sample. First, 6 single dimensional scans were run. All scans were from -5cm to +5cm from a center zero with a step size of 0.5cm. 3 scans in just X and 3 in just Y are performed first, gathering 21 A scans as the output data. The groups of three scans are performed at 25dB, 30dB, and 35dB of emitted pulse amplitude. After these scans are complete, two further scans are performed. The first, is a 2 dimensional scan over the same window, gathering 21^{2} or 441 A scans. The second, and last, scan was performed in Z to gather data on the focal window of the transducer. This scan was perfomed of a window of ±1cm with a stepsize of 0.1cm.

These scans were run consecutively on all samples under test. The scans were all initiated using the Matlab GUI command window. To help minimize data errors, all scans were directly observed by the author. This was done so that any inconsistencies or problems that may arise could be seen on the oscilloscope (showing constantly refreshed data), or problems with the mechanical aspect of the tank such as a stalled motor. To further help standardize data, all scans were run consecutively, and a rule was developed that no interaction with the system was allowable, except for using Matlab and JSR to configure and initiate scans. Further, any observed or suspected problem was determined to be cause to entirely dismiss the scan

set and repeat all scans of that sample. If a problem is either observed or suspected, all scans and data sets are deleted and the cycle is restarted with focusing of the transducer. The last procedural detail of note, is that testing determined a minimum 30 second dwell time between scans. The dwell delivered better quality data with less noise, and was implemented in all scans. It was theorized this dwell time helped reduce waves and water motion created by stepping the transducer through the water bath.

4.1.7 Thickness Measurement

One of the major intents of the ultrasonic measurement as applied here is the ability to determine the speed of propagation of the ultrasonic pulse inside the samples. It is often used as the basis for the measurement of mechanical material properties. The measurement of the speed of sound was already discussed, and derived in Equation 2-12, and is restated here.

$$C_{l,sample} = \frac{2\left(d_{sample}\right)}{t_1 - t_0}$$

Equation 4-4 The calculation of longitudinal speed of sound in a sample using a pulse echo experimental method.

The two independent parameters are the time of flight and the distance of propagation. It is possible from the ultrasonic data to measure the time of flight, but to accurately determine the speed of sound, the thickness of the sample must also be known.

4.1.7.1 Measurement Techniques

To achieve the necessary accuracy, measurement of sample thickness must be accurate on the micron scale. Measuring the thickness of the individual layers within a multilayered sample is of equal importance. Several different techniques were applied to achieve acceptable measurement results.

Initial tests were performed using a standard Starrett micrometer. The micrometer proved useful for providing quick measurements. The micrometer was used to roughly validate the thickness of the samples that were provided by CLiPS. It was also used to gather initial measurements of sample thickness and to validate more complicated techniques that were used for higher precision and more information. The micrometers however, did not meet the intended requirements for accuracy. The reported accuracy is ±0.0001in (±2.54μm) for the micrometer used.

The micrometer was also used to measure and understand the spread of thicknesses over the surface of the sample sheets provided. This proved important as the variance of the sheets proved significant.

The other mechanical technique was the use of a Brown and Sharpe coordinate measurement machine (CMM). The CMM was calibrated and qualified at a probe accuracy of 0.000017in (0.432μm). The CMM results were utilized for calculating speeds of sound from ultrasonic data. However, the CMM does contain the same limitation as other mechanical techniques. The CMM is unable to measure individual layer thicknesses because the layers cannot be separated. This provides a limitation on the utilization of the data when the layer count increases beyond 1. This limitation increases dramatically as the layer count continues to increase.

Two other techniques were attempted to gain information about the individual layer thicknesses when multilayered samples were under test. Knowing the individual layer thicknesses would be useful. Without knowledge of individual layer thicknesses, assumptions must be made about the thickness of the individual layers based on only the overall sample thickness. The samples were requested with a nominal thickness of 60μm, which was validated

in single layers. The layer thicknesses in multilayer samples however, can be affected by the manufacturing process and does not necessarily follow a simple additive scheme.

The first technique that was applied was the use of a JEOL 6400V scanning electron microscope (SEM). SEM attempts proved futile for several reasons. The initial hope was that utilization of more magnification would allow visual differentiation between the individual layers. To perform this testing, small samples of multilayered materials were cross-sectioned and then

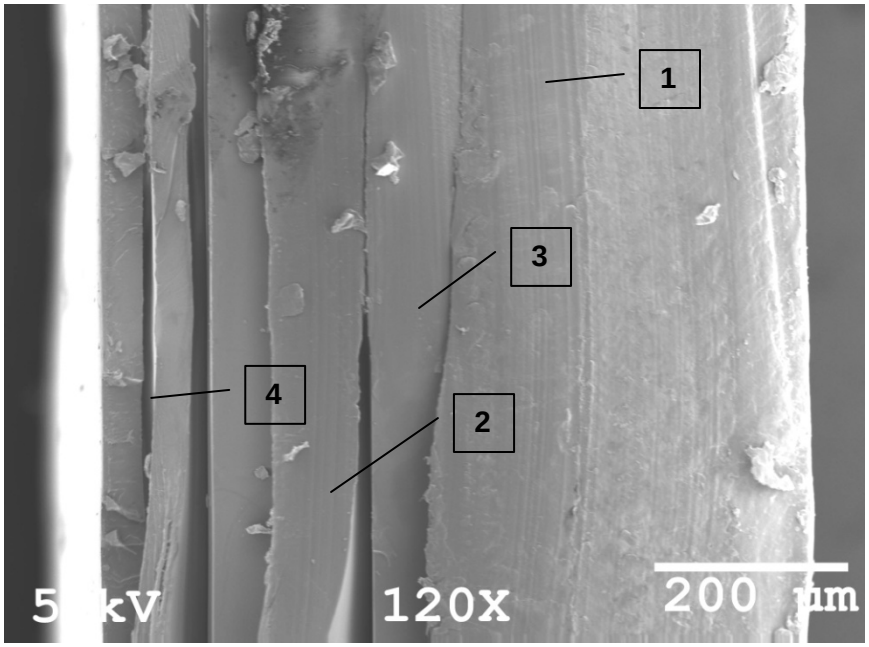

Figure 4-11 SEM image of 8 layered polymeric stack manufactured at CLiPS center Case Western University. Specific layer boundary phenomenon labeled

examined using an SEM microscope. Results, seen in Figure 4-13, show visual identification of separate layers of the polymeric stacks is possible. However, it also shows the problems that developed when utilizing the SEM technique. The polymeric nature of the layers, their viscoelasticity, and lack of overall stiffness contribute to the inability to measure the layers accurately. Portions of the image however, show the limitations of SEM imaging and reasons that it did not prove the best method for determination of individual layer thickness. In Figure 4-13, the first two noted items, 1 and 2, display the edges of individual layers. Location 1 shows a non-delaminated area of the sample at which the transition between materials is visible.

Location 2 notates a clean delamination between two layers, which appears to leave both layers in a measurable state.

However, locations 3 and 4 demonstrate problems with the technique that make measurements inaccurate. Locations 3 and 4 demonstrate plastic deformation of the constituent layers. Location 3 shows shearing where the boundary between layers is obscured through plastic deformation of one layer. This makes the determination of the location of the material boundary, and the measurement of the layers, effectively impossible. Location 4 shows another form of plastic deformation, pulling. The effect creates a narrowed layer, which is not useful for measurement purposes. When the sample is prepared, there is longitudinal force and deformation that creates a permanent plastic Poisson's contraction changing the thickness of the layer measured.

Given these problems at the interface, which appear to be formed during sample cross-sectioning, changes in sample preparation were made to reduce elastic behavior and make samples more brittle during cross-sectioning. The method chosen to enable this process was the lowering of temperature during sample preparation. Samples were cross-sectioned using both dry-ice (solid phase CO_2 approximate temperature −78.5 ℃) and liquid nitrogen (liquid phase N_2 approximate temperature −196 ℃) cooling. It is clear from the images in Figure 4-14 and Figure 4-15, that minimal improvement was made through changes in the processing.

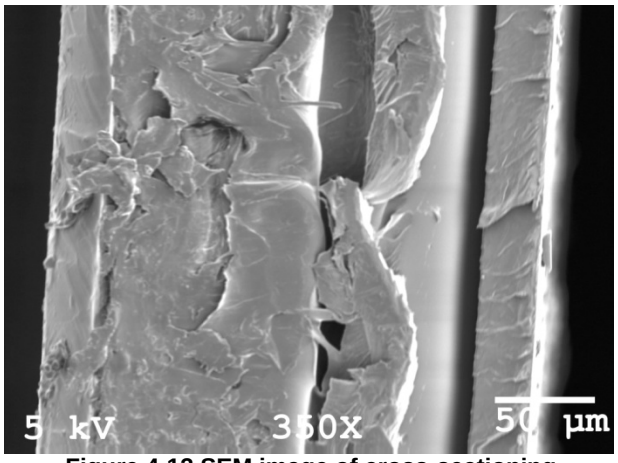

Figure 4-13 SEM image of cross-sectioning performed using CO_2 cooling

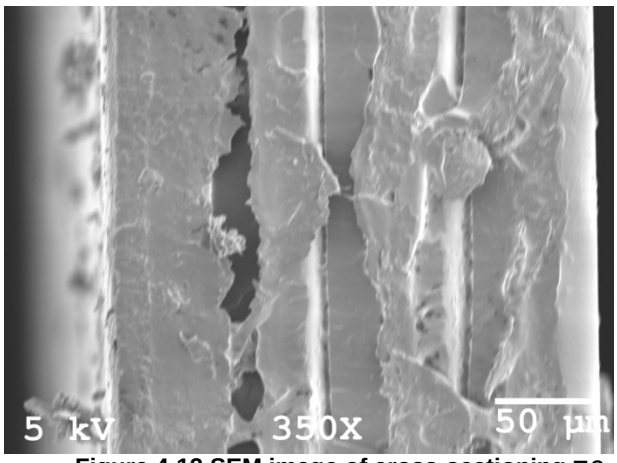

Figure 4-12 SEM image of cross-sectioning performed using N_2 cooling

Due to the lack of improvement, the SEM imaging as a measurement technique was abandoned. SEM proved to provide minimal benefit and did not return the intended results. However, visual spectrum imaging was pursued as well to try to provide work-arounds for the SEM problems.

4.1.7.2 Thickness Data

The initial measurement attempts were made over a relatively wide sample area to help determine general thickness of the samples that were manufactured for the experiments. When preliminary testing was complete, the samples were found to be of varied and greater thickness than reported to the author by CLiPS. Two sets of samples were used for testing. An initial set of 1, 2, 4, and 8 layer samples were used for development of the experimental techniques. The average thickness provided by CLiPS for these samples was 60µm. Initial testing showed the thickness of the layers to be closer to 70µm. For final testing, a larger number of samples were requested from CLiPS. The samples requested were 1, 2, and 4 layer comprising PMMA and PC layers of 60µm nominal thickness.

Samples the same size as those to be used for ultrasonic testing (approximately 2.5in (51mm) by 5in (127mm) were cut and measured using a micrometer. The measured samples were a 1 layer PC, 1 layer PMMA, and 2 layer (1 PC and 1 PMMA layer). Two samples of each type were measured. The results showed that the layers were of tighter thickness control than the preliminary samples, both sample to sample, and within each sample area. However, the results also showed that the samples did have statistically significant variation. Variation occurred across the surface of individual, and between separate samples of the same material. The most significant variation came at the edges of the sample. For the 1 layer PC sample and the 2 layer sample, significant measurement outliers near the edge were removed from the calculation of the mean and the standard deviation. However, these measurements are still included in the max and range portions of the calculation. The outlier measurements were

outside of the area of the sample that would be exposed to ultrasonic measurement. They were useful in demonstrating the full sheet variation of the samples, but not in validating the data that would be used for ultrasonic testing. The full results can be seen in Table 4-1.

Data	PC[1]		PMMA		2 layer		4 layer	
Units	**in**	**µm**	**in**	**µm**	**in**	**µm**	**in**	**µm**
Mean	0.0023	58	0.0022	55	0.0053	134	0.0104	264
Std Dev	0.0001	1.80	0.0002	4.47	0.0003	8.02	0.0002	5
max	0.0055	140	0.0025	64	0.0078	198	0.0107	272
min	0.0022	56	0.0018	46	0.0050	127	0.0100	254
Range	0.0033	84	0.0007	18	0.0028	71	0.0007	18
Tolerance	±0.0001	±2.54	±0.0001	±2.54	±0.0001	±2.54	±0.0001	±2.54

Table 4-1 Initial measurement data for experimental sample thicknesses.

The results show that both PC sample and the PMMA single layer samples were slightly (~1σ) thinner than anticipated at an average thickness of 58 and 55 µm respectively. Conversely, the 2 layer sample, which comprises 1 layer of each material, was thicker than would be expected. The 2 layer sample measurements showed a mean thickness of 134 µm. This is greater than both the expected thickness of 120 µm and the thickness expected from the measurement of the two individual layers (58 µm + 55 µm) of 113 µm. Likewise, the 4 layer sample measurements found a mean thickness of 264 µm, thicker than expected if the single layer thicknesses were used. The expected thickness would be 226 µm calculated from individual layers, but would be 268 µm if calculated from a doubling of the 2 layer sample. This tells us there may be some under prediction of the layer thickness using the single layer samples. Over the wide area measured, both the PMMA and the 2 layer sample showed significant standard deviations that bring will likely affect the ability to find areas with a low level of variation and effectively calculate speeds of sound and other material properties.

The data collected demonstrated an increase in variation as the number of layers increased. This information, serves to experimentally validate expectations. The 2 layer samples have an increased instance of manufacturing variability. Rather than thickness being dictated by the setting of a single melt pump, it is influenced by the variation of a separate melt pump for each layer material. Further, machinery responsible for processing the individual layers into a multi layer stack also adds variation in the resulting thickness. Based on the data collected measuring samples with a micrometer, when the ultrasonically tested samples were measured with the CMM, the area over which they were measured was significantly reduced. This was done by trimming the samples, and measuring only over the area that was exposed to ultrasonic measurements. The sample was trimmed while in the sample holder by cutting around the edge of the ultrasonic opening. This reduces the size of the measured sample to 2in (5.08mm) by 2in (5.08mm). It also ensured that the thickness measurements accurately represented the thickness of the area being ultrasonically investigated.

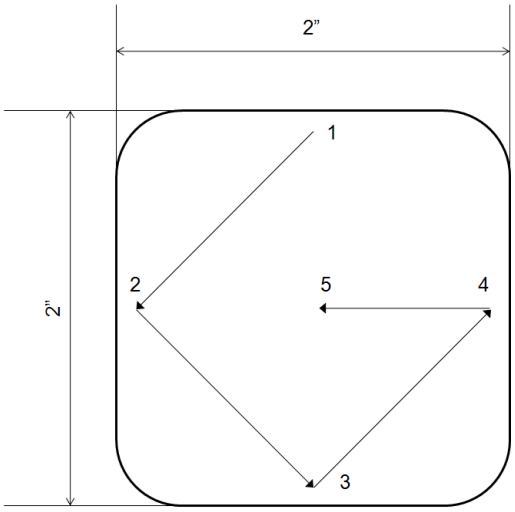

Figure 4-14 Measurement pattern for CMM measurements

The CMM allowed for a much greater accuracy of measurement. For each sample, 5 measurement points were taken over the window of measurement. The samples were taken in a cross pattern as seen in Figure 4-16. The measurements gathered where within 1σ of those measurements from the micrometer for both single layer materials. This was achieved along

with a significant reduction in the standard deviation. The reduction of standard deviation is expected both due to the improvement of the accuracy of the measurement technique, and the reduced area over which the measurements occur. The data from this technique can be seen in Table 4-2, and are the data that are applied to ultrasonic testing later. With the CMM, individual measurements were taken from the samples measured ultrasonically. The thickness results for individual samples were applied only to the ultrasonic results from that specific sample.

Thicknesses from the CMM (in)							(in)		(μm)	
Sample #	**Material**	**Loc # 1**	**Loc #2**	**Loc #3**	**Loc #4**	**Loc #5**	**Mean**	**Std Dev**	**Mean**	**Std Dev**
5	**PC**	0.00226	0.00217	0.00223	0.00221	0.00222	0.00222	0.00003	56.3	0.83
6	**PC**	0.00233	0.00230	0.00236	0.00234	0.00233	0.00233	0.00002	59.2	0.55
9	**PMMA**	0.00237	0.00245	0.00248	0.00230	0.00239	0.00240	0.00007	60.9	1.79
14	**2Layer**	0.00469	0.00441	0.00418	0.00476	0.00450	0.00451	0.00023	114.5	5.87
15	**2Layer**	0.00426	0.00457	0.00444	0.00492	0.00453	0.00454	0.00024	115.4	6.14
18	**4Layer**	0.00978	0.01001	0.00961	0.00962	0.01007	0.00982	0.00022	249.4	5.45
19	**4Layer**	0.01002	0.00976	0.00963	0.00981	0.01002	0.00984	0.00017	250.1	4.32

Table 4-2 Data gathered from CMM thickness measurements

Notably, both single layer types showed a mean closer to the expected when compared to the measurements with the micrometer in addition to a reduced variation. This was also the case for 2 layer samples. Both 2 layer samples showed a mean thickness slightly below the thickness that would be achieved from the combination of independent layers of PC and PMMA.

What is demonstrable from these data though, is that the measurement technique employed with the CMM is of a higher tolerance than the control provided by CLiPS and is not the limiting factor in data collection and analysis. This variation is clear in the measurement of discrete samples outside the standard deviation, specifically in PC. The manufacturing variation is further demonstrated through the significant increase in sample thickness variation within both 2 layer samples over the variation of the single layer experiments. This correlates with visible striations that were noted in the surface of samples (2 and 4 layer) that were processed through

the layer multiplying equipment. These striations are not visible in the samples of either single layer material.

4.2 Ultrasonic Testing Data

The experimental sample data collected consists of two facets. First, is the ultrasonic A scan signals which are generated, and second is thickness. These two pieces of information comprise the raw data necessary for drawing results about the properties of the material samples manufactured by Case. From the raw data, analysis is performed in the time domain and further analysis is performed using wave transform and frequency spectrum techniques, which allows for results and conclusions to be drawn that are not identifiable in the raw data.

4.2.1 Data Collected and Preliminary Processing

As noted, the raw data points collected from the ultrasound are in the form of an A-scan. This is visually expressed as a plot of the voltage recorded by the oscilloscope versus time. An example A-scan is seen in Figure 4-17. This scan is from an aluminum sample which was used for calibration and reference. The scan itself shows several pieces of information that are important to note. The most visible of these is the clear peaks that occur at different points

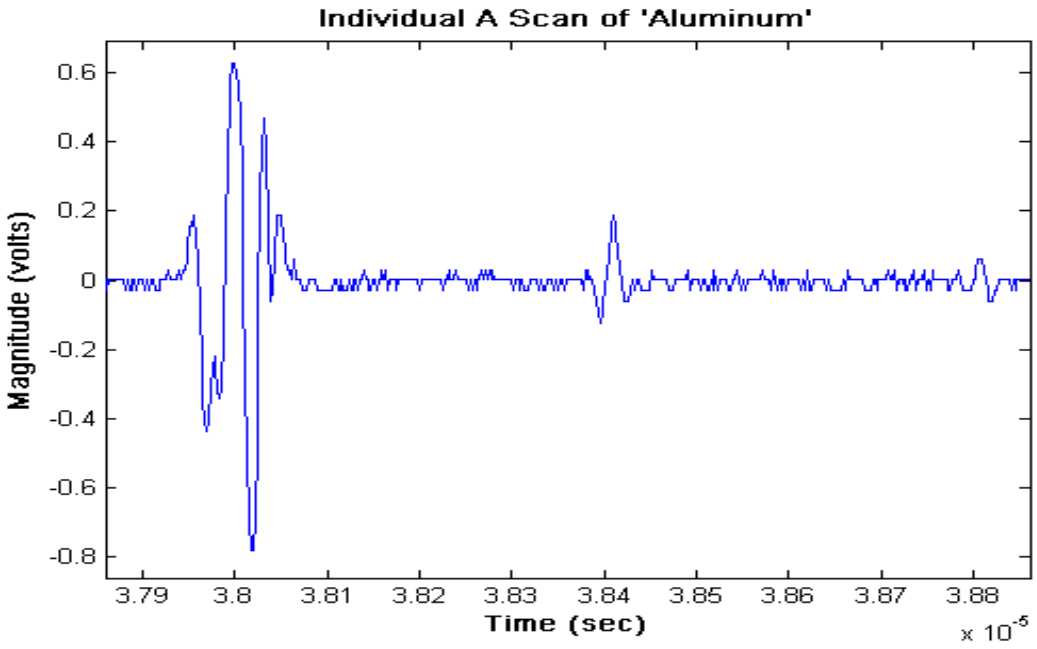

Figure 4-15 Raw A scan of aluminum.

along the time axis. These peaks reflect when the energy of the ultrasonic pulse encounters a change in the propagation medium, entering or exiting the aluminum sample under test. Using the aluminum sample, three pulses are visible. The largest (visible at $3.80x10^{-5}$sec), occurs when the pulse encounters the front surface of the material sample. The second pulse (visible at $3.84x10^{-5}$sec) is returned by a reflection on the rear side of the sample. The third (visible at $3.88x10^{-5}$sec), occurs from the division of energy as the 2^{nd} peak crosses the front surface reflecting back to the rear surface. The visibility of the third peak in the window of time recorded is a useful tool. The spacing between the peaks should be identical as the distance traveled is the same. Therefore, the time between them should be the same, a fact that was used to validate the results during development. However, this phenomenon will not be as apparent in polymer samples, the lower stiffness of these materials causes smaller magnitude reflections, and makes it more difficult to identify secondary reflections.

For all experimental samples, scans were recorded for 1 layer samples of both PC and PMMA, 2 layer samples consisting of 1 layer of each material, and 4 Layer sample consisting of 2 alternating layers of each material. They were also recorded for a single, specific, aluminum sample, which was used as a perfect reflector for calibrating the system. Each of the sample types showed a repeatable and identifiable signature in the A scans.

For the single layer PC samples, 525 A scans were collected. However, only 105 scans were used for analysis. For each of the single layer PMMA, the 2 layer, and the 4 layer samples, 105 A scans were recorded. The 105 single layer PC scans that were used were those that matched the procedures for all other sample types. A representative scan of each material can be seen on the following pages.

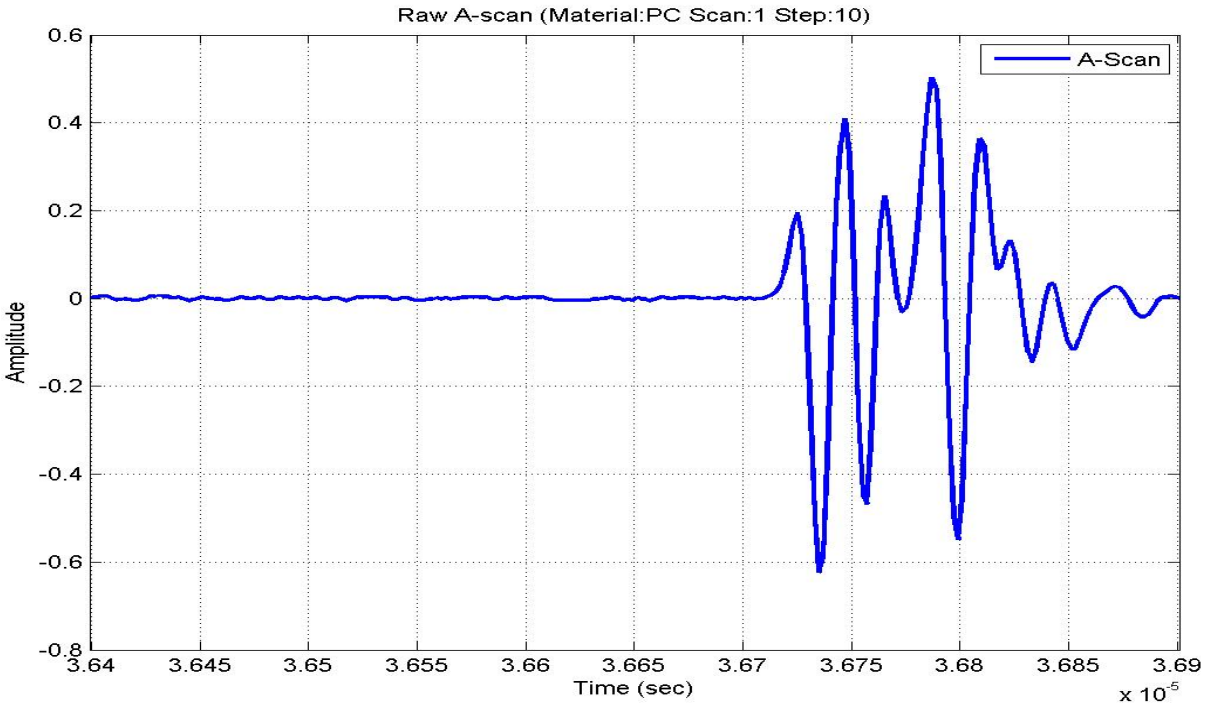

Figure 4-16 A scan of single layer PC sample with nominal 60µm thickness

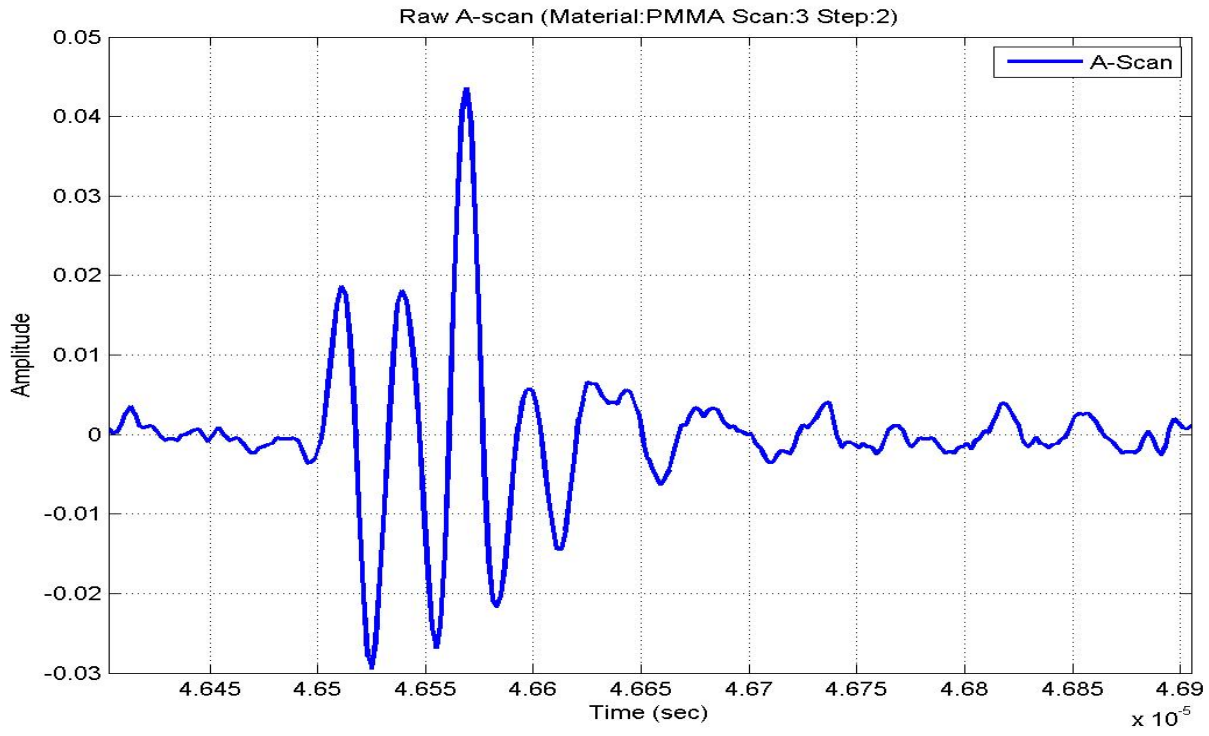

Figure 4-17 A scan of single layer PMMA sample with nominal 60µm thickness

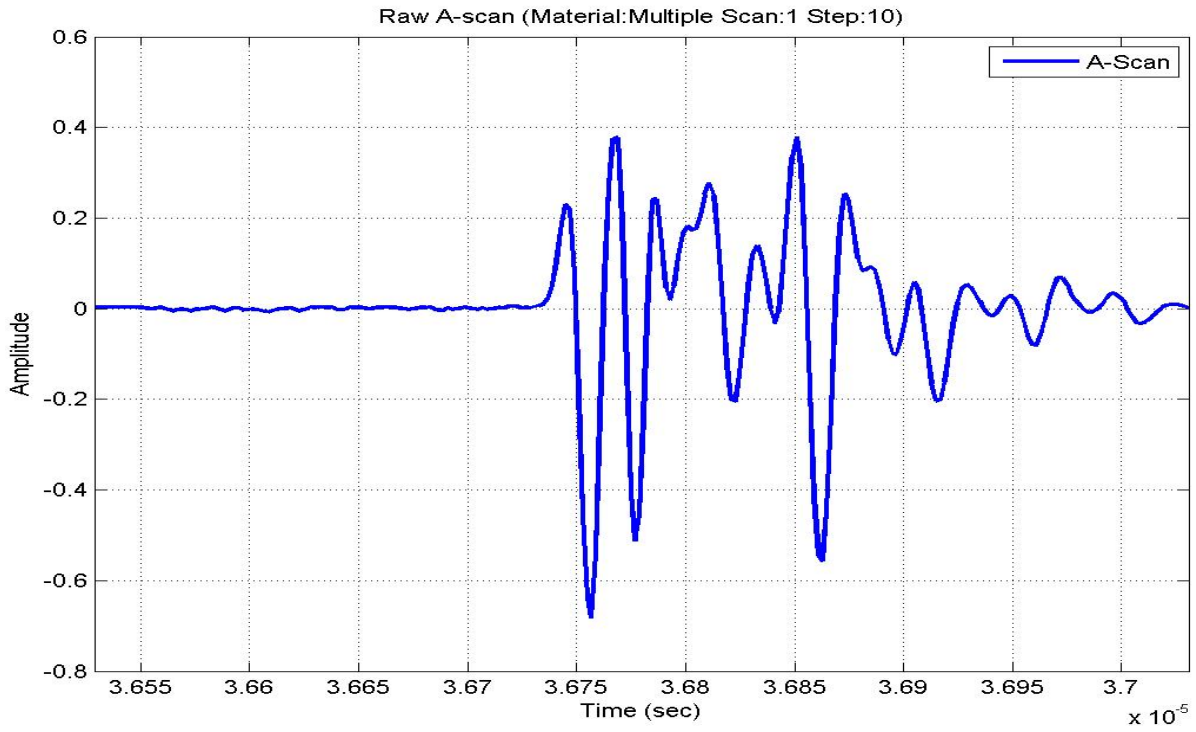

Figure 4-18 A scan of 2 layer sample with nominal 60µm layer thickness

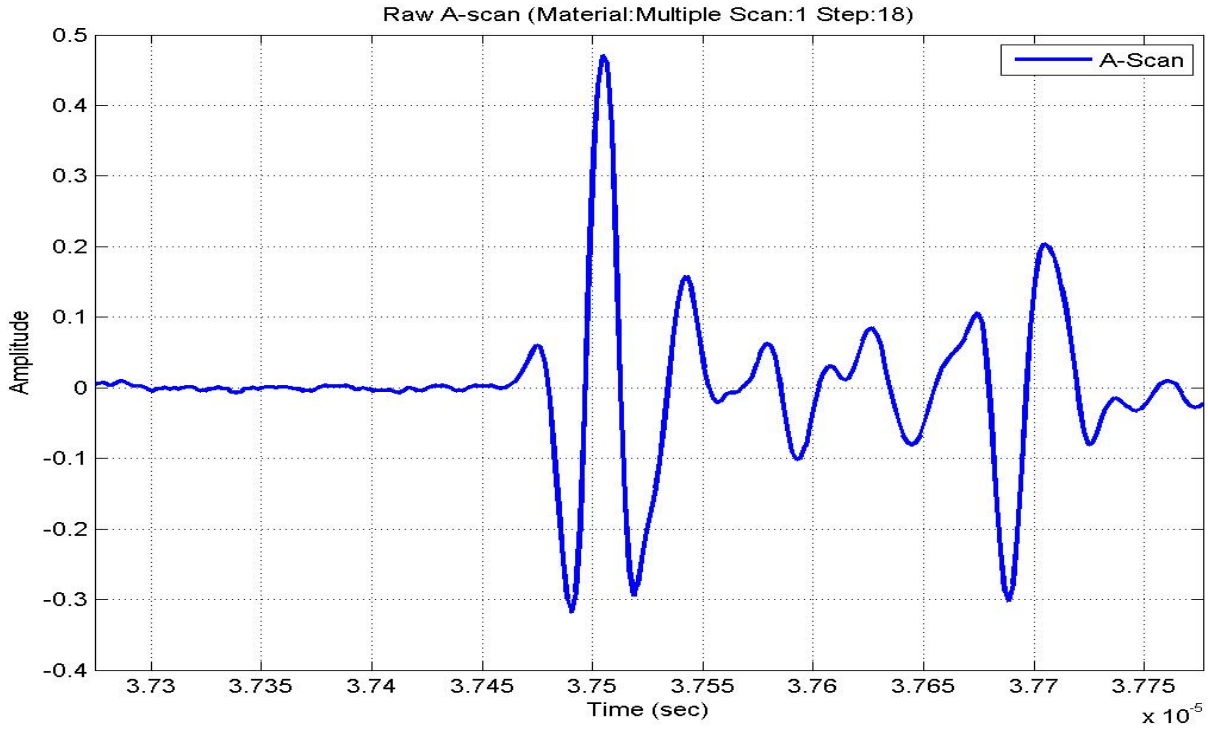

Figure 4-19 A scan of 4 layer sample with nominal 60µm layer thickness

The figures on prior pages show the representative waveform of each material. From this information, some basic analysis was performed. To help determine the peak location, a Hilbert transform[52] was taken from each signal. The Hilbert transform, produces a function over the same domain. It is mathematically expressed as:

$$H(u)(t) = -\frac{1}{\pi}\lim_{\delta \downarrow 0}\int_{\delta}^{\infty}\frac{u(t+\tau)-u(t-\tau)}{\tau}d\tau$$

Equation 4-5 Formulation of the Hilbert Transform

The Hilbert transform produces a conjugate consisting of a real and imaginary portion. The magnitude of the conjugate can be used to measure the envelope of the signal. The envelope of the signal can be used to more easily identify peaks of the signal, and help measure the time of flight of the signal. An example of the Hilbert transform can be seen in Figure 4-22 and an overlay of the Hilbert transform on the A scan signal is seen in Figure 4-23.

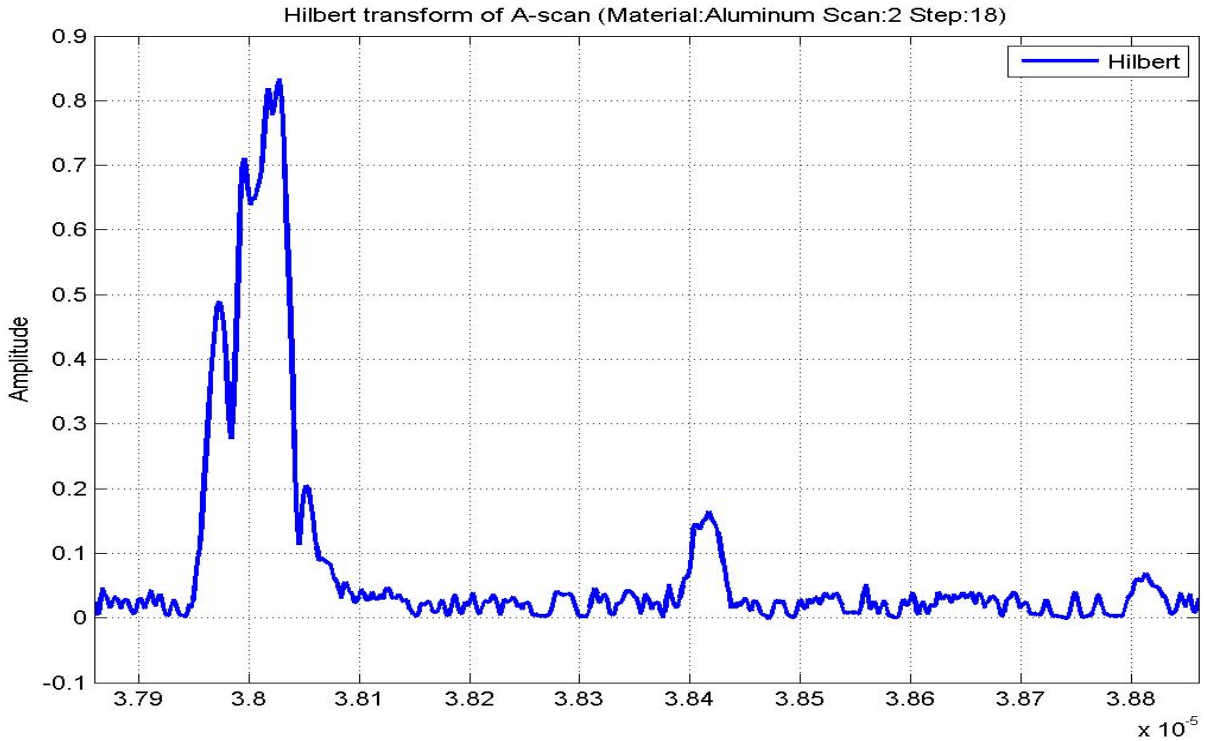

Figure 4-20 Hilbert transform magnitude of aluminum test sample

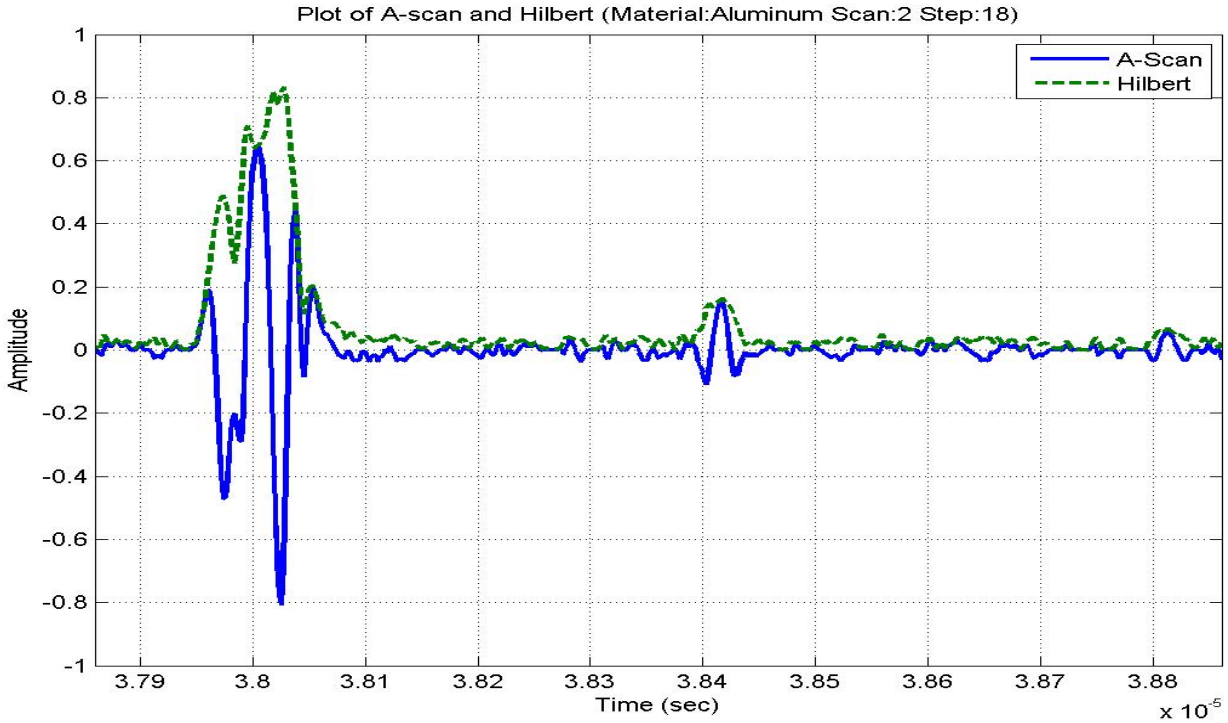

Figure 4-21 Overlay of Hilbert Transform on A scan signal of Aluminum sample

The Hilbert transform envelope helps create a more clear determination of where pulse maximums occur. Using an envelope transform, measurement is significantly quicker and more accurate. This allows for easier measurement of the time of flight and the peak locations.

The Hilbert transform and magnitude calculation were applied to all the samples under test. Examples of these can be seen on the following pages. These two forms were used for all further data processing and analysis. These signals theoretically contain all the information necessary to make a determination on the material behavior both of the sample and the individual layers. The analysis of these signals is covered in the following sections, however there are phenomena that can be observed in the different A scans and Hilbert transforms that can help clarify and identify some of the materials.

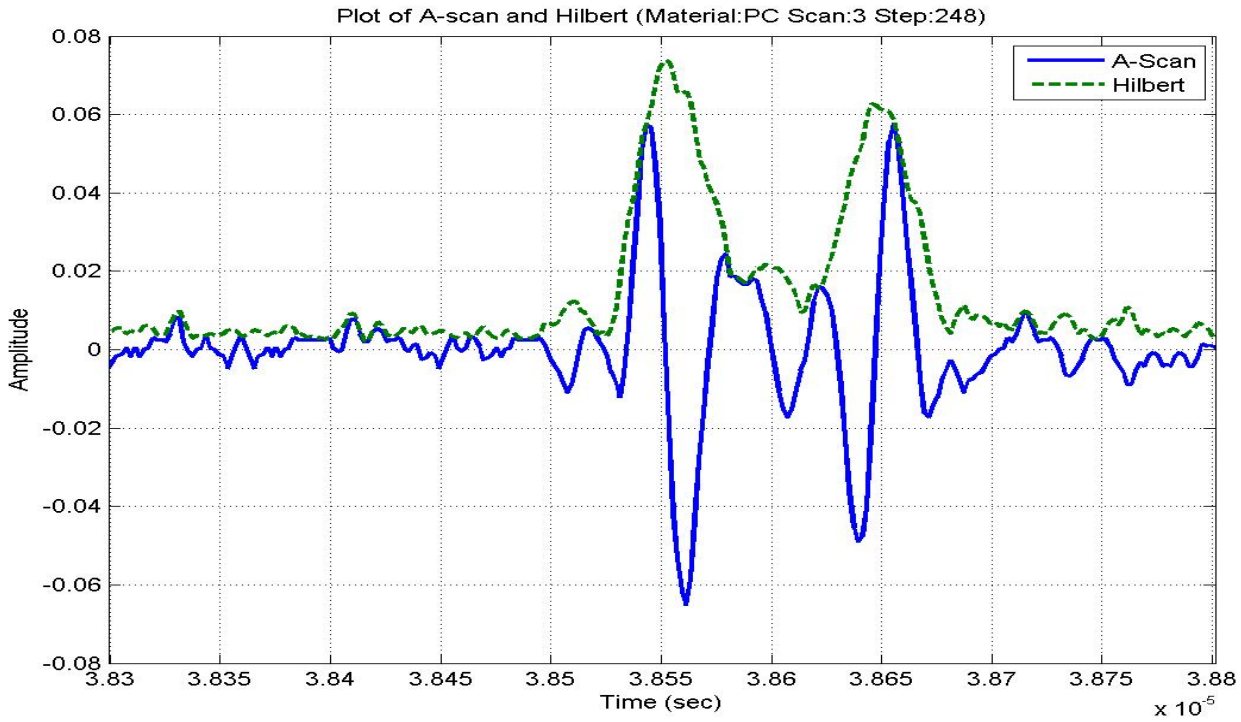

Figure 4-22 Overlay of Hilbert transform on A scan of PC sample

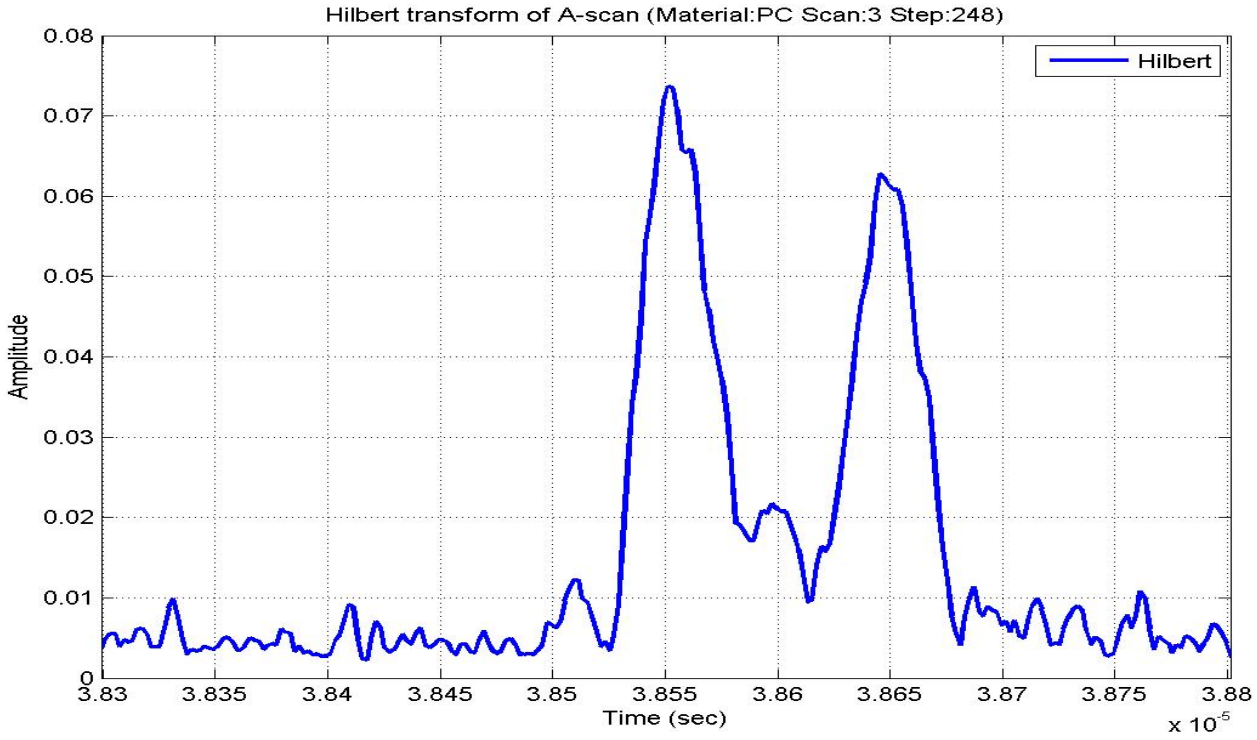

Figure 4-23 Hilbert transform of PC sample

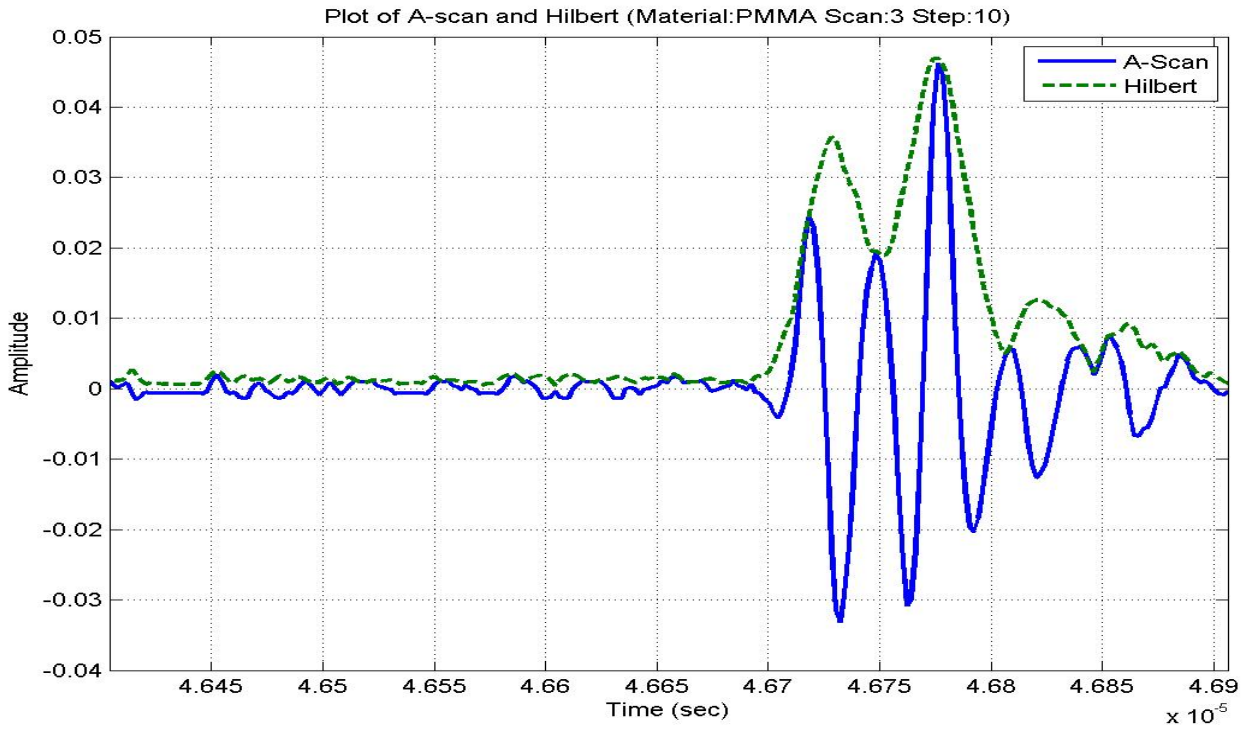

Figure 4-25 Overlay of Hilbert transform on A scan of PMMA sample

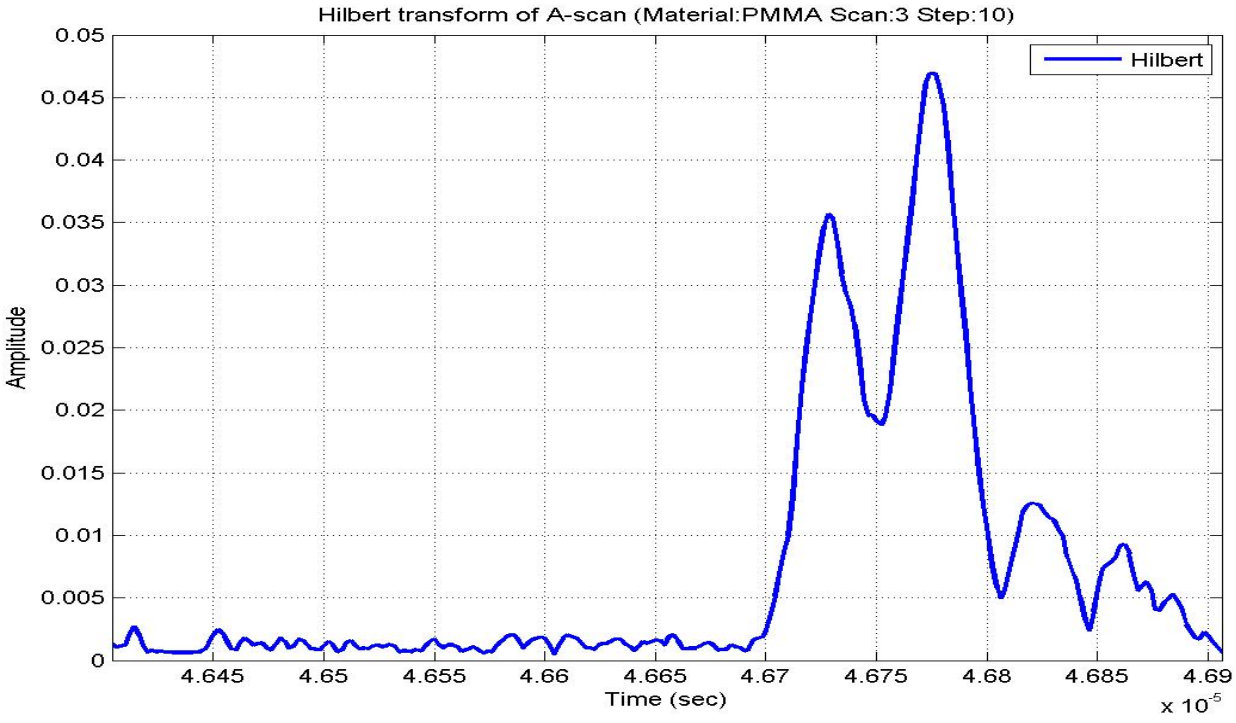

Figure 4-24 Hilbert transform of PMMA sample

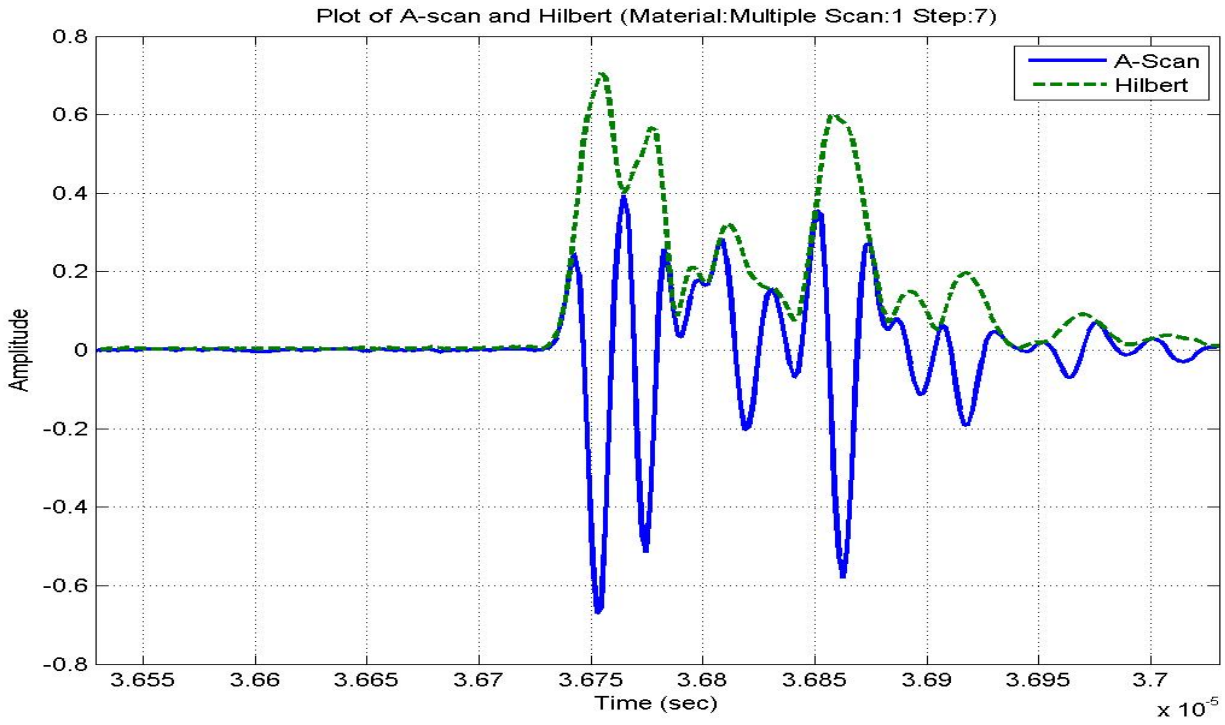

Figure 4-27 Overlay of Hilbert transform on A scan of 2 layer sample

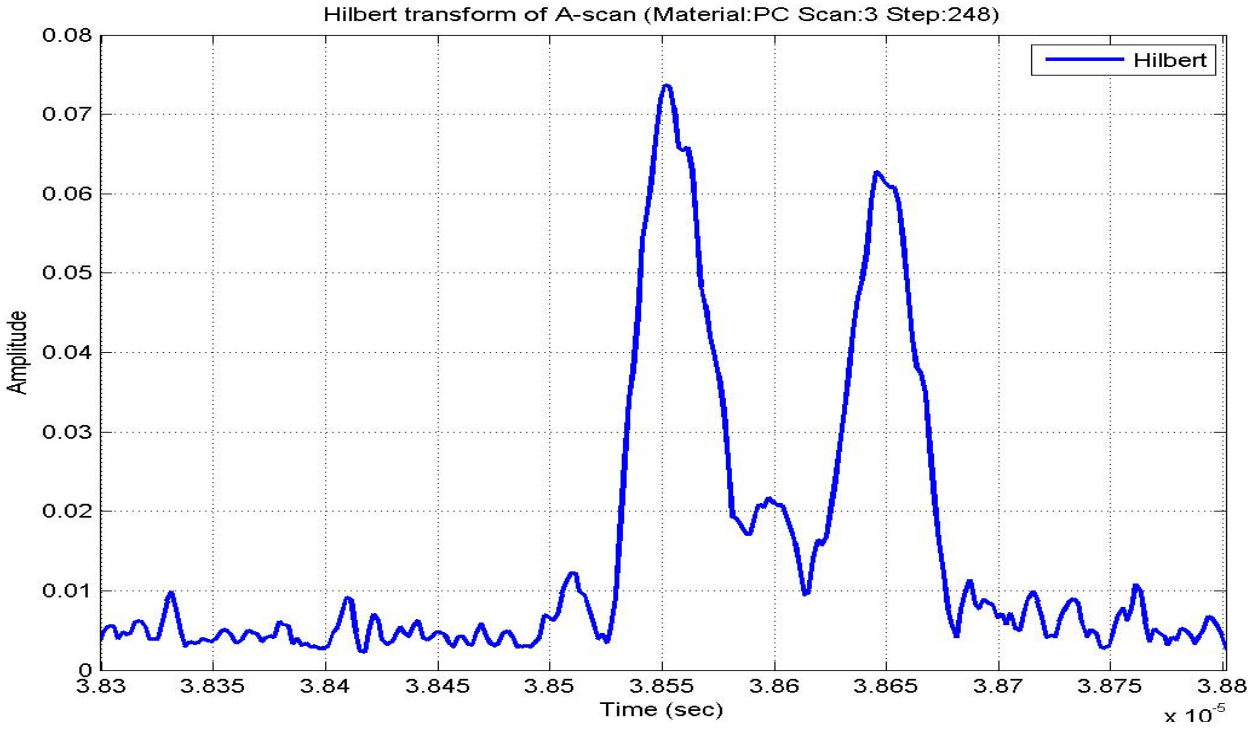

Figure 4-26 Hilbert transform of 2 layer sample

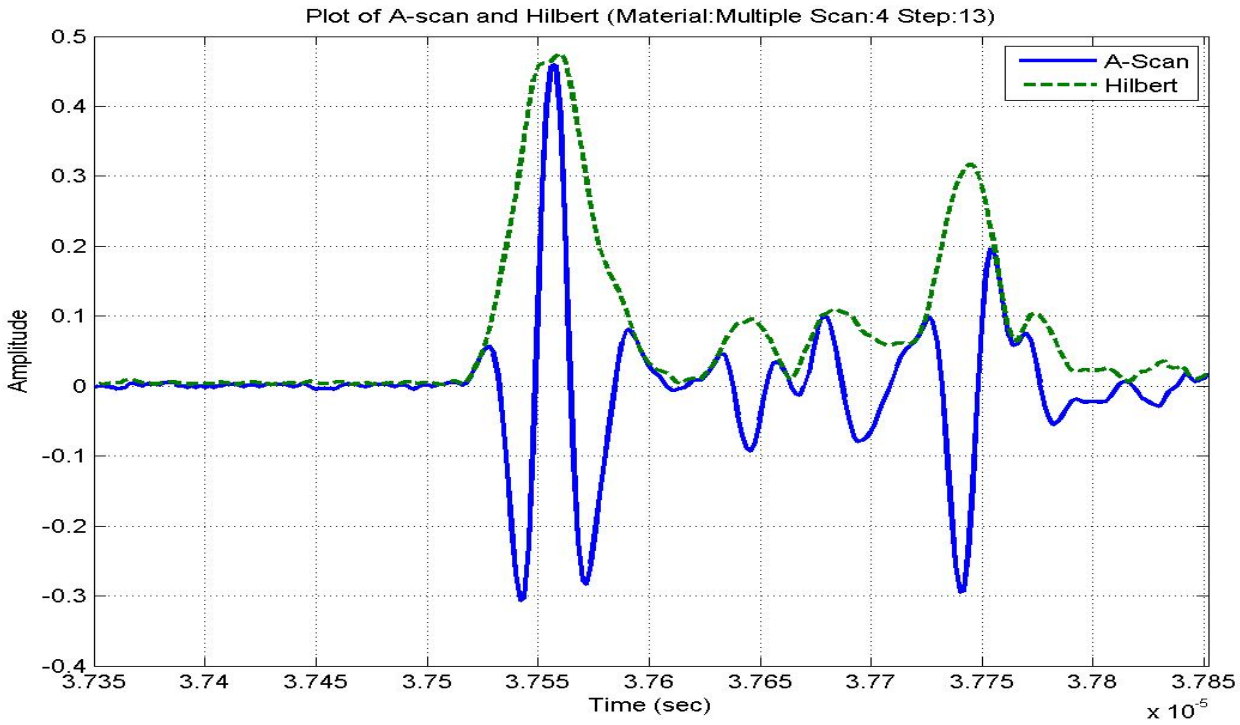

Figure 4-28 Overlay of Hilbert transform on A scan of 4 layer sample

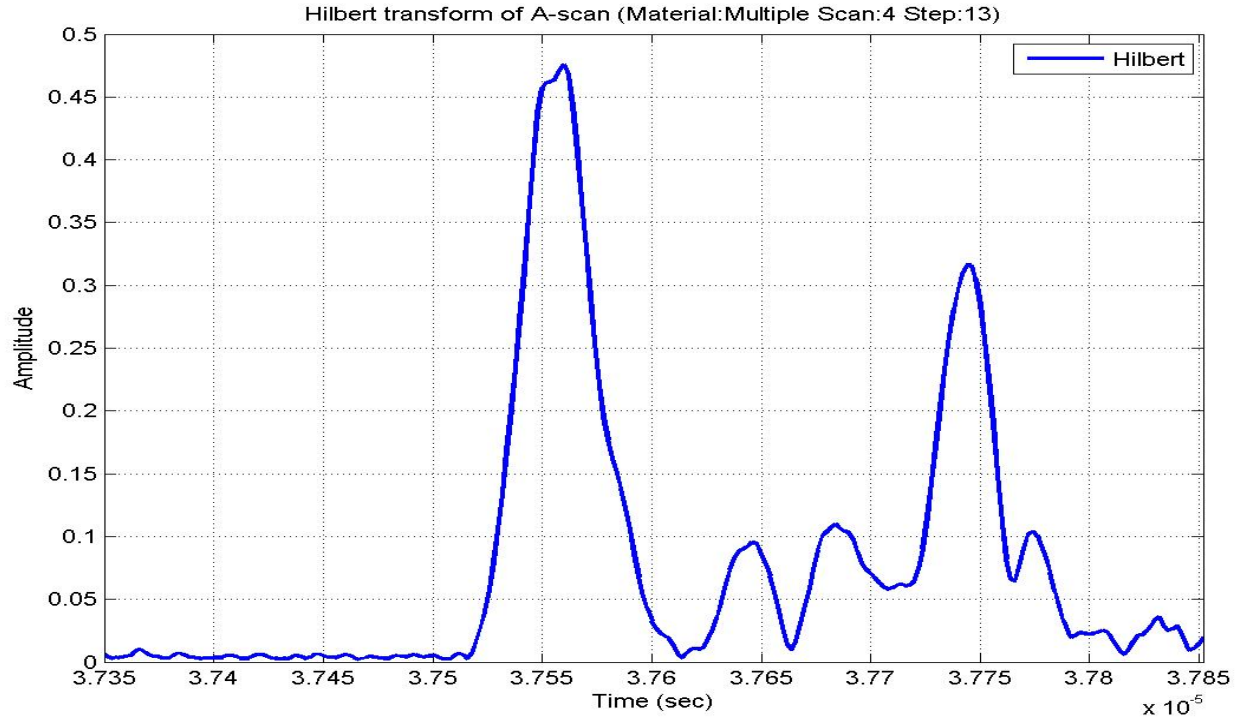

Figure 4-29 Hilbert transform of 4 layer sample

What is visible from each of these plots, is the basic outline of the reflecting signals. From the Hilbert transforms of the PC and PMMA single layer samples, there is a pair of dominant peaks in the envelope plot. They correspond with the A scan reflected pulses. This peak pair is effectively highlighting the reflection off of the front and back surface of the sample. As such, the difference between the time of their occurrence can show the time of flight. A similar phenomenon occurs for the 2 layer sample. There are 3 clear peaks in the Hilbert transform. The first and last , which locate the front and rear surface reflections, are quite large. This is expected given the significant impedance difference between the sample polymers and the water used as a couplant. The center peak, while much smaller, is of further importance. The smaller magnitude correlates with the comparatively small difference in impedance between the 2 polymers in the sample. This peak can still be used to locate the time of flight for the individual layers while the two larger peaks show the entire time of flight. A similar phenomenon appears on the 4 layer sample. However, with the 4 layer sample, there are 3 internal interfaces. Therefore, 3 internal reflections would be expected between the dominant reflections from the front and back surface. Instead, only 2 peaks occur between the dominant peaks. The lack of a 3rd peak demonstrates the limitations of the ability to locate the internal reflections in the time domain from the A scan data. Without the 3rd peak, we cannot measure the individual layer TOF's. This will be where the simulation and indirect analysis is used in the continued work.

4.2.2 Data Processing

Once the experimental scans were collected, a mathematical analysis was performed. The goal of these analytical processes is to determine the material properties from the experimental data. Two separate styles of analysis were performed. First, a time domain analysis was performed. Second, an analysis was performed on FFT's generated from the experimental data. Combined, the goal was to determine the major viscoelastic properties. The

analysis was taken further than initially intended in an attempt to provide a more robust method of property determination given the problems that resulted from the simulation.

Most processing was done using Matlab code. Attempts were made to provide automated routines for repetitive tasks such as peak identification and location. However, these proved unstable and inaccurate do to the methods of peak identification available in the matlab API. Therefore, peak location and magnitude data was manually collected and recorded for analysis. This proved especially true as the layer counts increased and the returned waveforms became less plainly identifiable. For all peak-related data processing and analysis, tasks were handled in Microsoft excel.

4.3 Results

Several different analytical techniques were employed to analyze the scans that were gathered, and investigate the feasibility of parameter extraction from the test samples. Similar techniques were used on both single layer and multilayer samples. The overall goal was to determine whether direct extraction of mechanical properties from the complex multilayer cases was possible. Single layer testing results were determined first, and then those results were employed to help attempted analysis of the multilayered samples.

4.3.1 Single Layer

The single layer samples that were measured and analyzed first served three purposes. First, the results detailed here were used to validate the materials as PC and PMMA as well as calibrate the equipment and techniques. This area of work was successful, and good results were achieve validating the experimental and analytical techniques. This was true for both the time domain, and the FFT domain analysis.

The second purpose of the single layer testing is to demonstrate ultrasonic analysis in materials thinner then the ultrasonic pulse length. This was demonstrated for the determination

of the speed of sound, estimates of attenuation, and the generation of interpretable transforms. The third goal is the validation of these techniques for this specific case, as a lead in to their application on multilayered samples.

The results are presented in two parts. The time domain work was used for the measurement of the speed of sound, and the measurement of material attenuation. Second, the use of FFTs to differentiate the materials in systematically identifiable manner is discussed.

4.3.1.1 Time Domain

The first analysis that was performed was in the time domain. Measurements were taken from the A scans gathered, and from the calculated Hilbert transforms discussed in the previous section. The measurements recorded where the time of the return of the reflected peaks. These measurements, as noted earlier, allowed for the calculation of the time of flight and speed of sound.

For the single layer materials, aluminum, PC, and PMMA, the full time of flight was all that was collected. For multi layered samples, individual layer time of flights were calculated as well (when possible). Testing showed no difference between data collected from the raw A

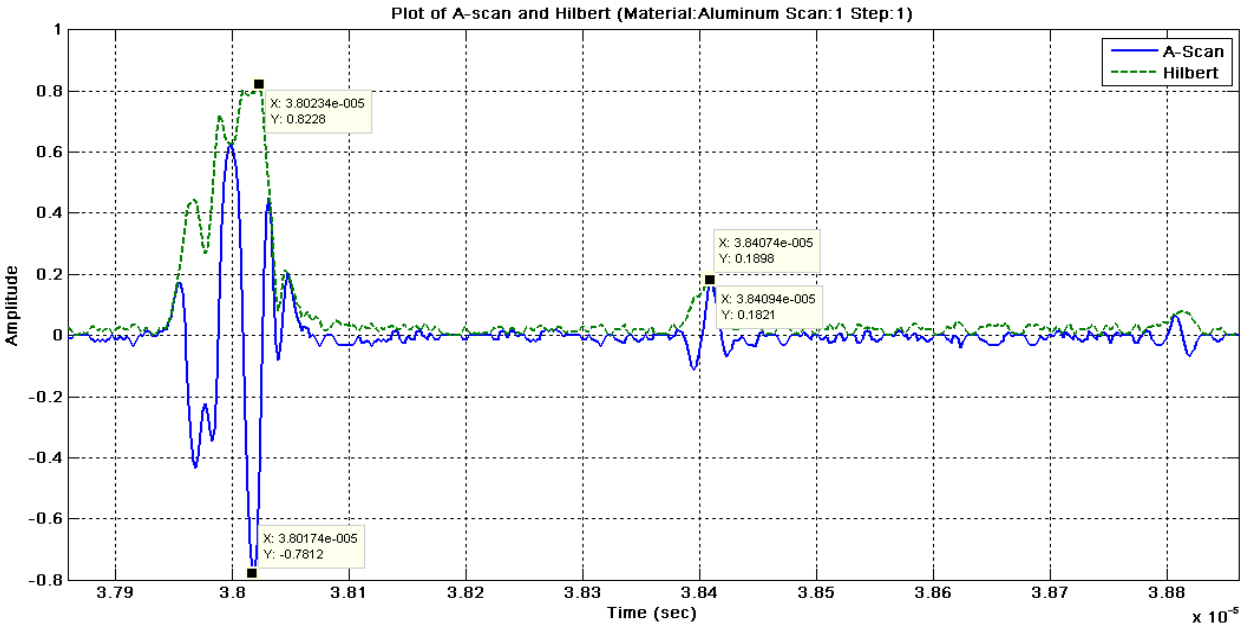

Figure 4-30 A scan and Hilbert Transform of Aluminum test sample

scan and the data collected from the Hilbert. The peak measurements were taken manually from plots of the data made using Matlab. The time of the peaks was recorded, which allowed calculation of the time of flight. An example of this can be seen in Figure 4-32 for the aluminum calibration sample. In Figure 4-32, the maxima are labeled for the 1st and 2nd reflected peaks on both the Hilbert transform and the raw A scan of aluminum. For the Hilbert transform, the 1st peak occurs at 3.8023×10^{-5}sec and the 2nd peak occurs at 3.8407×10^{-5}sec. For the raw A scan, the 1st peak occurs at 3.8017×10^{-5}sec and the 2nd peak occurs at 3.8409×10^{-5}sec. This gives a time of flight for the signal of 3.84×10^{-7} and 3.92×10^{-7} for the Hilbert and A scan calculation respectively. Using Equation 3-1, the speed of sound for the aluminum sample can then be calculated as 6427m/s and 6492 m/s using the different methods. This compares relatively favorably to the literature value of 6420m/s for aluminum. The measurements from the envelope show 0.12% error to the literature value, while the results from the A scan show 1.13% error. It should be noted that the lower error from the envelope is not necessarily representative, and the error of both techniques fluctuated depending on the specific scan.

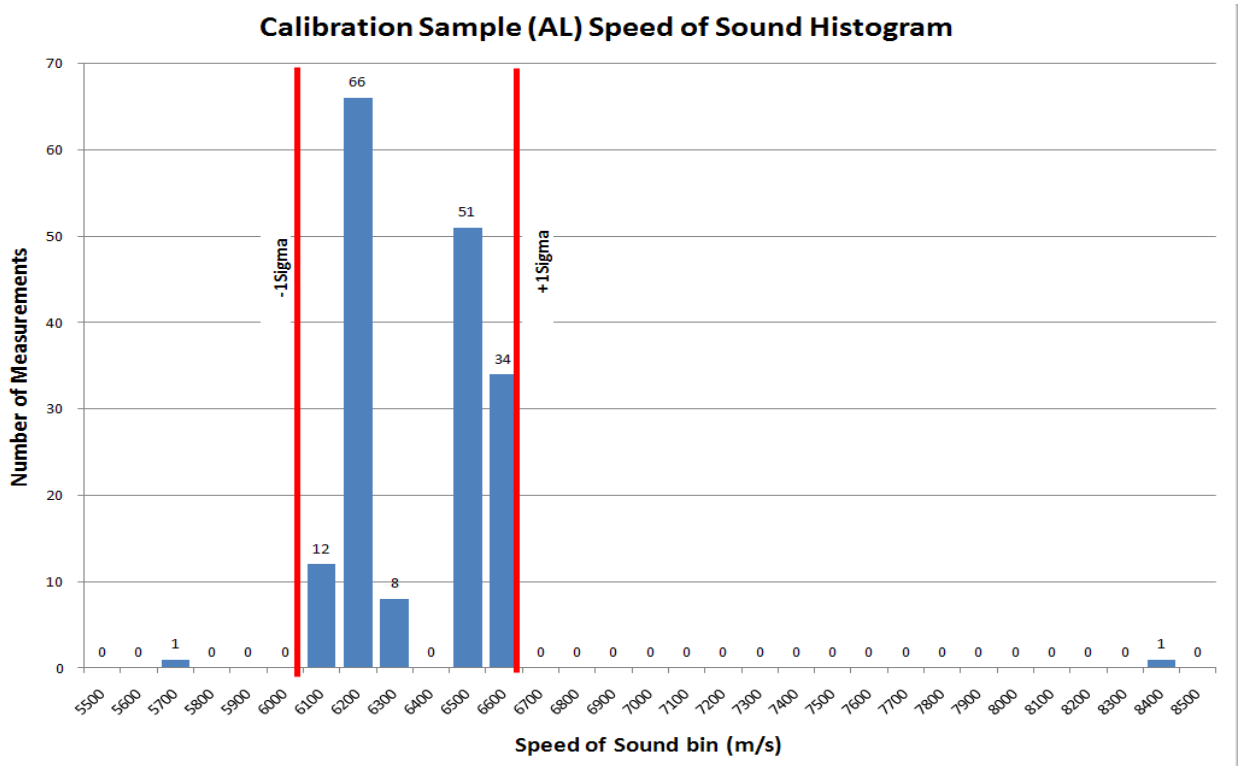

Figure 4-31 Histogram of aluminum sample measurement of speed of sound

A large number of samples were taken to gather each data set. The scans from the aluminum sample were used as a calibration tool to validate the methods and the techniques that were to be used on all other samples. Using the data collected, the equipment and technique was shown to be well calibrated. As noted, mean speed of sound measured longitudinally in the aluminum test sample was 6418m/s with an error of 0.03% to literature values. The standard deviation on the 173 sample measurements taken was 257m/s or 4.00% of the mean. The standard deviation information was used to exclude two points from the calculation of the mean. The two points occur well outside the distribution of the majority of the points that were measured. The first point occurred at 5784m/s and the second occurred at 8484m/s. The rest of the distribution can be seen in Figure 4-33. The bounds ±1σ are in the middle of the bins that make up the edges of the center distribution (6161m/s and 6675m/s). The results show that the technique employed is quite accurate. While there is some variation, it is small and within the range of acceptable error. What is important is that the technique is demonstrated as valid with its ability to effectively and quite accurately measure the speed of sound in the aluminum calibration sample.

Sample	Calibration	5	6	**Average**	9	11	**Average**
Material	Aluminum	PC	PC	**PC**	PMMA	PMMA	**PMMA**
Thickness Technique	Micrometer	CMM	CMM	**N/A**	CMM	CMM	**N/A**
Thickness Mean (µm)	1272.5	56.3	59.3	**N/A**	61.0	63.5	**N/A**
Thickness Std. Dev. (µm)	7.6	0.8	0.5	**N/A**	1.8	1.0	**N/A**
C_{long} Mean (m/s)	6418	2354	2299	**2327**	2663	2720	**2692**
C_{long} std. Dev. (m/s)	257	231	259	**246**	165	152	**158.5**
C_{long} N (N/A)	173	63	63	**63**	63	63	**63**
C_{long} Lit. (m/s)	6420	2220	2220	**2220**	2750	2750	**2750**
C_{long} % Error (%)	0.03%	6.04%	3.56%	**4.82%**	3.16%	1.09%	**2.13%**
C_{long} % Std Dev (%)	4.00%	9.81%	11.27%	**10.57%**	6.20%	5.59%	**5.89%**

Table 4-3 Single layer data on measured speed of sound

The same calculations were performed on the experimental samples. For single layer polymer samples, and 2 layer polymer samples, a lower number of samples was needed. This is because the samples were not validating the technique, and instead were utilizing it. The number of measurements for the samples was set at 63. These 63 measurements were manually selected from among the larger data set recorded during scans. This was done to remove scans where issues arose in the data, and also because attempts at automation of the measurement technique were found to be inaccurate do to the somewhat noisy nature of the signal. The results of the single layer analysis can be seen in Table 4-3.

From the data, both PC and PMMA are determined to be within acceptable limits. The two samples of PC tested showed a deviation of 6% and 3.5% from the expected speed of sound[53], with an overall average change of 4.8% from the expected value. The PMMA values where slightly closer to literature results[54]. The PMMA samples were measured to be within 3.2% and 1.1% of expected results with an average of 2.1% deviation from the expected results. The standard deviation of the measured results was relatively high (10.6% and 5.9% for PC and PMMA respectively) when compared to the results for the aluminum calibration sample, but remain within the bounds of acceptable error.

Using the A scan data of the single layer data, an analysis was also made of the attenuation occurring within the individual layers. An attenuative analysis could be used in combination with the information gathered from the TOF data to calculate the complex moduli which are the core goal of this work. The magnitude of a set of peaks was collected for the aluminum, PC, and PMMA single layer tests. The magnitudes of the peaks can be comparatively used to calculate the amount of attenuation that the wave undergoes. The formulation used was developed by Chen et al[55]. For the determination of impedance and attenuation from the through transmission testing of a multilayered sample. However, we can

make use through a rederivation of their work for the determination of the attenuation coefficients from the amplitude ratio of the pulse echo returns. This is possible for 2 reasons. The first, is that the impedance of both the water couplant and the material sample are already available from the TOF data. The second is that with the pulse echo, the returned magnitudes have traveled through equidistance in the couplant material and its effects can be ignored as they apply equally. The formulation is done in the most general method, so that it can be applied to the multilayer samples if necessary. In Equation 4-6, α_i refers to the attenuation coefficient for a given layer i, the subscript i is carried throughout. Di is the thickness of the layer. The a_i and a_{i+1} values refer to the magnitude of the reflected signals of the reflected front and back pulses respectively. The final variable, r_i and r_{i+1}, are the reflective coefficients between the layer being analyzed and the previous layer or next layer respectively. The reflective coefficient is calculated using Equation 2-13. For a single layer case, the coefficients become moot, as the reflective coefficient on the front and back surface is the same.

$$\frac{a_i}{a_{i+1}} = \frac{r_i}{r_{i+1}(1 - {r_i}^2)e^{-2\alpha_i D_i}}$$

Equation 4-6 Chen formulation for the amplitude ratio of successive pulses in a material with a known rate of attenuation.

Of the variables in Equation 4-6, D and the r terms are known from measurements and the TOF data discussed earlier. The amplitudes are measured from the A scans in a manner similar to that used for the TOF data. With a single unknown variable, the equation can be reformulated algebraically to solve for the attenuation coefficient.

$$\alpha_i = \frac{\ln\left[\left(\frac{r_i}{r_{i+1}(1-{r_i}^2)}\right)\left(\frac{a_{i+1}}{a_i}\right)\right]}{-2D_i}$$

Equation 4-7 Attenuation formulation solved for attenuative coefficient.

However, the utilization of this approach does encounter some problems. With this formulation for the calculation of ultrasonic attenuation, the authors make 3 assumptions[55]. They assume that samples are normal to the transducer and the layers are continuous and parallel. These conditions are satisfied, as part of experimental procedure, flatness was tested and the sample used here is of a single layer. The authors also assume that the signal is from a narrowband transducer and the attenuation is, therefore, modelable as an exponential decay system. This is again suitable for our experimental technique and samples. The third assumption is that the layers within the sample (or in this case the thickness of the sample) are thick enough to create a time delay between the individual returned pulses. By calculating the wavelength and the pulse in each material, we can check if we will encounter problems. For our 50MHz transducer, the wavelength in each material can be determined from the longitudinal speed of sound data discussed earlier. Further, the length of the ultrasonic pulse is known from the manufacturer to be approximately 1.5x the wavelength. The results, seen in Table 4-4, demonstrates that the pulse length in PC and PMMA is slightly longer than the constituent layers, but the single wavelength would fit, while the aluminum calibration sample will have plenty of delay between reflected pulses. This is something that was observable in the A scans discussed in section 4.2.1. Given the minor potential for echo overlap, the technique is pursued with knowledge that the potential exists due to constructive and destructive interference.

Material	C_{long} (m/s)	λ (μm)	Pulse Length (μm)
Water	1497	29.94	44.91
Al	6418	128.36	192.54
PC	2327	46.54	69.81
PMMA	2692	53.84	80.76

Table 4-4 Wavelength and pulse length by material for 50MHz pulse.

The other problem that arises is more physical. Ultrasonic attenuation displays a strong frequency dependence. The experimentation herein works with a 50MHz transducer partially because of the thin layers, and problems like those just discussed. Models do exist to predict,

often in a linear fashion, the attenuation at a specific frequency. These models though often rely on data in the 1-5MHz range. Some work[56] has demonstrated the limits of these linear models. We have been unable to find published results for measurements of ultrasonic attenuation at high frequencies for any of the materials under test. The literature found uses a maximum experimental value of 10MHz for aluminum, and a maximum of 5MHz for polymers.

Attenuation (dB/mm)		
Material	**Avg**	**Std. Dev**
Al	0.36	0.03
PC	1.94	0.36
PMMA	10.67	0.65

Table 4-5 Attenuation results measured from A scan data.

For the control sample, aluminum, experimental results showed attenuation of 0.36±0.03 dB/mm. Some attenuation is to be expected in all materials, the attenuation being a function of both absorption and scattering. Despite being treated as a purely elastic material in most cases, nearly all materials, including aluminum, do exhibit some components of viscoelastic behavior. Compared to the aluminum, the attenuation measured in the PC and PMMA was significantly higher. In PC, the measured attenuation was 1.94±0.36 dB/mm. For the PMMA, the measured attenuation was 10.67±0.65 dB/mm. This variation is qualitatively validated by the transform data that will be presented in 4.3.1.2.

With the attenuation data, Equation 3-3 from Jarlach[26] can be employed. The density is known from the material spec sheet, while the attenuation and speed of propagation have been determined experimentally. The results are shown in Table 4-6. The table contains the components of the complex modulus, as well as the magnitude of the modulus, and the tangent of the phase angle. The longitudinal modulus is the same parameter used in the finite element simulation to calculate elemental stiffness.

Longitudinal Modulus				
Parameter	**Units**	**Al**	**PC**	**PMMA**
v_{long}	m/sec	6418	2327	2692
ρ	kg/m^3	2780	1200	1190
α	dB/m	361	1943	10670
Z	Ns/m^3	17842	2792	3169
E'	**GPa**	**114.49**	**6.49**	**8.41**
E''	**GPa**	**1.69**	**0.19**	**1.55**
Tanδ	**N/A**	**0.0148**	**0.0288**	**0.1844**
E*	**GPa**	**114.50**	**6.50**	**8.55**

Table 4-6 Data table for experimental materials including complex longitudinal modulus

The longitudinal modulus results were compared to literature values where those were available. For PC, some comparative values were drawn from Arisawa[57]. The technique was also applied the PMMA samples[57]. However, the values from Arisawa are not exactly and directly comparable. The testing carried out by Arisawa occurred over a range of frequencies that were near 3 MHz. This is significantly different from our testing, carried out at 50MHz. While the results from the different tests are in the same order of magnitude, the results do show variation. This variation is likely attributable to the difference in frequency at which testing was carried out. The principle that causes this is similar to the material changes that occur as the temperature of a material changes. It is known as time-temperature superposition and creates significant changes in material behavior at varying temperatures. Due to the variation in methodology, the values are compared qualitatively here, but we do not quantitatively compare error between the two sets of values.

Polycarbonate (GPa)		
Value	**Experimental**	**Literature**
E'	6.49	5.75
E''	0.19	0.25
E*	6.50	5.76
Tanδ	0.0288	0.0435

Table 4-7 Comparison of experimental data for PC to literature values for the complex longitudinal modulus and its components.

Poly(methyl methacrylate) (GPa)		
Value	**Experimental**	**Literature**
E'	8.41	7.41
E''	1.55	1.33
E*	8.55	7.53
Tanδ	0.1844	0.1800

Table 4-8 Comparison of experimental data for PMMA to literature values for the complex longitudinal modulus and its components.

Arisawa notes the variation of the modulus components due to temperature, and also compares the temperature variation to changes in testing frequency. Arisawa specifically demonstrates that as temperature is decreased, akin to an increase in the testing frequency, the storage modulus will increase while the loss modulus will decrease. This matches most of our observations. For our higher frequency, the storage modulus increases in both cases as expected. The loss modulus decreases, also as expected, in the PC case. The PMMA loss modulus however increases slightly compared to Arisawa's data, this is the only deviation from the expected difference of values for the two different tests. The PMMA difference can easily be understood given the number of experimental variables that go into the determination of the modulus. The attenuation and the speed of sound are both experimentally determined, and use the measured thickness as part of those solutions.

Despite the variation, the techniques above demonstrate the ability to use experimental A-scans with a zero or negative delay between reflections to measure the complex moduli. This is one of the core goals of the thesis, and allows real-time monitoring or accurate material property identification in unknown samples. The techniques demonstrated for a single layer should be expandable to multilayered cases. The two analyses performed, using TOF and Jarlath to determine speed of sound and attenuation, should also be applicable in a general form, expanding the analytical potential to the multilayer case.

4.3.1.2 Transform

The second portion of the analysis performed on the single layer samples, was the use of fast Fourier transforms (FFTs) allowing a frequency domain analysis of the experimentally gathered data to be performed. FFTs are a form of calculating the discrete Fourier transform in a more computationally efficient manner. The FFT employed uses the Cooley-Tukey algorithm. The implementation was performed on manually bounded portions of the waveform, allowing only the relevant reflections to be selected. The bounded waveform portions were zero-padded to create a vector of 1024 entries. This allowed for a spectrum analysis to be performed with reasonable levels of accuracy. The FFTs were generated for 4 single layer cases. All FFTs were also normalized to enable comparative analysis. The 4 cases occurred because 2 FFTs were performed of the aluminum calibration sample. The FFTs can be seen on the following pages from Figure 4-32 to Figure 4-35. The major peaks in each spectrum are labeled for location and magnitude. The spectra are plotted from 0 to 150MHz. While the 150MHz extreme is well above the functional bandwidth of the transducer, the higher frequencies do serve to represent the magnitude of the returns any high frequency electrical noise generated by the experimental aparatus.

From the spectrum returns, it was possible to determine some material properties and make observations about the behavior of the single layer materials. Similar to the time domain work, aluminum was used as a calibration sample or 'perfect reflector' to provide a baseline signal. As noted, 2 transforms were performed on the aluminum sample. This was done because the return measured off of the front peak did not give the results expected. Given the higher speed of propagation, and the thicker material, the reflected pulses in the aluminum were clearly seperated in time. This is different than the polymer samples in which there was no clear definition between the reflections. For the aluminum, the first FFT's were taken from a zero padded bounding of the front reflected peak. The resulting FFT (Figure 4-32) shows a major

peak at 32.14MHz. Given that the transducer has a center frequency of 50MHz, this did not achieve the goal of accurately measuring a baseline. We believe this to be related to the surface finish of the sample However, a second transform was performed on the back surface reflection of the aluminum sample. This second transform, seen in Figure 4-33, shows a peak directly at 50MHz, and the expected spectrum shape.

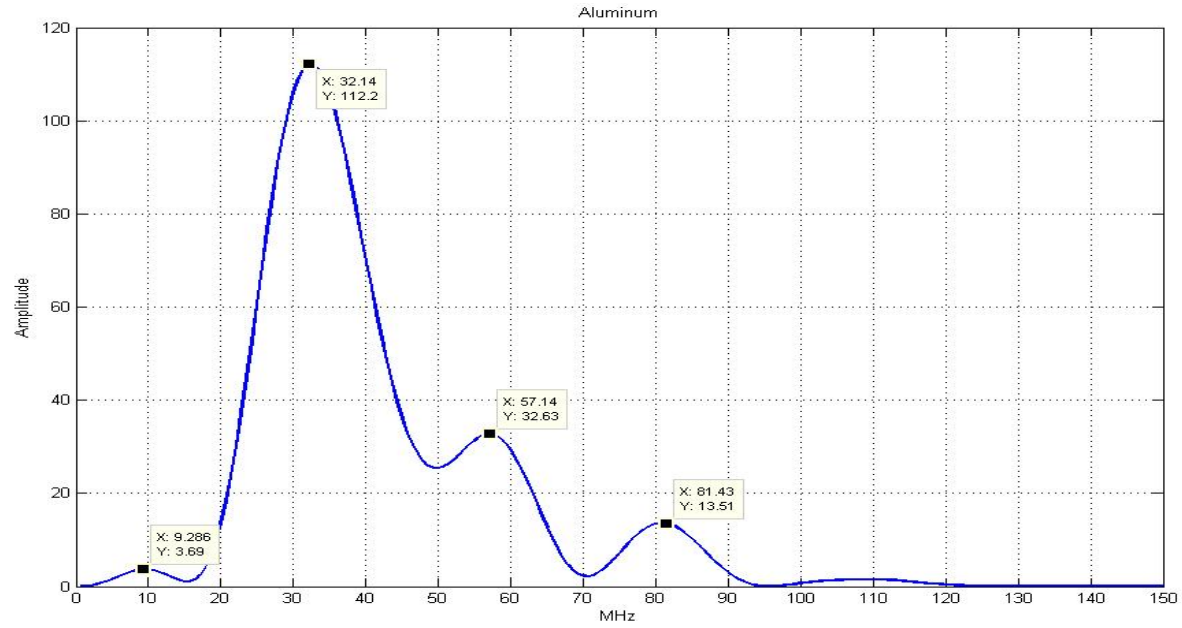

Figure 4-32 Spectrum plot of aluminum A scan front surface (1st) reflection

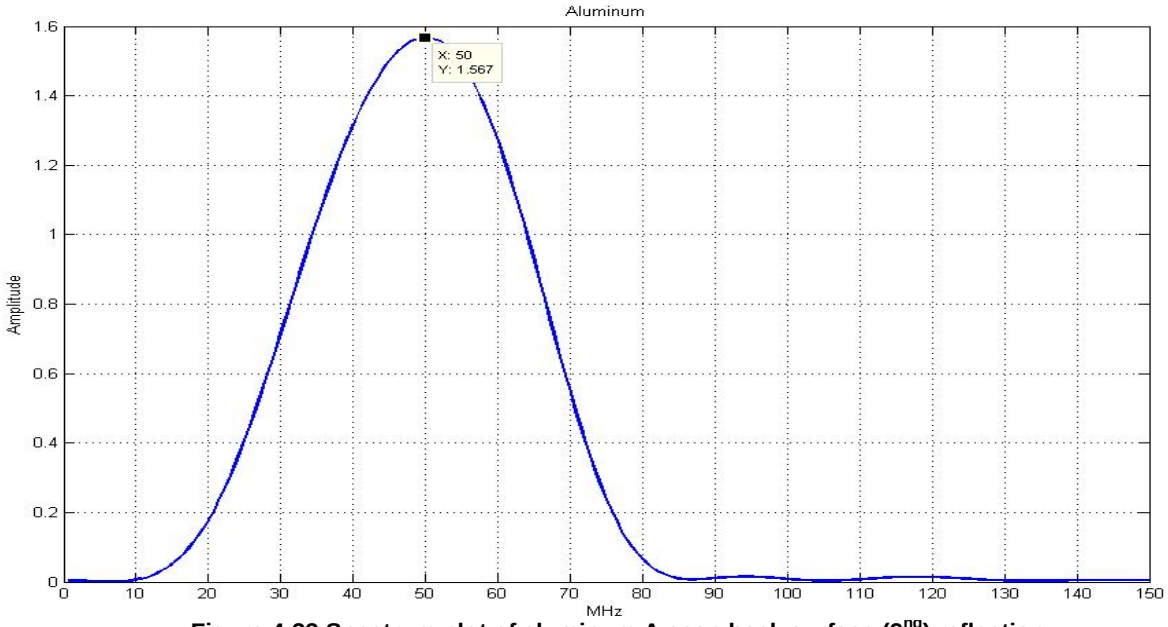

Figure 4-33 Spectrum plot of aluminum A scan back surface (2nd) reflection

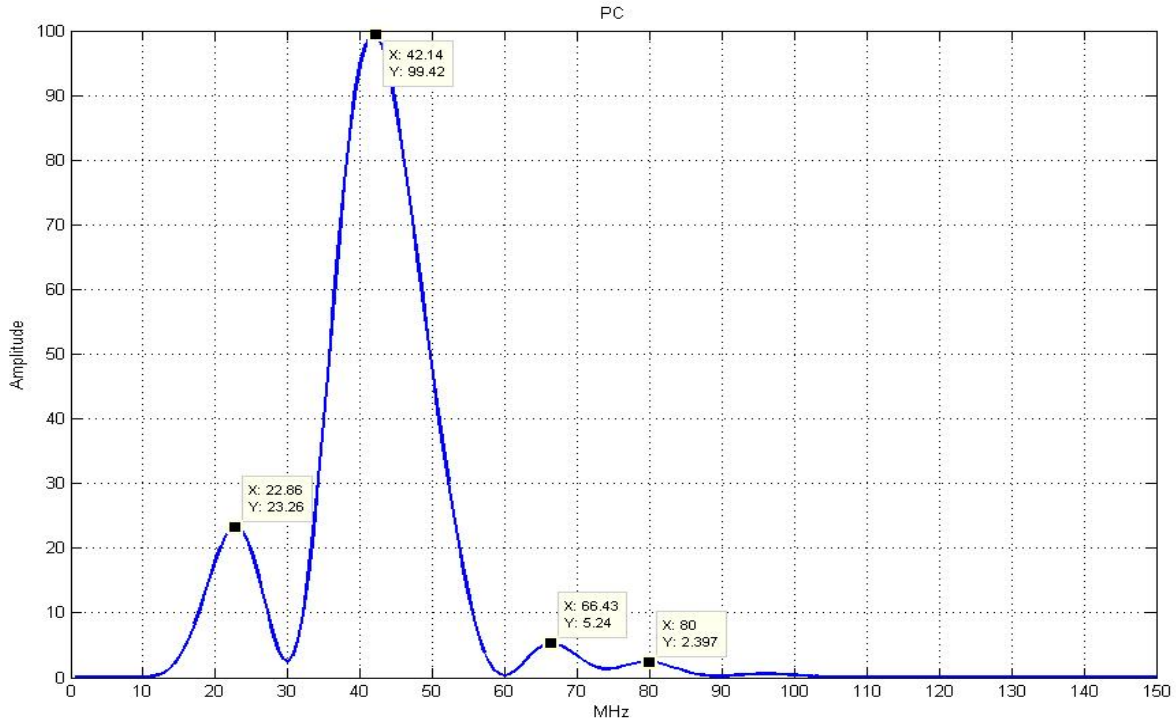

Figure 4-34 Spectrum plot of PC A scan combined reflection

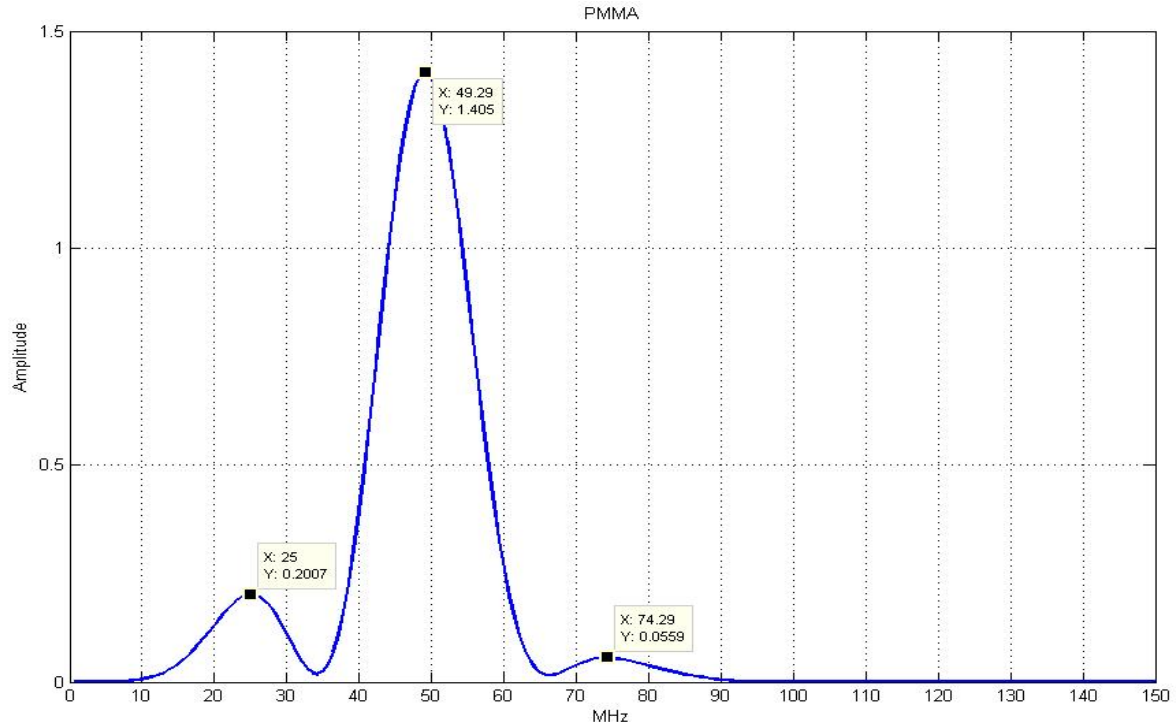

Figure 4-35 Spectrum plot of PMMA scan combined reflection

The cleaner response from the back reflection of aluminum, or more accurately, the poor response from the front surface, can be attributed to a number of factors. These include imperfect alingment, and an imperfect surface. However, the ability to generate an accurate return from the back surface performs the frequency calibration need. Further, it allows an identification to be done of the transducer bandwidth. From the FFT in Figure 4-33, the transducer bandwidth can be identified as 20MHz. With these results, it is also possible to calculate the wavelength of pulse in the aluminum material given both the center frequency from the FFT, and the speed of propagation calculated earlier.

Wavelength Determination From FFT Peaks			
Material	**Peak (MHz)**	**C_{long} (m/s)**	**λ (μm)**
Water	50	1497	29.94
Al (front)	32.14	6418	199.69
Al (back)	50	6418	128.36

Table 4-9 Table of wavelengths for aluminum calibration and water.

Similar analytical techniques can be applied to the single layer polymer samples. However, for the single layer polymers, it was not possible to separate the front and rear peaks. As such, the entire returned pulse was bounded and zero padded, comprising both the front and rear surface reflections. From Figure 4-34 and Figure 4-35, we can identify the location of the major peaks as 42.14MHz and 49.29MHz for PC and PMMA respectively. The frequency of the dominant peaks, combined with the respective measurements of the speed of sound allow calculation of wavelengths as seen here.

Wavelength Determination From FFT Peaks			
Material	**Peak (MHz)**	**C_{long} (m/s)**	**λ (μm)**
Water	50	1497	29.94
Al	50	6418	128.36
PC	42.14	2327	55.22
PMMA	49.29	2663	54.03

Table 4-10 Wavelength calculation of all single layer materials

Notably, despite having a difference in speed of sound of 14%, the polymer samples have a difference in reflected wavelength of just 2%. It should also be noted, that different materials displayed significant differences in peak magnitude. The first returned peak for aluminum and PC were 112dB and 99dB respectively. However, the returned dominant peak for PMMA was experimentally shown as 1.4dB. The significantly lower magnitude of the dominant peak belies a more absorptive material. A determination that PMMA is significantly more absorptive agrees with the results obtained using the time domain data.

Using the Fourier transform, it is possible to mathematically extract both the speed of sound (c) and the attenuation coefficient (α) as a function of frequency. This can be done using Equation 4-8 and Equation 4-9. Equation 4-8 uses the phase change (v) between the two spectra and the acoustical impedance (z) to calculate the speed of sound over a known interval. The two spectra are formed from the reflection off of the front surface, and the reflection off of the back surface of the sample. Equation 4-9 uses the relative amplitudes of the front and back spectra to calculate the attenuation per distance.

$$c(v) = -\frac{2\pi v(z_2 - z_1)}{Arg\left(\frac{\tilde{p}(z_2,v)}{\tilde{p}(z_1,v)}\right)}$$

Equation 4-8 Expression for the determination of the frequency dependant speed of propagation (c) from the FFT of the front and back reflected peaks $\tilde{p}(z_1, v)$ and $\tilde{p}(z_2, v)$

$$\alpha(v) = -\frac{\log\left(\left|\frac{\tilde{p}(z_2,v)}{\tilde{p}(z_1,v)}\right|\right)}{z_2 - z_1}$$

Equation 4-9 Expression for the determination of the frequency dependant coefficient of attenuation (α) from the FFT of the front and back reflected peaks $\tilde{p}(z_1, v)$ and $\tilde{p}(z_2, v)$

The technique requires the separation of the front and back reflections, and the generation of an FFT for each. This immediately discounts the use of the equations on the single layer polymer samples. As noted in the time domain results, we have not been able to

fully and accurately separate the front and back reflections of the polymer samples. This prevents the use of these equations, because the equations use comparative relations between the two peaks.

Despite being inapplicable to the other samples, the aluminum samples were calculated, as a check of the time domain results and a check of the methodology were future work able to accurately identify the individual reflections, not just the individual peaks, of the single and multilayered samples. The results are seen in Figure 4-39 and Figure 4-38. Using the transform equations, the resulting speed of sound from the FFT data is $2.5*10^{17}$m/s. Obviously,

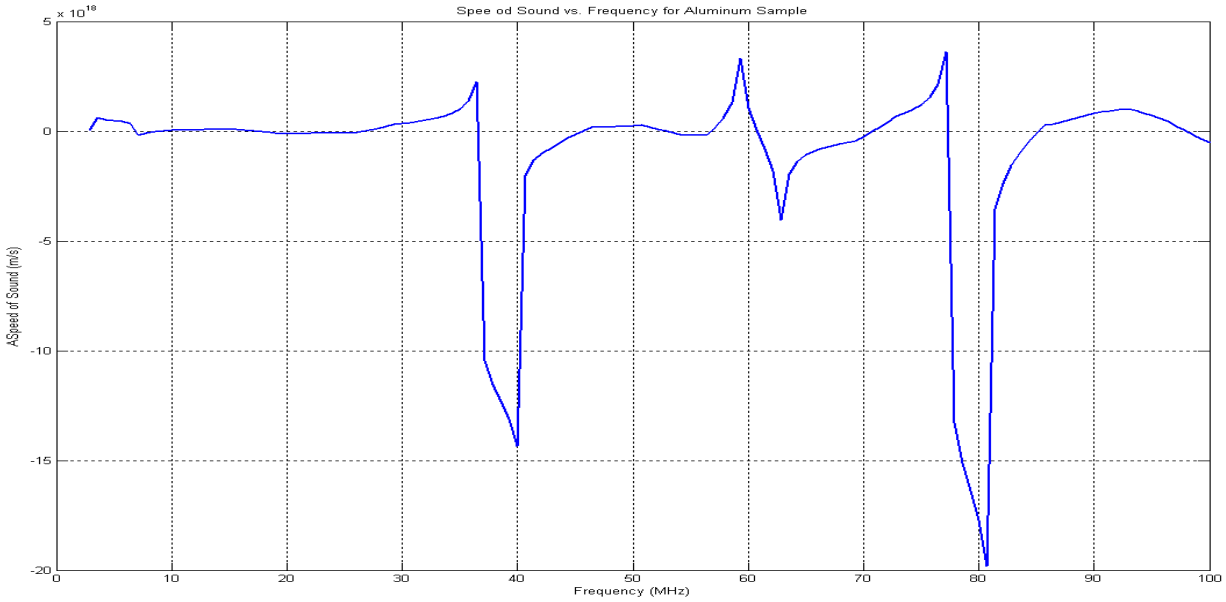

Figure 4-36 Speed of Sound versus frequency for aluminum calibration sample

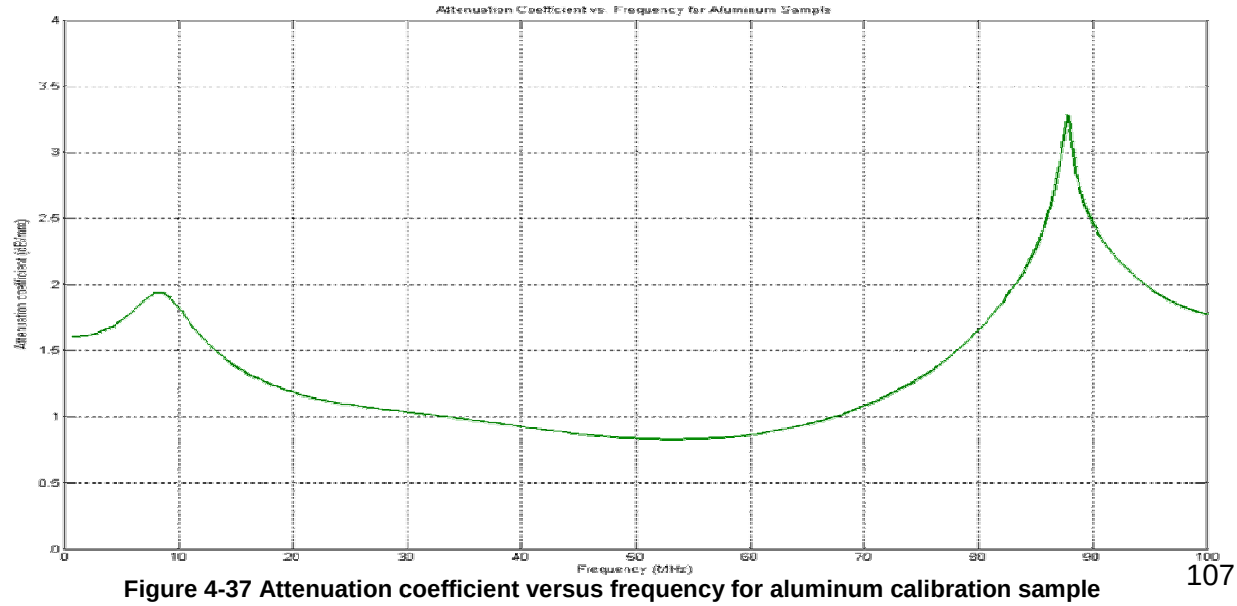

Figure 4-37 Attenuation coefficient versus frequency for aluminum calibration sample

this does not match the 6418m/s determined from the time domain data. The calculated attenuation also does not match the time domain results. The attenuations calculated are 0.36dB/mm and 0.84dB/mm (at 50MHz) from the time domain and FFT data respectively. While this is closer than the results for the speed of sound, the curves and results from both pieces of information lead us to conclude this technique is ineffective. The reason for the failure in the aluminum case is likely due to the poorly formed reflection of the front peak. As noted in the time domain discussion, and the discussion of the FFT returns, the front surface reflection from the aluminum calibration sample did not appear to form properly. The exact reason is not entirely clear, and likely subject to numerous factors. However, using comparative techniques between the poorly formed front reflection, and the properly formed back reflection demonstrated that the technique requires relatively refined experimental data and is not likely to be successful with the complicated returns demonstrated here. Some attempts were made to perform an estimated splitting of the front and back reflections of the single layer A scan returns, but they were no more successful and were based on an interpretation of the A scan that would be considered borderline arbitrary. Overall, this technique is not applicable to our results. Refinement of the techniques for analyzing the FFT's and methods for extracting results is necessary for further applicability

A final phenomenon that was visible in the spectrum plots was the creation of secondary harmonics. Both polymer samples display what are believed to be sub harmonics at regular intervals. The sub harmonics are visible at approximately $f_{peak}/2$ and $3f_{peak}/2$ for both PC and PMMA. While we have not been successful in interpreting their exact meaning, we believe they may be useful to future researchers. It has been proposed that sub harmonics, and harmonic spacing may be a method for the determination of resonant frequencies of materials and allow the ability to determine their representative material properties. However, the area is not sufficiently studied yet to produce reliable conclusions for viscoelastic materials. The use of

subharmonics for mechanical property determination has been studied. Specifically, it is reported on by Jhang[58]. The technique is used for damage identification through comparison to a 'known good' spectrum, in a manner similar to that proposed by us for extraction of properties in the multilayered samples. The authors also use the subharmonics to determine non-linear coefficients of stiffness. However, the non-linearity is only discussed in terms of the elastic materials. The authors do not apply the technique to viscoelastics, and we have been unable to find prior work, or develop methodology, at this point, to determine a method for the direct utilization of sub harmonics to extract viscoelastic properties from the FFT spectra. We believe that further study would be of benefit and make such a suggestion in the discussion of future work.

4.3.2 Multi-layer

With a thorough analysis of the data collected for single layer samples, efforts were made to apply similar techniques to the multilayered test samples. The efforts were intended to make use of the data collected on the individual layers as a basis for calibration of the constituent material properties. Given that the multilayer and single layer samples were made from the same batch of material, the resultant material properties should be similar. The analysis of multilayered samples proved to be less successful in the ability to determine bulk sample properties, and the ability to identify and characterize layers within the sample.

4.3.2.1 Time Domain

The time domain analysis of the multilayered sample was performed in much the same way as the single layer analysis. The peaks were manually located from the A scans gathered experimentally. The determination of the correct peaks was significantly more difficult in the multilayered samples. As discussed in section 4.3.1.1, the wavelength of the pulse, and the length of the entire pulse, is slightly larger than the thickness of the single layers. This

phenomenon can cause interactions of the reflections. With the single layers, the front and back echos were identifiable. However, in the multilayered sample, identification of the reflected peaks was significantly more difficult. As such, only the 2 layer sample was analyzed.

Testing on the 2 layer showed significant difficulty in correlating experimental measurements to expected values from models created from the single layer or literature data. Example A scans, with the best estimate peaks labeled are shown in Figure 4-40 and Figure 4-41. In the 2 layer sample, a total of 3 labeled peaks are visible. These account for the reflection off of the front surface, the back surface, and the one internal interface between the two layers. For the 4 layer sample, 5 reflections are visible as expected, relating the 3 internal boundaries as well as the sample surfaces. Because of the inability to develop a full, workable, analysis for the 2 layer samples, the techniques were never expanded to the 4 layer case and the discussion and results concentrate on the 2 layer case. While the 2 layer analysis was not fully successful, an analysis of the speed of sound and the determination of bulk and individual

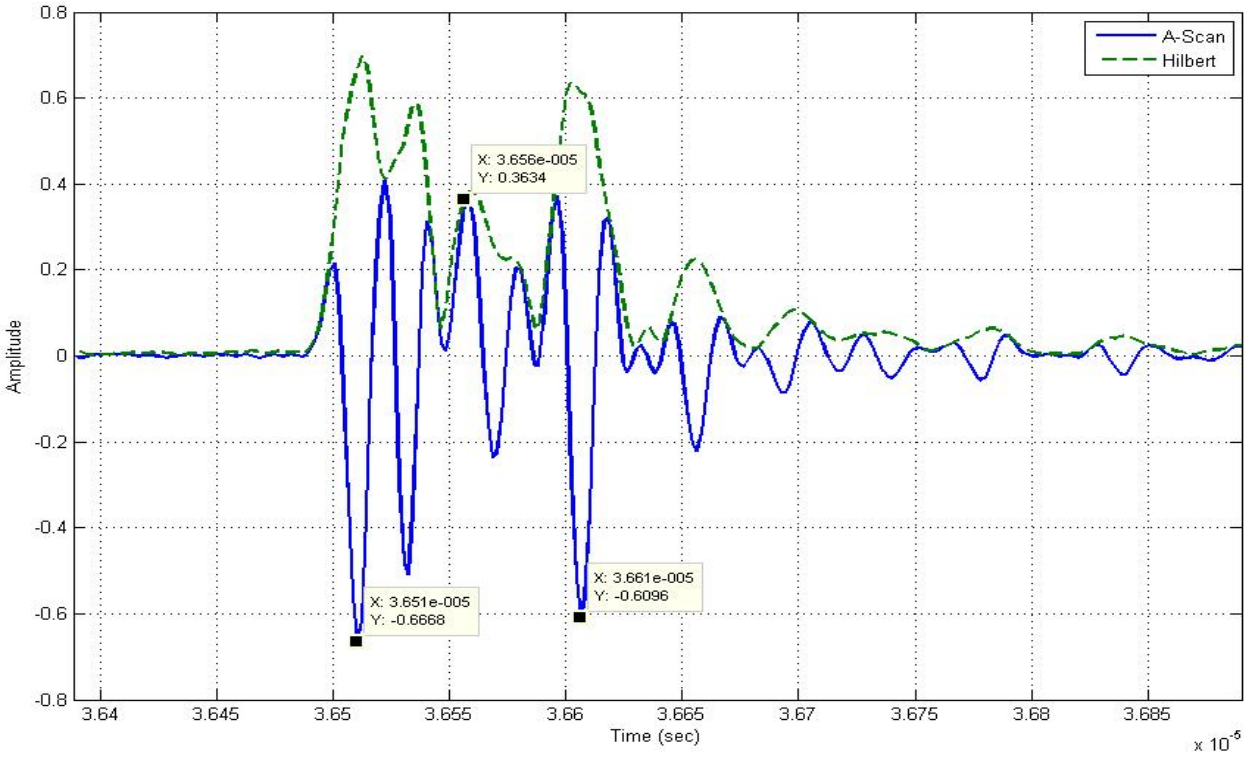

Figure 4-38 A scan and Hilbert transform of 2 layer experimental sample.

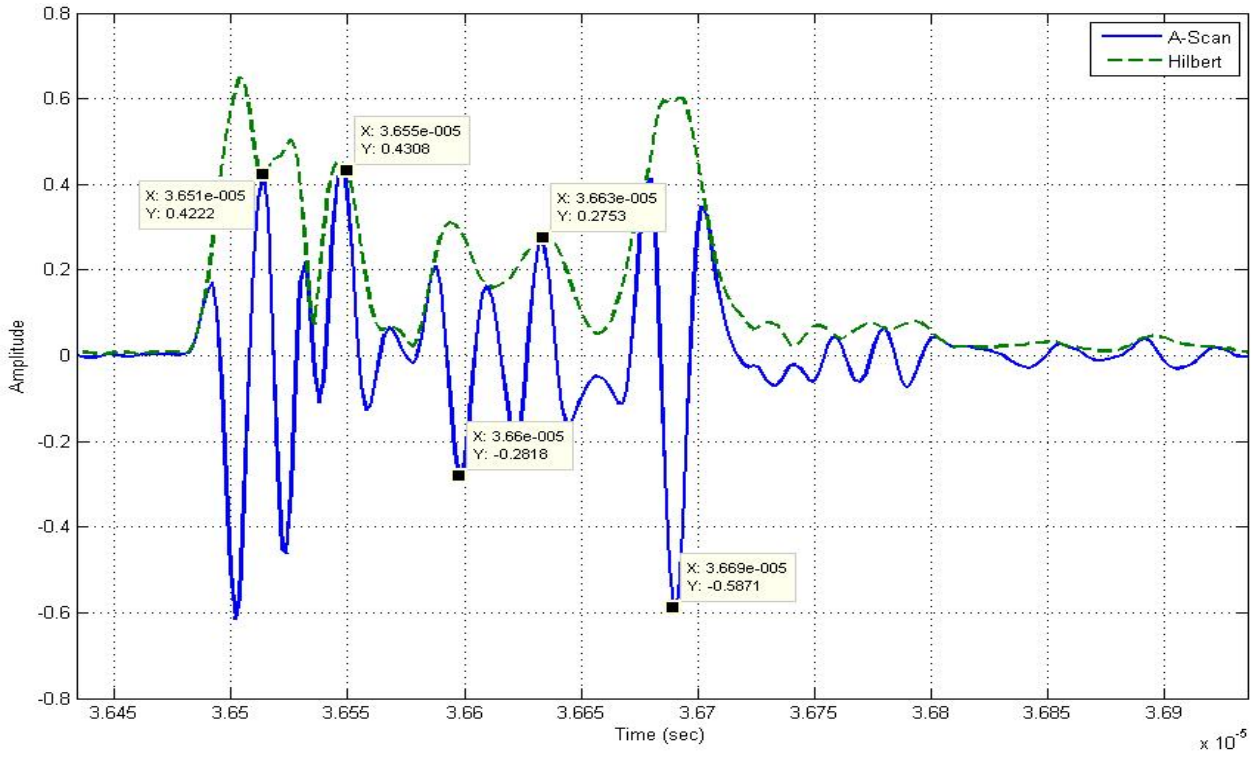

Figure 4-39 A scan and Hilbert transform of 4 layer experimental sample

layer speeds of propagation is demonstrated.

To use the peak times to determine layer and sample speed of sound, a number of different methods were employed. These can be separated into two categories, attempts made to determine the bulk speed of sound in the sample, and attempts made to determine the speed of sound of the individual layers in the sample. All attempts relied on varying unknown parameters within the equations for determination of the speed of sound from the time of flight. Iteratively varying the unknown parameters was then performed to determine a best fit result from the assumptions and constraints for each specific method.

To measure the bulk speed of sound, the first and last reflected peaks were used to determine the total TOF in the sample. The total TOF can be determined using a modified version of the TOF equation from Equation 2-12. The derivation, and the final equation are shown in Equation 4-10 and Equation 4-11. This is shown for 2 layers, but applies for all

multilayered materials of any number of layers of any material. We assume that the total time of flight is the sum of the times of flight of the individual layers within the sample. With layers that are significantly thicker than the interphase regions reported by Possart[25] and others. If the inclusion of the interphase model was deemed necessary for a specific experimental case, Equation 4-11 could be modified using the interphase model from Liu[5] and the implementation of the interphase as a separate, defined, layer of a given thickness and property.

$$TOF_{sample} = TOF_{layer1} + TOF_{layer2}$$

$$TOF_{sample} = \frac{2d_{layer1}}{c_{long}{}_{layer1}} + \frac{2d_{layer2}}{c_{long}{}_{layer2}}$$

Equation 4-10 Equation for TOF in 2 layer sample

$$TOF_{sample} = \sum_{i=1}^{n} \frac{2d_i}{c_{long}{}_i}$$

Equation 4-11 Formulation for the total time of flight in a multilayered sample of n layers.

The drawback, is that the formulation requires a large number of variables, 2n, or 2 times the number of layers. In a 2 layer case, the number of variables in calculating the TOF is 4. In situations where the overall TOF or the TOF within an individual layer is known, the equations can be used in reverse. For the bulk, the overall TOF is known, the speed of propagation for each material is known, and the overall thickness of the sample is known. Knowing the overall thickness, the equation for the bulk TOF can be reduced to one variable. This is unique to the 2 layer case, where the two layer thicknesses can be expressed as one unknown variable and the overall thickness.

$$d_{layer\,1} = d_{total} - d_2$$

$$d_{layer\,2} = d_2$$

Equation 4-12 Expression of layer thickness in 2 layer sample using one variable

This in effect allows the bulk speed of sound to be generated as a weighted average of the individual layers and their properties. The solution for the total TOF is derived to be as follows. One benefit of this technique is that it does not require a knowledge of which layer is on top. Knowing which material is the top and which material is the bottom layer is a challenge that affects only the attempts to determine the speed of sound in the individual layers.

$$TOF = \frac{2(d_{total}c_2 + d_2(c_1 - c_2))}{c_1 c_2}$$

Equation 4-13 2 layer TOF using total thickness and second layer thickness

Sample	Total Thickness	Measured TOF	Bulk C_{long}
#	µm	ns	m/s
14	114	88.9	2581
15	115	98.4	2354

Table 4-11 Bulk speed of sound experimental measurements for 2 layer samples.

Equation 4-13 was used to fit a solution for the measured total time of flight. The goal is to minimize the difference between the weighted average and the experimental bulk speed of sound. The bulk speed of sound was calculated from the total TOF and the total thickness and is shown in Table 4-11. The weighted average is calculated from the total thickness of the sample, and the speed of sound found previously in the single layer samples. The minimization was performed by iteratively manipulating the d_2 parameter in Equation 4-13.

The second model that was used calculates the time of flight of the individual layers within the sample. This is done by using all three A scan peaks labeled in Figure 4-40. This method determines the times of flight of the individual layers, as well as the overall time of flight in the sample. Calculating the time of flight of the individual layers was theorized to create a lower level of error by making the calculations more independent. Again, a single independent variable, and the total sample thickness, were used to model the layer thicknesses. The major difference, was that the second model required making an assumption about which was on top,

and which was on the bottom during testing. This dictated that the model was run twice, once with the top layer assumed to be PC, and once with the top layer assumed to be PMMA. The results of the best-fit case only are presented for both experimental samples. The minimization was performed slightly differently. The manipulation of the layer thicknesses was the same. However, the goal was to minimize the difference to the speed of sound at the layers not the bulk. The minimization routine would attempt to match the speed of sound calculated in each layer to the speed of sound for that material previously found in the single layer tests. The bulk speed of sound was a resultant of the model, but not part of the minimization scheme. The results of the bulk speed of sound are shown below.

Measurement	Thickness			Bulk C_{long}		
Sample	Total	Layer 1	Layer 2	Experimental	Model 1	Model 2
#	µm			m/s		
14	114.6	55.0	59.6	2581	2502	2620
15	115.3	58.8	56.5	2354	2492	2382

Table 4-12 Comparison for bulk speed of sound of experimental data to model data.

Notably, model 2 better predicts the bulk speed of sound in both cases. Model 1 is 80m/s (3.1%) low for sample #14, and 138m/s (5.9%) high for sample #15. Model 2 over predicts by 39m/s (1.5%) for sample #14 and for sample #15, it over predicts by 28m/s (1.2%). Obviously, both models predict relatively low error.

The results are useful for demonstrating an accurate assessment of the layer thickness within the sample. However, the usefulness of the models is limited. The concentration on the bulk speed of sound is one of validation of results. The bulk models do serve to validate the comparisons between the single layer and multi layered samples. Nevertheless, they require assumptions about the internal layer behavior which are made from the single layer testing. To perform further characterization, including calculation of attenuation and mechanical properties, we must approach analysis from the individual layer, not from the bulk. Further, we must

attempt to determine the exact speed of sound in each layer rather than make an assumption of it from the single layer testing.

To clarify the longitudinal speed of sound of the internal layers, several tests were carried out. Again, the ability to model the thickness of the layers as a single variable was leveraged. The result was a cycle of testing assumptions about the orientation and layer makeup of the sample. Given that the configuration of the layers in the sample are unknown, four test cases were developed. In each case, the speed of sound of one layer was constrained to match the data from the one material as determined in single layer testing. The four cases that were used are:

1) Assume the top layer of the sample is PMMA
2) Assume the top layer of the sample is PC
3) Assume the bottom layer of the sample is PMMA
4) Assume the bottom layer of the sample is PC

In this case, no iteration is required. By setting a speed of sound, and knowing the time of flight, the thickness of the constrained layer can be calculated. As noted earlier, knowing one layer and the overall thickness allows the second layer thickness to be determined. The resulting speed of sound of the other "free" layer can then be calculated. The results demonstrate the constrained parameters, noted in **bold**.

Sample #14		C_{long} (m/s)			Error	
Test	**Constraint**	**Top Layer**	**Bottom Layer**	**Bulk**	**Free Layer**	**Bulk**
#1	PMMA top	**2692**	2547	2608	9%	1%
#2	PC top	**2327**	2905	2639	9%	2%
#3	PMMA bottom	2554	**2692**	2608	10%	1%
#4	PC bottom	2869	**2327**	2635	8%	2%

Table 4-13 Layer speed of sound constrain scenarios.

The results show that when a constraint was applied to a specific layer, matching it to the values from single layer work, the bulk speed of sound would remain at a very low error state. However, the free layer which was unconstrained showed significantly higher error than when the single layer samples were measured. This demonstrates an interesting property of the samples and their testing. No matter the assumption that was made, the error in the samples hovered close to 10%. This likely demonstrates the impact of the interphase or other outside phenomenon. The interphase effects would create error that does not map to an individual area of the sample. Instead, error from the interphase would show as inconsistencies in measurement at the internal interfaces. In a 2 layer sample, there is one interface, which occurs between the two independent layers being modeled and tested here.

The final method that was employed was to iteratively determine the lowest total error for both speeds of sound in comparison to the speed of sound generated in single layer tests. This method attempted to find an overall best fit, as opposed to constraining a single layer. However, the orientation of the sample, and which material was the top layer, is still unknown. The data from Table 4-13 was used to the most promising orientation. The error, as calculated in Equation 4-14, is minimized for the best fit solution.

$$Error = \sqrt{\left(c_{PC\ measured} - c_{layerA}\right)^2 + \left(c_{PMMA\ measured} - c_{layerB}\right)^2}$$

Equation 4-14 Total error for individual layer speed of sound in multilayered sample.

By iterating the layer thickness, again using the relation in Equation 4-12, it was possible to achieve good results for both samples, shown in Table 4-14. The routine determined a best fit of the individual layers and the bulk based on the minimization of the error function above.

Layer	C_{long} (m/s)		%	Thickness
Sample #14	**Best Fit**	**Single Layer**	**% error**	**µm**
Top	2773	2663	4%	63
Bottom	2430	2327	4%	52
Bulk	2618	2581	1%	114.5
Sample #15	**Best Fit**	**Single Layer**	**% error**	**µm**
Top	2209	2327	5%	59
Bottom	2565	2663	4%	58
Bulk	2384	2353	1%	115.4

Table 4-14 Results from multi parameter fit of layered experimental samples

From Table 4-14, it is noted that the maximum error is found to be 5%. It is noted, that both samples achieve similar error rates for the individual rates, and similar (and lower) error rates for the bulk speed. This effectively demonstrates the usability of this technique as a method for the sample orientation when the constituent materials are known. Further, it demonstrates the ability of the ultrasonic testing methodology to determine the speed of sound of the individual layers in the multilayered material, which was a major goal of the work. While this has been previously demonstrated[37],[55],[59], all of those cases utilized testing setups wherein the samples were much thicker than the length of the ultrasonic pulse. The determination of the speed of sound in multilayered materials with layers thinner than the length of the ultrasonic is important, and will continue to be useful as the layer thickness being characterized is decreased further in future work at CLiPS.

Sample	Attenuation (dB/mm)	
#	**PC**	**PMMA**
14	23.8	-24.2
15	-19.2	24.3

Table 4-15 Attenuation data calculated for multilayer sample.

Given that the ability to measure the individual layer speed of sounds was demonstrated, an attempt was made to determine the attenuation from the peak heights. Because Equation 4-7 was written generally, it can be applied directly to the multilayer case. Unfortunately, the resulting data did not support the implementation of this method. The

calculated attenuation values are seen in Table 4-15. The resulting data showed negative attenuation in the top layer for both samples. The attenuation calculated in the top layer of both samples is negative, a highly unlikely event in the experimental case used. Further, the magnitude of the attenuation was far too high in both cases and for both materials.

These results are likely attributable to the prior discussed interference within the multilayered samples. Given the internal boundary, this is not surprising. It is also not surprising that the interference has a larger disruptive impact on the attempts to measure the attenuation. The interference causes changes in amplitude, but does not have as direct an effect on the location of the physical peaks.

The time domain analysis of the multilayered samples proved partially successful. The capability to determine bulk sample and individual layer speeds of sound was identified and demonstrated. However, the inability to accurately determine attenuation within the individual layers prevented this analysis from being wholly successful. Without the attenuation data, it is not possible to extract the complex moduli. The complex moduli must include information on the loss of energy during cyclical loading, a fundamental characteristic of viscoelastic materials. The mechanism of that loss in ultrasonic testing is attenuation. Without accurate attenuation data, the resulting characterization values for E' and E" would not be accurate. To attempt a secondary method of determining attenuation and direct mechanical properties, an analysis of the FFT's of the individual A scans for the multilayer samples was also performed.

4.3.2.2 Transform

Similar to the single layer work, a FFT analysis of the returned signals was carried out for the multilayered samples to supplement the time domain work. The results that were found were similar to the results of time domain analysis for multiple layers and the transform data for single layer samples. There are qualitatively notable phenomena in the FFTs of the multilayered

samples, however, without the ability to separate the returned reflections, drawing conclusions is difficult. This is partially due to simply the complexity of the reflected returns, which are shown below. The returns feature multiple major peaks. The multiple peaks are different from the sub harmonics discussed with the single layer samples. Despite an inability to quantitatively extract values and parameters, the characteristics of the multilayer FFTs do yield useful qualitative information. As with the spectra generated from the single layer samples, the multilayer spectra are generated from the entire reflected pulse. The individual reflections are not able to be accurately separated.

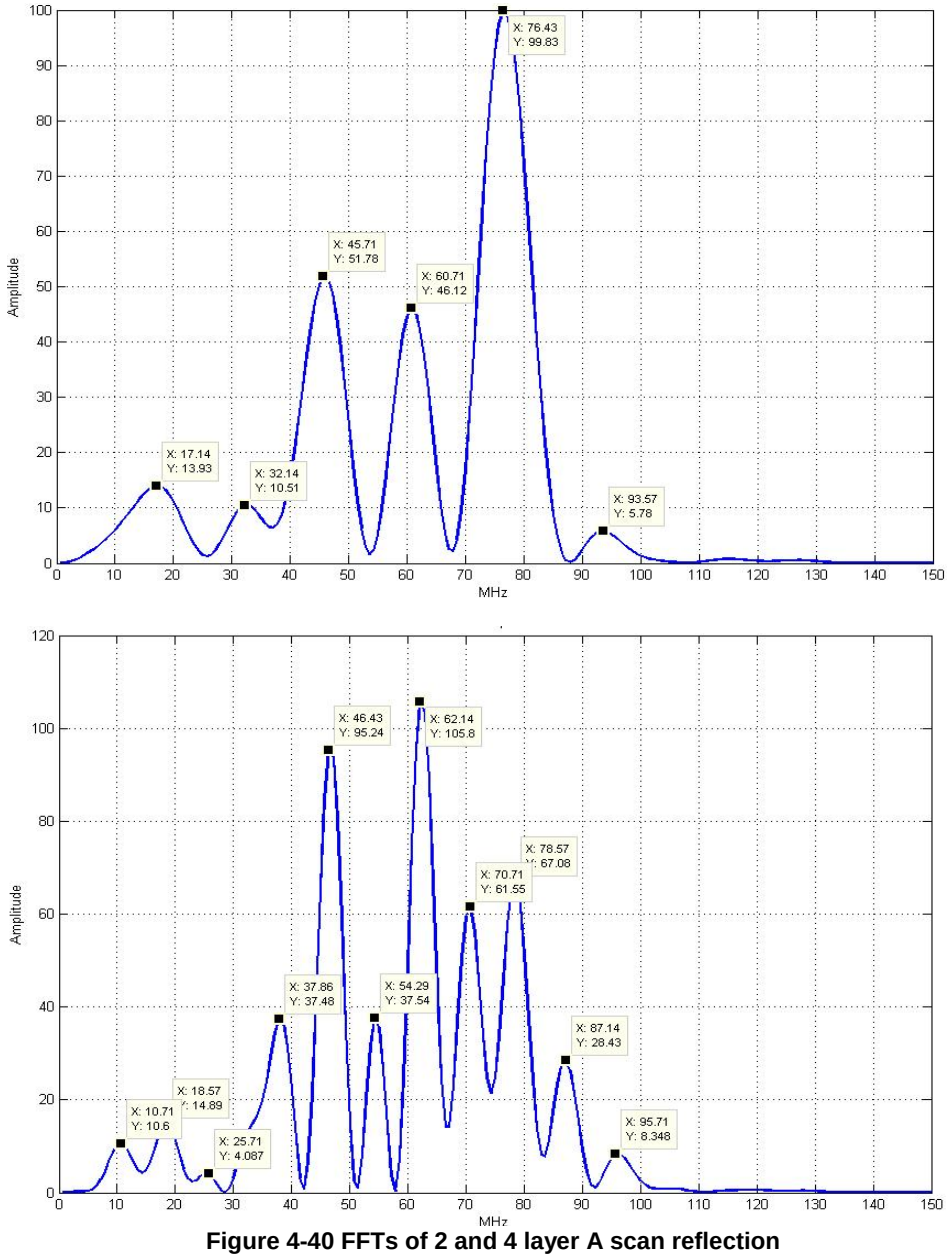

Figure 4-40 FFTs of 2 and 4 layer A scan reflection

From the spectra in Figure 4-42, it is clear that the multilayered samples do not have a singular major dominant frequency as was present in the single layer. Instead, the spectra show a number of major peaks, with one maximum peak. These peaks occur both inside and outside (above and below 70MHz and 30MHz respectively) the bandwidth of the 50MHz transducer used. Within the bandwidth, the two layer spectrum creates 3 major peaks, at 38MHz, 46MHz, and 61MHz. The four layer sample creates 5 major peaks at 31, 38, 46, 54, and 62 MHz. Notably, the 3 peaks from the two layer sample align closely with 3 of the 5 peaks from the four layer sample. Further, the spacing of the peaks also appears to be repeatable. The spacing between the 3 peaks in the two layer sample is 14 and 15 MHz respectively. For the four layer sample, the peaks are spaced at 7, 8, 8, and 8 MHz on center.

We believe this shows definable, repeatable characteristic of the spectrum generated from multilayered samples. In both cases, the number of peaks within the bandwidth is equal to the number of reflections expected to occur. Further, as noted, the spacing is regular in the frequency domain between the peaks. It is also approximately half for the four layer case what it is in the 2 layers case (14.5MHz in 2 layer 7.75MHz in 4 layer).

Despite the identifiable phenomena though, we have been unable to find any literature providing guidance or even suggested explanations on the quantitative evaluation of these results. We have attempted to investigate the spectra as representative of harmonic oscillation of the sample, or the layers, which could be used to determine some stiffness properties, but have been unsuccessful. However, we believe that with further, directed study, the extraction of properties using the spectra may be possible and suggest specific efforts as future work.

Chapter 5

Modeling Work

As discussed, there are situations where simple analysis of experimental results in ultrasound is not always easy or feasible. There are situations wherein a returned signal will display characteristics of elastic or viscoelastic propagation phenomenon that may not be directly identifiable due to interference and other propagation phenomena. Even if it is possible to identify via the trained eye, it may not be possible to automate. This slows and disrupts the process of data analysis. In the non-destructive testing (NDT) realm of ultrasonic utilization, an experimental result is often compared to a known good area of a sample to either validate sections, or highlight imperfections. The goal here is to develop a similar technique wherein a simulation is used to determine the inputs responsible for a specific output.

5.1 Discussion of Approach

In the usage of ultrasound for mechanical characterization, the measurements are analytical and analog as opposed to digital and pass-fail. The interpretation and analysis of data is based on measurement and interrogation of the returned waveforms. Measurement of the relative sizes of reflected and transmitted peaks and the times between those peaks is used to determine the material properties under test. Using these methods for characterization and material property measurement makes small changes in peak magnitude and location more important than in NDT. As discussed above, these realities also make direct analysis difficult in more complicated situations. Specifically in the case presented, the materials under test display similar but unique material properties. In our case, not only does this make it difficult to identify the individual materials, but it significantly reduces the size of the reflected internal peaks

needed to measure and determine material parameters from the experimentally gathered ultrasonic scans.

However, if it were possible to generate a simulated signal, a comparative analysis would be possible. In this case, simulation is required utilizing the intended experimental outputs as simulation inputs. By creating a simulation with inputs that match the intended outputs of the experiment, it should be possible to iterate until a solution is found wherein error between the simulation and the experimental setup is minimized and the inputs of the simulation effectively match the output of the experiment. However, with the multitude of factors involved in simulating the proposed experiment, this is not a straightforward option.

5.2 Mathematical Overview

For this work, two different methods were utilized to provide simulation of the experiments performed. Initially, as a tool for development and parametric study, a finite difference method was used to understand and ensure all necessary behavior was captured mathematically. Later, a finite element simulation was utilized to try to model behavior completely representative of the experiment performed in parallel.

5.2.1 Formulation of Problem - Operator

To simulate ultrasonic propagation, the wave equation is used as the basic operator. The wave equation is a linear second-order partial differential equation (PDE). The solution to the wave equation is a scalar function that satisfies:

$$\frac{\partial^2 u}{\partial t^2} = c^2 \nabla^2 u$$

Equation 5-1 Operator expression of the wave equation for scalar function u

The c term is a constant, which represents the speed of propagation of the wave. For example, an electromagnetic wave would have a c equal to the speed of light. In the case at hand, the speed of propagation, c, is variant based on the medium in which it is propagating and is colloquially referred to as the speed of sound.

This is a relatively generalized case, where u can be expressed in any number of dimensions. For a full solid system, u would commonly be expressed in 3 dimensions. However, in the case at hand, only one dimension is necessary. Herafter, u(z) is used to represent the single dimensional expansion of terms.

$$\frac{\partial^2 u(z)}{\partial t^2} = c^2 \nabla^2 u(z)$$

Equation 5-2 Operator expression of the single dimensional wave equation

For sound propagation, it is possible to expand the wave equation using notation more familiar to the study of mechanics. Using Newton's second law, it is possible to change to an expression using the stress tensor (T) and the density and including any applied body forces, F.

$$\nabla \cdot T = \rho \frac{\partial^2 u(z)}{\partial t^2} - F$$

Equation 5-3 operator expression of the wave equation using the stress Tensor and including the effects of body forces.

From the stress tensor notation, it is possible to implement a number of complicating factors which are present in the case we are attempting to simulate. First, is the method of calculation of the stress tensor. Using the stress tensor form, the full stress matrix must be used. This is because sound waves in an elastic material propagate at different speeds whether propagating in a longitudinal manner or in shear. The general speed of sound in a non-solid can be seen here:

$$c = \sqrt{\frac{K}{\rho}}$$

Equation 5-4 General expression of speed of sound in a non-solid with K representing the bulk modulus and ρ the density

However, this is unable to express the full complement of behavior. To do this, the solution must be decoupled. The decoupled speed of sound for motion in solids is as follows:

$$c_l = \sqrt{\frac{E(1-\nu)}{\rho(1+\nu)(1-2\nu)}}$$

$$c_s = \sqrt{\frac{G}{\rho}}$$

Equation 5-5 Expressions for the speed of propagation of a sound wave in a solid longitudinally and in shear.

In Equation 5-5, G refers to the shear modulus while E and ν refer to the elastic modulus and the Poisson's ratio respectively. This makes sense when one considers that the sound wave propagation occurs in the pressure realm and generates deflections in the materials as its method of propagation. A material demonstrates a difference in stiffness between axial and shear loading.

Even this formulation however, does not account for time domain stiffness effects as used to model viscoelastic materials. There are a number of ways in which this phenomenon can be addressed. The methods in which they are modeled varies depending on the situation and they are discussed in the relevant sections.

5.2.2 Formulation of Problem – Boundary Conditions

Given that the problem solved is a second order differential equation, there are two types of boundary conditions necessary for the determination of a solution. The first that is used here, is an initial condition of zero throughout the solution z domain. The other boundary

conditions occurs in the z domain and are implemented independent of the time domain. For the global solution, a boundary condition is placed at each edge of the domain. The boundary condition is an infinite tank assumption. The water bath in which propagation occurs is assumed much larger than the domain of interest. Therefore, any waves that pass fully through the material, or return to the transducer, are of no interest. These waves will continue to propagate in their respective directions and do not impact the experiment. The transducer side boundary condition also must include the input function from the transducer. This is the only input to the system.

Within the simulation, each of the layers must be treated as a smaller domain. This is because at the material boundaries, the ultrasonic energy splits, with a portion reflecting and a portion transmitting due to the sudden change in material properties. This condition is known as a natural boundary condition and is inherently satisfied in the solutions to the problem. With the discussion of the boundary conditions, all the mathematical components that will become a simulation are in place and a discussion of the derivations and mathematical implementations of the two different techniques can take place

5.3 Finite Difference

The first simulation attempt that was made was an application of the finite difference method to the solution of the problem at hand. This simulation was intended to provide a baseline analysis of the problem and investigate feasibility. The goals were to demonstrate solution stability, accurate definition of the problem, and to demonstrate that the generalized problem and boundary conditions modeled all expected behavior. There was no attempt to develop a full simulation from finite difference; viscoelasticity was not included in the finite difference solution.

5.3.1 Applicability

For the case at hand, a finite difference solution is simple and effective way of developing a model. While there are specific and definite drawbacks, it can be used to demonstrate the expected behavior quite well. This was effectively demonstrated by Chertov[27] as discussed earlier. Chertov discusses a model that models the propagation of ultrasonic waves in varying elastic solids. The reason this model was used as a basis for our work is that the author derives his solution with material conditions that closely match those used here. The author's model includes both asymptotic material changes, such as the boundary between a couplant and an experimental sample, and continuous material changes. Continuous material changes in the authors work include heat-affected areas of a weld where the material properties governing propagation change both in the physical dimension of propagation, and in the time domain as well. Therefore, the author's model is developed to use an arbitrary distribution of material properties dependant on time, location, or a combination of these.

Our work does not include time dependant changes in material properties. However, the method of implementing continuous material changes, and asymptotic changes, is useful in a modeling of the material properties in the interphase region. The interphase region, as discussed in section 3.1, is a product of the manufacturing process creating a varying set of material properties in a small zone at the material interface.

5.3.2 Model

Based on Chertov's[27] work, we begin with the equation of motion for a particle wave which can be derived from Newton's Second Law. This uses the same form developed in section 5.2.1.

$$\nabla \cdot T = \rho \frac{\partial^2 u}{\partial t^2} - F$$

Equation 5-6 Equation for particle wave motion.

We assume boundary forces, F, are negligible and set F to 0. T is known to be the stress tensor. Generally, T can be expressed as a function of all three directions as seen here using the first Láme parameter, λ, the second Láme parameter, μ, and the Dirac function, δ.

$$T_{ik} = \lambda(\epsilon_{11} + \epsilon_{22} + \epsilon_{33})\delta_{ik} + 2\mu\epsilon_{ik}$$

Equation 5-7 Expanded stress tensor using tensor notation

We are only interested in wave travel in one direction, known as the 'A scan'. A scan being the term utilized to refer to a measurement on an axis normal to the surface of a plate. For this case, we can simplify and still utilize the intended material properties. We use the z direction, which signifies the direction normal to the plate and the emitting surface of the transducer. This form utilizes the Láme constants for longitudinal propagation and does not model propagation in shear.

$$T_{ik} + T_{zz} + (\lambda + 2\mu)\frac{\partial u_3}{\partial x_3} == (\lambda + 2\mu)\frac{\partial u}{\partial \mathrm{z}}$$

Equation 5-8 Simplified single dimensional stress tensor in x_3, referred to as z.

With the simplified version of T found in Equation 5-8, we can substitute and formulate the governing equation in one dimension as shown in Equation 5-9. This form uses determinable material constants and the primary variable. This is the problem form we will be solving for all further steps.

$$\nabla(\lambda + 2\mu)\frac{\partial u}{\partial \mathrm{z}} = \rho \frac{\partial^2 u}{\partial \mathrm{t}^2}$$

Equation 5-9 Single dimensional wave equation in a solid.

Once we reach the refined governing equation, the left hand side can be expanded. For simplicity, an arbitrary function 'f' is employed to represent the material constants. To keep the solution as general as possible, the arbitrary function f is assumed to be differentiable in both z and t at this point in the problem. The LHS expands into two terms:

$$\nabla f \frac{\partial u}{\partial z} = \rho \frac{\partial^2 u}{\partial t^2}$$

Equation 5-10 wave equation using arbitrary function for material properties

$$\frac{\partial}{\partial z}\left(f \frac{\partial u}{\partial z}\right) = \rho \frac{\partial^2 u}{\partial t^2}$$

$$\frac{\partial f}{\partial z}\frac{\partial u}{\partial z} + f \frac{\partial^2 u}{\partial z^2} = \rho \frac{\partial^2 u}{\partial t^2}$$

Equation 5-11 Expanded form of wave equation

From Equation 5-11, a choice is made to either create a solution for the entire stack of polymer layers, or create an equation that only models the behavior inside the individual layers. In either case, the term affecting the outcome is the partial f function in the first term on the left side. The first option would appear far simpler and more robust, creating a solution for the entire stack of polymers. However, with the discrete material layers present in the stack, the expression of f in terms of material properties would need to be performed as a series of step functions that trigger at the layer boundaries with independent boundary conditions. Issues would also occur at the layer boundaries, making a full stack solution difficult. This is due to the reflective and transmissive characteristics of material boundaries in waves.

Further, it would be more difficult to construct f functions, which capture the material changes at the interphase. This method would lead to an f function which is non differentiable at the material boundaries and the edges of the interphase unless a modification is made to the interphase model proposed by Liu[9] to create a continuous expression for material properties.

The other option is to utilize Equation 5-11 as a model of solely intra-layer behavior. Given the construction of the layer stack, it is reasonable to assume constant material behavior within each layer of a material. The material differences between layers are much larger than the differences within the layers. This is supported both by the experimental work performed, and by the information provided from the manufacturer. Intra-layer modeling also creates a simpler case for the inclusion of the properties at the interphase. Using the interphase model from Liu[9] an intermediary layer can be employed rather than developing a multipart step function describing the properties of the whole sample as would be required in option 1. From the constant assumption for intra-layer properties, the f function is inherently differentiable. This actually simplifies the case given that the differentiation of a constant is 0.

At the ends of the intra-layer solution, boundary conditions are necessary, which model the transmissive and reflective behavior. This also solves the problems the full stack solution would cause at the material interfaces. Rather than accommodating the conditions *within* a solution, they are employed at the edges of the solution to force continuity between the layers.

For these reasons, the second option is used and the PDE will be used to develop a model for behavior within a single layer. The partial f term is zeroed based on our assumption of constant properties within each layer. This is the point at which our simulation deviates from the work by Chertov[27]

$$f\frac{\partial^2 u}{\partial z^2} = \rho\frac{\partial^2 u}{\partial t^2}$$

Equation 5-12 Intra-layer form of wave equation with constant material property assumption

$$f = \lambda + 2\mu = \nu^2 \cdot \rho$$

Equation 5-13 Reformulation of f function using speed of sound and density

To further simplify, we could substitute out the f function for a more simplified version using more commonly available properties as seen in. The reformulated f is then substituted into Equation 5-12 and simplified into the PDE model for behavior.

$$c_{long}{}^2 \frac{\partial^2 u}{\partial z^2} = \frac{\partial^2 u}{\partial t^2}$$

Equation 5-14 Final form of PDE for finite difference solution

With the PDE in the final form for modeling propagation within each layer, we expand it to a simple finite difference scheme . Within the solution, the i index refers to the direction of the simulation (z), and the n index referring to the time direction (t). These indices hold within the individual layer.

$$c_{long}{}^2 \frac{u_{i-1}^n - 2u_i^n + u_{i+1}^n}{\Delta z^2} = \frac{u_i^{n-1} - 2u_i^n + u_i^{n+1}}{\Delta t^2}$$

Equation 5-15 PDE in finite difference form

A linear finite difference assumption was used. Prior experimentation[27] showed that this level of solution creates a level of error that is small; their simulations showed .23%, assuming controls are put into place to effect reasonable error propagation prevention over the course of the simulation. A solution for u^{n+1} then is created from Equation 5-15. This is done via simple algebraic techniques.

$$u_i^{n+1} = \frac{{c_{long}}^2 \Delta t^2}{\Delta z^2}(u_{i-1}^n - 2u_i^n + u_{i+1}^n) + 2u_i^n - u_i^{n-1}$$

Equation 5-16 solution for next time step using finite difference technique.

Equation 5-16 is the formulation that was employed in the finite difference code. While the formulation is relatively simple, the goal is not to provide a highly accurate complete model, simply to provide a basic model which can be used to demonstrate accurate simulation behavior and validate more complicated simulation like that which will be developed using FEA and employing the full viscoelastic material models necessary.

To implement the solution, we need to implement a set of boundary conditions, initial conditions, and inputs. The initial conditions and input conditions are defined in the time domain. The initial condition is set throughout the modeled z domain, and the input occurs at a single node. The boundary conditions are defined at specific locations (interfaces) in the z domain and are mathematically constant throughout time.

Looking back to the solution of the governing equation in Equation 5-15, we know that it is necessary to include two previous time steps to calculate for the next time step. This means that the initial condition will be used for the calculation of the second and third time step.

$$u_{all}^0 = 0$$

Equation 5-17 Initial condition for all nodes in z

Given that, the primary variable has a 0 initial condition and, it is necessary to have an input condition to create a response in the system. This input, is in the form of an ultrasonic pulse. The length of the pulse is defined by the transducer frequency. It is generally 3π cycles in length. The mathematical definition used in the simulation can be seen here. While this is not an exact expression, it serves our purpose for this simulation.

$$u_{input}^{n} = \begin{cases} \sin(\omega_{input} t) & 0 \leq t \leq \dfrac{3\pi}{\omega_{input}} \\ 0 & t \geq \dfrac{3\pi}{\omega_{input}} \end{cases}$$

Equation 5-18 Model of ultrasonic input pulse.

With the initial and input conditions defined, the only remaining portion of the problem is to define the boundary conditions. Given that the model only simulates propagation within the individual layers, these boundary conditions handle the more complex behavior that occurs at a material interface. To define the boundary conditions, the physics of the problem must first be considered. Once we define the physics mathematically, they must be translated into the finite difference regime. Based on the known construction of the particle wave governing equation that we are using, we can express two BC's at each layer interface. First, we know that the wave motion must be 0^{th} order continuity. This allows us to create the first BC stating that the particle displacement on the boundary from both directions is equal, creating this continuity.

$$u_1^B = u_2^B$$

Equation 5-19 0^{th} order continuity boundary condition

This boundary condition ensures that we have only one potential physical solution at a point in the material stack. The B superscript in Equation 5-19 signifies the boundary location, which occurs at one node only. The subscripts (1 and 2) signify the material change at the interface. The second boundary condition that we create is a condition on the stress tensor. Based on the derivation, we know that the stress tensor normal to the interface must be continuous across the boundary between materials. This condition is initially expressed relatively simply using similar notation to the continuity condition.

$$(T_{ik}n_i)_1^B = (T_{ik}n_i)_2^B$$

Equation 5-20 Expression of normal stress tensor continuity across a material boundary

Looking back to Equation 5-8, there has already been a derivation of the specific form of the stress tensor for our solution. We can substitute that form in to Equation 5-20 creating a material dependant first derivative boundary condition at the layer interface.

$$(T_{ik}n_i)_1^B = {c_{long}}_1{}^2\rho_1\frac{\partial u_1^B}{\partial z}$$

Equation 5-21 Expanded stress tensor expression for a material boundary

This can then be substituted into the tensor continuity condition, Equation 5-20. We can further simplify if necessary into a solved solution for the partial from one side of the material as appropriate. The solution actually requires Equation 5-23 to be solved in both directions. This is because they will occur on the opposing surfaces of the material.

$${c_{long}}_1{}^2\rho_1\frac{\partial u_1^B}{z\partial} = {c_{long}}_2{}^2\rho_2\frac{\partial u_2^B}{\partial z}$$

Equation 5-22 Stress tensor boundary condition in differential form.

$$\frac{{c_{long}}_1{}^2\rho_1}{{c_{long}}_2{}^2\rho_2}\frac{\partial u_1^B}{z\partial} = \frac{\partial u_2^B}{\partial z}$$

Equation 5-23 Tensor boundary condition solved for one edge of layer

For our implementation, it is necessary to use imaginary points to use the boundary conditions in the finite difference formulation. To do this for Equation 5-19, an expression that creates the intended effect is created.

$$if \quad u_i^n = u_{1,2}^B$$
$$then \;\; u_{i+1}^n = u_2^{B+\Delta z}$$

Equation 5-24 Finite difference form of 0th order boundary condition.

The statement forces the continuity of the finite difference scheme across the boundary; identical to how the solution occurs, only changing the material if necessary.

The second boundary condition doesn't need to be expressed in the finite difference scheme. While it does exist mathematically (and is important), it is a natural boundary condition. Natural boundary conditions are automatically satisfied in the implementation of the governing equation. This is unlike the essential boundary condition from the expression of continuity at the layer interfaces, which must be included in the implementation. This means that Equation 5-20 will be automatically satisfied and does not need to be implemented.

The only exception to this is the reflection that occurs at the ends of the stack. That is, at the ends of the 1-D finite difference grid. The assumption is made of the experimental environment being effectively infinite. This assumption is viable because the thickness of the material stack is far less than the depth of the tank. However, this assumption (and the end of our grid) necessitates us creating a fictitious point on both sides of the stack, at the echo side of the stack and at the input side. These points are set to ensure 1st derivative continuity which creates the effect of infinite propagation. They are calculated just before the calculation of the adjacent nodes.

$$u_{inf\ input} = \frac{u_1 - u_2}{\Delta z} \qquad u_{inf\ echo} = \frac{u_{N-1} - u_N}{\Delta z}$$

Equation 5-25 Fictitious point calculations to ensure infinite BC and derivative continuity at ends of simulation space. N is used to refer to the total number of nodes

In addition to fulfilling the boundary condition, the fictitious points also provide the necessary additional information for solving the discretized form of the governing equation. Without these points, it would not be possible to solve for the first or last nodes in the solution space because the necessary u_{n-1} and u_{n+1} information would be outside the solution domain.

The creation of the fictitious points on either side of the simulation area creates the full compliment of mathematical tools necessary to create the simulation. The simulation was implemented using Matlab code. All boundary conditions and simulation inputs were modeled as double precision variables. For the finite difference simulation, only small, partial, simulations of 1 layer were used to demonstrate the intended behavior. This was the path taken to allow for storage of the entire time history of all points. The necessary output for comparison to experimental data is only the storage of the time history of a single point outside the polymer materials. Storing all points allowed deeper investigation of behavior, especially at the interfaces where the boundary conditions where most important. The problems, results, and drawbacks of this implementation are discussed below.

5.3.3 Results

With the finite difference simulation, we were able to establish and demonstrate our goals of validating the basic mathematical model in the specific application. From the derivation above, results were obtained demonstrating the underlying principles of the numerical model of the wave equation. However, the model was not entirely successful in demonstrating all phenomena. The phenomena that we intended to demonstrate were, propagation, reflection at

a material boundary, transmission at a material boundary, and stability over a wide range of material properties. We have successfully demonstrated the bulk propagation at the boundary. Further, we have demonstrated some cases of the reflective and transmissive phenomena that serve to validate the underlying mathematical behavior. However, the demonstration of the reflection and transmission has been limited by numerical instabilities in the solution. This will be addressed in the following discussion.

The testing of the solution progressed in phases. The first results that were pursued were those demonstrating the bulk propagation of the input wave in a material. The demonstration of correct bulk propagation creates a baseline for the intended future use of modeling and extracting data from propagation and boundary interactions of multilayered samples. Given that the bulk propagation is a time based phenomenon, the results are presented through the use of snapshots in time of the pressure wave propagation at specific timesteps. The input pulse used for the simulation was 0.1MHz ($1*10^5$Hz) with C_{long} set to 1000m/s and density set to 1000kg/m^3. While these properties do not directly replicate the materials used in testing, they do allow us to prove the validity of the equations and their underlying ability to demonstrate the effective behavior. These phenomenon are not dependant on the material properties to demonstrate the expected response.

The time steps are visible in Figure 5-1 on the following page. The plots show the displacement of the solution at all spatial steps (nodes). From left to right, they show the pulse being emitted into the bulk material(a), the pulse fully formed in the bulk material(b), and the pulse propagating into the center of the bulk material(c). The plots then show the pulse as it is absorbed by the infinite boundary condition on the back edge of the simulation(d-f). Specifically the 4^{th} image(d) shows the pulse just as it encounters the back edge, and then shows the pulse beginning to be absorbed(e) and nearly fully absorbed as it propagates out of the simulated area(f), modeling the effective infinite tank from the experimental work.

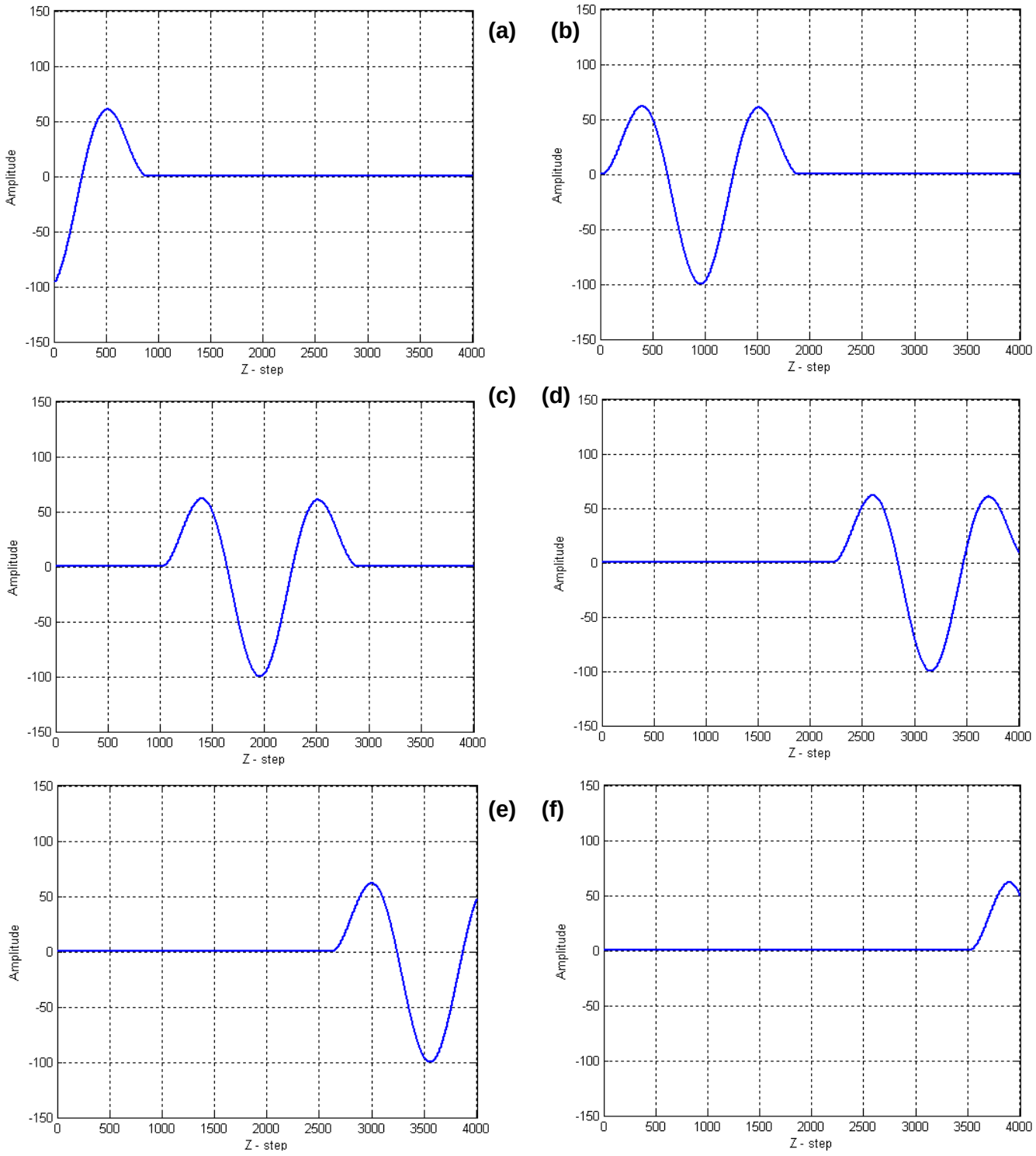

Figure 5-1 Finite difference simulation results at different time steps showing bulk propagation. Time step of 50ns and spatial step of 50μm. Input pulse of 0.1MHz

The bulk propagation testing was also carried out using multi layered 'samples' of identical material properties. This was to demonstrate that bulk propagation would continue to occur if the material identifier was changed. The reflective coefficient was set to 0 and the transmissive coefficient to 1. The test was successful, resulting in identical behavior to the single material/ single layer case shown in the bulk propagation results.

The next test run models a perfect reflector with a transmissive coefficient of 0. The simulation does not model an entire single layer ultrasonic test. Instead, it only models a single interface propagation from an arbitrary material A to a material B. The first samples that were run used materials A and B simulating a 'perfect reflector' where the entirety of the energy encountering the material boundary. The perfect reflector would have a transmission coefficient of 0 and a reflective coefficient of 1. This simulates the exact opposite of the bulk propagation. The results demonstrated that the model was accurately simulating the physical behavior where the material changed. Plots of the results, visible in Figure 5-2 on the following page, show the simulation at notable timesteps. Going from left to right, the plots show the simulation at a simulated time of 9.5μs, 12μs, 14.75μs, 19μs, 19.5μs, and 25μs. The first plot(a) shows the input pulse fully formed and propagating in the bulk of material A. At this point, the simulation is no different from the simulation of pure bulk propagation. The second plot(b) the pulse starting to reflect at the boundary between material A and material B. The first peak of the input pulse has disappeared, as the forward traveling portion begins to destructively interfere with the reflecting portion. The extreme of that phenomenon is seen in the 3rd plot(c). Almost exactly half of the pulse has encountered the boundary, reflected and inverted. With a symmetric pulse, the interference between the pulse will create a zero deflection situation when it is exactly half reflected. The 4th plot(d) shows the fully reflected and inverted pulse propagating

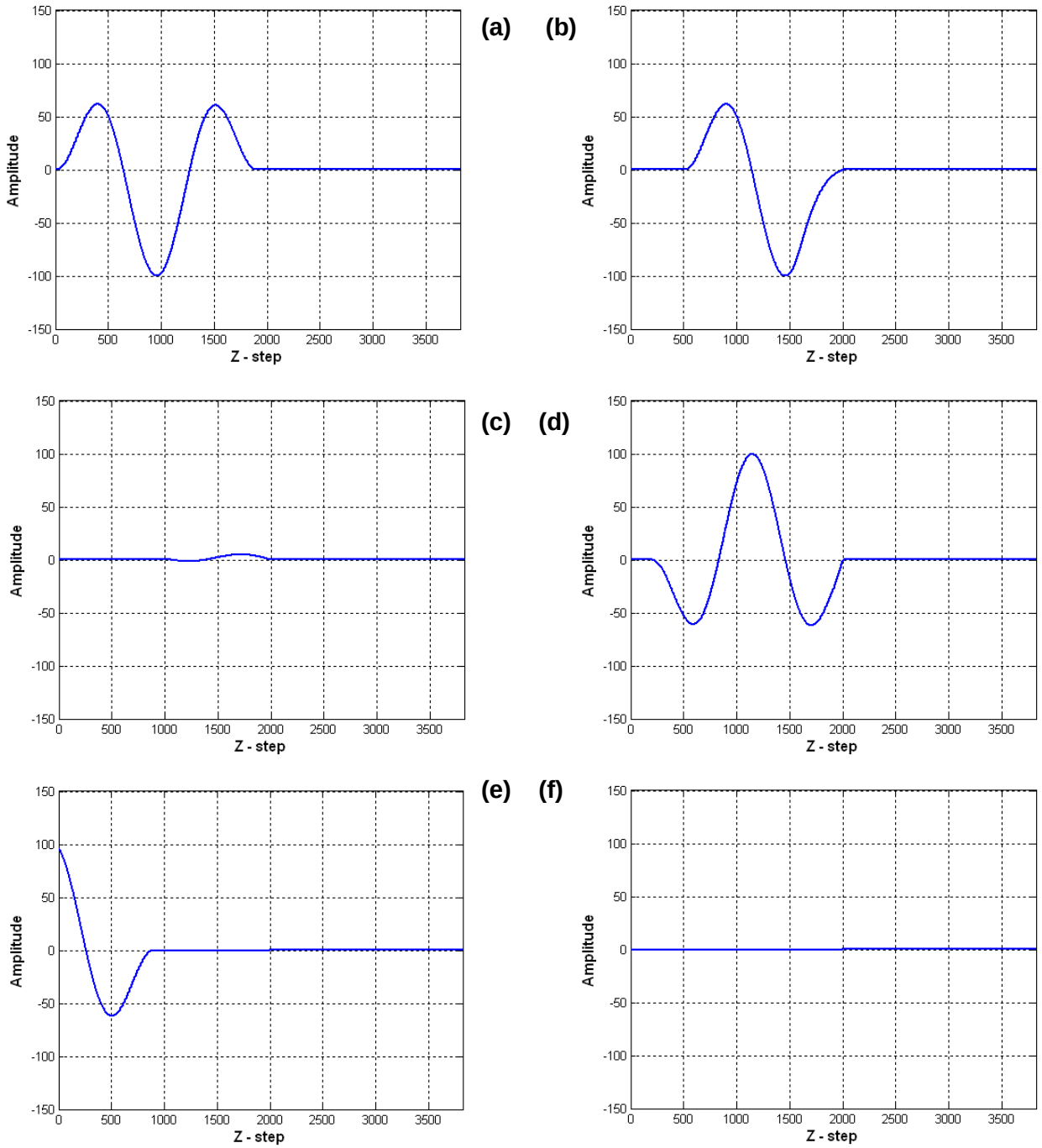

Figure 5-2 Finite difference simulation results at different time steps showing perfect reflection. Time step of 5ns and spatial step of 5μm. Input pulse of 1MHz

backwards in the bulk of material A. The pulse has fully reformed and the inversion of the pulse is clear. The 5th and 6th plots then show the pulse propagating back to infinity(e) and the solution returning to zero(f). The results show that the stability is demonstrated for the perfect reflector case. The pulse propagated properly in material A, reflected and inverted properly at the interface, and then propagated back to infinity in material A while maintaining stability and accuracy. Further, the maximum amplitude stays the same between the forward and backward (inverted) travelling pulses, and the pulse width stays the same. These expected phenomena demonstrate that the mathematical formulation of the interface behavior is accurate.

The two initial tests met the goal of demonstrating propagation across a purely transmissive boundary (the bulk propagation test) and a purely reflective boundary (the perfect reflector test). Having demonstrated the major constituent behavior, the next simulation utilizes another set of arbitrary materials A and B, but the materials do not form a perfect reflective boundary. The properties that were used for the simulation are seen in Table 5-1. The simulation was run with a layer thickness of 1mm, a spatial step of 5μm in material A and 5.5 μm in material B. The same layer configuration as the perfect reflector test was used. A single interface was simulated instead of a full single layer bounded on both sides. The simulation was run with an input pulse frequency of 1MHz with a time step of 5ns.

Material	C_{long} (m/s)	Density (kg/m^3)	Z (kg/m^2s)
A	1000	1000	$1000*10^6$
B	1100	1100	$1331*10^6$

Table 5-1 Material properties for finite difference simulation

The arbitrary material properties result in a transmissive coefficient of 0.98 and a reflective coefficient of 0.02 using Equation 2-13. Again, the results of the simulation are shown through a series of time steps in Figure 5-3.

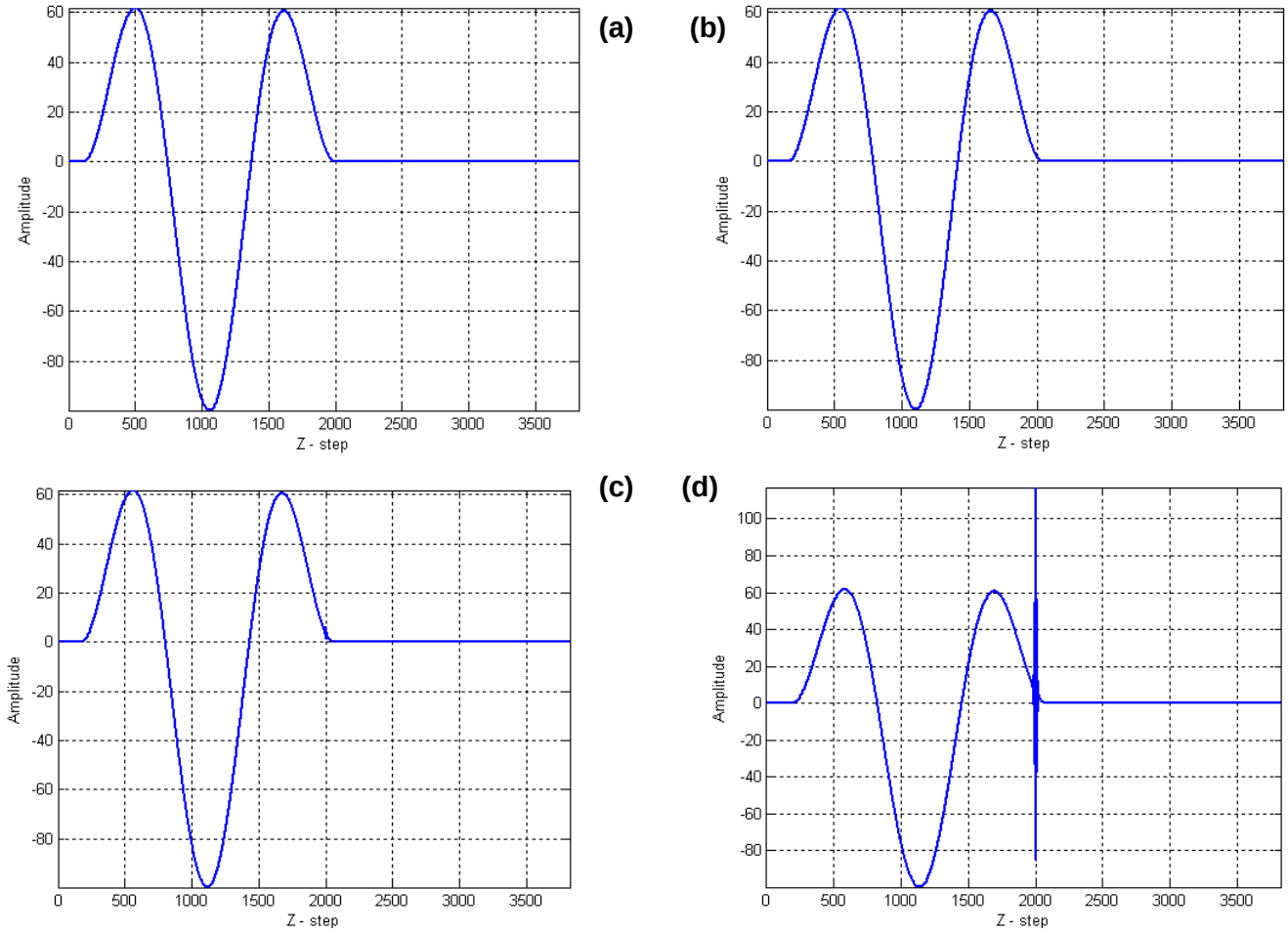

Figure 5-3 FD simulation with single reflective transmissive boundary

The results show the instabilities that were encountered with the simulation. The plots above show a series of time steps as the pulse begins to cross the material boundary. The 1st plot occurs at 10.0μs into the simulation shows the input pulse fully formed and entirely within the material A. The 2nd plot shows the material as it has just begun to cross the boundary. What is apparent in the 2nd plot is a small change in the shape of the leading edge of the pulse near the 2000th Z-step. This small change is indicative of the reflective transmissive boundary condition coming into effect. What follows however, is demonstrated in the final two plots. Within 0.1μs, the solution at the interface has begun to become unstable. This is visible as a blurring of the solution near the interface (Z-step of 2000) in. At this point, the change at the interface apparent in the 2nd plot is no longer apparent, having been masked by numerical

instability. By the last plot, Figure 5-3d, the simulation has clearly become unstable. Within 0.1μs, 20 time steps, the instability has grown to be larger than the input pulse. From this point, the instability continues to grow and envelopes the simulation. This phenomenon was found throughout a large range of testing of material properties as well as spatial and time steps and similar results were found. transmissive coefficients in the range of 0.01 to 0.99 were tested.

As discussed in the development of the model, the condition at the boundary must enforce both displacement (0^{th} derivative) and strain (1^{st} derivative) continuity. Given the instability that occurred with these settings, testing was performed to see if one of the continuity conditions was the cause. However, testing showed that the simulation produced the same results with one or both of the conditions relaxed. Attempts were also made to utilize solution smoothing techniques based on a running average algorithm to attempt to prevent the singularity from occurring. While the smoothing did serve to slow the growth of the instability in magnitude, it also caused the unstable region to grow more quickly in the spatial domain. We have not been able to determine a final cause of this problem. Notably, the simulation also demonstrated further issues to come in terms of the computational size of the simulation. The simulations presented for the three cases took between 3 and 4.5 hours when run on the Large Memory Computer (LMC) belonging to the RIT research computing department[60]. Most of the variability in simulation time being due to the multi user environment and variable processor and memory loading. When smoothing was introduced to combat the instabilities, those times increased to between 5 and 6 hours. This was for the partial version of the simulation at a rougher than intended discretization. Estimates for the whole simulation time would put it in the 96-130 hour range. However, the finite difference simulation had proven its usefulness and fulfilled the majority of its goals. The plan of work had always involved the use of a finite element simulation for reasons that are described.

5.3.4 Drawbacks

While the finite difference was useful in developing the mathematical formulation of the problem, it does not provide the level of capability necessary to completely simulate the complex propagation behavior required for modeling the experiment and the layered stacks. A number of drawbacks were encountered. Some of the drawbacks were practical while some where more theoretical.

The first, and more important, set of drawbacks comes from theoretical problems associated with the finite difference formulation of this problem. These problems prevent the finite difference from being accurately employed to model the full behavior of the experiment. The first of these was the necessary interface assumptions. To create the simulation, a mesh was first generate locating the points in both the physical and time domains at which a solution would be generated. Given the nature of the finite difference method, a node must be placed at the interface location between material layers. The solution at this node is problematic. The problem results because of the necessary boundary conditions for an accurate solution. As discussed, the solution must be continuous in both the 0^{th} and 1^{st} derivative at the boundary. Locating a node at the boundary creates a stability problem for this condition. This is because at the boundary, the node must be assumed to have both material properties. A special condition must be written to handle the solution from both sides. However, this does not truly solve the problem of the value at the boundary condition. A better solution is that employed be finite element. Using finite element, two elements are created adjacent to the boundary, allowing better continuity because the solution is not forced by the need to associate material properties with an arbitrary single point.

The second major theoretical issue with the implementation of the finite difference scheme is the implementation of viscoelasticity into the solution. This implementation is difficult partially from a mathematic standpoint, requiring the inclusion of higher time domain derivatives.

Implementation is also complicated by practical concerns with memory usage. While the implementation is possible, with examples in multiple fields[61-63], it is also quite difficult for several reasons. A thesis published in 1994 by Hayner from MIT[62] probably offers the best assessment of the problems. The thesis is entirely based on lowering the error and reoptimizing a formulation very similar to ours. The author notes that the formulation only achieves acceptable error over a low bandwidth and does not have direct applicability to low loss materials such as those in the CLiPS samples.

The same author discusses the comparative memory usage for 1D, 2D, and 3D simulations. He shows that a 2 dimensional simulation and 3 dimensional simulation require 4 and 8 times more memory than the 1 dimensional simulation. The memory usage is in fact a significant drawback to the finite difference formulation. One of the problems with modeling viscoelasticity, especially using finite difference[63] is the storage of time history. Given a large model, as in the case here, storage of a full solutional time history can become unwieldy if not entirely infeasible. The methods for the reduction in simulation size unfortunately cause secondary problems which result in the necessity of a higher number of points being used for the finite difference calculation, or a reduction in mathematical accuracy. However, simply increasing the number of nodes, and the fineness of the mesh presents separate challenges. As the numerical derivative step size decreases, the numerical derivatives have a tendency to become unstable due to the limitations of the computational precision and very small values in the denominator of the fractional derivative expression.

5.3.5 Conclusions

The finite difference simulation attempt was both successful and unsuccessful in important ways. Importantly, the finite difference simulation demonstrated both the working physics, and the problematic behavioral areas of the derived problem. It clearly demonstrated

the issues related to the simulation of the material interface, and issues with the size and speed of the resulting calculation.

These issues combined create a simulation that has proven useful for development and validation, but has limitations that prevent it being used as the sole simulation tool for this project. To attempt to find solutions to the problems, another simulation was developed using the finite element method of analysis for its basis.

5.4 Finite Element

The second method of simulation that was attempted utilized the finite element method (FEM). The FEM method allows more control over the simulation parameters and, among other benefits, allows better inclusion of the attenuative behavior expected of polymer materials. FEM, also called FEA referring to finite element analysis, is another method of numerically solving PDEs. FEA can either be used to wholly solve PDEs, or be used to render the PDE into an ODE, which can be solved either numerically, or 'exactly' so referred because of the prior numerical technique used to turn the PDE into an ODE.

5.4.1 Applicability

For the situation at hand, the finite element technique is very useful. Using finite element allows overall higher precision and more control over the numerical solution than can be implemented with finite difference. This should be no surprise, given that the history of the finite element method was for the solution of problems involving elasticity. FEA, however, is similarly or more computationally and memory intensive than the equivalent simulation run using finite difference.

The FEA technique is applicable to our problem because of the complexity of the material properties and mesh design that will go into the preprocessor. The solution is designed in a general manner to allow for a simple rewriting of the preprocessor module, responsible for

the creation of the mesh and mesh information. Such a rewriting would not affect the solution and would allow future refinement of the model to include interface effects in any manner the user wishes. In our case, finite element is further helpful because it allows for a more delicate approach to the discretization that occurs in both time and space domains. The FEA solution employed uses the FEA techniques to numerically differentiate the space domain, creating a time domain ODE that can then be more simply solved.

For the finite element implementation, a purely elastic derivation was performed and implemented, followed by work on the viscoelastic form. This was done for two reasons. First, the purely elastic behavior demonstrates proper implementation easier through a simpler implementation. This reduces the troubleshooting components and speeds the work. Second, the viscoelastic simulation builds on the derivation and implementation of the elastic simulation. Implementing the elastic first creates a set of functions that can more quickly allow the implementation of the viscoelastic form.

5.4.2 Model

We use the same operator as was used for finite difference. For the FEA derivation, the solution is created in 1 dimension over the domain of the element in Z. Again, u is a function of both location (z) and time (t) as shown in Equation 5-26.

$$-\nabla \cdot T = \rho \ddot{u}$$

$$1D\ in\ Z \in [0\ L_e]\ \ with\ u(z,t)$$

Equation 5-26 Problem definition for FEA solution.

To being, we define the stress tensor using its relationship to the strain tensor. This allows for the substitution into the equation and a definition solely in terms of u and constants. Given the 1 dimensional assumption, we define the strain tensor only in z in Equation 5-27.

$$\varepsilon_{zz} = \frac{1}{2}\left(\frac{\partial u}{\partial z} + \frac{\partial u}{\partial z}\right) = \frac{\partial u}{\partial z}$$

$$T = \mathrm{M_L}\varepsilon = \mathrm{M_L}\frac{\partial u}{\partial z}$$

Equation 5-27 Relationship between strain and stress tensor

This formulation of the stress tensor can then be substituted into the operator formulation. We can also assume that the material properties M_L and ρ are constant over the domain of the solution.

$$-\frac{\partial}{\partial z}\left(\mathrm{M_L}\frac{\partial u}{\partial z}\right) = \rho\ddot{u}$$

Equation 5-28 Wave equation formulated using strain tensor and material stiffness

From Equation 5-28, we apply a variational formulation. This creates a weak formulation of the problem and allows the implementation of the numerical scheme.

$$-\int_{\Omega} \frac{\partial}{\partial z}\left(M_L\frac{\partial u}{\partial z}\right) v\, dz = \int_{\Omega} \rho\ddot{u}\, v\, dz$$

Equation 5-29 Variational formulation of system PDE

Equation 5-29 can be further simplified, knowing that the material property, M_L, is assumed constant over the domain. This gives the leftside the form

$$-M_L \int_{\Omega} \frac{\partial}{\partial z}\left(\frac{\partial u}{\partial z}\right) v \; dz = \int_{\Omega} \rho \ddot{u}\, v \, dz$$

Equation 5-30 Variational formulation with constant properties assumption.

The variational form or functional, involves the introduction of an unknown function, v, and its derivatives. The use of the functional allows the introduction of basis functions[7], which allow the satisfaction of all boundary conditions. At this point, it is important to apply the boundary conditions on the domain.

$$T(t)|_{z=0} \cdot n = h(t) \qquad u(0,t) = u_0(t)$$

Equation 5-31 Boundary conditions on element domain.

These boundary terms allow the creation of the full functional permutation. The functional is set to 0 as the goal is the minimization of the functional over the solution domain. The entire function is multiplied by an unknown function v(t) and integration by parts is performed. A surface integral is applied to the Dirichlet[43] boundary conditions which are what is used to generate the inclusion of the h(t) term. The entire function is of the form:

$$M_L \int_0^{L_e} \frac{\partial u}{\partial z}\frac{\partial v}{\partial z} dz - vh(t) = \int_0^{L_e} v \frac{\partial^2 u}{\partial t^2} dz$$

Equation 5-32 Variational form after integration by parts.

From this form, the individual matrices can be identified. For the elastic implementation, three matrices are used. The first, a mass matrix (M) which implements the necessary inertia terms for the time domain solution. Second, a stiffness matrix (K) implements that material propagation resistance and behavior. Finally, a residual vector (R) is also created. The residual matrix implements the necessary error controls and boundary conditions. The three matrices

[7] Basis function and shape function are interchangeable terms.

are expressed using the basis function representation, and the elemental matrix notation. One must carefully note the second shape term in the Mass matrix. Given that the functional was applied to the Z dimension only, the second derivative of time (ü) is replaced with the 0^{th} derivative of the shape function because it is not differentiated with respect to the domain of the functional, z.

$$K_{ij}^{e} = M_L \int_0^{L_e} \frac{\partial \varphi_i}{\partial z} \frac{\partial \varphi_j}{\partial z} dz$$

$$M_{ij}^{e} = \rho \int_0^{L_e} \varphi_i \varphi_j \, dz$$

$$R_i^e = h(t)\varphi_i(L_e)$$

Equation 5-33 Elemental matrix equations from functional using ij notation. Superscript e denotes elemental matrices.

The matrix equations, shown in Equation 5-33, are used to create an ODE with the global matrices and vector expression of the displacement at all global nodes. The ODE reduces the dimension of the equation, creating an equation solely in the time domain.

$$M^e \ddot{U}^e + K^e U^e = R^e$$

Equation 5-34 Elemental ODE result in the time domain from finite element method deconstruction of the initial PDE

Once the formulation of the matrices and the ODE are complete, there are two remaining steps. First, the z domain must be discretized, and second we must solve the ODE. To generate the elemental and global matrices, a set of basis functions are selected. The basis functions need to be chosen carefully as they are a source of significant potential error in the simulation. For a 1D simulation, the minimum number of nodes per element is 2. While higher node elements such as 3 and 4 node elements would have given more precision within the

element, 2 node elements were used for several reasons. These include the very small nature of the elemental step size, and the reduced memory footprint. For each element, we generate an elemental mass matrix (M), and an elemental stiffness matrix (K). The later derivation will also include an elemental damping matrix (D). Each of these matrices is formed of a size nxn where n is the number of elemental nodes. Going from a 2 to a 3 node element creates a 2.25x increase in the size of each elemental matrix. A 4 node element creates a 4x increase over a 2 node. While the difference is trivial when a single element is considered, considering the global nature of the system, the size of the simulation has increased by that factor in computational memory draw. Therefore, a two node element was chosen. The resulting matrices are seen below.

$$K^e = M_L \begin{bmatrix} \int_0^{L_e} \frac{\partial \varphi_1}{\partial z}\frac{\partial \varphi_1}{\partial z}\,dz & \int_0^{L_e} \frac{\partial \varphi_1}{\partial z}\frac{\partial \varphi_2}{\partial z}\,dz \\ \int_0^{L_e} \frac{\partial \varphi_2}{\partial z}\frac{\partial \varphi_1}{\partial z}\,dz & \int_0^{L_e} \frac{\partial \varphi_2}{\partial z}\frac{\partial \varphi_2}{\partial z}\,dz \end{bmatrix}$$

$$M^e = \rho \begin{bmatrix} \int_0^{L_e} \varphi_1\varphi_1\,dz & \int_0^{L_e} \varphi_1\varphi_2\,dz \\ \int_0^{L_e} \varphi_2\varphi_1\,dz & \int_0^{L_e} \varphi_2\varphi_2\,dz \end{bmatrix}$$

$$R^e = h(t) \begin{bmatrix} \varphi_1(L_e) \\ \varphi_2(L_e) \end{bmatrix}$$

Equation 5-35 Elemental matrices in integral form.

The choice of the basis functions is driven by the same phenomenon. While optimally, the basis functions used would be of a sinusoidal form, doing so would require a numerical integration step to be performed for each entry in each matrix in each element. A total of 10 integrations in this form, and 14 in the damped form would likely cause any improvements in

memory to be traded for reductions in speed. While it is suggested in future work that higher nodal elements, and more robust basis functions, linear basis functions were used here. In a higher node element, these functions would be so called piecewise tent functions, and would not be continuous over the elemental domain. With a 2 node element they are not piece wise and are continuous. The shape functions must meet certain requirements. First, they must be equal to 1 at the elemental location of the node and 0 at all other nodal locations. The other requirement is that the sum of basis functions at all locations within the element are equal to 1.

$$\sum_{i=1}^{n} \varphi_i(z) = 1$$

Equation 5-36 Additive condition for validity of basis functions at any point x

The shape functions that were chosen to satisfy those conditions were straight lines as mentioned above. The shape functions can be seen in Equation 5-37 and Equation 5-1.

$$\varphi_1(z) = -\frac{1}{L_e}z + 1 \qquad \varphi_2(z) = \frac{1}{L_e}z$$

Equation 5-37 Linear basis functions for 2 node elements

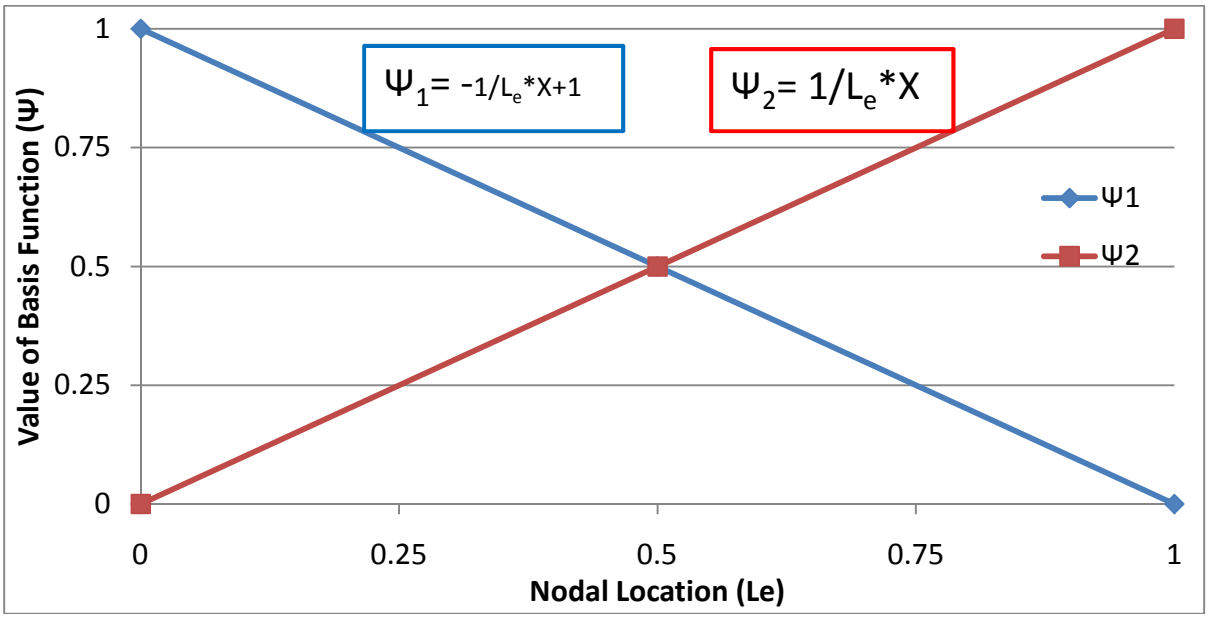

Figure 5-4Plot of basis functions over the elemental length (Le)

To use the basis functions in the Equation 5-35 integral matrices, we must also take the derivatives of the functions. The derivatives of linear functions are constants, making this simple. The resulting basis functions in integral matrix form can then be simplified significantly into the following form.

$$K^e = M_L \int_0^{L_e} \frac{1}{L_e^2} dz \begin{bmatrix} 1 & -1 \\ -1 & 1 \end{bmatrix}$$

$$M^e = \rho \begin{bmatrix} \int_0^{L_e} \left(-\frac{1}{L_e} z + 1\right)^2 dz & \int_0^{L_e} \left(-\frac{1}{L_e} x + 1\right)\left(\frac{1}{L_e} x\right) dz \\ \int_0^{L_e} \left(\frac{1}{L_e} x\right)\left(-\frac{1}{L_e} x + 1\right) dz & \int_0^{L_e} \left(\frac{1}{L_e} x\right)^2 dz \end{bmatrix}$$

$$R^e = h(t) \begin{bmatrix} \left(-\frac{1}{L_e}(L_e) + 1\right) \\ \left(\frac{1}{L_e}(L_e)\right) \end{bmatrix}$$

Equation 5-38 Shape function substituted form of elemental matrix integrations

The next step is to integrate the matrix values. For a more complicated basis function, this may need to be done numerically within the simulation. However, using the simple basis functions allows this to be done directly, manually, before the simulation. Eliminating the numerical integration within the simulation both saves computational power and reduces error by calculating an exact derivative. This is a significant benefit over calculating numerical derivatives over an already discretized function. These integrations simplify significantly, and the results allow a very simple creation of the elemental matrices.

$$K^e = \frac{M_L}{L_e} \begin{bmatrix} 1 & -1 \\ -1 & 1 \end{bmatrix} \qquad M^e = \rho L_e \begin{bmatrix} \frac{1}{3} & \frac{1}{6} \\ \frac{1}{6} & \frac{1}{3} \end{bmatrix} \qquad R^e = h(t) \begin{bmatrix} 0 \\ 1 \end{bmatrix}$$

Equation 5-39 Integrated and fully simplified elemental matrices

With the elemental matrices created, all that is necessary to fully define the ODE is to combine the elemental matrices into the global form. Given that two node elements are used, there is no need to form an elemental connectivity matrix as all nodes are shared between two adjacent except the first and last global nodes. The matrices that are formed (M, K, and D) form tridiagonal matrices. The matrices are extremely sparse. The same simplicity applies to the R vector. Because the first elemental value for all elements is zero, the global vector can be formed simply.

Once the global matrices are formed, we are left with the global form of the ODE from. A number of techniques can be used to solve the ODE. Initial attempts to use finite difference proved unstable at a variety of timesteps and input conditions. Instead, The ODE was solved directly for $\ddot{U}$, which was used to calculate $\dot{U}$, and U. However, this form required a matrix inversion to be performed on M to solve for $\ddot{U}$, seen in Equation 5-40. This presents a mathematical problem. The determination of the inverse of a tridiagonal matrix is a well-studied problem[64]. A number of algorithms to solve this problem have been developed. The issue that develops is one of singularity of the matrix. The method employed by Matlab to form matrix inverses does not handle this phenomenon well. Instead, the linsolve command, is used to solve the linear system without forming the inversion of M. The linsolve command within the Matlab implementation uses LU decomposition and forms a more accurate solution for $\ddot{U}$.

$$\ddot{U} = M^{-1}(KU - R)$$

Equation 5-40 Solution for d^2U/dt^2 in matrix form

$$M\ddot{U} = KU - R$$

Equation 5-41 Linear system form of Equation 5-40. Solved in implementation.

The issues that arose with the implementation of the FEA model will be addressed in section 5.4.3. However, they made an implementation of the damping matrix and the more

complex polymer properties implausible at this time. Despite not being implements, the derivation of the model was performed, and is shown in appendix A.1

5.4.3 Results

For testing, the same procedures as used in the FD results were employed. First, correct bulk propagation was demonstrated, followed by perfect reflection and then a non perfect reflector single boundary simulation. Unlike the FD simulation, the solution was found to model the expected behavior at the material interface without becoming numerically unstable and asymptotic. However, the solution was found to have a relatively narrow range in which this stable behavior occurred. Our determination is that the stable range resulted from adjustment of the ratio of step size in the time domain to step size in the spatial domain. Nominally, the spatial step would be related to the time step using the speed of sound using Equation 5-42. However, testing found that the solution was most stable at a spatial step of approximately 1/20th of that calculated using Equation 5-42.

$$\Delta z = c_{long}\Delta t$$

Equation 5-42 Base stable relation for spatial and time domain discretization

The required time stepping for stability drove decisions on the selection of spatial steps and time steps, the material properties were chosen to match, match in this case meaning minimize the size of the simulation's memory footprint, attempt to limit the time of simulation, and to provide simulative results as close as possible to the experimental case. To do so, a input pulse of 5MHz with a time step of .4ns and a z step of 30nm was used for all simulations. Again, arbitrary material properties were found necessary for stability and speed.

Because the testing was redundant, only two cases are shown. The bulk simulation case is shown to demonstrate the differences and benefits of the FEA simulation. While the perfect reflector and single interface test are not shown, they both proved successful as

mentioned earlier. The second simulation that is shown is more representative of the actual experiment that was run, and more comparable to the experimental results achieved. The second simulation is a full single layer simulation in an infinite material.

For the bulk simulation, a similar method of visualizing the results is used. On the next page, in Figure 5-5, plots show the simulation at 6 time steps. The simulation is visible in the plots as it begins to form the input pulse (a), forms the major peak(b), forms the entire peak(c), propagates the peak(d), and then absorbs the pulse (e), and finally returns to a zero(f). The simulation performs much like the results obtained from the FD model. However, it should be noted, that the FEA simulation performs this task with a total of 41 nodes and 40 elements. Identical material properties were used to that of the FD bulk propagation. A similar level of accuracy in the FD simulation required approximately an order of magnitude higher discretization density.

This is possible because in the FEA simulation, the entire solution for a given time step is solved at once. In the FD simulation, each node is solved for individually at each time step. The FEA time step solution is determined from the ODE that was formed using the variational formulation from the PDE. This solution causes the cumulative error to propagate much more quickly through the simulation. In our implementation, time step ODE is solved by forming a system of ODEs to reduce the 2nd order ODE into a first order ODE which can be solved directly using matrix manipulation. Equation 5-41 is changed to the form below and solved for U.

$$\begin{pmatrix} \dot{U} \\ \ddot{U} \end{pmatrix} = \begin{bmatrix} 0 & I \\ KM^{-1} & 0 \end{bmatrix} \begin{pmatrix} U \\ \dot{U} \end{pmatrix} - \begin{pmatrix} 0 \\ RM^{-1} \end{pmatrix}$$

Equation 5-43 System of ODEs for formed from variational form of PDE

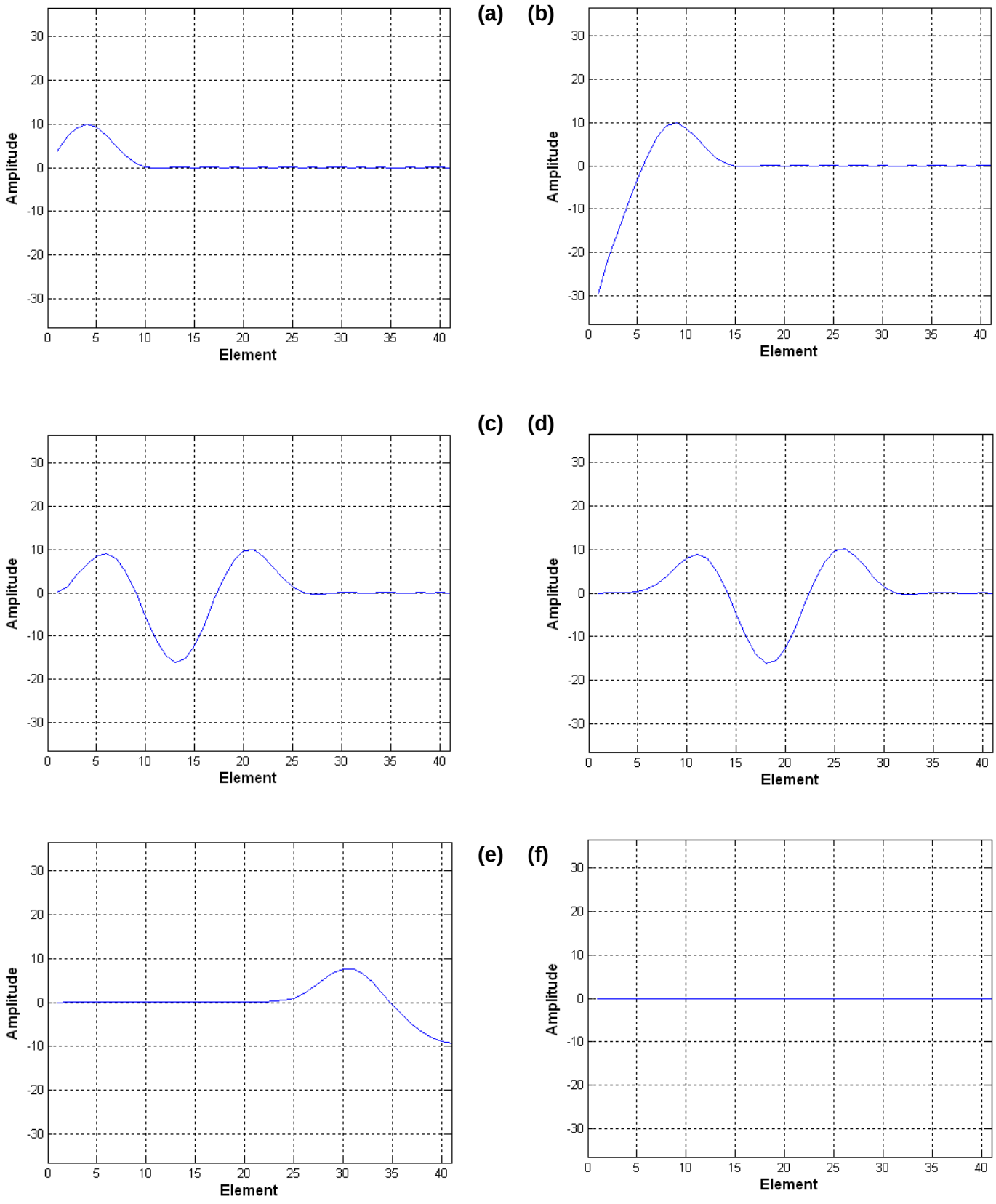

Figure 5-5 Results at specific time steps from FEA simulation of bulk propagation.

Once the initial model testing was complete, the full single layer simulation was used to demonstrate the simulation and its relation to the experimental work. The simulations were run using an [A B A] material setup to simulate a single layer of a material in a bath of infinite couplant. The layer thicknesses used were 3mm for both A material layers, and 1mm for the B layer. The material properties were as follows. The properties used where chosen to allow manual spot checking of calculations and solution tracking. They do not represent real material properties and, like in the FD simulation, are intended to validate the underlying equations.

Material	C_{long} (m/s)	P (kg/m^3)	M_L (GPa)	Z (kg/m^{2}s)
A	1000	10	1	100*10^3
B	1500	15	2	337.5*10^3

Table 5-2 Material properties for full single layer simulation

This will create a reflective coefficient of 0.295 and a transmissive coefficient of 0.705. To present the results, the time history at a single element is plotted first. This shows the simulated A scan created with the model. It is visible in Figure 5-6. In the simulated A scan, three peaks are visible. The first, largest, peak is the input pulse propagating towards the sample. The second and third peaks are formed by reflections off the front and back surface of the sample respectively. This A scan demonstrates to simulation of all major phenomena. The rest of the simulation is demonstrated via time step plots of the solution on the following pages.

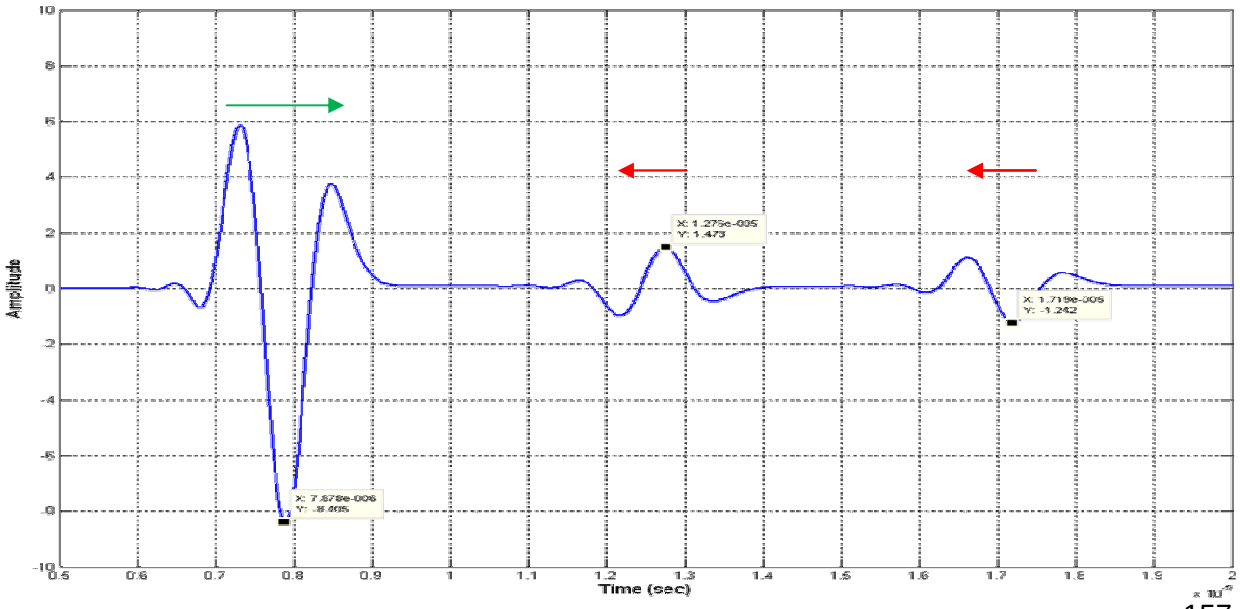

5-6 Time history of FEA solution at single node

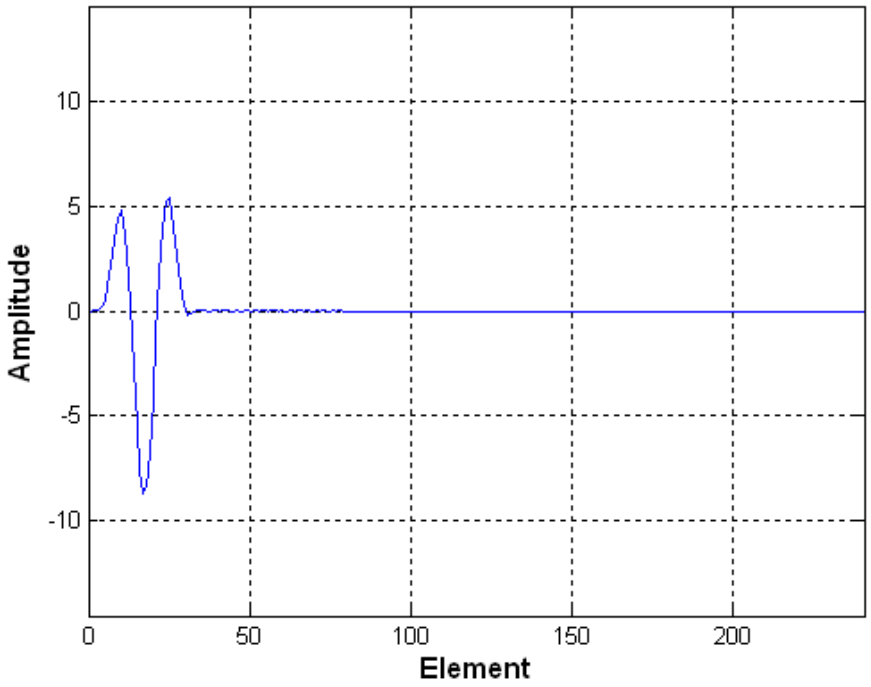

Figure 5-7 FEA single layer simulation. Solution shown at single time step

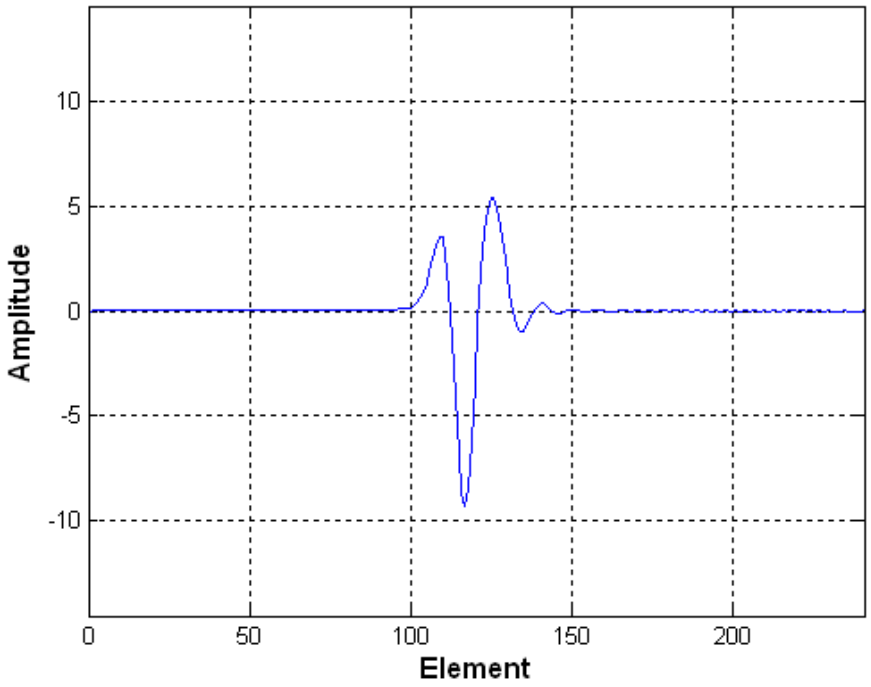

Figure 5-8 FEA single layer simulation. Solution shown at single time step

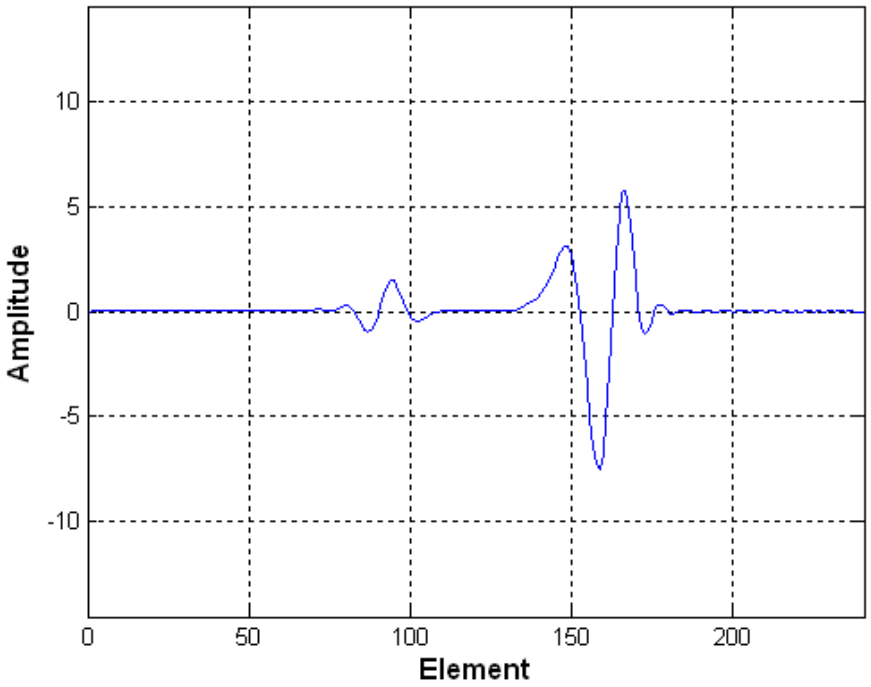

Figure 5-9 FEA single layer simulation. Solution shown at single time step

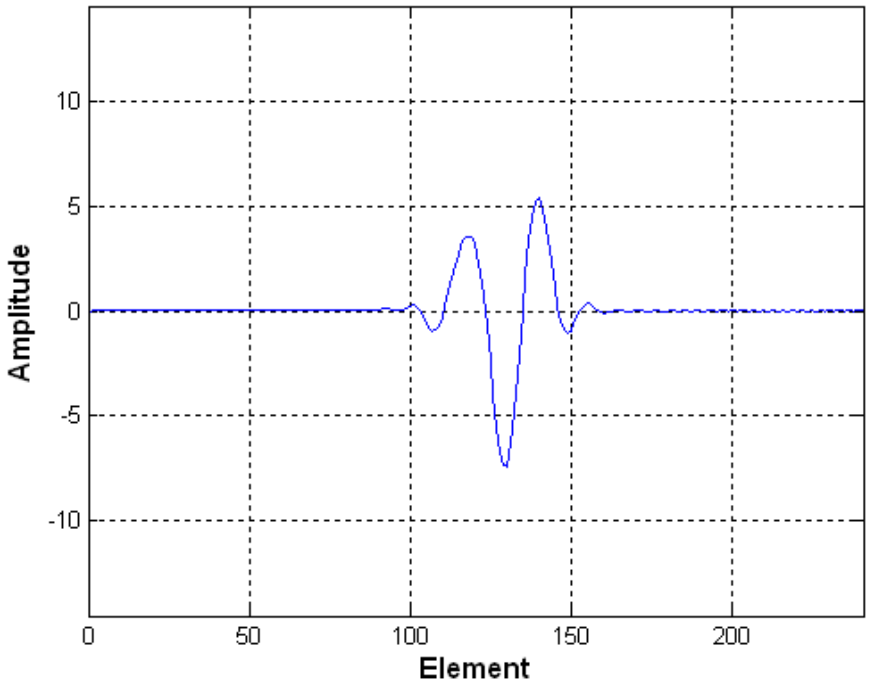

Figure 5-10 FEA single layer simulation. Solution shown at single time step

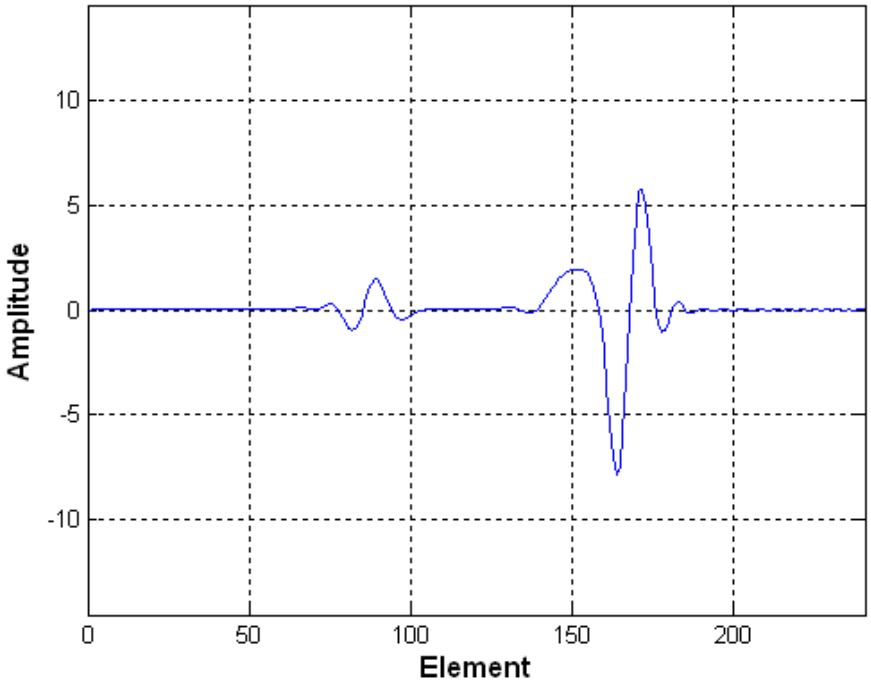

Figure 5-7 FEA single layer simulation. Solution shown at single time step

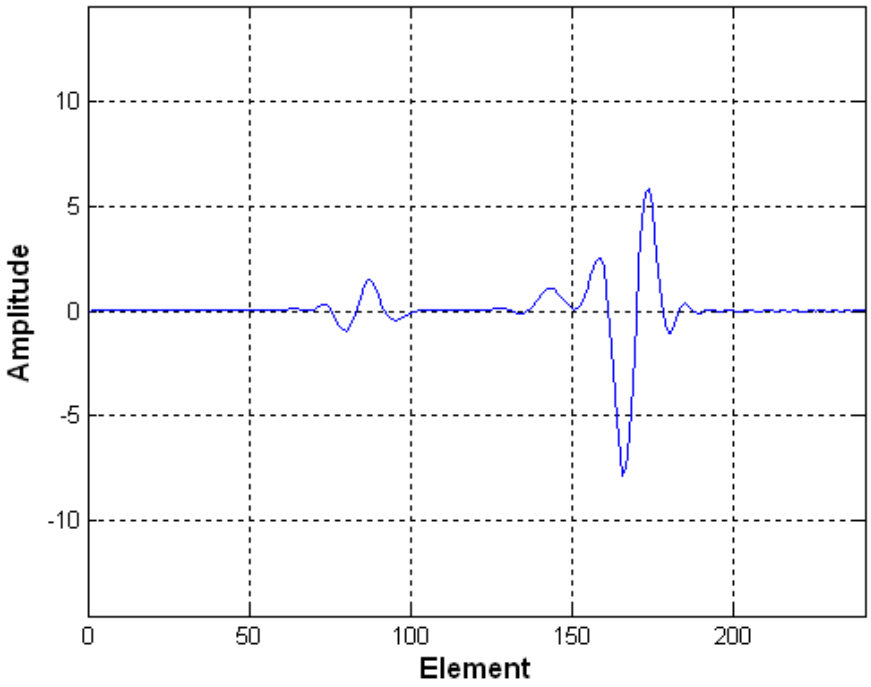

Figure 5-8 FEA single layer simulation. Solution shown at single time step

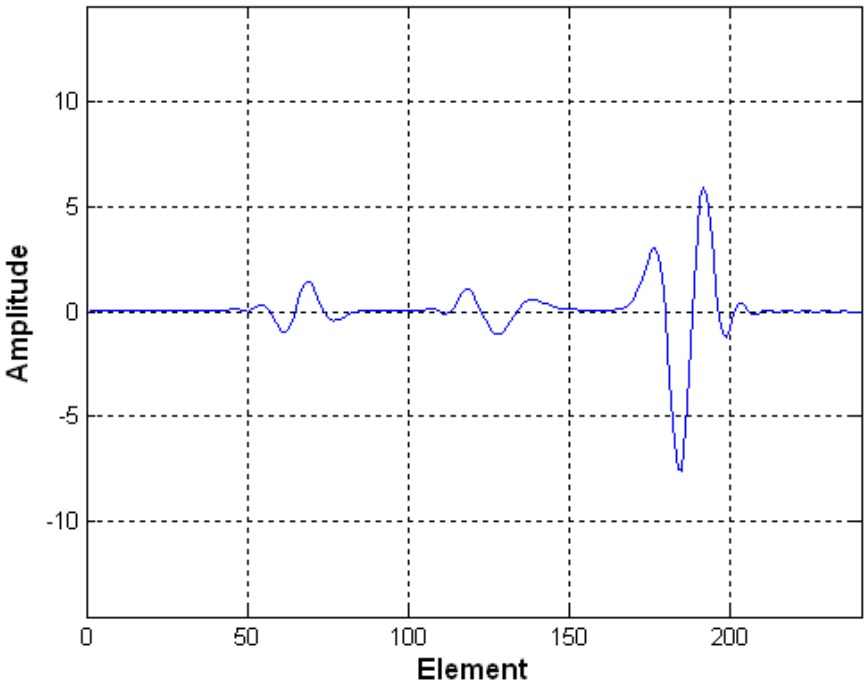

Figure 5-9 FEA single layer simulation. Solution shown at single time step

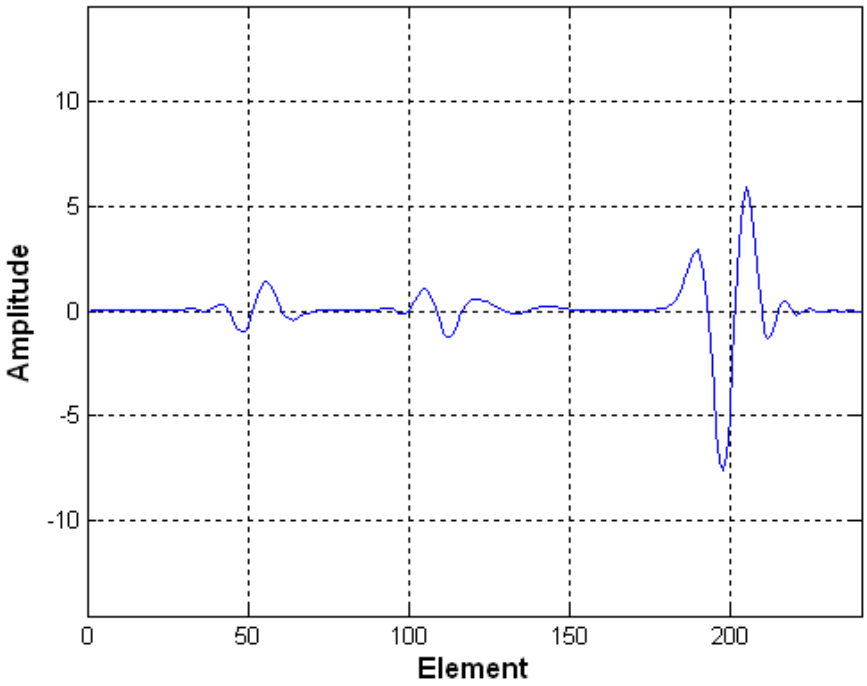

Figure 5-10 FEA single layer simulation. Solution shown at single time step

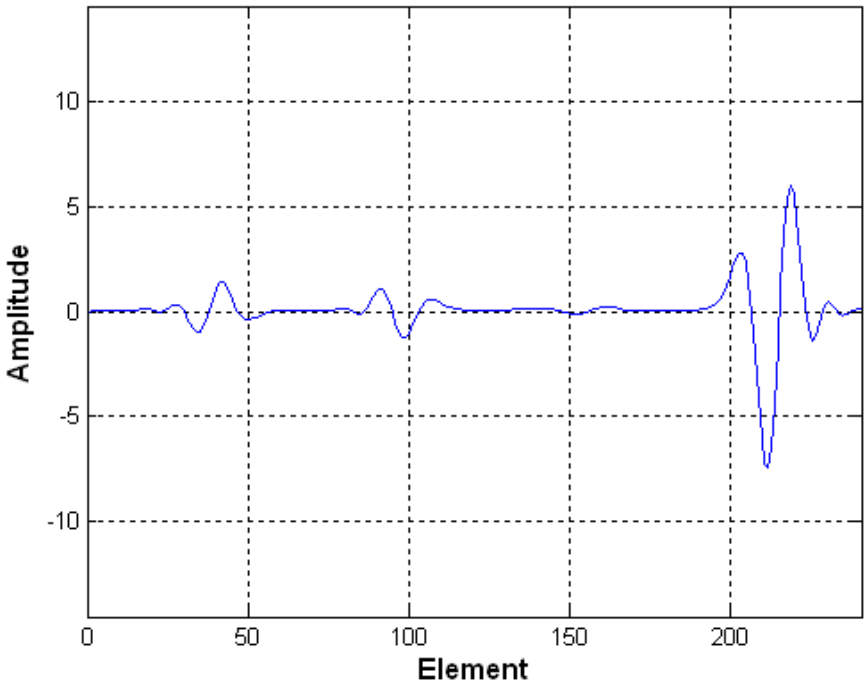

Figure 5-11 FEA single layer simulation. Solution shown at single time step

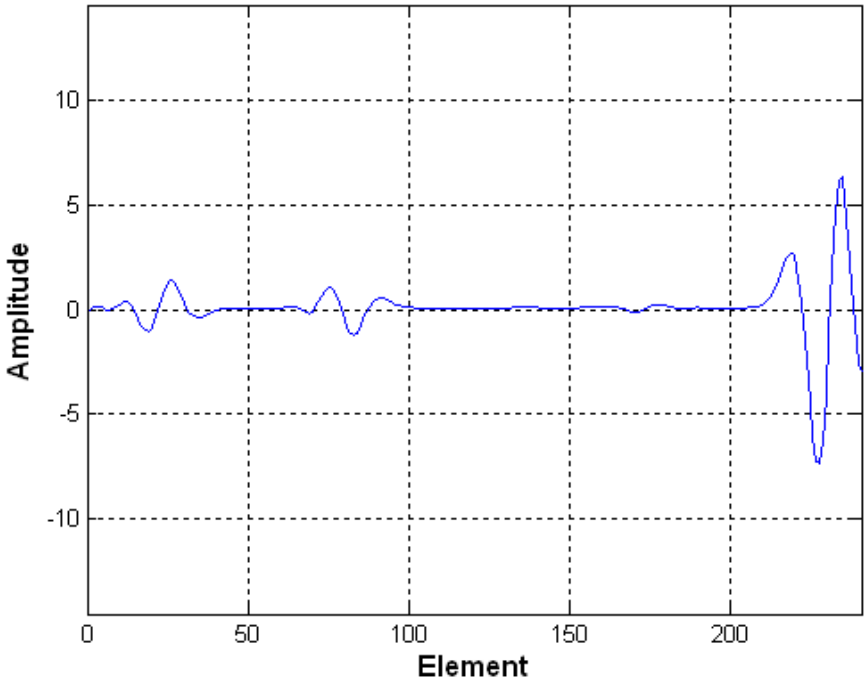

Figure 5-12 FEA single layer simulation. Solution shown at single time step

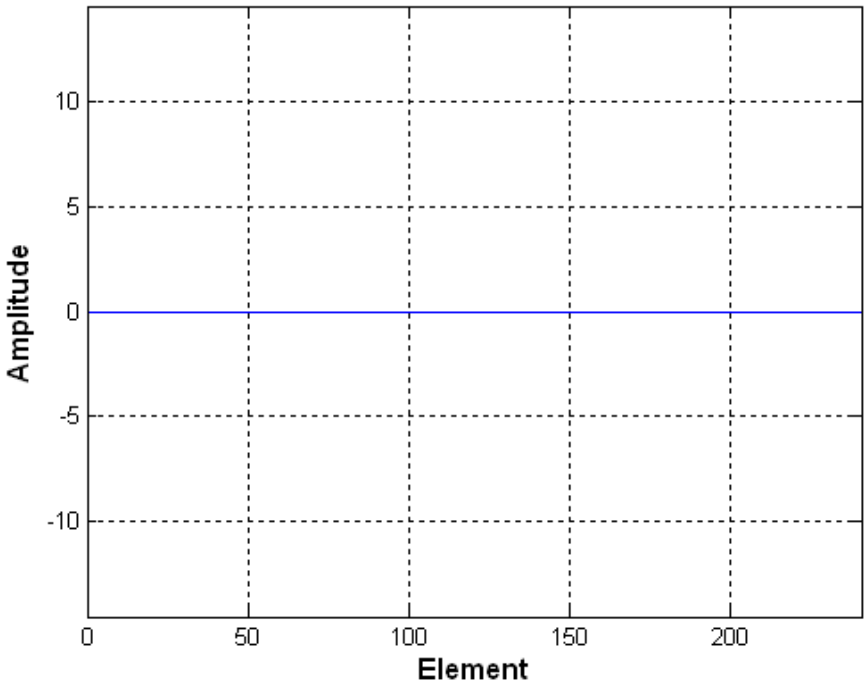

Figure 5-13 FEA single layer simulation. Solution shown at single time step

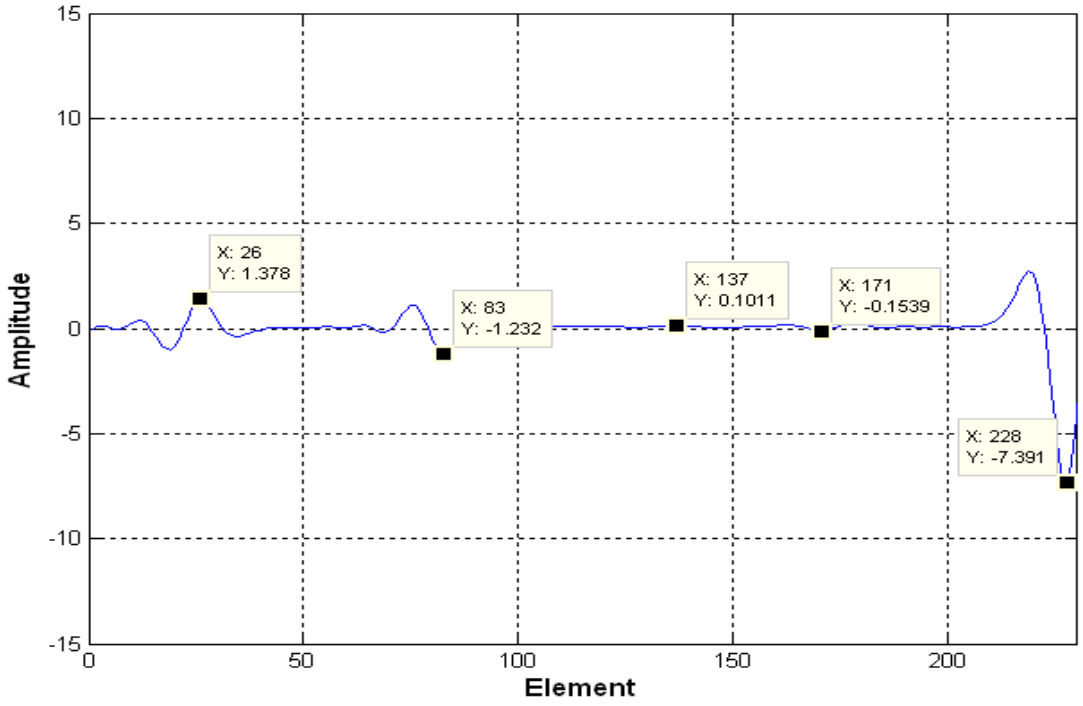

Figure 5-14 Solution at single time step with multiple reflections labeled.

The plots in Figure 5- through Figure 5-13 show the full single layer simulation achieved. They demonstrate the input pulse propagating through the front and back surface as reflective transmissive boundary conditions. They also show the secondary reflections that occur within the layer due to the back surface reflection. The peaks themselves are labeled in Figure 5-14. The labeled peaks in Figure 5-14 show, from left to right, the front surface reflection, the back surface reflection, the 4^{th} reflection, the 3^{rd} reflection, and the remaining energy of the input pulse. The 3^{rd} reflection is formed when the back surface reflection crosses the front surface, and the 4^{th} reflection forms from the 3^{rd} reflection crossing the back surface. This phenomenon actually serves to further validate the simulation, showing multiple internal reflections as would be expected. These plots demonstrate that the solution is viable, and that with increased computing power, and improvements in stability, it can achieve the goals intended. The suggestions for future work are discussed in Chapter 6.

5.4.4 Drawbacks

The FEA simulation effectively modeled wave propagation in simple cases. However, the system requirements necessary to create a full and accurate model were not effectively and timely available. The main simulational issues that arose were stability and numerical accuracy. Related to these issues were the number of elements in the simulation and the required number of mathematical operations to solve. These combined to cause a simulation with a large memory footprint, and necessity for significant computational power. As such, secondary resources were pursued to try and maximize simulation capability. The research computing center at RIT[60] provided access to their 'large memory computer'. This was necessary because of the level of discretization that was necessary to accurately simulate.

The simulation size, and the necessary memory and computing power, are drawn from the simulation parameters. The base simulation parameter for our work was the input ultrasonic pulse. The frequency used experimentally was 5MHz ($5*10^6$HZ). The time step in the simulation must be selected to minimize error generated in the input pulse. Any error generated in the input pulse will be reflected (and magnified) by the simulation itself. The time step also dictates the spatial elemental length throughout the simulation. For numerical stability, the wave must propagate as close to 1 spatial node as possible per time step. The relationship used for determining elemental lengths, and a discussion on the error propagation is found in Chertov[27].

For the generation of the time step itself, a study was carried out on the relative error created by different levels of discretization of the input pulse. A visualization of the results is seen in Figure 5-19. What is shown is a comparison of different choices of discretization for a single cycle of an arbitrary sin wave. An initial approximation of 10 steps for each cycle was used. This would generate a time step of one order of magnitude less than the frequency of the

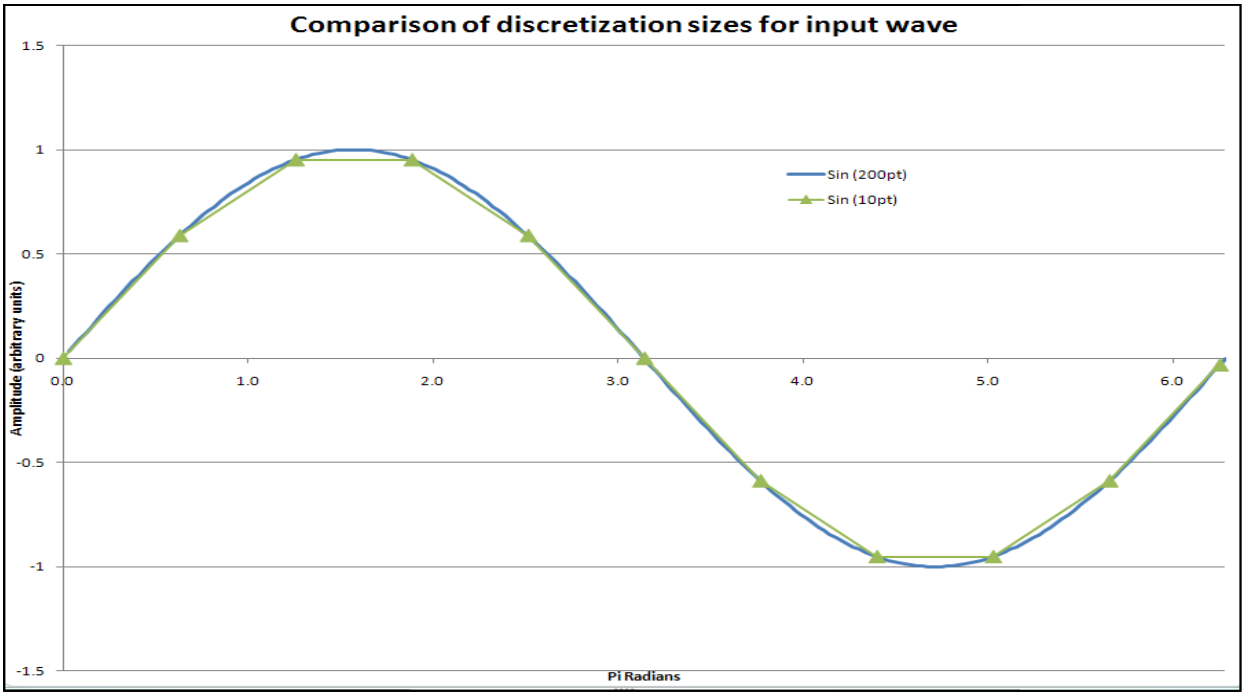

Figure 5-15 Visualization of discretization error for 10 and 200 pt per cycle discretizations of a single sine wave period.

pulse, a standard starting point. The error created by this level of discretization are clear from the figure. A final solution was developed of using a 200 step discretization. This can also be seen plotted versus the 10 step method.

To compare the relative amount of error, the integrals of the different discretizations were computed. The exact integral over a 2π interval is zero, however for the 10 step discretization, the integral value was calculated to be -0.00014 using the trapezoid rule between points. The 200 step returned a numerical integral of $9.5*10^{-16}$, a significant improvement of error. Simulations were taken forward with a use of 200 step/cycle discretization. With this discretization, a 50MHz pulse with a 20nsec period will use a time step of 0.1ns. Using the known relation for stability, $\Delta z = c\Delta t$, this will generate a z step of approximately 0.22μm for PC, 0.275μm for PMMA, and 0.15μm for water. However, these step sizes often showed themselves to be incompatible with a stable solution. This is due partially to a step size, which is at the maximum potentially stable level. While this level of discretization is potentially stable, and has the potential for low error as Chertov[27] demonstrated, they rely on approximating a larger domain as a linear function. This is the negative impact of the computational power reduction that the linear functions create.

The elimination of the numerical integration requirements comes at the cost of a linear assumption within the elements. This is something that can be combated with a smaller spatial domain step. However, this restarts the tradeoff between memory requirements, computational power, and computational accuracy. It was determined that for the specific application, increased memory usage from a finer discretization step would be an acceptable tradeoff to reduce the processor power required to perform significant numbers of integrations for the population of the elemental matrices. For a 2 node formulation, the full simulation would generate three 2 by 2 matrices, and one 2 entry vector for each element. Cumulatively, this requires the performance of 14 numerical integrations for each individual element. It was

demonstrated that utilization of the more complex basis functions required computational power beyond what was available. Despite the drawbacks, which prevented a full simulation from being performed, significant basic results were obtained from the finite element model.

5.4.5 Conclusions

Having demonstrated the ability to simulate a single layer sample of arbitrary properties, we can conclude that we have successfully developed a simulation that has the capability of modeling the experiment performed in chapter 4. Despite the drawbacks from the simulation as it stands now are outweighed by the successes in formulating a stable solution to the wave equation for our case.

The drawbacks all relate to the size of the simulation and the computational power. The simulation would benefit in terms of accuracy from two improvements. First, the utilization of more robust basis functions, such as a sine wave or parabola. This would allow higher accuracy within the element and improve overall accuracy. The second improvement would be to run at a higher spatial element density.

Unfortunately, these two changes were shown to induce instability into the simulation over several different attempts. They would also significantly increase in simulation time. The single layer simulations took between 5 and 9 hours, averaging approximately 7.4hrs. For the full simulation case, simulating multiple layers at the 50MHz frequency, with viscoelasticity, and a higher layer thickness is projected to take between 72 and 96 hours utilizing the research computing LMC. This becomes a larger issue as the simulation is developed for the extraction of the complex moduli. With the complex moduli as the inputs, the simulation is run with varying complex moduli to determine a best fit solution to the experimental data. With each iteration of the input properties requiring a complete run of the simulation, the use of the FEA simulation as an analytical technique may be limited.

Chapter 6

Conclusions and Recommendations for Future Work

With the experimental and theoretical work performed, we have been able to determine a significant number of important pieces of useful information regarding the mechanical characterization of the multilayered polymer stacks manufactured at CLiPS. We have fully completed 2 of the 3 major research goals, and have had some success and some failures with the third.

The first part of this work was the experimental ultrasonic testing that was carried out. With the ultrasonic testing, we have been able to look at the properties of the bulk material and the individual layers within the same test. This provides a significant benefit in terms of time involved with testing. Using the ultrasonic testing, we have demonstrated the capability of measuring certain properties of the stacks. With the single layer samples, we have demonstrated the ability to measure the speed of sound and the attenuation. We have further, utilized those two properties to determine the complex moduli of the layers. For both single layer polymers, we have achieved results within the expected realm. For the PMMA, we demonstrated the expected higher level of attenuation that is attributable to the side radicals in PMMA that represent a structural difference in the chain configuration between PMMA and the PC. As mentioned in the experimental results, the differences between the values we measured, and published results for the tested polymers, and our measured results are in line with expected frequency based variation using a mechanism similar to the time temperature superposition. As future work, we do suggest validation of the superposition curves using temperature controlled DMA.

By demonstrating the ability to measure complex moduli, we have also demonstrated the use of work by Jarlath[26] to some cases where the delay between the front and back reflected

pulses is either negligible or negative. This extends at least some experimental analysis techniques for ultrasound data to situations where the ultrasonic pulse is longer than the thickness of the material. For our case, this is beneficial for two reasons. The first is that it allows characterization in ever-smaller layers. Traditionally, characterization of a thinner layer would require the use of a higher frequency transducer. We have demonstrated that in some cases, this is not necessary. The second reason it is beneficial is that it opens the potential to study the interphase more fully using ultrasound. If the model of Liu[5] is valid, the model for multilayer mechanical properties must include some representation of the interphase region, which has been shown[5],[9],[65] to be thinner than the layers used in the sample tested in our work. The other notable conclusion we can draw from the single layer results, is that the FFT spectrums are unlikely to be a viable quantitative analysis technique when reflected delays are small. We have not determined a method to utilize the spectra for the determination of attenuation, partially due to the inability to accurately separate the front and back reflected pulses.

For the multilayer case, we have had important successes as well. A scans from the multilayered samples though, are more complicated and cannot be directly analyzed as discussed in chapter 4. This was expected, and is the reason the simulation was pursued. In the multilayer sample testing, we have demonstrated the ability in the two-layer case to determine a bulk speed of sound, and the speed of sound in individual layers. We have also demonstrated that the speed of sound measured in single layer materials is comparable to those materials when used in multilayer stacks.

This was done using only the bulk sample thickness. We have also been unable to determine the attenuation within the multi layer materials. The generalized formula for attenuation presented in Equation 4-6 from Chen[55] was applied successfully to a zero delay case during single layer testing. However, the application did not prove successful. When

applied to the two layer case, the resulting values were well outside the expected range. The formulation was not applied to the 4 layer case due to the lack of an ability to accurately determine peak locations and magnitudes. In both cases, this shows the limitations of the zero delay cases. While we were able to use Jarlath when testing single layers, we did not achieve those results in the 2 layer case. Unfortunately, the extension of Jarlath appears limited. The 2-layer case demonstrated that even when the peaks are identifiable, utilization of the magnitude of the peaks may not be possible. We can conclude this is due to the combination of low reflective coefficients created at a boundary between PC and PMMA, and due to the internal interference created by the multiple reflections. As shown in the results, we were not able to determine the attenuation of the layers in the multilayer samples from the experimental results.

The internal interference phenomenon was more notable in the 4 layer case. In the four-layer case, it is nearly impossible to accurately determine the location of the internal peaks. This is especially notable in the area where we would expect to find the second peak. At that location, there is a absolute magnitude minima. This is an area of destructive interference, and represents the problem with using the time domain analysis to determine attenuation through comparison of peak magnitude. The phenomena limiting interpretation is unavoidable at these frequencies. We do not suggest further work on direct analysis of the A scans of multilayered samples. We believe that the analytical work done on the A scans to date has demonstrated the reasoning behind the goal of the simulation to replicate the experiment. As explained in chapter1, creating a simulation with known inputs that can be checked comparatively against experimental results, direct analysis of the ultrasonic returns can be minimized.

For the FFTs of the multilayer sample, we conclude that there are identifiable phenomena within the spectra measured. However, at this point, we have only been able to observe qualititative phenomenon. From the experimental work, we do recommend further on the analysis of the FFTs. The periodicity and other phenomena appear to contain yet

unaccessed information useful for mechanical characterization. If a method for determination of properties from the FFTs could be developed, it would be useful in allowing inline, quick, determination of internal properties. It would also likely allow the automation of the procedure, something would be viable due to the more pronounce and identifiable peaks of the FFT compared with the barely identifiable peaks in the A scan.

While we have seen the capabilities of the ultrasonic testing, and have suggested areas of future work, there are mechanical limitations on the resolution of ultrasound. With the 50MHz transducer, the pulse length is 83μm in PMMA and 67 μm in PC. This is within the realm in which we can interrogate properties. However, as the layer thicknesses decrease, a much higher frequency must be used. Current CLiPS state of the art is approximately 50nm[5] with goals nearer to 5nm. If we follow the frequency curve in both PMMA and PC, we can see the potential resolution using ultrasound in both materials. As the frequency goes into the GHz range, it is possible to extend this into the low and sub micron range. However, to extend resolution to the 50nm range, a frequency of 82GHz in PMMA and 66GHz in PC is required.

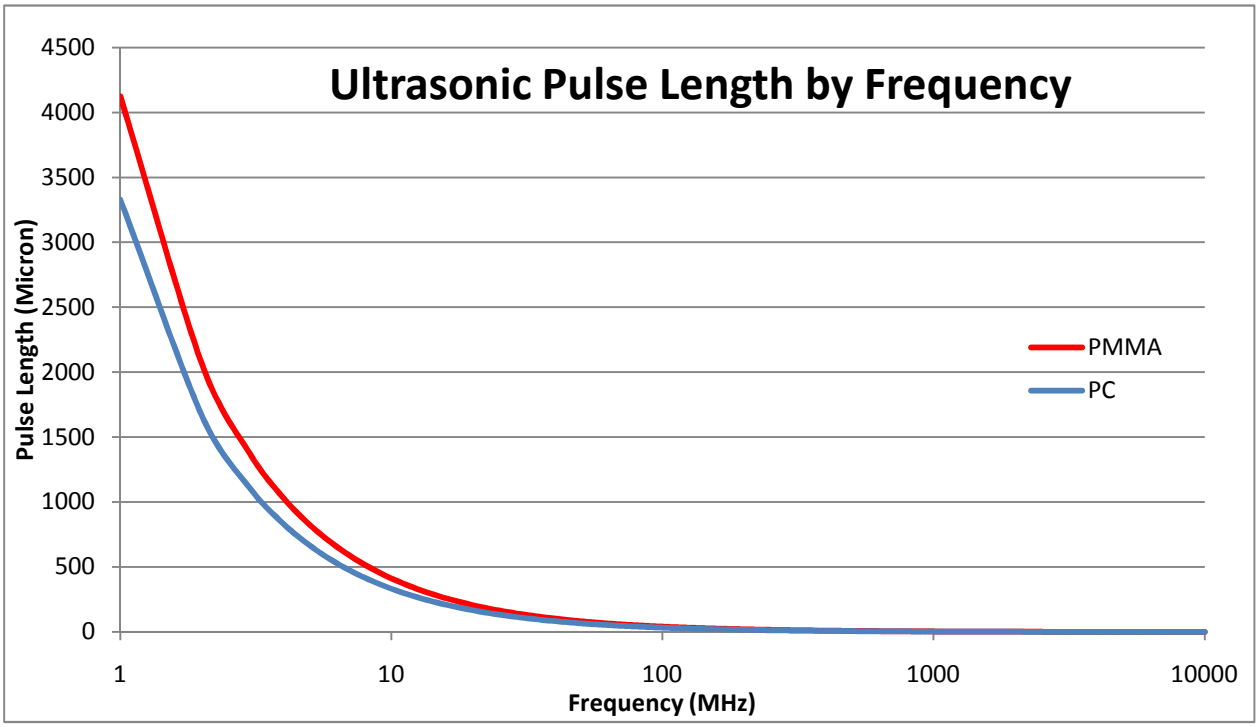

Figure 6-1 Frequency wavelength curves

The interphase dimensions found by Liu[5] is in the range of 12nm. This would require even higher frequencies, in the realm of 250GHz. These frequencies are not practical in normal ultrasonic testing. As such, other methods of analyzing the signals gathered using the available, lower frequency, techniques were pursued. This was in the form of a simulation of the lower frequency experiments. This was demonstrated, and is suggested for future work as a theoretical improvement on the available technology.

As discussed in the goals and objectives, work on a simulation of the ultrasonic experiments was carried on in parallel to the data collection and analysis. The goal is to develop a system of comparatively analyzing the experimental A scans in a manner similar to that employed when ultrasound is used in non destructive evaluation. For this case, we employed two simulations, a finite difference (FD) simulation was used first, and a finite element analysis (FEA) simulation. We demonstrated using the FD simulation that we could mathematically represent the different phenomenon involved in non-attenuative propagation. However, we also demonstrated the limitations and problems in terms of stability and simulation size. With the FD simulation, we demonstrated the ability to discretized the simulation of bulk propagation and reflection. The FD simulation did not successfully demonstrate reflection and transmission though. This phenomenon was not demonstrated due to the numerical instabilities. The numerical instabilities are the basis of our conclusions regarding the FD simulation. The FD simulation was useful in demonstrating the phenomena, using a simpler formulation, and simpler implementation. However, the simulation also showed through testing that stability and time of simulation were both extremely dependant on the step size in the discretization scheme. Varying the step size proved extremely critical. This was a critical learning for the FEA simulation, and led to the conclusion that finding a fully stable point was unlikely. Despite producing useful results, we believe the FEA provides superior capabilities and do not suggest further work on the FD simulation. The FD simulation was intended to

provide a simpler implementation of the problem, and demonstrate the basic behavior of the solution. It was successful in doing so. The FEA simulation provides further capabilities and was intended to be the focus of work.

The FEA simulation proved more successful than the FD work. With the FEA simulation, we were able to stably demonstrate all phenomenon expected for the simulation. This was demonstrated in chapter 5. Like the FD simulation, there was a range in which the simulation was less stable. Unlike the FD simulation, there was a truly stable range. Within the stable range, we demonstrated the ability of the simulation to replicate an A scan and can conclude it can be a useful tool for future work replicating the experiment. We have demonstrated the case for small-scale simulations using basic material properties and lower frequency inputs than the experimental work. This partially meets our goal. We conclude that the simulation is viable, and can likely be developed into an effective tool for analysis of the returned A scans. However, the simulation is the focus of our future work. This is partially because we have been unable to entirely meet our goal of developing a full simulation of the experiment, and partially because going forward, we still believe it to be the most viable technique for analysis of the complicated ultrasonic returns generated experimentally.

The first focus of ongoing work for the simulation should be on implementation of the viscoelastic model. The viscoelastic model was not implemented due to limitation of computational resources and the lack of a significant stable range of inputs. Not implementing the solution also allowed more, and more efficient, implementation testing to be carried out. Testing of the simulation for stability and run time was able to be performed more quickly without the inclusion of the viscoelastic component. The viscoelastic derivation is detailed in appendix A.

The other focuses of continued work to improve the simulation include incorporation of the interphase, utilization of more accurate and flexible basis functions, and improvements in the memory footprint and speed of the simulation. These three items are to some extend interrelated. All three items relate to the length of time the simulation takes to run. The inclusion of the interphase would allow a more complete simulation, but a decision would need to be made on which model to implement. Several interphase models[5],[9],[45] have been proposed, and the selection of which model is implemented. The selection of model will have a significant impact of the simulation time. A model selection will need to be based on a tradeoff between impact on simulation time and accuracy of results. We suggest further evaluation of the impact of the models on the overall simulation before implementation. We also suggest further work on the basis functions. The functions used, linear intra element approximation, are sufficient, the utilization of sine or parabola functions will improve accuracy and likely have a positive impact on time of simulation as well. The improvement will be indirect, coming from a reduction in the number of time and spatial steps required for equal accuracy. This leads to the last suggested focus of work going forward. The code as it stands is sufficient, accurately simulates the required phenomena. However, improvements in computational efficiency and memory are suggested, and may be necessary, to allow the full use of the simulation.

Despite the suggestions for continued work, we have achieved significant progress in the mechanical characterization of the CLiPS polymer systems. We have achieved the baseline work that helps to generate a plan forward and enables future advances in the intralayer and bulk characterization necessary for many of the uses proposed for these novel materials. We have fully completed our experimental goals, and have provided a significant theoretical basis for future work on an improvement of the present state of the simulation. Any opinions, findings, and conclusions expressed in this material are those of the author and do not necessarily reflect the views of the National Science Foundation

References

[1] Kenneth D. Singer, Tomasz Kazmierczak, Joseph Lott, Hyunmin Song, Yeheng Wu, James Andres, Eric Baer, Anne hiltner, and Christopher Weder., "Melt-processed all-polymer distributed Bragg reflector laser.," *optics Express*, vol. 16, Jan. 2008.

[2] E. Baer and A. Hiltner, "Forced assembly of layered polymers," Cincinnati, OH, United states: Society of Plastics Engineers, 2007, p. 1738.

[3] "Center for Layered Polymeric Systems - Home," Jan. 2010.

[4] National Science Foundation, "Award#0423914 - NSF Center for Layered Polymeric Systems," Jan. 2010.

[5] R.Y.F. Liu, A.P. Ranade, H.P. Wang, T.E. Bernal-Lara, A. Hiltner, and E. Baer, "Forced Assembly of Polymer Nanolayers Thinner Than the Interphase," *Macromolecules*, vol. 38, Dec. 2005, pp. 10721-10727.

[6] H. Wang, J.K. Keum, A. Hiltner, E. Baer, B. Freeman, A. Rozanski, and A. Galeski, "Confined Crystallization of Polyethylene Oxide in Nanolayer Assemblies," *Science*, vol. 323, Feb. 2009, pp. 757-760.

[7] C. Mueller, J. Kerns, T. Ebeling, S. Nazarenko, A. Hiltner, and E. Baer, "Microlayer coextrusion processing and applications," *Polymer Process Engineering 97*, 1997, pp. 137–157.

[8] Y. Lin, P. Dias, H. Chen, A. Hiltner, and E. Baer, "Relationship between biaxial orientation and oxygen permeability of polypropylene film," *Polymer*, vol. 49, May. 2008, pp. 2578-86.

[9] R. Liu, T. Bernal-Lara, A. Hiltner, and E. Baer, "Interphase materials by forced assembly of glassy polymers," *Macromolecules*, vol. 37, 2004, pp. 6972-6979.

[10] R.J. Freemantle and R.E. Challis, "Combined compression and shear wave ultrasonic measurements on curing adhesive," *Measurement Science and Technology*, vol. 9, 1998, pp. 1291-1302.

[11] S. Lippert, E. Rang, and M. Grimm, "The wave-in-a-tube method for estimation of mechanical properties of viscoelastic materials using ultrasound," *Journal of Testing and Evaluation*, vol. 31, Jan. 2003, pp. 73-8.

[12] K.F. Graff, *Wave motion in elastic solids*, Courier Dover Publications, 1991.

[13] B.A. Auld, *Acoustic fields and waves in solids*, (Malabar, Fla): R.E. Krieger, 1990.

[14] I.M. Ward and J. Sweeney, *An introduction to the mechanical properties of solid polymers*, Wiley, 2004.

[15] D.I. Bower, *An introduction to polymer physics*, Cambridge University Press, 2002.

[16] T.A. Osswald and G. Menges, *Materials Science of Polymers for Engineers*, Hanser Gardner Publications, 2003.

[17] W.N. Findley, J.S. Lai, and K. Onaran, *Creep and relaxation of nonlinear viscoelastic materials*, Courier Dover Publications, 1989.

[18] Y. Lipatov, "Interphase phenomena in polymer blends," *Vysokomolekulyarnye Soedineniya, Seriya A*, vol. 20, Jan. 1978, pp. 3-16.

[19] J. Ren, A. Silva, and R. Krishnamoorti, "Linear Viscoelasticity of Disordered Polystyrene-Polyisoprene Block Copolymer Based Layered-Silicate Nanocomposites," *Macromolecules*, vol. 33, May. 2000, pp. 3739-3746.

[20] W.F. Ames, *Numerical Methods For Partial Differential Equations*, Academic Press Inc, 1984.

[21] N. Sottos and R. McCullough, “Interphase in polymer-matrix composites,” New York, NY, United States: Publ by ASME, 1994, pp. 328-350.
[22] T. Kazmierczak, H. Song, A. Hiltner, and E. Baer, “Polymeric one-dimensional photonic crystals by continuous coextrusion,” *Macromolecular Rapid Communications*, vol. 28, 2007, pp. 2210-2216.
[23] J. Zhou and K. Komvopoulos, “Interfacial viscoelasticity of thin polymer films studied by nanoscale dynamic mechanical analysis,” *Applied Physics Letters*, vol. 90, 2007, p. 021910.
[24] A. Krupicka, M. Johansson, and A. Hult, “Viscoelasticity in polymer films on rigid substrates,” *Macromolecular Materials and Engineering*, vol. 288, 2003, pp. 108-116.
[25] G. Possart, M. Presser, S. Passlack, P. Geiss, M. Kopnarski, A. Brodyanski, and P. Steinmann, “Micro-macro characterisation of DGEBA-based epoxies as a preliminary to polymer interphase modelling,” *International Journal of Adhesion and Adhesives*, vol. 29, Jul. 2009, pp. 478-87.
[26] M.H. Jarlath, D. Joachin, and S. Wolgang, “Relationship between the Mechanical and Ultrasound Properties of Polymer Materials,” 2006.
[27] A. Chertov and R. Maev, “A one-dimensional numerical model of acoustic wave propagation in a multilayered structure of a resistance spot weld,” *IEEE Transactions on Ultrasonics, Ferroelectrics and Frequency Control*, vol. 52, Oct. 2005, pp. 1783-90.
[28] A. Safaeinili, O. Lobkis, and D. Chimenti, “Air-coupled ultrasonic estimation of viscoelastic stiffnesses in plates,” *IEEE Transactions on Ultrasonics, Ferroelectrics and Frequency Control*, vol. 43, Nov. 1996, pp. 1171-80.
[29] Y. Song and S. Yang, “A method for acoustic parameter measurement of viscoelastic material,” *Ultrasonics*, vol. 44, 2006, pp. e1453-e1456.
[30] A. Baghani, H. Eskandari, S. Salcudean, and R. Rohling, “Measurement of viscoelastic properties of tissue-mimicking material using longitudinal wave excitation,” *IEEE Transactions on Ultrasonics, Ferroelectrics and Frequency Control*, vol. 56, Jul. 2009, pp. 1405-18.
[31] “Acoustical Properties,” *Food Physics*, 2007, pp. 417-426.
[32] Hull J.B., Langton C.M., Barker S., and Jones A.R., “Identification and characterisation of materials by broadband ultrasonic attenuation analysis,” *Journal of Materials Processing Technology*, vol. 56, Jan. 1996, pp. 148-157.
[33] L. Peirlinckx, P. Guillaume, R. Pintelon, and L. Van Biesen, “A global system identification approach for the accurate parametric modeling of ultrasonic reflection and transmission experiments,” *IEEE Transactions on Ultrasonics, Ferroelectrics and Frequency Control*, vol. 43, Jul. 1996, pp. 628-39.
[34] M. Hirao, H. Ogi, and K. Sato, “Interface delamination of layered media: acoustic spectroscopy and modal analysis,” *IEEE Transactions on Ultrasonics, Ferroelectrics, and Frequency Control*, vol. 51, Apr. 2004, pp. 439-443.
[35] R. Raisutis, L. Mazeika, R. Kazys, and A. Vladisauskas, “Application of the ultrasonic pulse-echo technique for quality control of the multi- layered electronic components,” *Ultragarsas*, vol. 62, 2007, pp. 33-8.
[36] S.-. Wooh and C. Wei, “A high-fidelity ultrasonic pulse-echo scheme for detecting delaminations in composite laminates,” *Composites Part B: Engineering*, vol. 30, Jul. 1999, pp. 433-441.
[37] J. de Belleval and C. Potel, “Numerical modelling of ultrasound propagation in

multilayered structures - application to adhesive bond testing," *IEE Seminar Digests*, vol. 1997, Jan. 1997, p. 3.
[38] C. Potel and J. de Belleval, "Acoustic propagation in anisotropic periodically multilayered media: A method to solve numerical instabilities," *Journal of Applied Physics*, vol. 74, 1993, p. 2208.
[39] B. Hosten and M. Castaings, "Transfer matrix of multilayered absorbing and anisotropic media. Measurements and simulations of ultrasonic wave propagation through composite materials," *The Journal of the Acoustical Society of America*, vol. 94, 1993, pp. 1488-1495.
[40] S. Huo and H. Reis, "A parametric study of guided mechanical waves in windshields: a three-layer laminated structure," San Diego, California, USA: SPIE, 2008, pp. 69322O-12.
[41] W. Cheng, N. Gomopoulos, G. Fytas, T. Gorishnyy, J. Walish, E. L. Thomas, A. Hiltner, and E. Baer., "Phonon Dispersion and Nanomechanical Properties of Periodic 1D Multilayer Polymer Films.," *Nano Letters.*, vol. 8, Mar. 2008.
[42] P. Stucky and W. Lord, "Finite element modeling of transient ultrasonic waves in linear viscoelastic media," *IEEE Transactions on Ultrasonics, Ferroelectrics and Frequency Control*, vol. 48, Jan. 2001, pp. 6-16.
[43] Z. You, M. Lusk, R. Ludwig, and W. Lord, "Numerical simulation of ultrasonic wave propagation in anisotropic and attenuative solid materials," *IEEE Transactions on Ultrasonics, Ferroelectrics and Frequency Control*, vol. 38, Sep. 1991, pp. 436-45.
[44] D. Belgroune, J.F. de Belleval, and H. Djelouah, "A theoretical study of ultrasonic wave transmission through a fluid-solid interface," *Ultrasonics*, vol. 48, Jul. 2008, pp. 220-230.
[45] F.T. Fisher and L.C. Brinson, "Viscoelastic interphases in polymer-matrix composites: theoretical models and finite-element analysis," *Composites Science and Technology*, vol. 61, Apr. 2001, pp. 731-748.
[46] Y. Benveniste, "A new approach to the application of Mori-Tanaka's theory in composite materials," *Mechanics of Materials*, vol. 6, Jun. 1987, pp. 147-157.
[47] "Ultrasonic Testing Equipment & Information Ultrasonic Testing Equipment & Information Ultrasonic Testing Equipment & Information," May. 2010.
[48] "Imaginant - Maker of Digital Cameras, Ultrasonic Pulser/Receivers and Thickness Gauges," May. 2010.
[49] L. Reinisch and R.H. Ossoff, "Acoustic effects during bone ablation," Los Angeles, CA, USA: Publ by Society of Photo-Optical Instrumentation Engineers, 1993, pp. 112-121.
[50] "LeCroy - Oscilloscopes," May. 2010.
[51] "Motorized Products Index," May. 2010.
[52] A.V. Oppenheim, R.W. Schafer, and J.R. Buck, *Discrete-Time Signal Processing (2nd Edition)*, Prentice Hall, 1999.
[53] A. R\ätzer-Scheibe, M. Klasing, M. Werner, M. Ivanenko, and P. Hering, "Acoustic monitoring of bone ablation using pulsed CO2 lasers."
[54] J. Carlson, J. Van Deventer, A. Scolan, and C. Carlander, "Frequency and temperature dependence of acoustic properties of polymers used in pulse-echo systems," *2003 IEEE Ultrasonics Symposium - Proceedings, October 5, 2003 - October 8, 2003*, Honolulu, HI, United states: Institute of Electrical and Electronics Engineers Inc., 2003, pp. 885-888.
[55] T. Chen, B. Ho, and H. Zapp, "Impedance and attenuation profile estimation of multilayered material from reflected ultrasound," *IEEE Transactions on Instrumentation and Measurement*, vol. 40, 1991, pp. 787-91.
[56] K.C. Hepfer and J.A. Rayne, "Ultrasonic Attenuation in Aluminum," *Physical Review B*,

vol. 4, 1971, p. 1050.
[57] K. Arisawa, H. Hirose, M. Ishikawa, T. Harada, and Y. Wada, “Mechanical Dispersions in Polycarbonate,” *Japanese Journal of Applied Physics*, vol. 2, 1963, pp. 695-701.
[58] K. Jhang, “Nonlinear ultrasonic techniques for nondestructive assessment of micro damage in material: A review,” *International Journal of Precision Engineering and Manufacturing*, vol. 10, Jan. 2009, pp. 123-135.
[59] W. Song, X. Wang, and M. Li, “Study on the denoising method for the electromagnetic ultrasonic echoes from multiple interfaces,” *Shengxue Xuebao/Acta Acustica*, vol. 32, 2007, pp. 226-231.
[60] “RIT's Research Computing | Home.”
[61] G.E. Quiroga-Goode, E.S. Krebes, and L.H.T. Le, “Modeling viscoelastic waves: a comparison of ray theory and the finite-difference method,” *Bulletin of the Seismological Society of America*, vol. 84, Dec. 1994, pp. 1882-1888.
[62] M. Hayner, “Optimized finite difference schemes for wave propagation in high loss viscoelastic material,” 1994.
[63] J.O. Blanch, J.O. Robertsson, and W.W. Symes, *Viscoelastic Finite Difference Modeling*, 1993.
[64] M. El-Mikkawy and A. Karawia, “Inversion of general tridiagonal matrices,” *Applied Mathematics Letters*, vol. 19, Aug. 2006, pp. 712-720.
[65] T. Downing, R. Kumar, W. Cross, L. Kjerengtroen, and J. Kellar, “Determining the interphase thickness and properties in polymer matrix composites using phase imaging atomic force microscopy and nanoindentation,” *Journal of Adhesion Science and Technology*, vol. 14, 2000, pp. 1801-12.

Appendices

Appendix A: Damped Finite Element Derivation

Definition of problem:

$$-\nabla \cdot T = \rho \ddot{u}$$
$$1D\ in\ Z \in [0\ L_e]\ \ with\ u(z,t)$$

Decoupling of problem into longitudinal and shear component:

$$M * \nabla\nabla \cdot u - G * \nabla\dot{x}\nabla x\dot{u} = \rho\ddot{u}$$

$$\left[M_g + \dot{M} *\right] * \nabla\nabla \cdot u - \left[G_g + \dot{G} *\right] * \nabla x\nabla x\dot{u} = \rho\ddot{u}$$

$$\left[M_g + \dot{M} *\right] * \nabla\nabla \cdot u \doteq \rho\ddot{u}$$

Determination of function for functional minimization and :

For time dependant stress condition: $T = CS + \eta\frac{dS}{dt}$

$$-\nabla \cdot \left(CS + \eta\frac{dS}{dt}\right) = \rho\ddot{u}$$

$$\nabla \cdot \mathrm{CS} + \nabla \cdot \left(\eta\dot{\mathrm{S}}\right) = \rho\ddot{u}$$

$$\mathrm{F} = M_L \int_0^{L_e} \frac{\partial u}{\partial z}\frac{\partial v}{\partial z}dz \int_0^{L_e} v\ddot{u}dz + \int_0^{\mathrm{L_e}} \frac{\partial\dot{\mathrm{u}}}{\partial \mathrm{z}}\frac{\partial \mathrm{v}}{\partial \mathrm{z}}dz - vh(t)$$

Note that the M, K, and R terms remain the same and a D matrix is created

$$D_{ij}^{e} = \eta \int_{0}^{L_e} \frac{\partial \varphi_i}{\partial z} \frac{\partial \varphi_j}{\partial z} dz$$

This makes the whole formulation of the viscoelastic form of the simulation:

$$D_{ij}^{e} = \eta \int_{0}^{L_e} \frac{\partial \varphi_i}{\partial z} \frac{\partial \varphi_j}{\partial z} dz$$

$$K_{ij}^{e} = M_L \int_{0}^{L_e} \frac{\partial \varphi_i}{\partial z} \frac{\partial \varphi_j}{\partial z} dz$$

$$M_{ij}^{e} = \rho \int_{0}^{L_e} \varphi_i \varphi_j \, dz$$

$$R_i^e = h(t)\varphi_i(L_e)$$

$$M\ddot{U}_t + D\dot{U}_t + KU_t = R_t$$

Using Finite Difference, the Matrix equation can be solved as:

$$\frac{M}{\Delta t^2} U_{t+\Delta t} = R_t - \left(K + \frac{D}{\Delta t} - \frac{2M}{\Delta t^2}\right) U_t + \left(\frac{D}{\Delta t} - \frac{M}{\Delta t^2}\right) U_{t-\Delta t}$$

Appendix B: B scan imaging of samples

While they were not used for analysis, B scan imaging could be performed. The B scan imaging does not allow direct extraction of properties, but is useful for visualizing the samples. With the B scan images generated, we can see the layer interfaces. This technique was used to demonstrate proper imaging during development of techniques, and during experimental work to verify expected results. Examples of the B scans can be are shown in the next pages

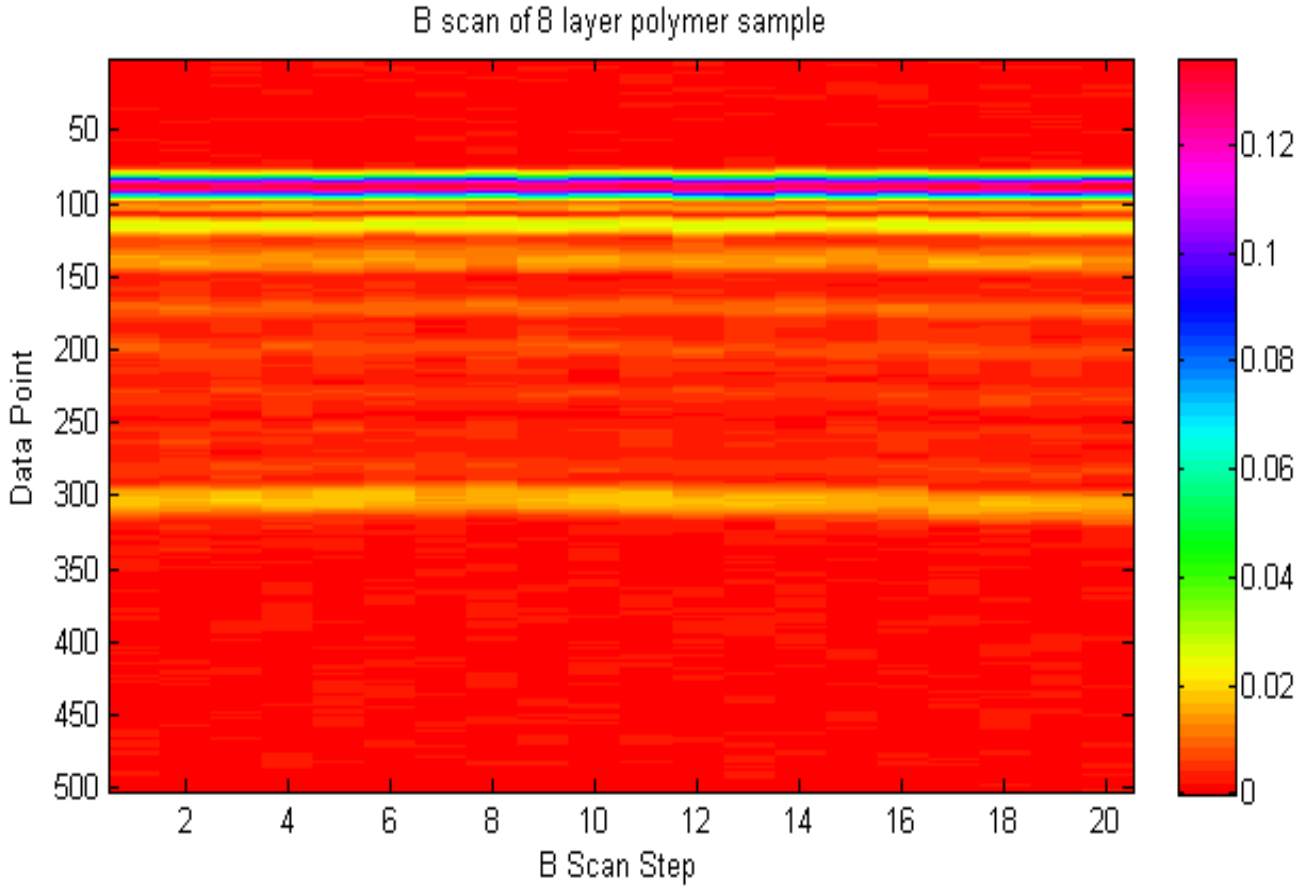

B scan showing individual Hilbert Transforms aligned adjacent to each other. Scan is of 8 layer PC and PMMA sample with layer thickness of approximately 70μm. Imaging of interface reflections is visible with decreasing magnitude internally and large front and back reflections.

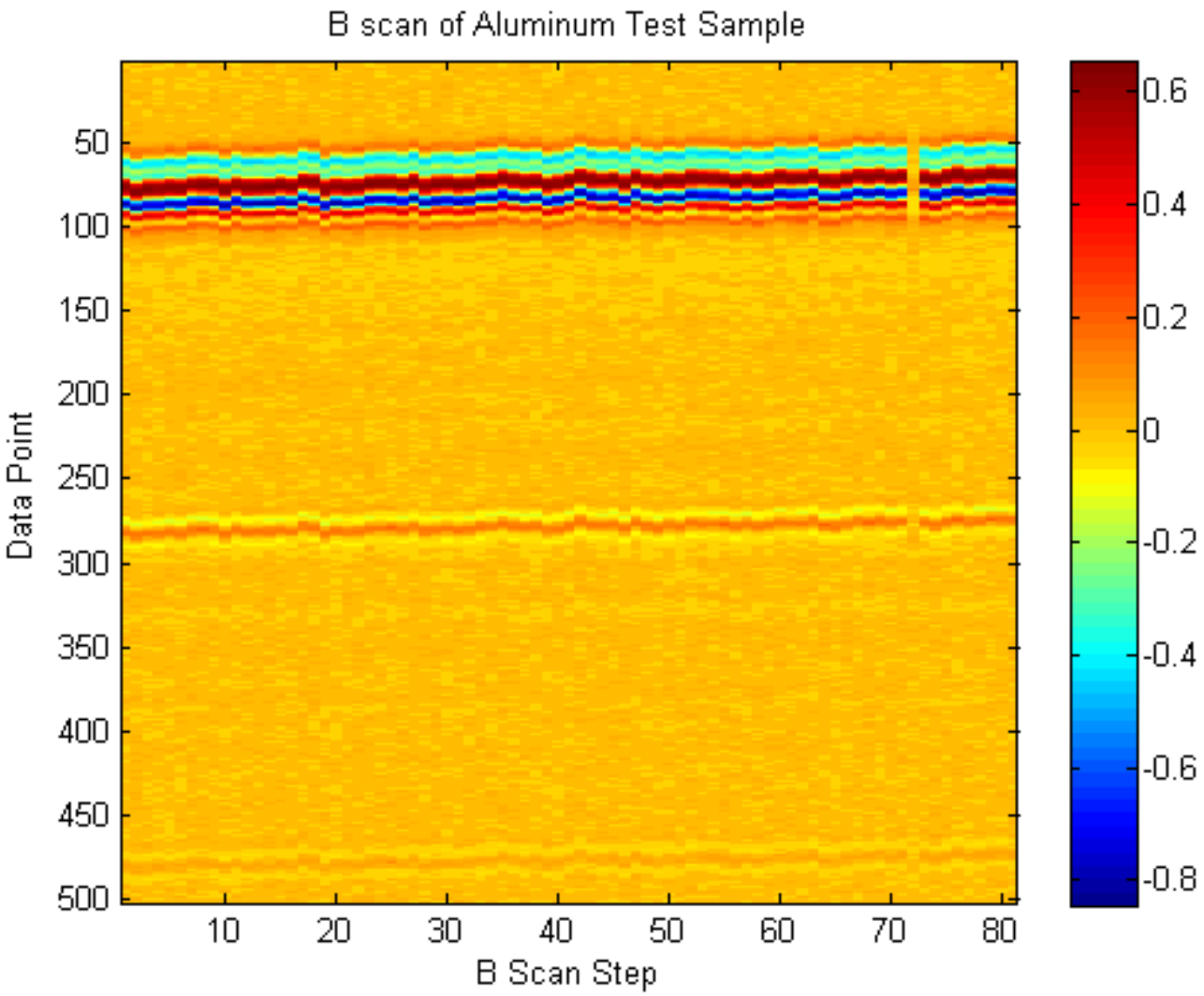

B scan showing individual A scans adjacent to each other. Scan is of aluminum calibration sample with thickness of 0.051in (1295μm). Imaging of front and back surface as well as second internal reflection. Image also shows Dropped scan (at x-axis=72) representative of type of error removed for analysis

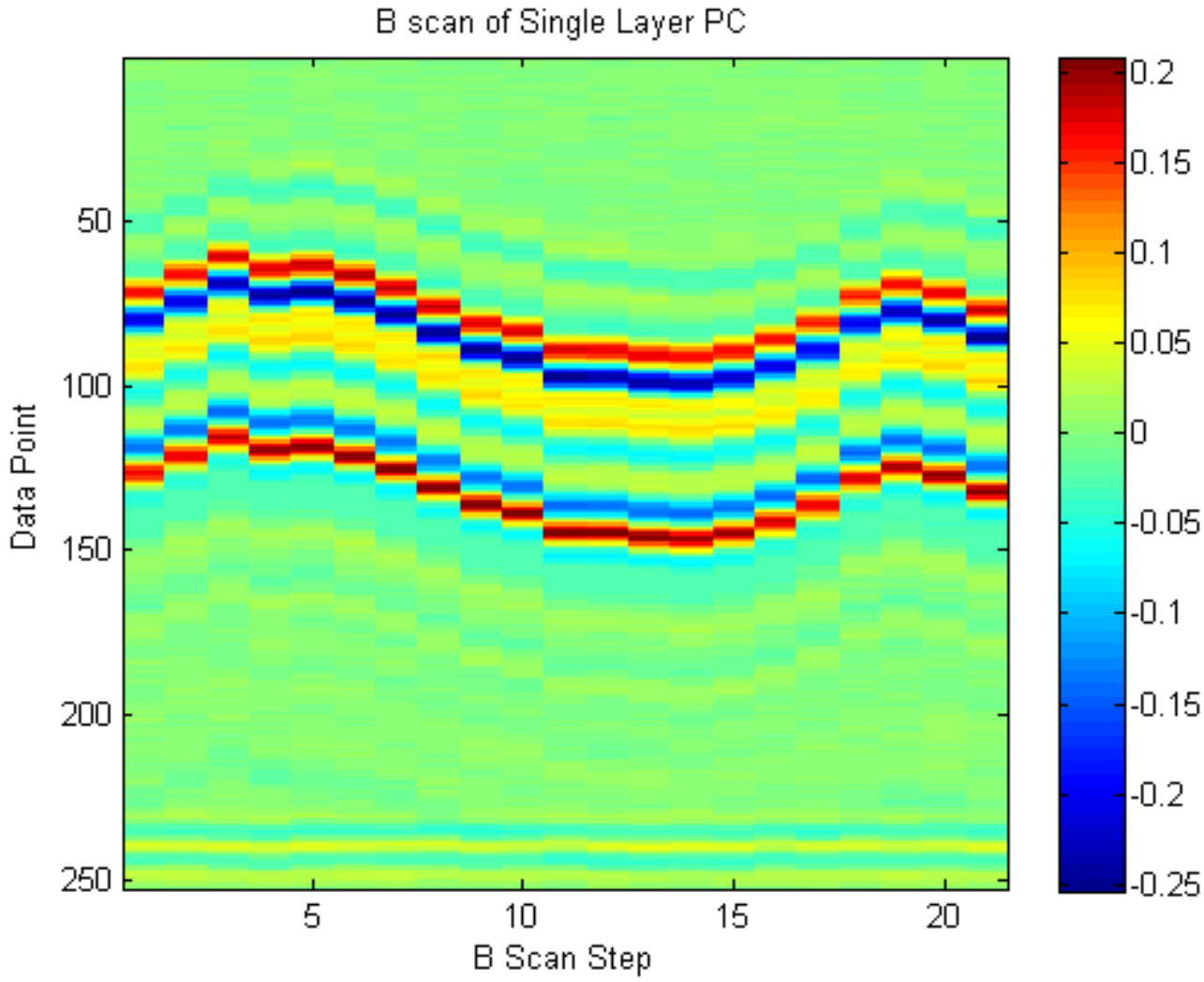

B scan showing individual A scans adjacent to each other. Scan of single layer PC with layer thickness of approximately 60μm. Scan shows surface variation, as well as the magnitude and location of the front and back reflections. Note higher magnitude region between major peaks when compared to area outside peaks. This is indicative of pulse overlap, zero delay, and internal interference.

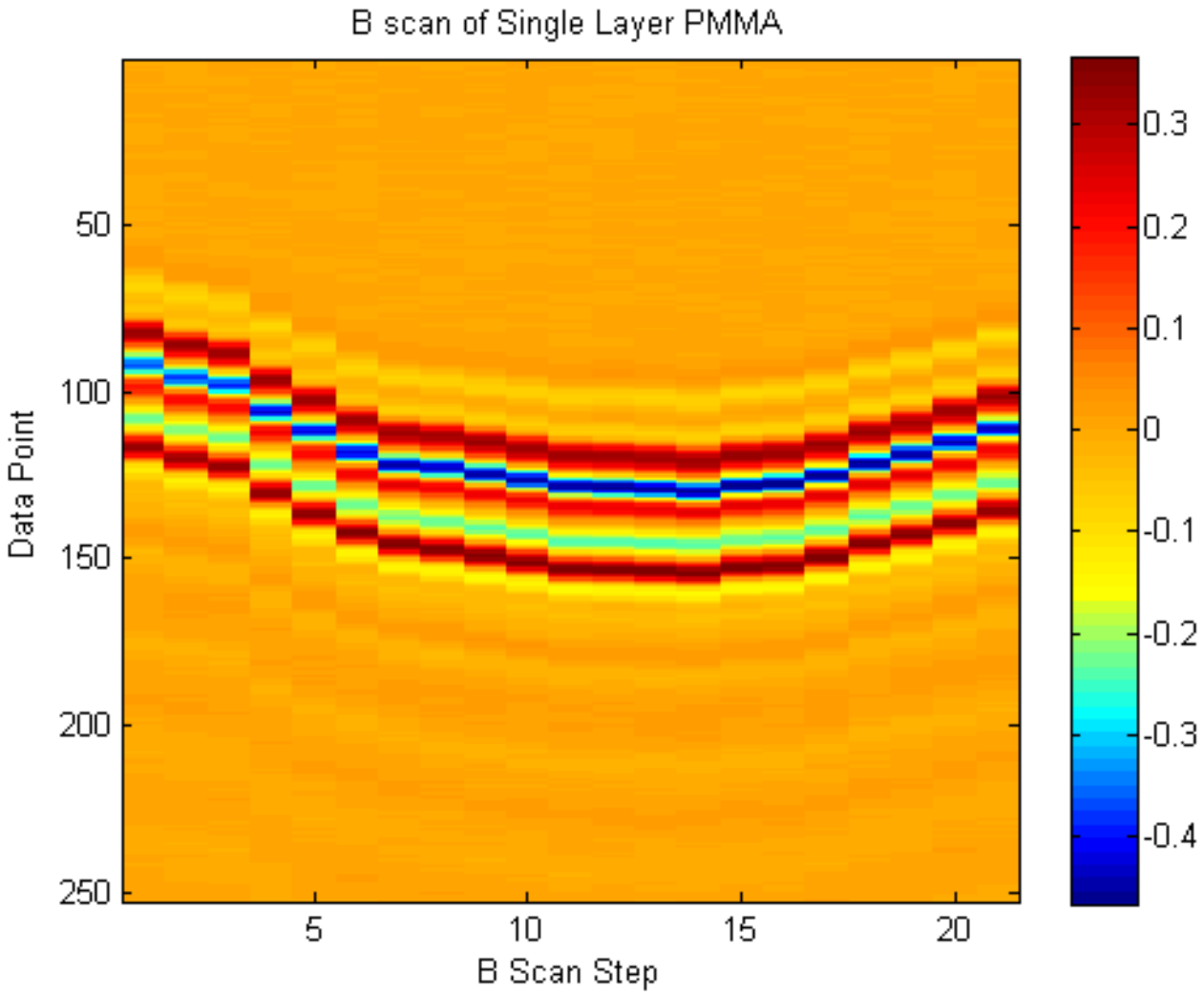

B scan showing individual A scans adjacent to each other. Scan of single layer PMMA with layer thickness of approximately 60μm. Scan shows surface variation, as well as the magnitude and location of the front and back reflections. Note higher magnitude region between major peaks when compared to area outside peaks. This is indicative of pulse overlap, zero delay, and internal interference.

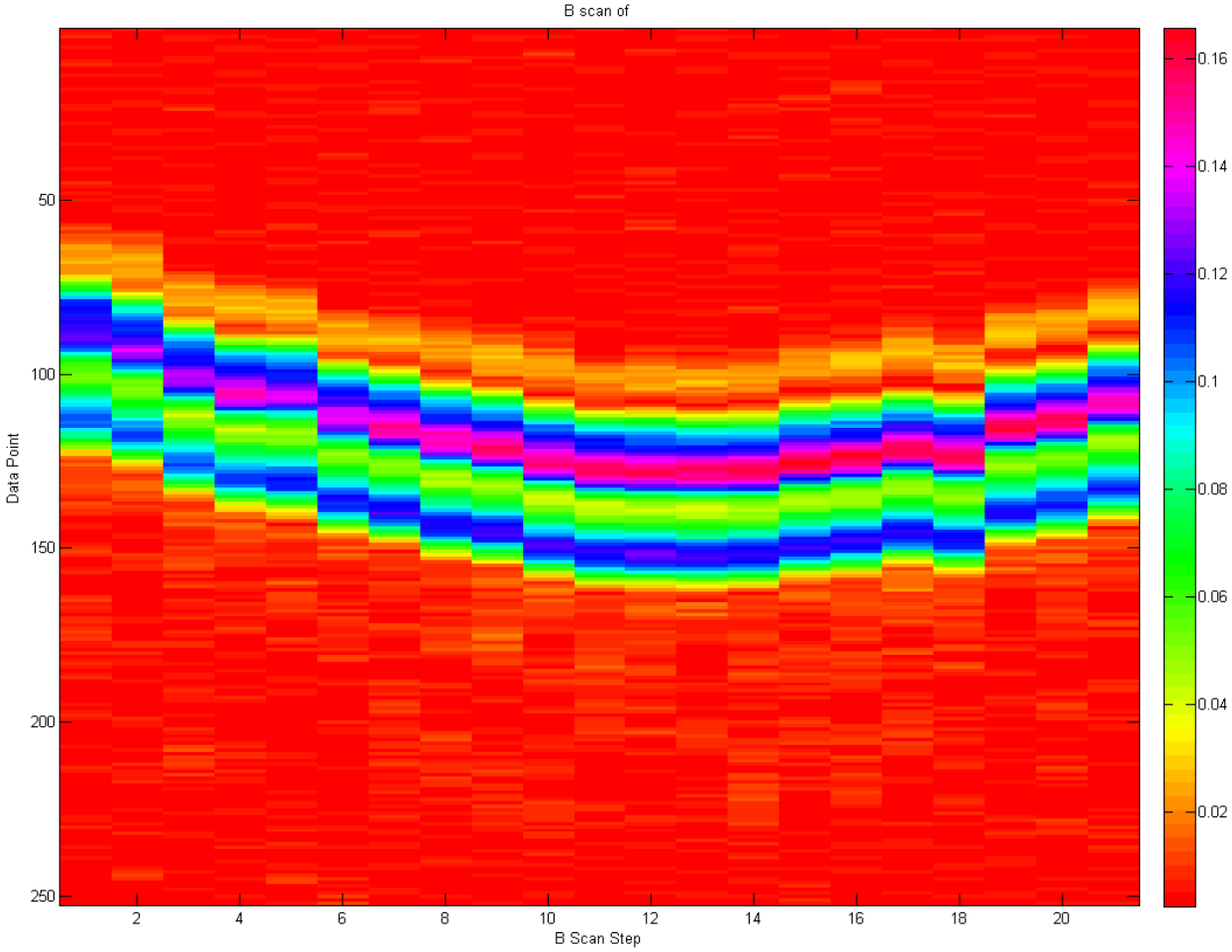

B scan showing individual Hilbert transforms adjacent to each other. Scan of two layer sample with layer thickness of approximately 60µm. Scan shows surface variation, as well as the magnitude and location of the front back and internal reflections (green areas). Note higher magnitude region between major peaks when compared to area outside peaks. This is indicative of pulse overlap, zero delay, and internal interference.

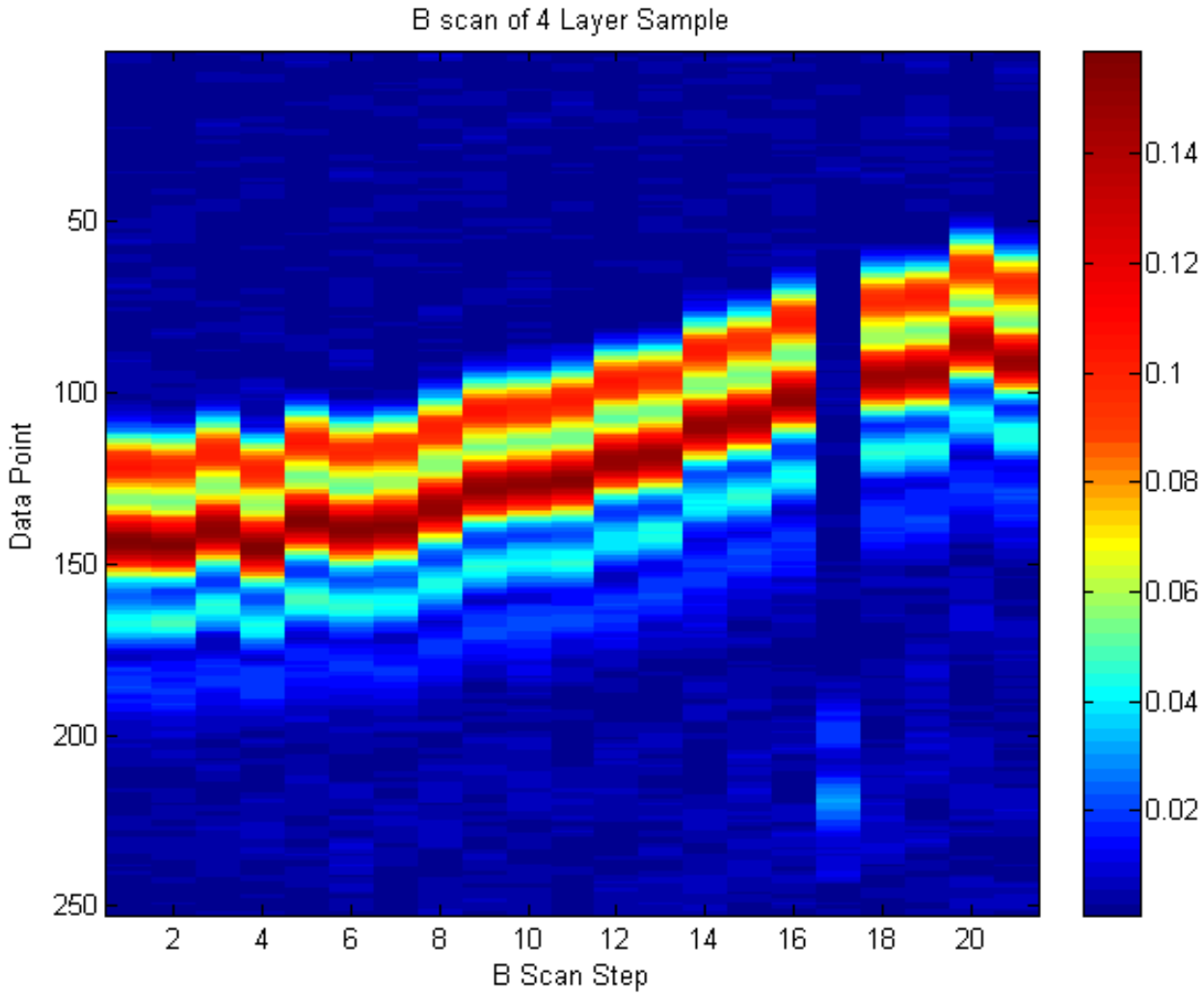

B scan showing individual Hilbert transforms adjacent to each other. Scan of four layer sample with layer thickness of approximately 60μm. Scan shows surface variation, as well as the magnitude and location of the front back and internal reflections. Note higher magnitude region between major peaks when compared to area outside peaks. This is indicative of pulse overlap, zero delay, and internal interference. Internal reflections are, unsurprisingly, more complicated and the internal peaks are less identifiable than those in the two layer sample.

Appendix C: Material Information

Polycarbonate (Makrolon 2207 from Bayer Material Science)

Bayer MaterialScience

Makrolon 2207

General purpose grades / Low viscosity

Global grade; MVR (300 °C/1.2 kg) 35 cm³/10 min; General purpose; Low viscosity; UV stabilized; Easy release; Injection molding - Melt temperature 280 - 320 °C; Available in transparent, translucent and opaque colors

ISO Shortname

ISO 7391-PC,MLR,(,,)-24-9

	Property	Test Condition	Unit	Standard	Value
Rheological properties					
C	Melt volume-flow rate	300 °C; 1.2 kg	cm³/10 min	ISO 1133	35
C	Molding shrinkage, parallel	60x60x2; 500 bar	%	ISO 294-4	0.65
C	Molding shrinkage, normal	60x60x2; 500 bar	%	ISO 294-4	0.65
	Molding shrinkage, parallel/normal	Value range based on general practical experience	%	b.o. ISO 2577	0.5 - 0.7
	Melt mass-flow rate	300 °C; 1.2 kg	g/10 min	ISO 1133	37
Mechanical properties (23 °C/50 % r. h.)					
C	Tensile modulus	1 mm/min	MPa	ISO 527-1,-2	2400
C	Yield stress	50 mm/min	MPa	ISO 527-1,-2	68
C	Yield strain	50 mm/min	%	ISO 527-1,-2	6.0
C	Nominal strain at break	50 mm/min	%	ISO 527-1,-2	> 50
	Stress at break	50 mm/min	MPa	ISO 527-1,-2	60
	Strain at break	50 mm/min	%	b.o. ISO 527-1,-2	115
C	Tensile creep modulus	1 h	MPa	ISO 899-1	2100
C	Tensile creep modulus	1000 h	MPa	ISO 899-1	1700
	Flexural modulus	2 mm/min	MPa	ISO 178	2350
	Flexural strength	2 mm/min	MPa	ISO 178	98
	Flexural strain at flexural strength	2 mm/min	%	ISO 178	7.0
	Flexural stress at 3.5 % strain	2 mm/min	MPa	ISO 178	74
C	Charpy impact strength	23 °C	kJ/m²	ISO 179-1eU	N
C	Charpy impact strength	-30 °C	kJ/m²	ISO 179-1eU	N
	Charpy impact strength	-60 °C	kJ/m²	ISO 179-1eU	N
	Charpy notched impact strength	23 °C; 3 mm	kJ/m²	ISO 7391/b.o. ISO 179-1eA	55P(C)
	Charpy notched impact strength	-30 °C; 3 mm	kJ/m²	ISO 7391/b.o. ISO 179-1eA	12C
	Izod notched impact strength	23 °C; 3.2 mm	kJ/m²	b.o. ISO 180-A	65P(C)
	Izod notched impact strength	-30 °C; 3.2 mm	kJ/m²	b.o. ISO 180-A	12C
C	Puncture maximum force	23 °C	N	ISO 6603-2	4900
C	Puncture maximum force	-30 °C	N	ISO 6603-2	5900
C	Puncture energy	23 °C	J	ISO 6603-2	55
C	Puncture energy	-30 °C	J	ISO 6603-2	80
	Ball indentation hardness		N/mm²	ISO 2039-1	116

	Property	Test Condition	Unit	Standard	Value
Thermal properties					
C	Glass transition temperature	10 °C/min	°C	ISO 11357-1,-2	144
C	Temperature of deflection under load	1.80 MPa	°C	ISO 75-1,-2	123
C	Temperature of deflection under load	0.45 MPa	°C	ISO 75-1,-2	138
C	Vicat softening temperature	50 N; 50 °C/h	°C	ISO 306	144
	Vicat softening temperature	50 N; 120 °C/h	°C	ISO 306	145
C	Coefficient of linear thermal expansion, parallel	23 to 55 °C	10^{-4}/K	ISO 11359-1,-2	0.65
C	Coefficient of linear thermal expansion, transverse	23 to 55 °C	10^{-4}/K	ISO 11359-1,-2	0.65
C	Burning behavior UL 94 [UL recognition]	0.75 mm	Class	UL 94	V-2 (CL)
	Burning behavior UL 94 [UL recognition]	2.9 mm	Class	UL 94	HB (CL)
C	Oxygen index	Method A	%	ISO 4589-2	27
	Thermal conductivity	23 °C	W/(m·K)	ISO 8302	0.20
	Resistance to heat (ball pressure test)		°C	IEC 60695-10-2	135
	Relative temperature index (Tensile strength) [UL recognition]	1.5 mm	°C	UL 746B	80
	Relative temperature index (Tensile impact strength) [UL recognition]	1.5 mm	°C	UL 746B	80
	Relative temperature index (Electric strength) [UL recognition]	1.5 mm	°C	UL 746B	80
	Glow wire test (GWFI)	1.0 mm	°C	IEC 60695-2-12	850
	Glow wire test (GWFI)	1.5 mm	°C	IEC 60695-2-12	850
	Glow wire test (GWFI)	2.0 mm	°C	IEC 60695-2-12	850
	Glow wire test (GWFI)	3.0 mm	°C	IEC 60695-2-12	930
	Glow wire test (GWFI)	4.0 mm	°C	IEC 60695-2-12	960
	Glow wire test (GWIT)	1.0 mm	°C	IEC 60695-2-13	875
	Glow wire test (GWIT)	1.5 mm	°C	IEC 60695-2-13	875
	Glow wire test (GWIT)	2.0 mm	°C	IEC 60695-2-13	875
	Glow wire test (GWIT)	3.0 mm	°C	IEC 60695-2-13	875
	Glow wire test (GWIT)	4.0 mm	°C	IEC 60695-2-13	875
	Application of flame from small burner	Method K and F; 2.0 mm	Class	DIN 53438-1,-3	K1, F1
	Needle flame test	Method K; 1.5 mm	s	IEC 60695-11-5	5
	Needle flame test	Method K; 2.0 mm	s	IEC 60695-11-5	5
	Needle flame test	Method K; 3.0 mm	s	IEC 60695-11-5	10
	Needle flame test	Method F; 1.5 mm	s	IEC 60695-11-5	60
	Needle flame test	Method F; 2.0 mm	s	IEC 60695-11-5	120
	Needle flame test	Method F; 3.0 mm	s	IEC 60695-11-5	120
	Burning rate (US-FMVSS)	>=1.0 mm	mm/min	ISO 3795	passed
	Flash ignition temperature		°C	ASTM D1929	480
	Self ignition temperature		°C	ASTM D1929	550

Electrical properties (23 °C/50 % r. h.)					
C	Relative permittivity	100 Hz	-	IEC 60250	3.1
C	Relative permittivity	1 MHz	-	IEC 60250	3.0
C	Dissipation factor	100 Hz	10^{-4}	IEC 60250	5
C	Dissipation factor	1 MHz	10^{-4}	IEC 60250	90
C	Volume resistivity		Ohm·m	IEC 60093	1E14
C	Surface resistivity		Ohm	IEC 60093	1E16
C	Electrical strength	1 mm	kV/mm	IEC 60243-1	34
C	Comparative tracking index CTI	Solution A	Rating	IEC 60112	250
	Comparative tracking index CTI M	Solution B	Rating	IEC 60112	125M
	Electrolytic corrosion		Rating	IEC 60426	A1

	Property	Test Condition	Unit	Standard	Value
Other properties (23 °C)					
C	Water absorption (saturation value)	Water at 23 °C	%	ISO 62	0.30
C	Water absorption (equilibrium value)	23 °C; 50 % r. h.	%	ISO 62	0.12
C	Density		kg/m³	ISO 1183-1	1190
	Water vapor permeability	23 °C; 85 % RH; 100 µm film	g/(m²·24 h)	ISO 15106-1	15
	Gas permeation	Oxygen; 100 µm film	cm³/(m²·24 h·bar)	b.o. ISO 2556	800
	Gas permeation	Oxygen; 25.4 µm (1 mil) film	cm³/(m²·24 h·bar)	b.o. ISO 2556	3150
	Gas permeation	Nitrogen; 100 µm film	cm³/(m²·24 h·bar)	b.o. ISO 2556	160
	Gas permeation	Nitrogen; 25.4 µm (1 mil) film	cm³/(m²·24 h·bar)	b.o. ISO 2556	630
	Gas permeation	Carbon dioxide; 100 µm film	cm³/(m²·24 h·bar)	b.o. ISO 2556	4800
	Gas permeation	Carbon dioxide; 25.4 µm (1 mil) film	cm³/(m²·24 h·bar)	b.o. ISO 2556	18900
	Bulk density	Pellets	kg/m³	ISO 60	660
Material specific properties					
	Refractive index	Procedure A	-	ISO 489	1.586
	Haze for transparent materials	3 mm	%	ISO 14782	< 0.8
	Luminous transmittance (clear transparent materials)	1 mm	%	ISO 13468-2	89
C	Luminous transmittance (clear transparent materials)	2 mm	%	ISO 13468-2	89
	Luminous transmittance (clear transparent materials)	3 mm	%	ISO 13468-2	88
	Luminous transmittance (clear transparent materials)	4 mm	%	ISO 13468-2	87
Processing conditions for test specimens					
C	Injection molding-Melt temperature		°C	ISO 294	280
C	Injection molding-Mold temperature		°C	ISO 294	80
C	Injection molding-Injection velocity		mm/s	ISO 294	200

C These property characteristics are taken from the CAMPUS plastics data bank and are based on the international catalogue of basic data for plastics according to ISO 10350.

Impact properties: N = non-break, P = partial break, C = complete break

Poly(methyl methacrylate) (Plexiglas® V826 acrylic resin)

Plexiglas® V826 acrylic resin

PROPERTIES	VALUE	UNITS	TEST METHOD
Physical			
Melt Flow Rate (230°C / 3.8 kg)	1.6	g / 10 min	ASTM D1238
Specific Gravity	1.19		ASTM D792
Mold Shrinkage	0.2-0.6	%	ASTM D955
Water Absorption (24 hr. immersion)	0.3	% weight gain	ASTM D570
Mechanical			
Tensile Strenght @ Maximum	10,200	PSI	ASTM D638
Tensile Elongation @ Break	6	%	"
Tensile Modulus	450,000	PSI	"
Flexural Strength, maximum (Yield)	15,000	PSI	ASTM D790
Flexural Modulus	450,000	PSI	ASTM D790
Notched Izod Impact(73°F/23°C)	0.3	ft-lb/in notch	ASTM D256
Rockwell Hardness	93	M	ASTM D785
Thermal			
HDT (0.455 MPa; annealed)[1]	221	°F	ASTM D648
HDT (1.82 MPa; annealed)[1]	216	°F	ASTM D648
Vicat Softening Point (50°C/hr; 10N)	232	°F	ASTM D1525
Vicat Softening Point (50°C/hr; 50N)	219	°F	ASTM D1525
Thermal Conductivity	1.3	BTU/hr*ft2*F/in	ASTM C177
Optical			
Refractive Index (ND @ 73°F)	1.49		ASTM D542
Luminous Transmittance (0.125"/3.2 mm.)	92	%	ASTM D1003
Haze (0.125 in./3.2 mm.)	<2	%	ASTM D1003
ASTM Classification		PMMA 0141V1	ASTM D788

Appendix D: Equipment Information

Equipment	Manufacturer	Model	Website
Transducer	Olympus	V3332 SU/RM	http://www.olympus-ims.com
Pulser	JSR	DPR500 w/Remote Pulser	http://www.jsrultrasonics.com/
Oscilloscope	LeCroy	LT 342	http://www.lecroy.com/
Motion Controller	Velmex	VXM-2 (2)	http://www.velmex.com/
Linear Slides	Velmex	MN10-0150-E01-21	
GUI	Mathworks	Matlab With custom code	http://www.mathworks.com/
Tank	Custom		
Sample Holder	Custom		
Couplant	Deionized and Degassed Water		

Appendix E: 30MHz scans

For testing purposes, scans were also taken using a 30MHz transducer. Scans were collected for single layer PMMA, 2 layer, and 4 layer samples. The results are seen on the following pages. They show furtherance of the influence of constructive and desctructive interference on the ability to measure properties. This is because the wavelengths are significantly thicker than the layer thicknesses. B scan images, and A sacan plots for the 3 different tested samples can be seen on the following pages. The wavelengths for the 30MHz transducer can be seen below.

Material	Clong (m/s)	Frequency (MHz)	λ(μm)
PC	2327	30	77.6
PMMA	2663	30	88.8

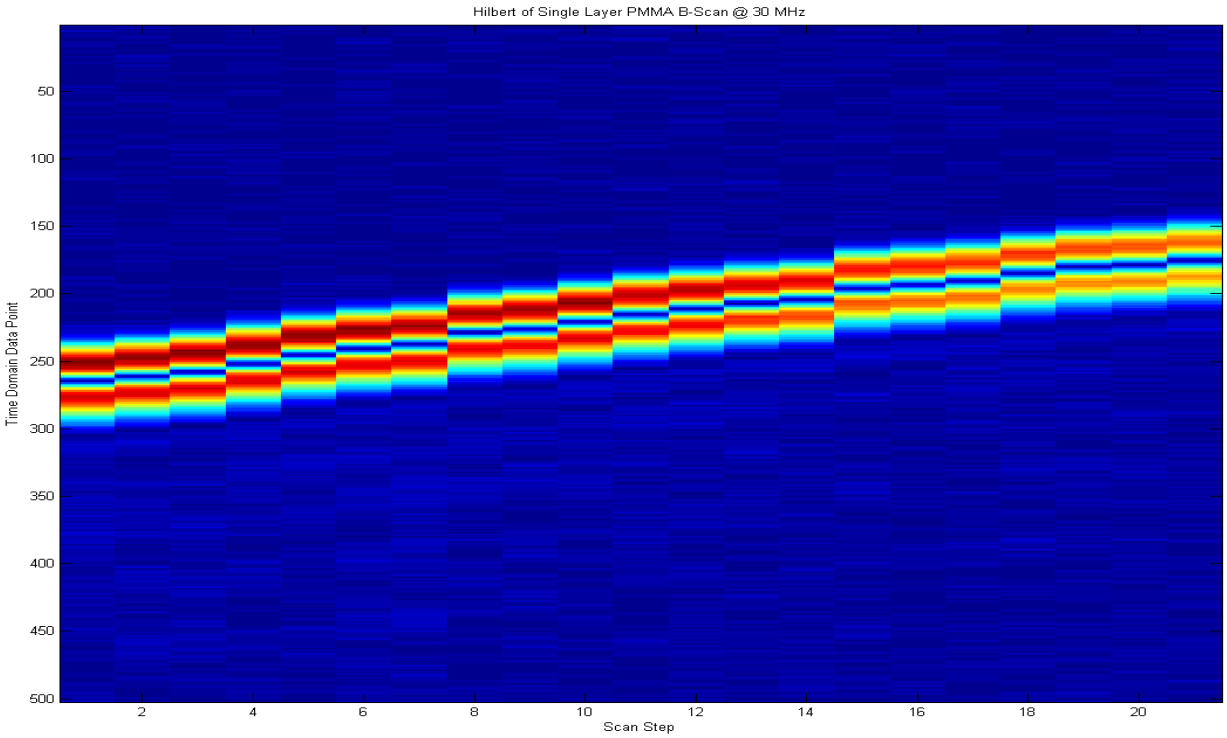
Hilbert of Single Layer PMMA B-Scan @ 30 MHz
Time Domain Data Point
Scan Step
50
100
150
200
250
300
350
400
450
500
2
4
6
8
10
12
14
16
18
20

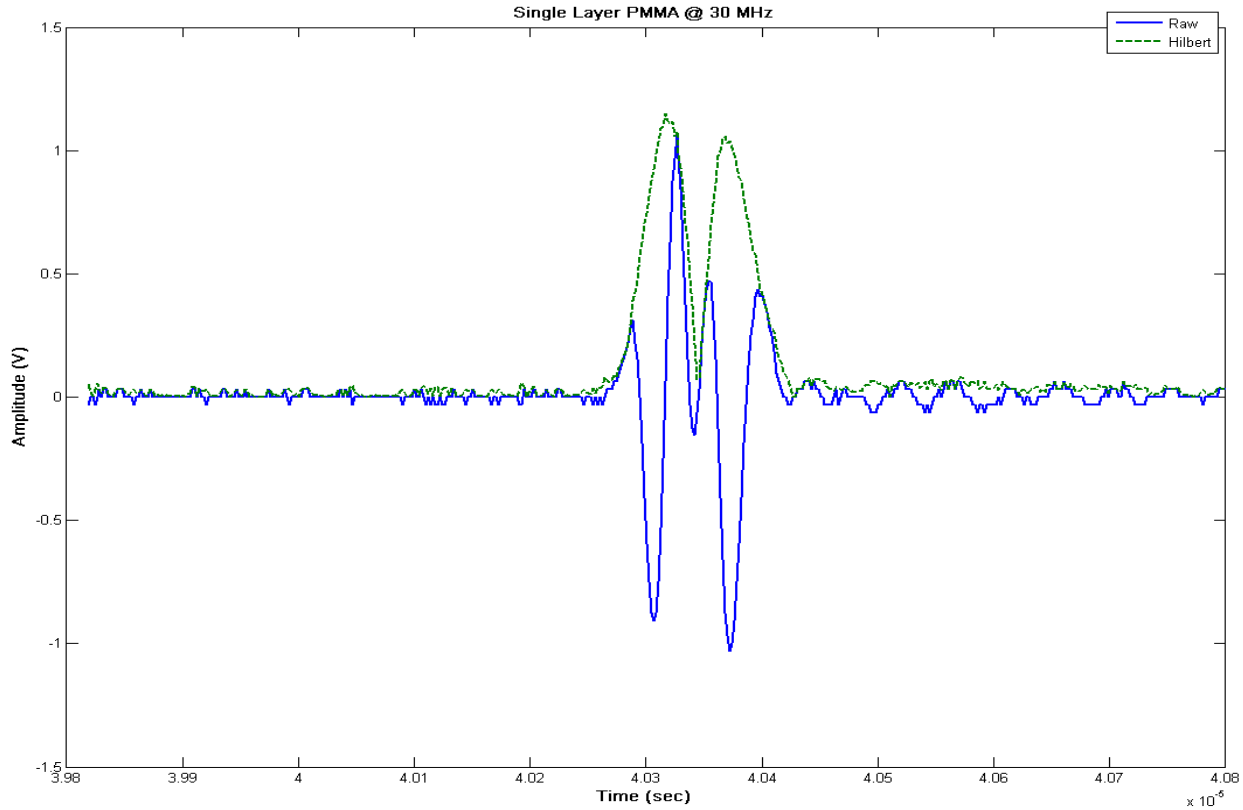
Single Layer PMMA @ 30 MHz
Raw
Hilbert
Amplitude (V)
Time (sec)
x 10^-5
1.5
1
0.5
0
-0.5
-1
-1.5
3.98
3.99
4
4.01
4.02
4.03
4.04
4.05
4.06
4.07
4.08

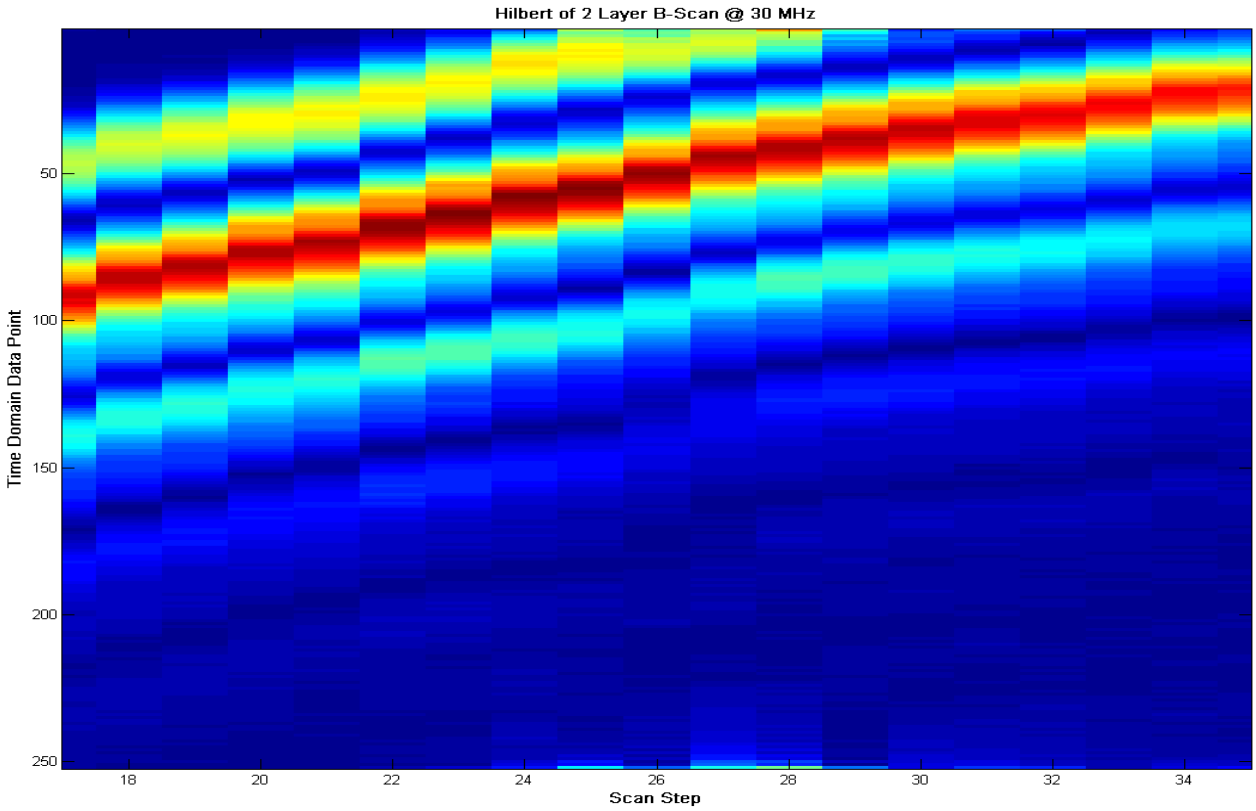
Hilbert of 2 Layer B-Scan @ 30 MHz
Time Domain Data Point
50
100
150
200
250
18
20
22
24
26
28
30
32
34
Scan Step

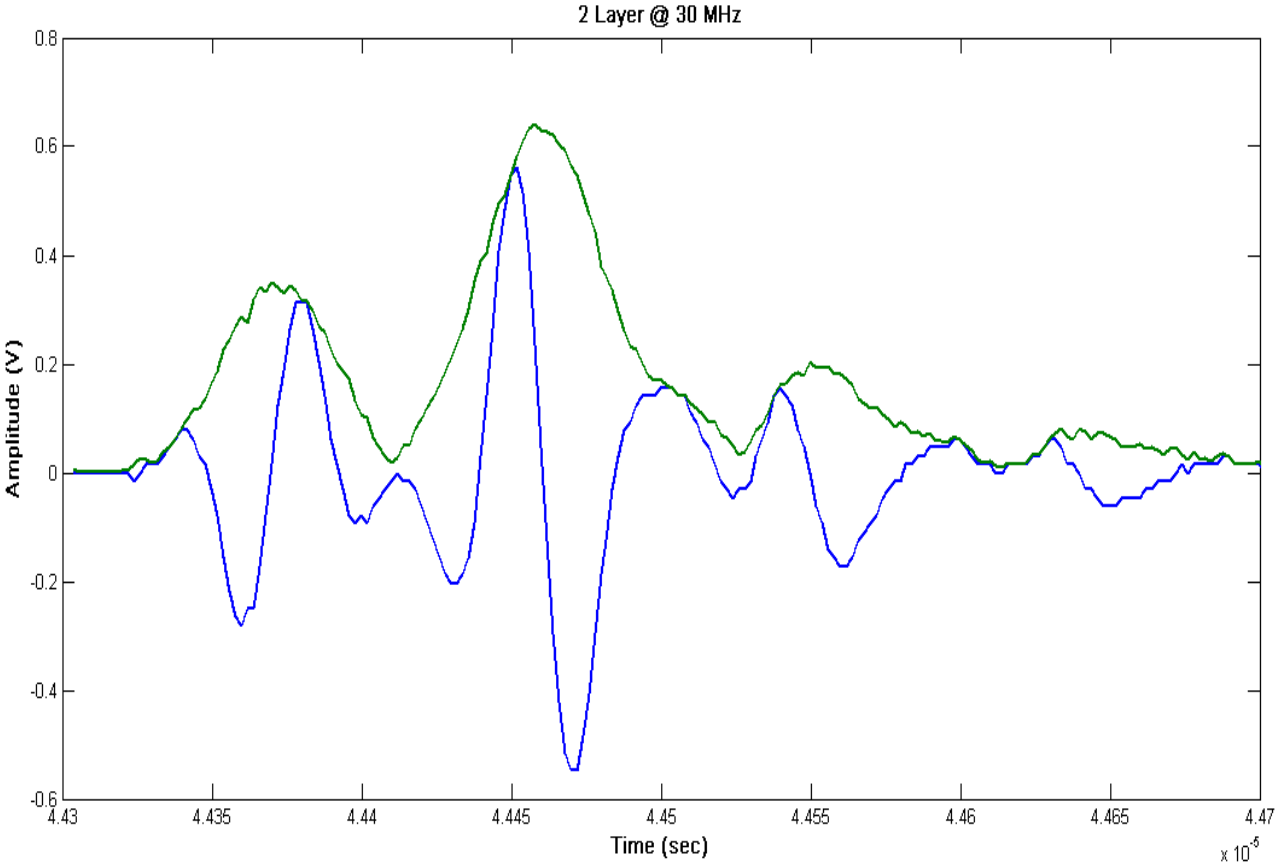
2 Layer @ 30 MHz
Amplitude (V)
0.8
0.6
0.4
0.2
0
-0.2
-0.4
-0.6
4.43
4.435
4.44
4.445
4.45
4.455
4.46
4.465
4.47
Time (sec)
x 10^-5

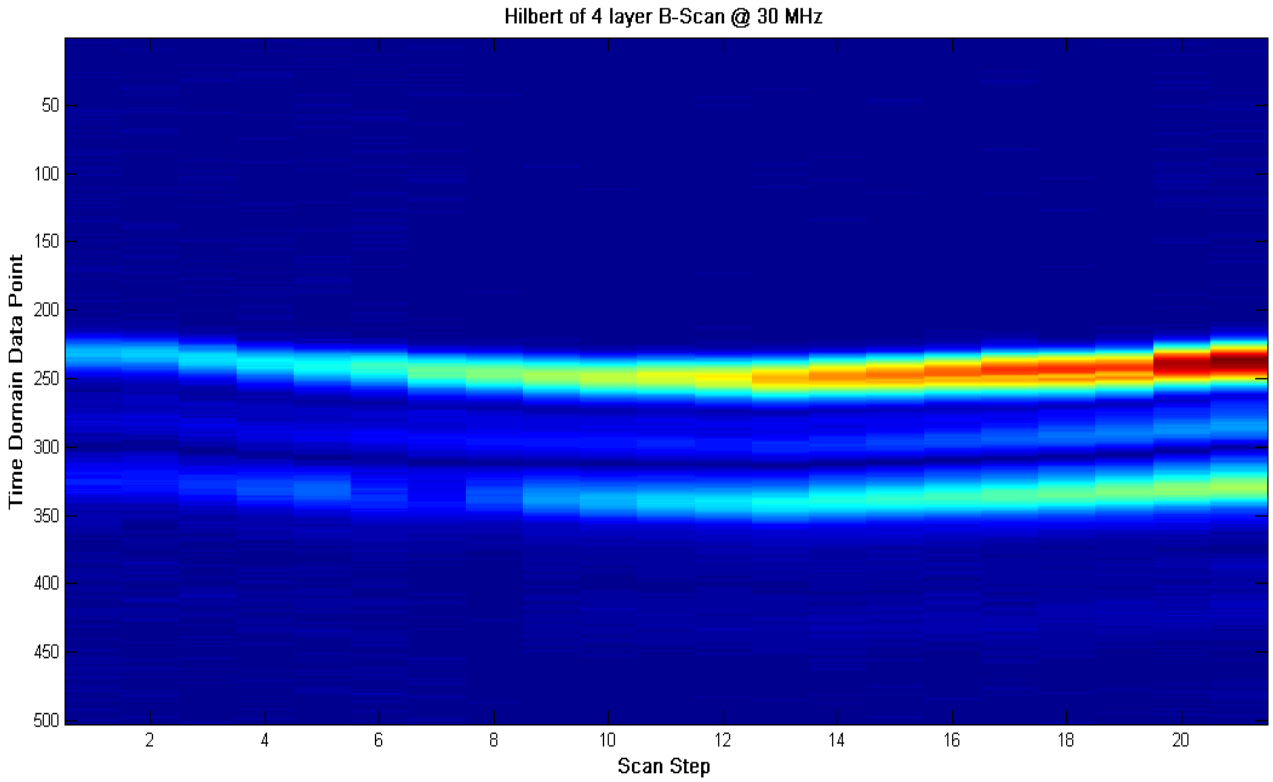
Hilbert of 4 layer B-Scan @ 30 MHz
Time Domain Data Point
50
100
150
200
250
300
350
400
450
500
2
4
6
8
10
12
14
16
18
20
Scan Step

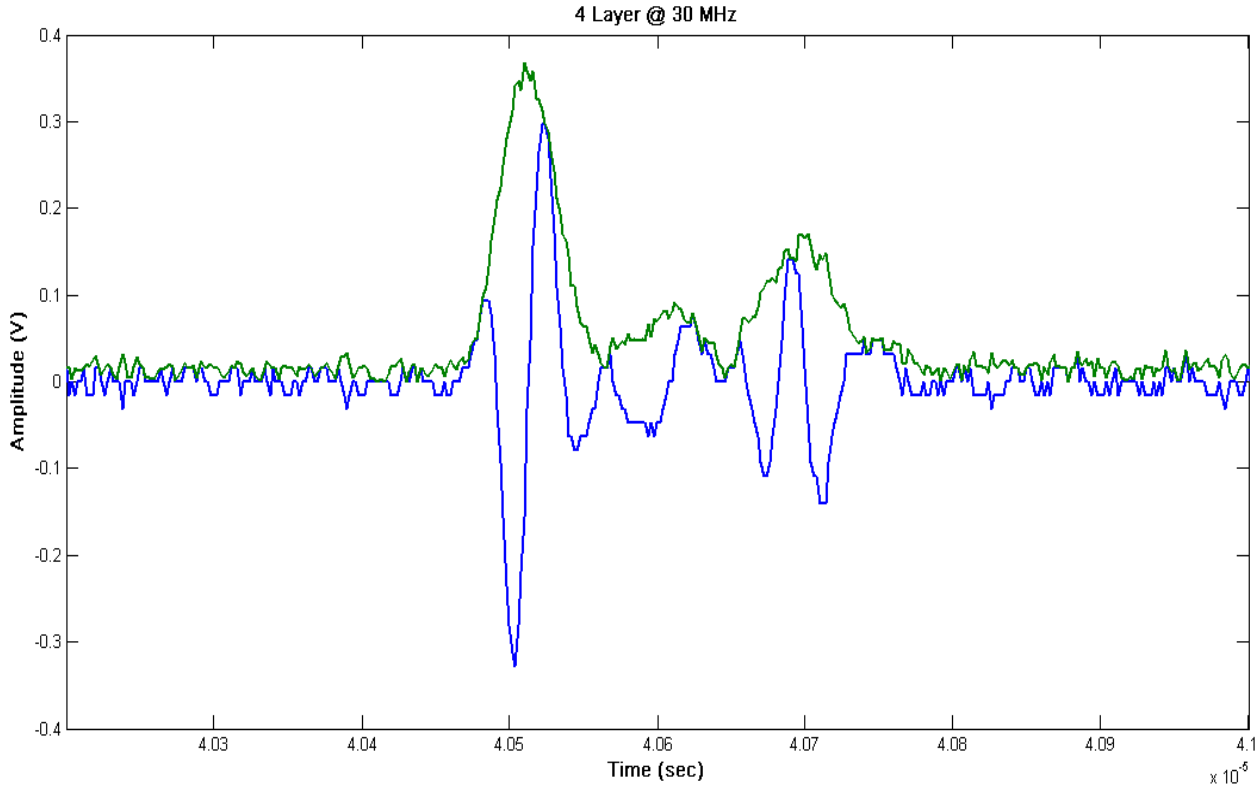
4 Layer @ 30 MHz
Amplitude (V)
0.4
0.3
0.2
0.1
0
-0.1
-0.2
-0.3
-0.4
4.03
4.04
4.05
4.06
4.07
4.08
4.09
4.1
Time (sec)
x 10^-5